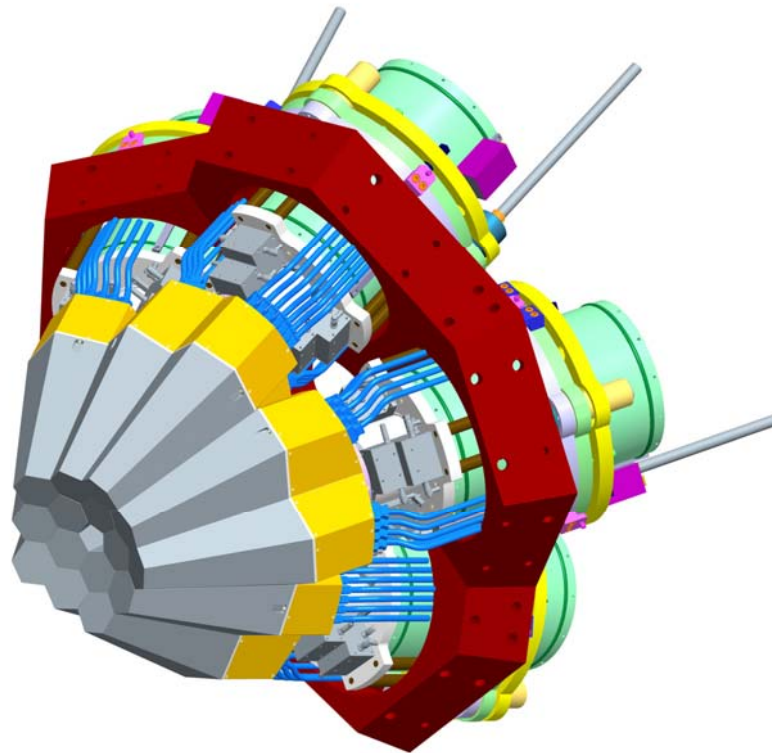


# AGATA

## *Advanced Gamma Tracking Array*

### TECHNICAL DESIGN REPORT



Edited by J. Simpson, J. Nyberg and W. Korten

December 2008



## Contributors

Dominique Curien, Gilbert Duchêne, Christian Finck, Camille Parisel, Cayetano Santos, Patrice Medina, Remy Baumann, Laurent Charles, El Mehdi Chambit, Marc Richer, Laurent Arnold, Jérôme Robin, Francois Didierjean, Inmaculada Piqueras, Christian Weber  
Institut Pluridisciplinaire Hubert Curien IPHC, Strasbourg BP28 67037, France

Eric Legay, Nicolas Dosme, Pierre Desesquelles, Araceli Lopez-Martens, H Ha, Karl. Hauschild, Nabil Karkour, Amel Korichi, Denis Linget, P. Pariset, J. Roccaz, Bruno Travers, Xavier Lafaye, Stephane Leboutellier, Sebastien Lhenoret  
CSNSM Orsay, France

Xavier Grave, Yann Aubert, Dominique Delbourg, Christophe Oziol, Valerie Chambert, Joel Pouthas, C. Diarra, Albert Olariu, Francois Le Blanc, L.Lavergne, J.-L. Cercus, C. Commeaux  
IN2P3 Orsay, France

Gilles de France, Emmanuel Clément, J-A. Ropert, Michel Tripon, Bruno Cahan, Luc Legiard, Frédéric Saillant, Rémy Beunard, Michel Ozille, Gilles Wittwer  
GANIL, France

Alexander Bürger, Andreas Goergen, Wolfram Korten, Joa Ljungvall, Alexandre Obertelli, Christophe Theisen; Marc Karolak, Julien Pancin; Roman Berthier, André Bouty, Sylvain Broussard, Ange Lotode, Yannick Mariette, Robert Touzery, Christian Veyssiere; Bertrand Hervieu; CEA/DSM/IRFU, Saclay, France

Q.T. Doan, Olivier Stézowski, Doan Quang Tuyen, Nadine Redon, Cécile Aufranc, G. Baulieu, N. Giraud, Bertrand Rosse  
IPN-Lyon, France

Peter Jones  
University of Jyväskylä, Finland

Bart Bruyneel, Peter Reiter, Andreas Wiens, Jurgen Eberth, Herbert Hess, George Pascovici, Nigel Warr, Daniel Lersch, Benedikt Birkenbach  
IKP, Univ. Cologne, Cologne, Germany

Heinz-Georg Thomas, CTT, Germany

Torsten Beck, J Gerl, T. Engert, Ivan Kojouharov, Tobias Habermann  
GSI, Darmstadt, Germany

Roman Gernhaeuser, Reiner Kruecken, Michael Schlarb  
TU-Munich, Germany

Werner Gast  
Julich, Germany

Barna Nyako  
ATOMKI Debrecen, Hungary

Piergiorgio. Bizzetti, Adriana Nannini,  
INFN-Firenze, Italy

Alessandro Zucchiatti  
INFN-Genova, Italy

Giacomo de Angelis, Simone Badore, Luciano Berti, Enrico Calore, Luciano Costa, Paolo Cocconi, Denis Conventi, Sergio Fantinel, Ernest Grodner, Michele Gulmini, Chuangye He, Andrea Latina, Francesco Lelli, Gaetano Maron, Pietro Molini, Daniel R. Napoli, Nicola Toniolo, Marco Rigato, Francesco Recchia, Davide Rosso, Eda Şahin, Paola Spolaore, Javier Valiente  
INFN Legnaro, Italy

Angela Bracco, Sergio Brambilla, Franco Camera, Andrea Capsoni, Simone Coelli, Angelo Cortesi, Fabio Crespi, Silvia Leoni, Bénédicte Million, Daniele Montanari, Marcello Pignanelli, Alberto Pullia, Fabio Tomasi, Ennio Viscione, Oliver Wieland, Francesca Zocca  
INFN Milano, Italy

Sezgin Aydin, Dino Bazzacco, Marco Bellato, Damiano Bortolato, Joel Chavas, Andrea Colombo, Claudio Fanin, Enrico Farnea, Roberto Isocrate, Santo Lunardi, Roberto Menegazzo, Raluca Marginean, Daniele Mengoni, Massimo Nespolo, Marino Nicoletto, Loris Ramina, Gabriele Rampazzo, Massimo Rebeschini, Carlo Rossi Alvarez, Andrea Triossi, Calin A. Ur, Roberto Venturelli, Fabio Veronese  
INFN Padova, Italy

Costel Petrache  
INFN Perugia

Marcin Palacz, Grzegorz Jaworski, Jan Mierzejewski  
Heavy Ion Laboratory, Warsaw University, Poland

Adam Czermak, Bogdan Sowicki, Piotr Bednarczyk, Witold Meczynski, Barbara Dulny, Mirosław Zieblinski, Jerzy Grebosz  
IFJ-PAN-Cracow, Poland

Andres Gadea  
IFIC, CSIC-University of Valencia, Spain and INFN Laboratori Nazionali di Legnaro, Italy

Bo Cederwall, L. Milechina: The Royal Institute of Technology, Stockholm, Sweden  
Stockholm, Sweden

Stanislav Tashenov: GSI and The Royal Institute of Technology, Stockholm, Sweden

Johan Nyberg, P-A. Söderström  
Uppsala, Sweden

Ayşe Ataç, S. Akkoyun, T. Hüyük, O. Kara, A. Kaşkaş, M. Şenyiğit: Ankara, Turkey

Elif Ince: Istanbul University, Turkey and INFN-LNL, Italy

Andrew J. Boston, Helen. C. Boston, Reynold J. Cooper, John . R. Cresswell, Matthew R. Dimmock, Alex N Grint, L J Harkness, Laura Nelson, D C Oxley, David P Scraggs, A R Mather, Paul J. Nolan, Sarah Rigby, Dave Seddon, Jim Thornill, Dave Wells Carl Unsworth, Oliver Lodge Laboratory, The University of Liverpool, Oxford Street, Liverpool L69 7ZE, UK

Alan Austin, Patrick Coleman-Smith, Robert Griffiths, Ian Lazarus, Simon Letts, Jonathan Strachan, John Simpson Vic Pucknell

STFC Daresbury Laboratory, Daresbury, Warrington WA4 4AD, UK

D. Bucurescu, M. Petcu, G. Suliman: National Institute of Physics and Nuclear Engineering,  
Bucharest, Romania

Dimiter Balabanski INRNE-BAS, Bulgaria

Pavel Detistov, University of Sofia, Bulgaria

I-Y. Lee  
LBNL



## Contents

1	Executive Summary	9
2	Motivation	11
3	Conceptual design and performance	13
4	Monte Carlo simulations of selected experiments	25
5	Detector module: Cryostat, cryostat and performance	33
6	Preamplifiers	49
7	Detector Characterisation	57
8	Pulse shape calculations	63
9	Pulse Shape Analysis and Algorithms	69
10	In beam experiments with the first triple cluster	75
11	Tracking	91
12	Electronics	103
13	Data Acquisition and GTS	137
14	The AGAVA Interface	167
15	Event Data Bases and Data Analysis	171
16	Mechanical Design	173
17	Mechanical Integration of complementary detectors	183
18	Infrastructure	189
19	Installation at Legnaro	205
20	Complementary Detectors	211
21	Impact of complementary detectors on AGATA performance	215
22	R&D on other gamma detectors and associated technology	221
23	Organisational Structure and Management	231



## 1. Executive Summary

The European nuclear-physics community pioneered the world-wide development of large gamma-ray spectrometer arrays and were responsible for many of the novel technical advances. These worldwide developments led to two state-of-the-art  $4\pi$  arrays of *escape-suppressed spectrometers*: Euroball in Europe and Gammasphere in the USA. With these devices, gamma-ray spectra are recorded by solid-state germanium detectors. Because the spectra are degraded when gamma rays scatter out of the detectors without depositing their full energy, the germanium is surrounded by BGO scintillator detectors, known as *suppression shields*, which veto any scattered gamma rays. Although this method of escape suppression significantly improves the quality of the spectra, the shields occupy a significant and valuable fraction of the  $4\pi$  solid angle which reduces the overall efficiency of gamma-ray detection. The global consensus of opinion now is that the next major step in gamma-ray spectroscopy involves abandoning the concept of physical suppression shields and achieving the ultimate goal of a  $4\pi$  germanium shell using the novel technique of gamma-ray energy tracking in electrically segmented germanium detectors. The resulting *gamma-ray tracking spectrometer* will have an unparalleled level of detection sensitivity to nuclear electromagnetic radiation. Its sensitivity for selecting the weakest signals from exotic nuclear events will be enhanced by a factor of up to 1000 relative to its predecessors, rendering it ideally suited to be used in conjunction with the new generation of radioactive beam accelerators.

A gamma-ray tracking system involves measuring the position and energy of every gamma-ray interaction in a detector so that the path and sequential energy-loss of a single gamma ray can be deduced using the Compton-scattering formula. The full energy of the event can then be reconstructed without the losses due to suppression shields, which covered nearly half the solid angle in the previous generation of spectrometers. The realisation of such a system will require highly segmented germanium detectors and digital electronics to extract energy, time, and position information using pulse-shape information. This radically new device will constitute a dramatic advance in gamma-ray detection that will have wide ranging applications in medical imaging, astrophysics, nuclear safeguards and radioactive-waste monitoring, as well as introducing a new plateau of detection capability for nuclear-structure studies.

Given the importance of this development and its far-reaching implications, a European collaboration, currently consisting of over 40 partners from 12 countries, has been established to develop and construct a  $4\pi$  tracking spectrometer called AGATA – the Advanced Gamma Tracking Array. The AGATA collaboration has prepared a technical proposal that addresses the needed developments and is available via [http://www-win.gsi.de/agata/Publications/Agata\\_pub-proposal.pdf](http://www-win.gsi.de/agata/Publications/Agata_pub-proposal.pdf). In the USA parallel developments of a gamma-ray tracking spectrometer are being made in the GRETINA/GRETA project.

The AGATA collaboration has defined that the full array will be realised in phases. In 2003 a Memorandum of Understanding (MoU) was signed by laboratories in 10 European countries for the research and development phase. The purpose of this MoU was to establish the AGATA collaboration and a framework to organise the project and to manage this first research and development phase of the project. This research and development phase of AGATA was supported by a Joint Research Activity within the Integrated Infrastructure Initiative (I3) EURONS to develop the new technology and to build the first AGATA module.

The new challenges for nuclear spectroscopy, which provide the scientific impetus for AGATA, are emerging principally from the new generation of high-intensity radioactive ion beam facilities currently being developed worldwide. These facilities provide beams with energies spanning the Coulomb energy regime, typical of the European ISOL facilities (SPIRAL, REX-ISOLDE), to the intermediate and relativistic energy regimes of fragmentation facilities, such as SIS/FRS at GSI. AGATA is a key instrument for these laboratories and also for the major new facilities at FAIR, SPIRAL2, SPES, HIE-ISOLDE and EURISOL.

The science case for the full array is, to a major extent, the science case for the future of nuclear-structure research itself which is covered in for example the NuPECC 2004 Long range Plan and the 2007 DOE NSAC Long Range Plan. AGATA is a fundamental part of the European nuclear-physics strategy in the study of exotic nuclei and will underpin the research programmes of the majority of the nuclear-physics research groups.

With the anticipated massive increases in resolving power and detection efficiency, it is the promised impact of this device, coupled to high intensity stable beam facilities and the new generation of radioactive beam facilities, which will permit access to the furthest reaches of the nuclear chart. Radioactive-ion beams will typically have intensities several orders of magnitude lower than stable beams, but AGATA will facilitate the study of the rarest reaction channels populated by these low-intensity beams. These studies will mark out the position of the new frontiers in the field.

This first phase of the AGATA project is now complete. Research and development has taken place to define the detector array design, specify the digital electronics acquisition system, deduce the algorithms to extract energy, time and position from the digitised signals, tune the tracking algorithms to construct the full events and design and implement all the necessary infrastructure to operate this complex device. All parts of the system have been developed, prototyped and evaluated as described in the following sections of this report. A first sub array of five AGATA modules known as the AGATA Demonstrator is being assembled at the Legnaro National Laboratory stable-beam facility in Italy.

The AGATA project is now starting its next phase of operation and science exploitation. The AGATA Demonstrator is a very powerful instrument in its own right and will move between laboratories to take full advantage of the different beams and facilities available so as to maximise the breath of science that can be addressed. The AGATA collaboration is performing a series of commissioning experiments at Legnaro National Laboratory which will be followed by an experimental campaign of at least 12 months. During this operation phase the array will be continually improved with increasing numbers of detectors and appropriate upgrades and will be operate in a series of campaigns at European laboratories. The next campaigns for AGATA detectors will be at the GANIL laboratory in France and the GSI facility in Germany. At GANIL the range of radioactive ions from the coupled cyclotrons and SPIRAL will be used with AGATA coupled to the EXOGAM and VAMOS spectrometers. At GSI, AGATA will be used at the target position of the fragment recoil separator (FRS) to study very exotic nuclei produced following high-energy fragmentation.

### **Outlook**

The AGATA collaboration is now operating under a new AGATA Memorandum of Understanding, which was agreed in 2008. This MoU define the planning, funding, construction and operation and management of the AGATA project. The full  $4\pi$  AGATA system will comprise 60 triple Cluster Ge detectors, the associated electronics, data acquisition and related equipment. The system will be built up and operated in phases. The aim of the first phase (2009-2012) is to build up and operate 1/3 of the full AGATA system and to pursue the construction and operation of 2/3 and 3/3 of the full system in subsequent phases.

The instrumentation and technical advances driven by this work and the knowledge gained by those involved will be important in a wide range of applications, such as in hospitals and industry. For example, in medical imaging, reconstruction of the gamma-ray energies and determination of their direction will result in vastly improved images. Another beneficiary will be in nuclear safeguards where one of the big problems is the identification of the range of isotopes in waste and the determination of their quantities.

This Technical Design report summarises the status of the AGATA project, the conclusions of the research and development phase of the project, which form the basis for the operation and build up of the array to the full AGATA  $4\pi$  spectrometer.

AGATA was supported by the European funding bodies and the EU contract RII3-CT-2004-506065.

## 2. Motivation

The nucleus is a unique, strongly interacting many-body system. Consisting of a few to a few hundred fermions, its structure combines the macroscopic features expected of nuclear matter in a bulk form, together with the microscopic properties associated with the motion of a finite number of fermions in a potential well. For decades, the study of the gamma-ray decay of the quantal states of the atomic nucleus has played a pivotal role in discovering and elucidating the wide range of phenomena manifested in its structure.

The study of structure at the very limits of nuclear stability is crucial in order to answer some of the most pressing questions in the field. These include the isospin dependence of the effective nuclear interaction, the ability to explain collective phenomena from the properties of the individual nucleons, the limits of nuclear existence, and indeed the upper-limit of Mendeleev's periodic table. In the last decade, it has become clear that many of our preconceptions of nuclear structure have to be revised. Nuclear radii are not always proportional to  $A^{1/3}$ ; instead, neutron-rich nuclei develop a diffuse region of neutron "skin" or "halo" which can extend well beyond the normal expectations for nuclear size. The values of the magic numbers, in the nuclear shell model, for neutrons and protons are no longer sacrosanct: the strength of the  $T=0$  part of the nucleon-nucleon interaction means that the position of the neutron (proton) shell closure varies with the proton (neutron) number. The number of neutron-rich nuclei which can exist is far greater than anticipated: improvements in the treatment of the self-consistent nuclear problem, including more realistic estimates of correlations and clustering, predict a neutron drip-line which seems to be constantly receding. AGATA will focus on all these aspects through studies of (i) proton-rich nuclei at and beyond the proton drip-line, extending the spectroscopic knowledge of  $N=Z$  nuclei to higher mass, (ii) neutron-rich nuclei towards the neutron drip-line and (iii) the heaviest elements towards new super-heavy elements. The response of nuclei to angular momentum and temperature will be investigated by, for instance, ultra-high spin states produced in extremely cold reactions, meta-stable states at high spins and at very large deformation and multi-phonon giant resonances as well as other high-temperature phenomena, such as quantum chaos. Some of the key questions which will be addressed by AGATA are listed below.

- What are the limits of nuclear existence?
- What is the heaviest element we can make and where does the neutron-dripline lie?
- Do new forms of collective motion occur far from the valley of beta stability?
- How does nuclear structure evolve at the highest angular momentum, just before the fission limit?
- Are there new forms of nuclear matter in very loosely bound nuclear systems?
- How does the ordering of quantum states, with all of its consequent implications for nuclear structure and reactions, alter in highly dilute or neutron-rich matter?
- Do symmetries seen in near-stable nuclei also appear far from the valley of beta stability and do we observe new symmetries?
- How are the elements and isotopes found in the Universe formed?
- Where are the sites of the r-processes of nucleosynthesis?
- What are the reaction rates of key exotic nuclei in the hot CNO cycles and rp processes?

The AGATA collaboration has prepared a physics case that addresses many of these questions and is available via <http://www-win.gsi.de/agata/Publications/apc-5r-F.pdf>

Each major technical advance in gamma-ray detection devices has resulted in significant new insights into the structure of atomic nuclei. The progress is illustrated in Fig. 2.1 which shows the sensitivity achieved in terms of the weakest nuclear states that can be observed with each advance in gamma-ray array technology. In order to observe still weaker states at ultra-high spins, in very exotic nuclei, and discover new modes of excitation, a much

more powerful spectrometer is required. A major step forward would be achieved by dispensing with shields, and building a  $4\pi$  spectrometer comprised solely of germanium. Instead of losing the gamma rays that scatter out of each detector, they would be tracked in electrically segmented germanium crystals.

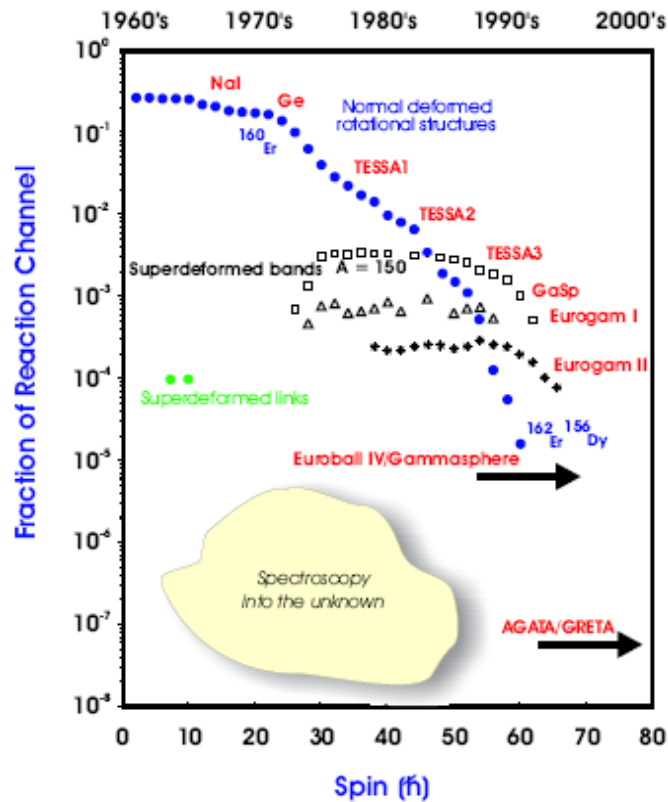


**Fig. 2.1** The sensitivity of gamma-ray detector arrays shown as the fraction of the reaction channel that can be observed as a function of spin for selected nuclear structure phenomena. The timeline and array names are indicated.

A gamma-ray tracking spectrometer will have an unparalleled level of detection power for nuclear electromagnetic radiation. Its sensitivity for selecting the weakest signals from exotic nuclear events will be enhanced by a factor of up to 1000 relative to the previous generation of gamma-ray spectrometers. It will have excellent efficiency, even at high multiplicity, and an unprecedented angular resolution and hence unprecedented high-energy resolution even at very high recoil velocities which can be up to 50% of the velocity of light. It will be ideally suited to be used in conjunction with the new generation of radioactive beam accelerators or existing stable beam facilities.

The gamma-ray tracking spectrometer AGATA will represent a dramatic advance in gamma-ray detection which will have wide ranging applications in medical imaging, astrophysics, nuclear safeguards and radioactive waste monitoring, as well as introducing a new standard of detection capability for nuclear structure studies.

### 3. Conceptual design and performance

#### 3.1. The geometry

The kind of detector arrangements which have been investigated for AGATA are composed of clusters of three or four encapsulated HPGe crystals, each of them hermetically sealed inside an aluminium can having thin walls and grouped inside the same cryostat, thus minimizing the amount of passive materials constituted by the cryostat walls.

In order to maximize the solid angle coverage using a few crystal shapes, an elegant possibility is to tile the spherical surface with the projection of the same simple pattern drawn on each of the faces of an enclosed regular polyhedron, namely one of the so-called “platonic” polyhedra. The maximum symmetry of the spherical tiling is obtained using the icosahedron, which, having 20 equilateral triangular faces, is the platonic solid with the largest number of faces. In the attempt to cover the sphere with the best approximation of circular figures, the pattern on the faces of the icosahedron should have the shape of regular hexagons. Such tiling’s will always end up with  $N_P = 12$  pentagons and with  $N_H = 20n$  hexagons, where  $n = [i^2 + 3j^2 - 4]/8$ ,  $i + j$  even,  $2n$ ,  $i$  and  $j$  integers. Some of the resulting configurations are shown in Fig. 3.1.

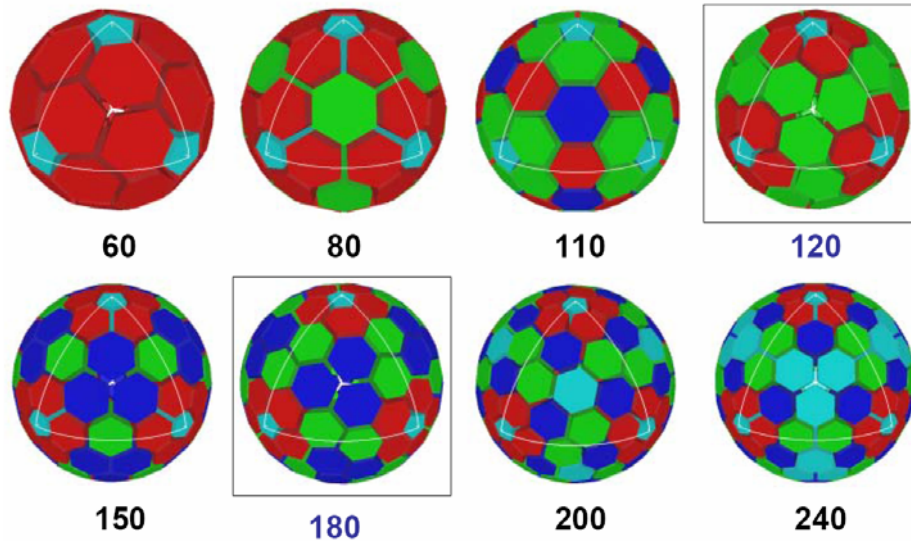


Figure 3.1: Geodesic tiling’s of the sphere obtained by decomposition of the regular icosahedron. For each configuration, the colours correspond to different crystal shapes. The configurations investigated for AGATA, corresponding to  $N_H=120$  and  $N_H=180$ , are enclosed in a square.

Not all the possibilities are attractive for an array such as AGATA. Fixing the maximum size of the crystals, the configurations corresponding to small values of  $n$  result in large discharge of Ge crystal material (due to the tapering) and in a very small inner radius for the array. This would make it impossible to place any ancillary detector device inside AGATA. On the other hand, many of the configurations with larger  $n$  values, having a sufficient inner space, are not attractive because of the impossibility to group easily the detectors into clusters consisting of three or four crystals. Here it should be noticed that the space for the cryostat is obtained from the cluster boundaries, resulting in irregular hexagons. Therefore, the shape of the detectors is obtained through the intersection of a cylinder with an irregular hexagonal prism as shown in Fig. 3.2. On the other hand, the pentagons are always regular. Given the cost for their development and their contribution to the overall performance of the array, it was decided to minimize their volume and consider

only arrangements of hexagonal (or *hexaconical*) crystals. The following parameters were considered:

- Maximum cylinder size: 90.0 mm length, 40.0 mm radius
- Coaxial hole size: 10.0 mm diameter, extension to 13.0 mm from the front face
- Passivated areas: 1.0 mm at the back of the detector, 0.6 mm around the coaxial hole
- Encapsulation: 0.8 mm thickness with a 0.4 mm crystal-can distance
- Cryostat: 1.0 mm thickness with a 2.0 mm capsule-cryostat distance

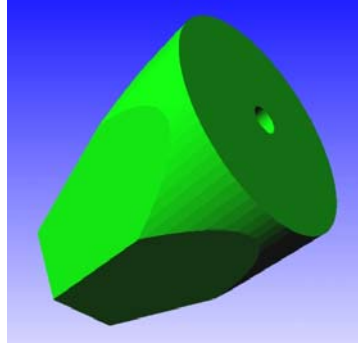


Figure 3.2: One of the possible crystal shapes for the detectors of AGATA

The configurations corresponding to  $N_H=120$  or  $N_H=180$ , marked in Fig. 3.1, were soon identified as the most attractive ones for AGATA. In the case of  $N_H=180$ , it is quite natural to form triple clusters out of three different crystal shapes. All of the clusters have the same composition. In the following, this configuration will be referred to as *A180*. In the case of  $N_H=120$ , three variants of the configuration have been considered instead:

- *A120G*: Composed of two kinds of triple clusters based on two different crystal shapes. It is possible to arrange the clusters in two different ways. Here only the arrangement having the highest degree of symmetry was considered.
- *A120F*: Composed of two kinds of triple clusters based on six different crystal shapes.
- *A120C4*: Composed of one kind of quadruple cluster based on two different crystal shapes.

It should be observed that the solid angle coverage is quite similar for the *A120F*, *A120C4* and *A180* configurations, being around 78% of the total solid angle, while it is significantly lower for the *A120G* configuration, being of the order of 71% of the total solid angle.

A specific code (called *marsview*) performing the solid angle decomposition into these kinds of configurations was developed, providing as an output the elementary crystal shapes (namely, the coordinates of the vertexes), the transformations needed to build a cluster and the transformations needed to place the clusters into the array. The kind of transformations which have been considered are of the kind  $T(x\ y\ z) \cdot R_z(\varphi) \cdot R_y(\theta) \cdot R_z(\psi)$ , where  $R_z(\psi)$  is a rotation of an angle  $\psi$  around the  $z$  axis and  $T(x\ y\ z)$  is a rigid translation along the vector with Cartesian coordinates  $(x\ y\ z)$ .

### 3.2. The simulation code

The performance of the configurations proposed for AGATA has been consistently evaluated by means of extensive Monte Carlo simulations. The main simulation code for AGATA is based on the C++ classes of Geant4. The code is suited for the evaluation of the response to ionising radiation (in particular gamma radiation) of an array of encapsulated germanium

detectors, grouped into multiple clusters, such as AGATA or GRETA, under a wide range of experimental conditions. The description of the shape(s) of the actual detectors, as well as their positions, are decoded from the formatted text files produced by *marsview*, making it possible to implement new detector shapes in a quick and efficient way. It should be pointed out that the shapes of detectors which have been considered for AGATA are not easily describable using the standard geometry tools provided by Geant4. Therefore, a specific class capable of handling such shapes, namely irregular convex polyhedra, was developed. The simulation code includes a built-in schematic event generator, suited to evaluate the response function of the array. More complex (“realistic”) events can be decoded from a formatted text file. Alternatively, a native Geant4 event generator can be coupled to the AGATA simulation code in a simple way. The output of the AGATA simulation code is essentially a list-mode file containing the list of interaction points (energies and positions) within the array. The process of gamma-ray tracking was not included into the main simulation code and should be performed with a suitable code, such as *mgt* or the *Orsay tracking code*, in order to obtain meaningful results.

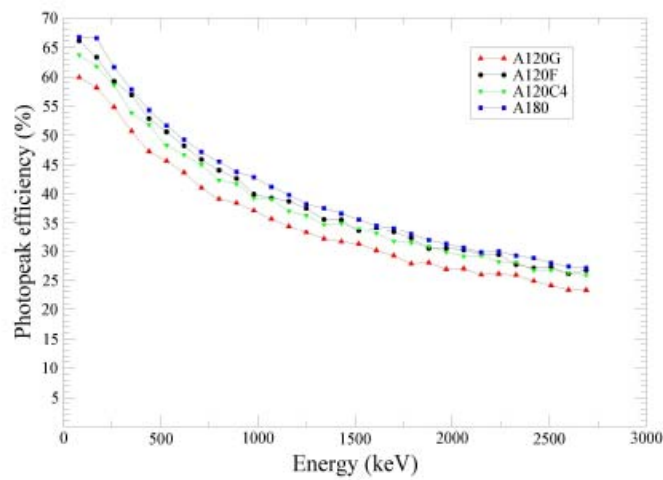


Figure 3.3: Photopeak efficiency extracted from the response function of the proposed configurations for AGATA, calculated in the case of a point source at rest in the geometrical centre of the array. No tracking has been applied to the simulated data.

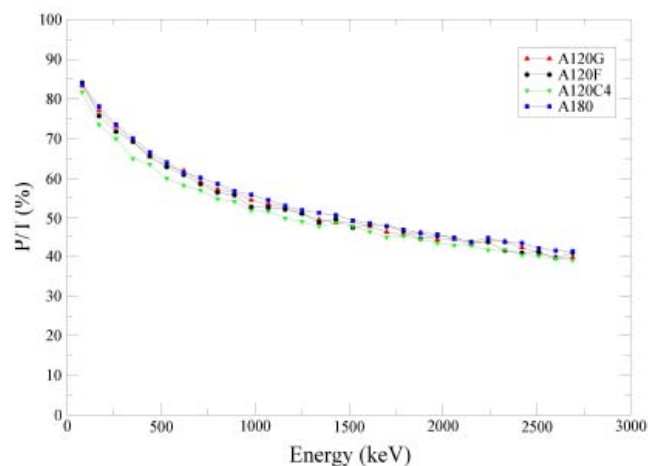


Figure 3.4: Peak-to-Total ratio extracted from the response function of the proposed configurations for AGATA, calculated in the case of a point source at rest in the geometrical centre of the array. No tracking has been applied to the simulated data.

### 3.3. Choice of the optimal configuration

The first kind of information which has been extracted from the simulated data sets is the response function of the array, namely the spectrum obtained when firing single monochromatic photons and summing the individual energy depositions within the whole array, which is therefore considered as a single conventional detector. This is equivalent to consider a tracking array where the tracking algorithm is perfect or has 100% efficiency.

The calculations were performed assuming a point source at rest positioned in the geometrical centre of the array. The plot of the photopeak efficiency as a function of the photon energy, presented in Fig. 3.3, shows very similar curves for the A120F, A120C4 and the A180 configuration, as one would expect since the crystal length and the solid angle coverage are roughly the same in all these cases. The plot of the P/T ratio as a function of the  $\gamma$ -ray energy is presented instead in Fig. 3.4. In this case, there is no appreciable difference between the four configurations.

In order to calculate the absolute photopeak efficiency of AGATA in a realistic way, the simulated data were processed with the tracking code *mgt*. Here and in the following, tracking has been performed assuming a position resolution of 5 mm FWHM for 100 keV photons, with an inverse dependence on the square root of the photon energy. The calculations shown in Fig. 3.5 assumed a point source at rest positioned in the geometrical centre of the array, emitting 30 photons in coincidence with regularly spaced energies (just as in a very long rotational band). The overall performance of the A180 configuration is superior compared to the A120F or A120C4 configurations, even if their response function is pretty much the same. This can be explained by noting that in all cases the assumed position resolution was the same, thus in the case of the A180 configuration, which has a larger inner radius, the “experimental” direction of the photons is on the average better defined and the interaction points are on the average more widely spaced. Under these conditions, the performance of the tracking algorithm is better, thus explaining the observed results.

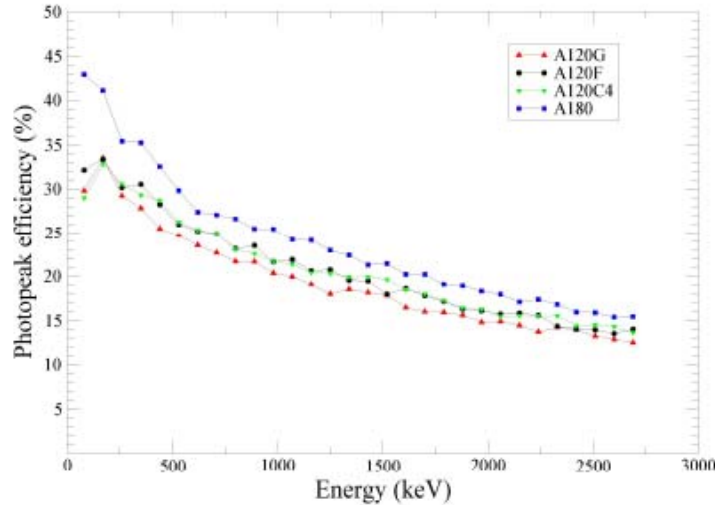


Figure 3.5: Absolute photopeak efficiency for the proposed configurations for AGATA. A point source at rest, positioned at the geometrical centre of the array and emitting a rotational cascade of 30 photons in coincidence, has been considered. Tracking has been performed with the *mgt* code.

From these results, the overall performance of the A180 configuration appears superior to the configurations based on 120 hexagonal detectors; in particular, A120G has the lowest photopeak efficiency, while A120F and A120C4 have very similar efficiency values, standing in between the values for A120G and A180. Given the total cost of the detectors and of the associated electronics, the A120F and A120C4 configurations appear as an attractive compromise between cost and performance. However, the A120F configuration implies higher costs for detector development and a higher number of spare crystals in order to keep the array in good working conditions. The A120C4 configuration, being based on four

segmented crystals, was considered too difficult to set up and to handle compared to the configurations based on triple clusters. For these reasons it was decided to build AGATA following the A180 configuration.

The geometry was further optimized trying to maximize the solid angle coverage, the photopeak efficiency and the P/T ratio over a wide range of photon multiplicities. The corresponding values of the final optimized A180 geometry are 82% solid angle coverage, 43% photopeak efficiency, 59% P/T ratio at  $M_\gamma=1$ , and 28% photopeak efficiency, 58% P/T ratio at  $M_\gamma=30$ .

### 3.4. Performance of the A180 configuration

In order to evaluate the effect of the source velocity on the overall photopeak efficiency of AGATA, calculations were performed considering a point source positioned in the geometrical centre of the array, moving along the z axis with constant velocity. The plot of Fig. 3.6 shows the photopeak efficiency of the A180 configuration of AGATA when a rotational cascade of 30 photons is emitted at various source velocities and  $\gamma$ -ray tracking is performed. It should be observed that the photopeak efficiency is not affected significantly by the source velocity up to quite large values, namely up to  $v/c = \beta = 20\%$ . The efficiency values at  $\beta = 50\%$  are instead significantly lower. This effect can be explained by noticing that at such a high source speed the photon emission is strongly forward focused, because of the Lorentz boost, resulting in densely packed interaction points which the tracking algorithm cannot resolve properly.

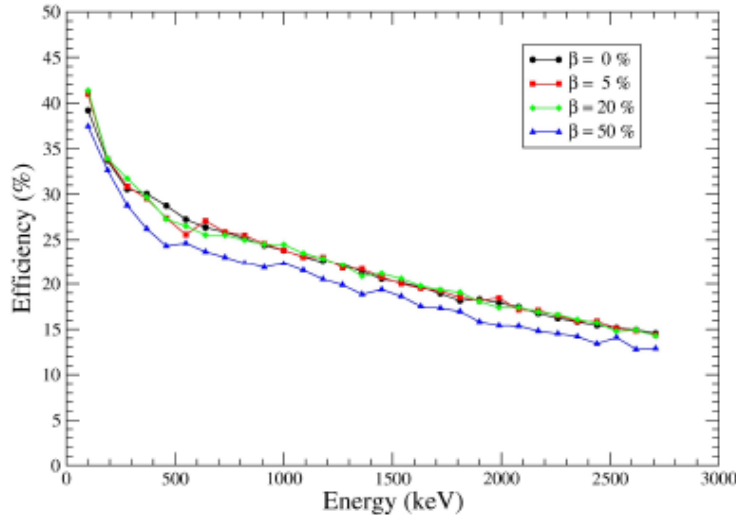


Figure 3.6: Absolute photopeak efficiency (including the effects of the tracking algorithm) calculated assuming a point source positioned in the geometrical centre of the array, emitting a rotational cascade of 30 photons in coincidence at various recoil velocities.

The assumption made in the previous paragraph of constant source velocity is quite schematic and it is not completely suited to describe most of the real life situations. When a beam of heavy ions interacts with a target (solid or gaseous), the velocity of the residual nuclei emitting the photons changes on an event-by-event basis, depending on the point in which the reaction occurs and on the detailed interactions of the residual nuclei with the target itself. The interaction point depends not only on the target thickness, but also on the beam spot size, which might be non negligible in the case of unstable beams produced by fragmentation of a primary beam.

In the case of a tracking array such as AGATA, the quality of the resulting spectra will depend critically on the knowledge, on an event-by-event basis, of the position and velocity of the emitting nuclei, since the capability to perform the Doppler correction depends on these quantities. Consider for instance the spectra shown in Fig. 3.7. Both spectra refer to the A180 configuration of AGATA, considering a point source positioned in the geometrical

centre of the array and emitting a rotational cascade of 30 photons. In both cases, the source has a velocity with constant module  $\beta = 5\%$  and  $\beta = 20\%$  for the top and bottom spectra, respectively, and a direction which is uniformly dispersed on an event-by-event basis into a cone centred on the z axis and having an opening angle of  $2 \times 10^\circ$ . Assuming that the source direction is perfectly known on an event-by-event basis, one obtains the spectra sketched with a thin line. The FWHM of the peak at 2330 keV is 3.5 keV and 5.8 keV at  $\beta = 5\%$  and  $\beta = 20\%$ , respectively. The spectra drawn with a thick line are instead obtained assuming an average source direction along the z axis. At  $\beta = 5\%$ , the same 2330 keV peak has a FWHM of 21.0 keV, while at  $\beta = 20\%$  it is not possible to identify a peak at this energy. Considering point sources of fixed velocity direction and variable velocity module, or diffused sources having fixed velocity, the situation is similar to that shown in Fig. 3.7.

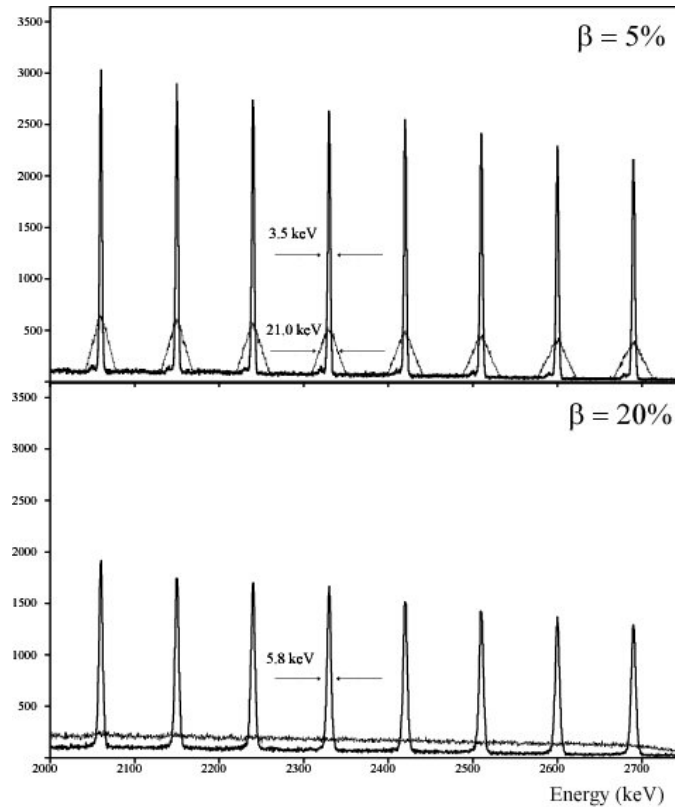


Figure 3.7: Calculated response of AGATA to a cascade of 30 coincident photons emitted from a point source positioned in the geometrical centre of the array at recoil velocities  $\beta = 5\%$  (top) and a 20% (bottom). In both cases a recoil cone opening of  $2 \times 10^\circ$  was considered and the tracking reconstruction was performed considering an average direction along the z axis (light line) or the true event-by-event direction (thick line).

In complex spectra such as those shown in Fig. 3.7, the parameter identifying most easily their quality is the energy resolution, namely the FWHM of the peaks. In order to estimate the degree of precision on the event-by-event measurement of the source position and velocity needed to maintain an adequate quality of the spectra, calculations were performed for the A180 configuration of AGATA, assuming a source of single monochromatic photons of energy 1 MeV. In each calculation, only one out of the three relevant parameters (source position, source velocity direction, source velocity module) could vary on an event-by-event basis, in order to get a clear indication of the impact of each parameter on the overall energy resolution. The results are summarized in the plots shown in Fig. 3.8, 3.9 and 3.10.

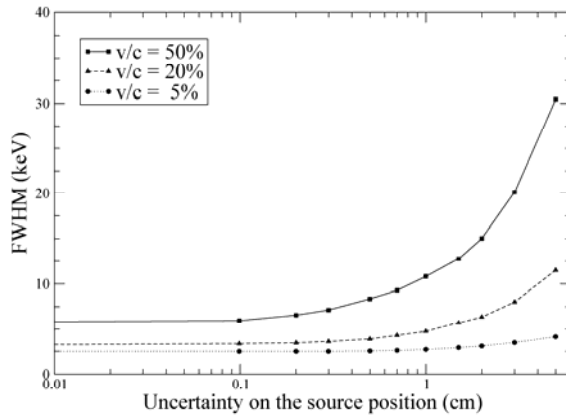


Figure 3.8: FWHM of a peak of 1 MeV obtained considering the A180 configuration of AGATA and a diffused source distributed in the xy plane with a Gaussian distribution centered on the origin and having  $\sigma_x = \sigma_y = 5$  cm, with a fixed velocity along the z axis. For each point,  $\gamma$ -ray tracking was performed assuming to measure with a limited precision the source position on an event-by-event basis. See text for more details.

In Fig. 3.8, the case of a huge beam spot was emulated by assuming a bi-dimensional source diffused in the xy plane with a Gaussian distribution centred on the origin and having  $\sigma_x = \sigma_y = 5$  cm. The finite precision with which the source position would be measured on an event-by-event basis was emulated by assuming a fixed precision  $\mu_x = \mu_y$  and adding to the true position  $(x, y)$ , known from the simulated data, an error  $(\delta_x, \delta_y)$  with a bi-dimensional Gaussian distribution having  $\sigma_x = \mu_x$  and  $\sigma_y = \mu_y$ .

In Fig. 3.9, the case of varying velocity module is considered. In the calculations, a point source positioned in the geometrical centre of the array and having a fixed velocity direction along the z axis, is assumed. The source velocity module has a Gaussian distribution centred on an average value  $\beta_{av}$  and a dispersion of  $\sigma = 0.1 \beta_{av}$ . Also in this case, a fixed precision  $\mu_\beta$  was assumed to generate, event-by-event, an error  $\delta_\beta$  with a Gaussian distribution having  $\sigma_\beta = \mu_\beta$ , which was summed to the true value known from the simulation (taking care to exclude negative values of  $\beta$ ). The values of  $\mu_\beta$  are presented in the plot as fractions of  $\beta_{av}$ .

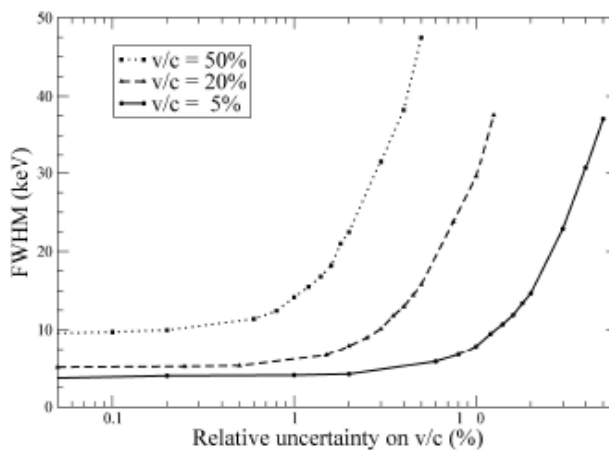


Figure 3.9: FWHM of a peak of 1 MeV obtained considering the A180 configuration of AGATA and a point source having fixed velocity direction along the z axis and velocity module with a Gaussian dispersion having  $\sigma$  equal to the 10% of the average value of the velocity module. For each point,  $\gamma$ -ray tracking was performed assuming to measure with a limited precision the source velocity module on an event-by-event basis.

The case of varying velocity direction is shown in Fig. 3.10. In the calculations, a point source positioned in the geometrical centre of the array and having a fixed velocity module, is assumed. The source velocity direction is uniformly dispersed in a cone centred along the z axis and having an opening angle of  $2 \times 10^\circ$ . In this case, a fixed precision  $\mu_\theta = \mu_\varphi$  was assumed for the measurement of the azimuthal ( $\theta$ ) and polar ( $\varphi$ ) angles of the velocity direction. Again, the errors  $\delta_\theta$  and  $\delta_\varphi$  were generated with a Gaussian distribution centred on the origin and having  $\sigma_\theta = \mu_\theta$  and  $\sigma_\varphi = \mu_\varphi$ , and summed on an event-by-event basis to the true  $\theta$  and  $\varphi$  values.

In the three cases, the plots show a similar behaviour, each curve tending to a limiting value when the uncertainty on the varying quantity becomes smaller than a limiting value and the resolution values getting worse with the increasing average velocity module of the source. The limiting resolution value depends essentially on the intrinsic resolution of the detectors and on the position resolution of the individual interaction point within the crystals. The degree of precision on the measurement of the source position, velocity module, and velocity direction needed to keep the quality of the spectra to good values can be extracted by the plots shown in Fig. 3.11 and 3.12, for instance by assuming the values for which the peak FWHM is 10% larger than the limiting values. These values are presented in Table 3.1. As one would expect, the requirements grow more stringent with the increasing average source velocity module, however they seem feasible with the present technology even at relativistic velocities.

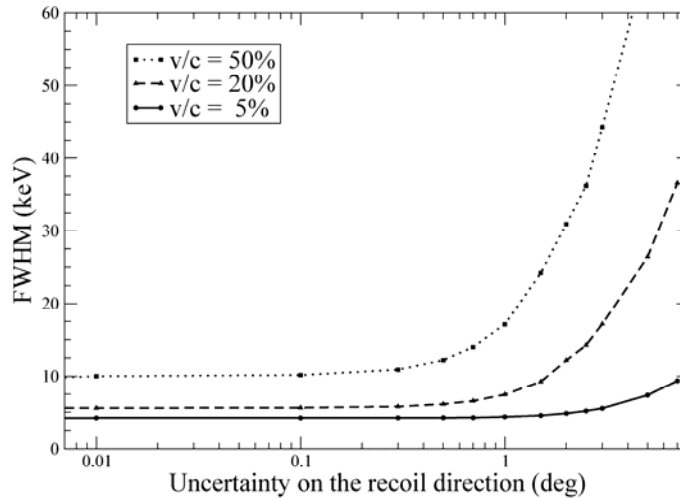


Figure 3.10: FWHM of a peak of 1 MeV obtained considering the A180 configuration of AGATA and a point source having fixed velocity module and velocity direction uniformly dispersed in a cone centred along the z axis with a half-opening of  $10^\circ$ . For each point,  $\gamma$ -ray tracking was performed assuming to measure with a limited precision the source direction on an event-by-event basis. See text for more details.

### 3.5. The AGATA Demonstrator Array

The AGATA Demonstrator Array is an arrangement of five triple clusters of the same kind which will be used to form the final A180 Configuration of AGATA. The performance of such an object will depend in a critical way on its placement relative to the target position. In particular, given the lack of a spherical symmetry, it is sensible to place the detectors closer to the target position compared to the "reference" distance being the target-detector distance of the full A180 Configuration, namely 23.5 cm. The photopeak efficiency and the P/T ratio as a function of the shift from the geometrical centre are shown in plots of Fig. 3.11 and 3.12, where it is assumed that 1 MeV photons are emitted from a point source at rest in the laboratory reference frame. The shift from the geometrical centre is calculated assuming to

move the Demonstrator as a whole towards the source position. The photopeak efficiency for a 30 photon rotational band is shown instead in Fig. 3.13. It is important to observe that the quality of the spectra is not lost even if quite high source velocities are assumed, as shown by the calculated peak FWHM values presented in Fig. 3.14. Actually, the photopeak efficiency of the Demonstrator Array placed at forward angles increases with the average recoil velocity, reflecting the increased solid angle coverage produced by the Lorentz boost, as shown in Fig. 3.15.

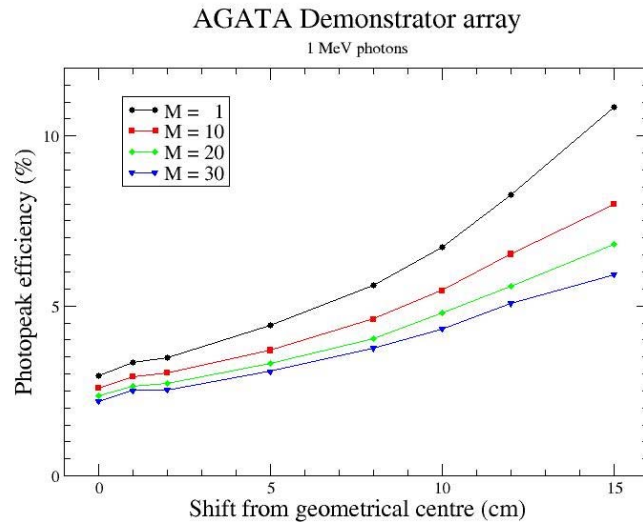


Figure 3.11: Absolute photopeak efficiency of the AGATA Demonstrator Array for 1 MeV photons emitted from a point source at rest. It is assumed that the whole array can translate rigidly towards the source position. See text for details.

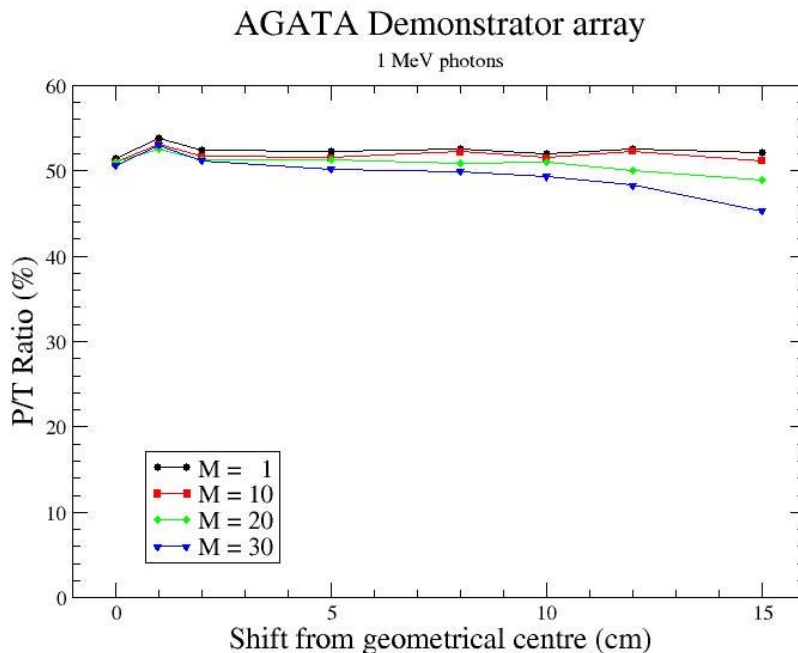


Figure 3.12: Peak-to-total ratio of the AGATA Demonstrator Array for 1 MeV photons emitted from a point source at rest. It is assumed that the whole array can translate rigidly towards the source position. See text for details.

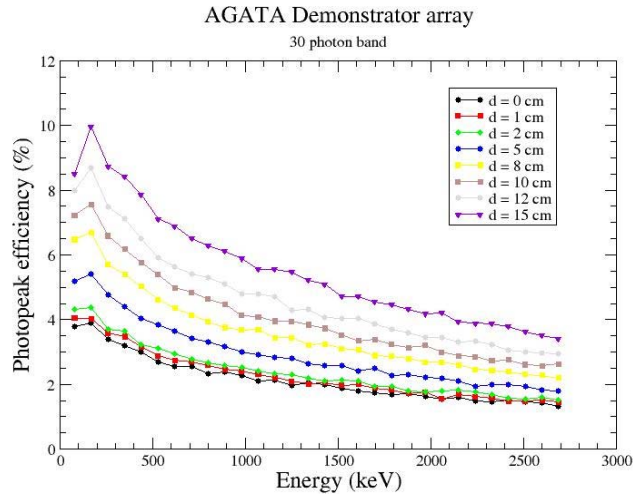


Figure 3.13: Absolute photopeak efficiency of the AGATA Demonstrator Array for a rotational cascade of 30 photons emitted from a point source at rest. It is assumed that the whole array can translate rigidly towards the source position. See text for details.

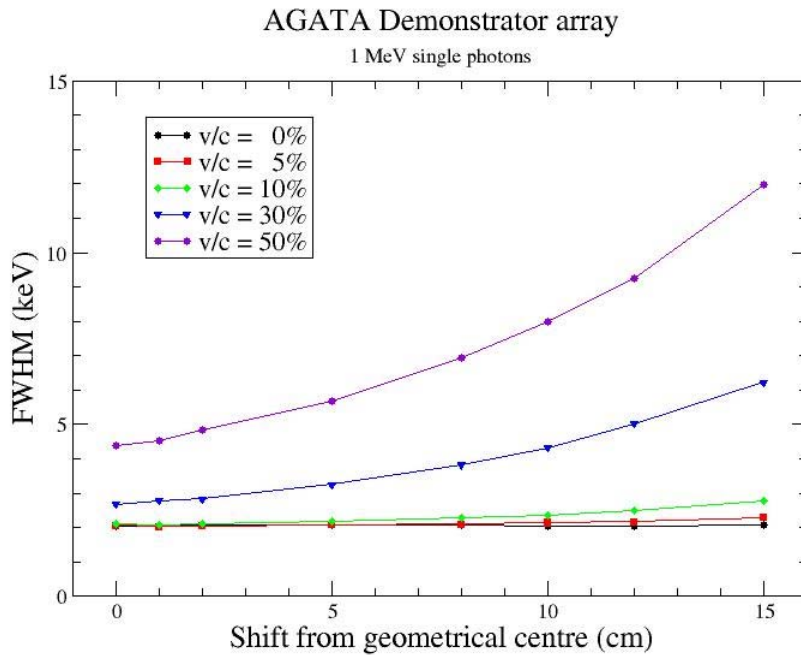


Figure 3.14: Calculated peak FWHM for 1 MeV photons emitted by a point source recoiling along the z axis and detected with the AGATA Demonstrator Array placed at forward angles. It is assumed that the whole array can translate rigidly towards the source position. See text for details.

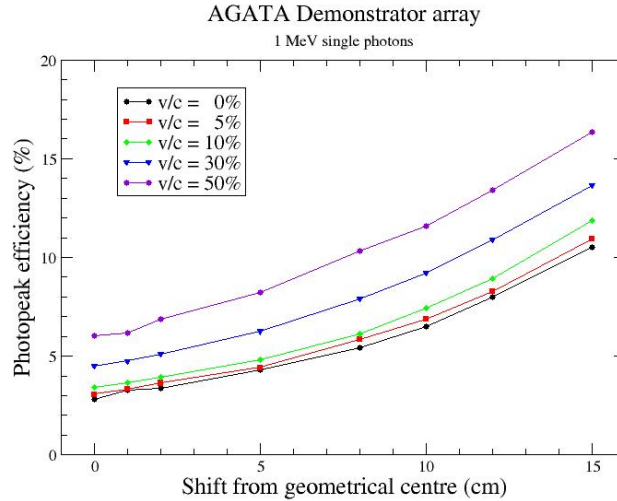


Figure 3.15: Absolute photopeak efficiency of the AGATA Demonstrator Array placed at forward angles for 1 MeV photons emitted by a point source recoiling along the z axis. It is assumed that the whole array can translate rigidly towards the source position. See text for details.

### 3.6. Summary of the performance of the 15 detector demonstrator and the 45 detector $1\pi$ configuration.

The photopeak efficiency, the peak-to-total ratio, and the resolution (FWHM) will depend strongly on the target-to-crystal distance for different reactions with different gamma-ray multiplicities and recoil velocities. Table 3.1 summarizes the performance characteristics for the two distances (13.5 cm and 23.5 cm) for a range of gamma-ray multiplicities (ranging from 1 to 30) and recoil velocities ( $v/c$ , ranging from 0 to 50%). For single gamma-ray events (multiplicity 1) the detection efficiency of the 15 detector system varies from 2.9% at 23.5 cm to 6.7% at 13.5 cm. In many of the first experiments at Legnaro, deep-inelastic reactions will be used with recoil velocities of  $v/c = 0.1$ . Such a high recoil velocity with a traditional gamma-ray spectrometer (such as EUROBALL) would lead to large Doppler broadening and poor energy resolution of over 15 keV. With the AGATA 15 detector Demonstrator, the energy resolution is reduced to just 2.4 keV.

	13.5 cm				23.5 cm			
	Gamma-ray multiplicity							
	1	10	20	30	1	10	20	30
Efficiency (%)	6.7	5.4	4.8	4.3	2.9	2.6	2.3	2.2
Peak-to-Total	52.0	52.2	50.8	49.9	51.4	51.0	51.0	50.6
	Recoil Velocity ( $v/c$ %)							
	0	5	10	50	0	5	10	50
Efficiency (%)	6.5	6.9	7.4	11.6	2.9	3.1	3.4	6.0
FWHM (keV)	2.0	2.1	2.4	8.0	2.0	2.1	2.1	4.4

**Table 3.1** Simulated performance of the AGATA 15 detector Demonstrator at two target-to-detector distances, 23.5 and 13.5 cm, for 1 MeV photons. The photopeak efficiencies and peak-to-total ratios are calculated for multiplicities of 1, 10, 20 and 30. The photopeak efficiencies and resolutions, (FWHM, keV) are calculated for recoil velocity velocities ( $v/c$ ) of 0, 5, 10, and 50%.

Towards the end of the first operation phase the array will be operating with the  $1\pi$  configuration. Table 3.2 summarises the performance of the  $1\pi$  array; this can be compared with the performance of the 15 detector Demonstrator array shown in Table 3.1. The

photopeak efficiency for multiplicity one events has increased from 2.9% to 10.1% at 23.5 cm and from 6.7% to 18.4% at 13.5cm. Even at the highest gamma-ray multiplicities the performance is excellent. The timescales of the GSI campaign are such that the  $1\pi$  configuration of 45 detectors will be available. The calculations (Table 1.4) show that the photopeak efficiency of the  $1\pi$  array is 20% for  $v/c = 0.5$ , with a resolution of 1%. This represents an increase of a factor of 12 in efficiency compared with RISING in singles and even higher for coincidence spectroscopy. This will enable highly selective  $\gamma$ - $\gamma$ -coincidences to be measured for the first time in fragmentation reactions.

	13.5 cm				23.5 cm			
	Gamma-ray multiplicity							
	1	10	20	30	1	10	20	30
Efficiency (%)	18.4	14.4	12.9	11.7	10.1	8.7	7.9	7.3
Peak-to-Total	59.5	61.7	58.4	54.0	55.7	55.1	53.5	51.7
	Recoil Velocity (v/c %)							
	0	5	10	50	0	5	10	50
Efficiency (%)	18.4	19.3	19.7	20.7	10.1	10.7	11.4	15.9
FWHM (keV)	2.5	2.6	3.0	10.1	2.5	2.5	2.7	6.7

Table 3.2 Performance of the  $1\pi$  array at the two target-to-detector distances, 23.5 and 13.5 cm for 1 MeV gamma rays. The photopeak efficiencies and peak-to-total ratios are calculated for a multiplicities of 1, 10, 20 and 30. The photopeak efficiencies and resolutions (FWHM, keV) are calculated for recoil velocities ( $v/c$ ) of 0, 5, 10, and 50%.

## 4. Monte Carlo simulations of selected experiments

### 4.1. Key Experiments

Early in the definition of the project, a list of key experiments, which were considered essential to benchmark the performance of AGATA, was defined. The full list can be found on-line at the following address:

<http://agata.pd.infn.it/documents/simulations/keyExp.txt>

Quoting from the on-line document, the list includes:

1. Binary reactions (Coulomb excitation, quasi-elastic reactions, etc...)
  - Feasibility of tracking with Doppler corrections for  $v/c < 0.1$
  - Large scattering angle for the products
  - Reconstruction of low multiplicity "simple" spectra.
2. Reactions close to the Coulomb barrier (fusion-evaporation reactions, deep-inelastic collisions)
  - Tracking with  $0^\circ$  recoils (fusion-evaporation reactions).
  - Tracking with high multiplicity and large scattering angle for the products (deep inelastic collisions)
  - High spin, reconstruction of high-multiplicity spectra.
3. Giant dipole resonances and high-energy gamma detection (fusion evaporation at the limits of angular momentum).
  - Tracking efficiency for high energy gammas
  - Explore the reconstruction on non-Compton processes (pair production)
4. Medium and high  $v/c$  reactions with stable beams (knock-out, fragmentation and relativistic Coulomb excitation)
  - Feasibility of tracking with Doppler corrections for  $v/c \gg 0.1$
  - Low-gamma multiplicity at large  $v/c$  (Coulomb excitation or knock-out)
  - High-gamma multiplicity at large  $v/c$  (fragmentation)
5. High-intensity stable beams (tracking at extreme counting rates)
  - Low multiplicity (Coulomb excitation, quasi-elastic collisions etc...)
  - High multiplicity (fusion-evaporation reactions, deep-inelastic collisions)
  - Proton-rich nuclides, medium spin,  $v/c = 0$ , (tracking with a compact array)
6. Reactions with radioactive ion beams (RIB) close to the Coulomb barrier
  - Define the sensitivity limits of the array
  - Explore the behaviour of the array under high radioactive background conditions
  - Check the techniques for background reduction
7. Medium and high  $v/c$  reactions with RIB's
  - Define the sensitivity limits of the array
  - Explore the behaviour of the array under high beam background conditions
  - Check the high energy hadronic background effects
8.  $\beta$ -decay and isomer decay studies.
  - Effects of the delocalized annihilation of the positron ( $\beta^+$  decay).
  - Effects of a large area gamma source.

### 4.2. "Realistic" event generation

#### 4.2.1. Fusion-evaporation reactions

Considerable effort has been put into simulation of "realistic" fusion-evaporation events, since expertise was available for the description of this kind of reactions. As an early test, the performance of the GASP array in configuration II (40 HPGe detectors positioned at a distance of about 22 cm from the target) was compared to the AGATA  $1\pi$  Array (45 crystals). In both cases, a symmetric reaction  $^{28}\text{Si}(100\text{MeV}) + ^{28}\text{Si}$  was considered. An event generator was developed for generic fusion-evaporation reactions. In this case, the production cross sections were calculated with the CASCADE statistical code. The residual nucleus was chosen event-by-event according to such cross sections.

The energies of the evaporated particles were chosen according to the centre-of-mass spectra calculated by CASCADE. The discrete gamma-ray transitions were generated using the GammaWare package. Both in the case of GASP and AGATA, light charged particles were detected using the EUCLIDES Si-ball, providing at the same time channel selection and useful information for the Doppler correction. The comparison of the spectra obtained with GASP and AGATA, shown in Figs. 4.1 and 4.2, proves clearly that with a comparable number of crystals it will be possible to obtain higher statistics (a factor of about 4 in singles and more than 100 for gamma-ray fold  $>3$ ) as well as a much better quality of the spectra. On the other hand, if the information from the EUCLIDES is not exploited, as shown in Fig. 4.3, the quality of the spectra provided by AGATA is very much similar to what is provided by GASP, proving clearly that the ancillary detectors will be essential for experiments with AGATA.

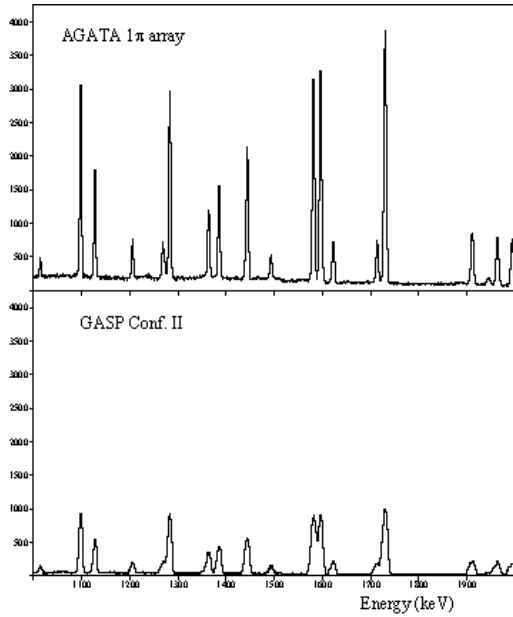


Figure 4.1: Comparison between the performance of GASP+EUCLIDES and AGATA  $1\pi$ +EUCLIDES for the reaction  $^{28}\text{Si}+^{28}\text{Si}@100\text{ MeV}$ . The information from EUCLIDES has been used to select the  $1\alpha 2p$  evaporation channel and to perform the Doppler correction. No conditions on the detected photon multiplicity were applied.

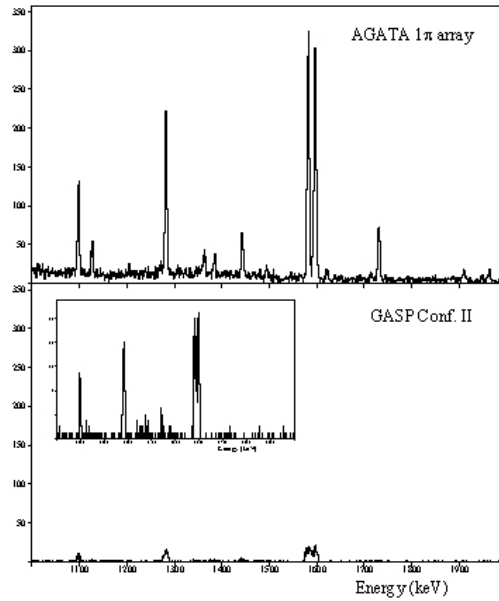


Figure 4.2: Comparison between the performance of GASP+EUCLIDES and AGATA  $1\pi$ +EUCLIDES for the reaction  $^{28}\text{Si}+^{28}\text{Si}@100\text{ MeV}$ . The information from EUCLIDES has been used to select the  $1\alpha 2p$  evaporation channel and to perform the Doppler correction. Photon multiplicity greater than 3 was requested.

Later attempts have tried using other fusion-evaporation codes (for instance COMPA) rather than CASCADE and to include a proper treatment of the effects of the target on the recoils (e.g. energy loss and angular spread). Using these event generators, it was shown, for instance, that a relatively simple device as RFD can help obtaining the intrinsic detector resolution also in cases in which the dispersion in velocity of the recoils is quite high (see Fig. 4.4). In other cases, the parameters of the event generator have been “trimmed” to reproduce data from actual experiments, for instance experiments performed at GANIL with EXOGAM (see Fig. 4.5). These simulated events were later replayed into the AGATA simulation, showing a clear improvement in quality of the spectra. Since only the Demonstrator was considered, the acquired statistics is lower than the case of EXOGAM (see Fig. 4.6).

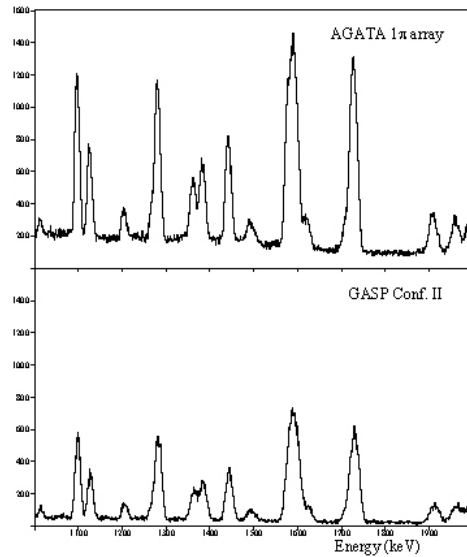


Figure 4.3: Comparison between the performance of GASP+EUCLIDES and AGATA  $1\pi$ +EUCLIDES for the reaction  $^{28}\text{Si}+^{28}\text{Si}@100\text{ MeV}$ . The information from EUCLIDES has been used to select the  $1\alpha 2p$  evaporation channel, but NOT to perform the Doppler correction. No conditions on the detected photon multiplicity were applied.

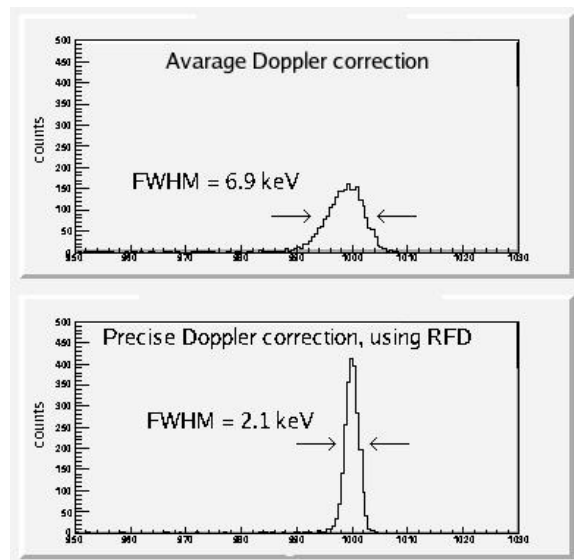


Figure 4.4 Peak FWHM for the AGATA Demonstrator detecting photons emitted after a fusion-evaporation reaction. Doppler correction was performed using an average recoil velocity (top) or detecting the recoils with RFD (bottom).

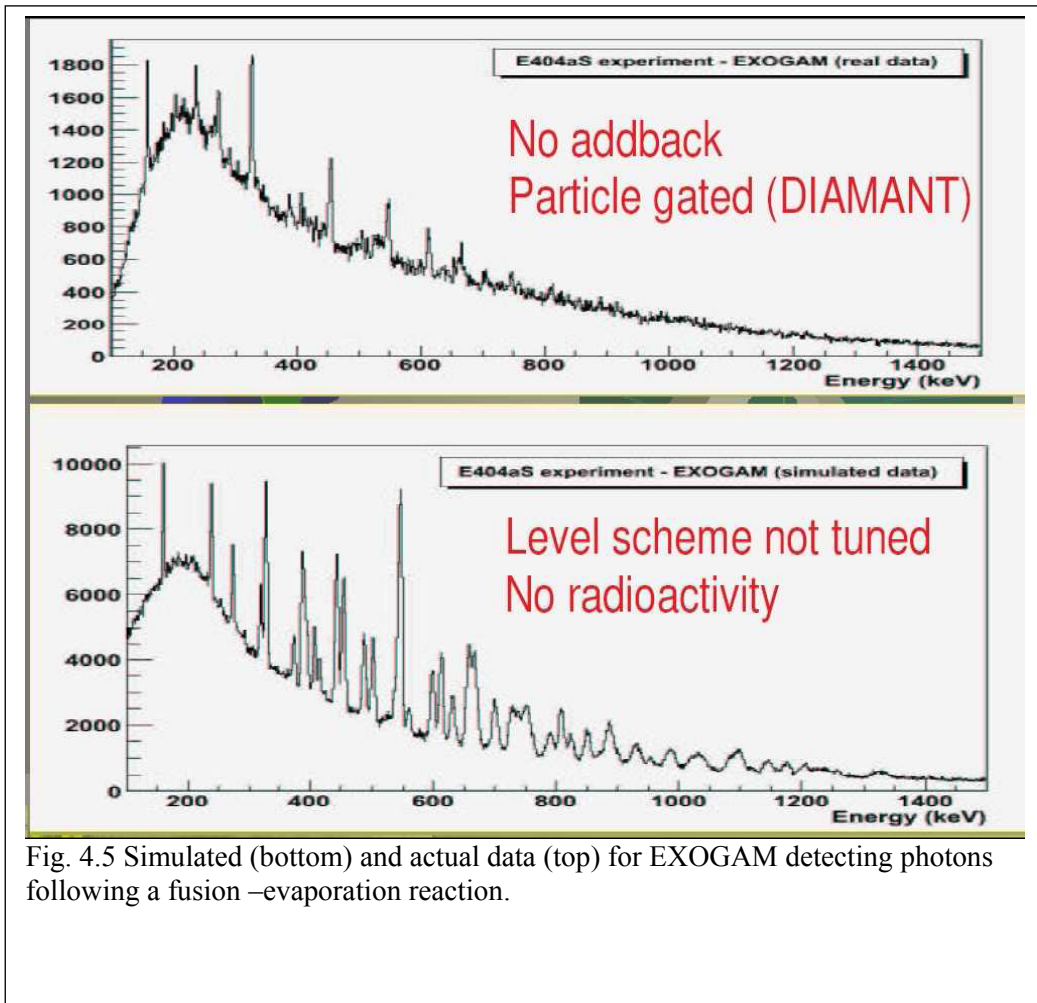


Fig. 4.5 Simulated (bottom) and actual data (top) for EXOGAM detecting photons following a fusion –evaporation reaction.

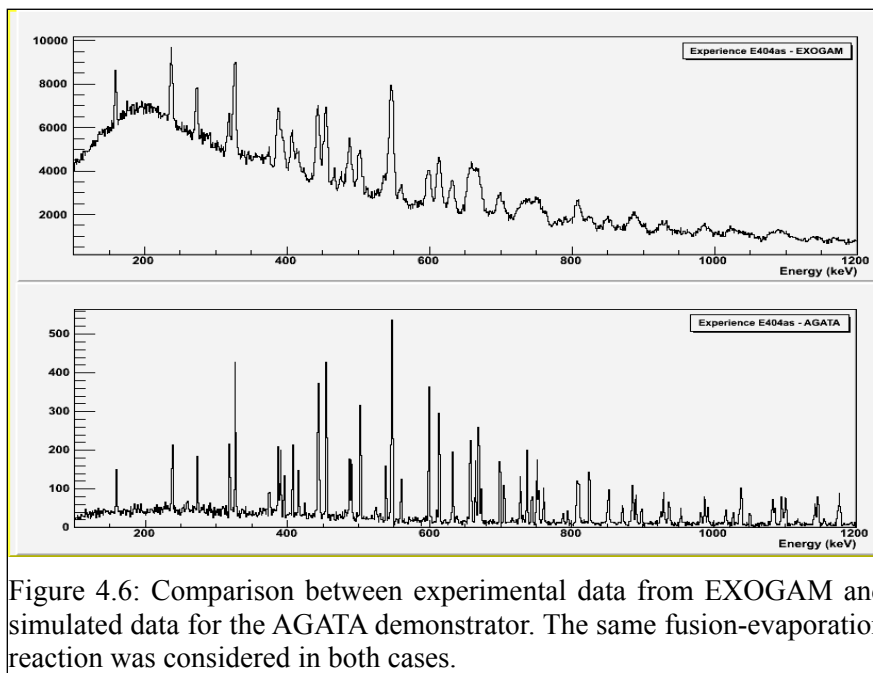


Figure 4.6: Comparison between experimental data from EXOGAM and simulated data for the AGATA demonstrator. The same fusion-evaporation reaction was considered in both cases.

#### 4.2.2. Other reaction mechanisms

There has been limited work concerning reaction mechanisms other than fusion-evaporation, although with good quality and interesting results. For instance, it was attempted to reproduce

an actual Coulex experiment performed at GSI with RISING as shown in Fig. 4.7. The event generation was performed through a native Geant4 code coupled to the main AGATA simulation code. In this case, the expected gain with the use of the Demonstrator array is only a factor 2 in statistics. The spectra have better quality but, given the low multiplicity, this does not seem to be a premium factor. A factor 10 increase in statistics is expected with the full AGATA array.

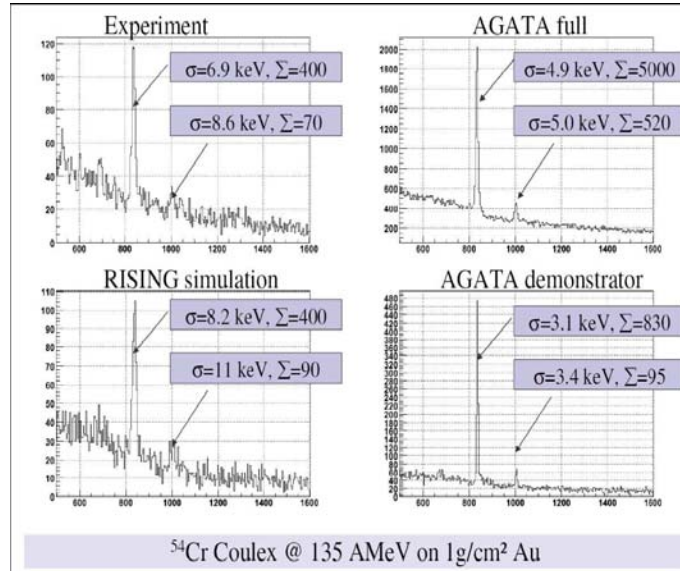


Figure 4.7: Comparison between experimental (top left) and simulated (bottom left) data for the RISING array. The Coulex reaction  $^{54}\text{Cr}(135\text{AMeV})+\text{Au}$  was considered. The same input data were simulated with the AGATA Demonstrator (bottom right) and with the full array (top right).

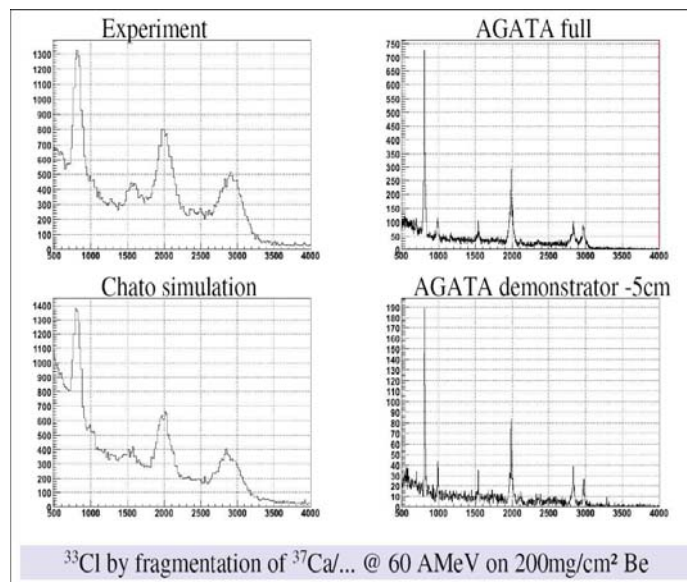


Figure 4.8 : Comparison between experimental (top left) and simulated (bottom left) data for the Chateau de Cristal. The fragmentation reaction  $^{37}\text{Ca}(60\text{AMeV})+\text{Be}$  was considered. The same input data were simulated with the AGATA Demonstrator (bottom right) and with the full array (top right).

A similar approach was used in the case of a fragmentation reaction, where the actual experiment was performed with the Chateau de Cristal (see Fig. 4.8). In this case the quality of the spectra provided by AGATA makes it possible to resolve a doublet which

could not be identified with Chateau de Cristal.

Since the Demonstrator Array will be first installed at the PRISMA site in Laboratori Nazionali di Legnaro, it was considered essential to evaluate in a realistic way the Doppler correction capabilities of AGATA coupled to PRISMA. As mentioned previously, separate simulation codes were available for AGATA and PRISMA, both of which can decode the same input event file. The output of the two programs can be combined into a single data file, based on the event number (in real life, a time stamp will be used for this purpose). So far, only preliminary attempts have been performed, using a very schematic event generation (ions with a narrow energy distribution around the average value extracted by an experiment). The data analysis, however, is “realistic” since it is performed with the same techniques as used with real data. It is clear that, in order to perform the Doppler correction properly, the sole information on the direction of the ions is not sufficient and the full PRISMA information should be used. This way, it will be possible to reach resolution values very close to the intrinsic values, even in case of the closest foreseen target-detector distance, as shown in Fig. 4.9 and 4.10.

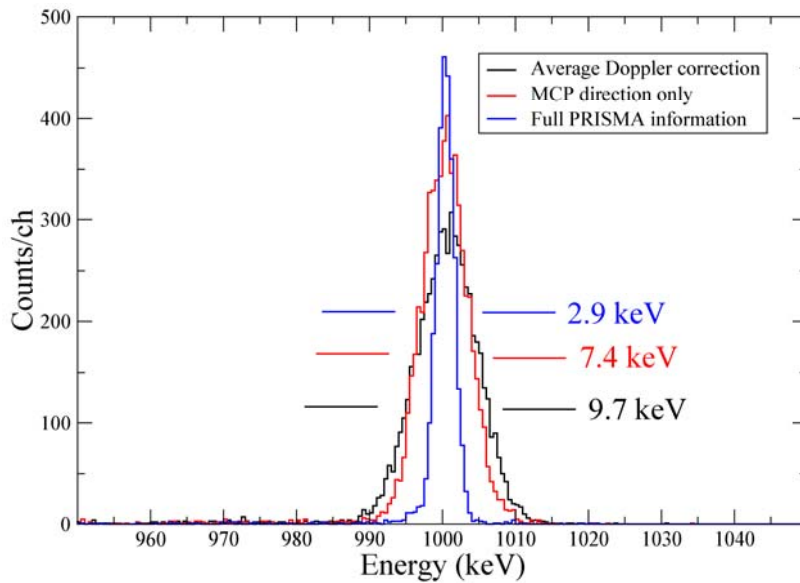


Figure 4.9: Simulated data for the AGATA Demonstrator + PRISMA setup. The AGATA detectors were placed at the closest foreseen distance to the target.  $^{90}\text{Zr}$  recoils with an average energy of 350 MeV were considered, each of them emitting a single 1 MeV photon. Doppler correction was performed by assuming an average recoil vector velocity, by assuming an average module and taking the direction from the start detector of PRISMA, or by using the full information provided by PRISMA.

### 4.3. Simulation of position resolution

The 3-dimensional position resolution of the interaction points within the HPGe crystals is of fundamental importance for a tracking based  $\gamma$ -ray array. The position resolution is therefore an important parameter to measure experimentally. Such a measurement is proposed to be performed during the commissioning phase of the AGATA demonstrator at LNL. One possibility of doing this directly is to use a collimated beam of  $\gamma$  rays, in order to get a well defined first interaction point. This requires, however, a very narrow beam in order not to be limited by the collimation. The consequence of this would be a very time consuming measurement in order to get good statistics. Instead, indirect measurements based on in-beam measurements of Doppler correction capabilities are being examined.

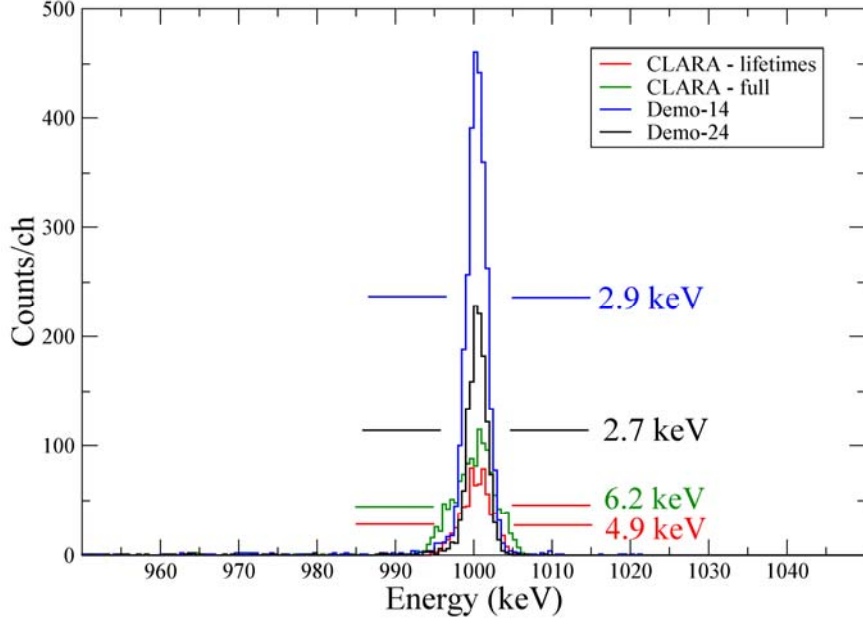


Figure 4.10: Simulated data for the AGATA Demonstrator +PRISMA setup (at two different target-detector distances) and for CLARA+PRISMA.  $^{90}\text{Zr}$  recoils with an average energy of 350 MeV were considered, each of them emitting a single 1 MeV photon. Doppler correction was performed by using the full information provided by PRISMA.

The contribution to the FWHM,  $W$ , of the full-energy peak in a  $\gamma$ -ray spectrum can be divided into four parts:

$$W^2 = W_i^2 + W_{v_r}^2 + W_{\theta_r}^2 + W_{\theta_\gamma}^2,$$

where  $W_i$  is the intrinsic resolution of the detector,  $W_{v_r}$  and  $W_{\theta_r}$  are the contributions from the uncertainties of the velocity and angle of the  $\gamma$ -ray emitting nucleus (recoil), respectively, and  $W_{\theta_\gamma}$  is the uncertainty in the emission angle of the  $\gamma$  ray relative to the beam axis. The last three terms in this equation are due to Doppler effects. Since the  $\gamma$ -ray emission angle is determined by the position of the first interaction point in the detector, there is a direct correspondence between  $W_{\theta_\gamma}$  and the position resolution,  $p$ , while  $W_i$ ,  $W_{v_r}$  and  $W_{\theta_r}$  are independent of  $p$ .

A strategy to obtain a Monte Carlo independent estimate of the position resolution has been proposed by F. Recchia et al. The idea is that measurements of the total widths  $W_{\text{close}}$  and  $W_{\text{far}}$  are made at two distances  $d_{\text{close}}$  and  $d_{\text{far}}$ . The position resolution can then be estimated through the equation

$$p^2 = \frac{1}{k^2} (W_{\text{close}} - W_{\text{far}}) \left( \frac{1}{d_{\text{close}}} - \frac{1}{d_{\text{far}}} \right)^{-1},$$

with  $k$  being a constant which is independent of  $W$  and  $d$ . Such a setup has been simulated for different reactions using the AGATA GEANT4 code and the MGT  $\gamma$ -ray tracking program. Preliminary results of the simulations are shown in fig. 4.11. The deviation between the obtained position resolution values (y axis) and the MGT smearing parameter (x axis) is due to the fact that, when placed close to the target, the AGATA Demonstrator covers a wide

angle around 90 degrees. Another contribution to the deviation is the use of average values of the distances  $d_{close}$  and  $d_{far}$  in the equation above. Future investigations are foreseen to refine the method.

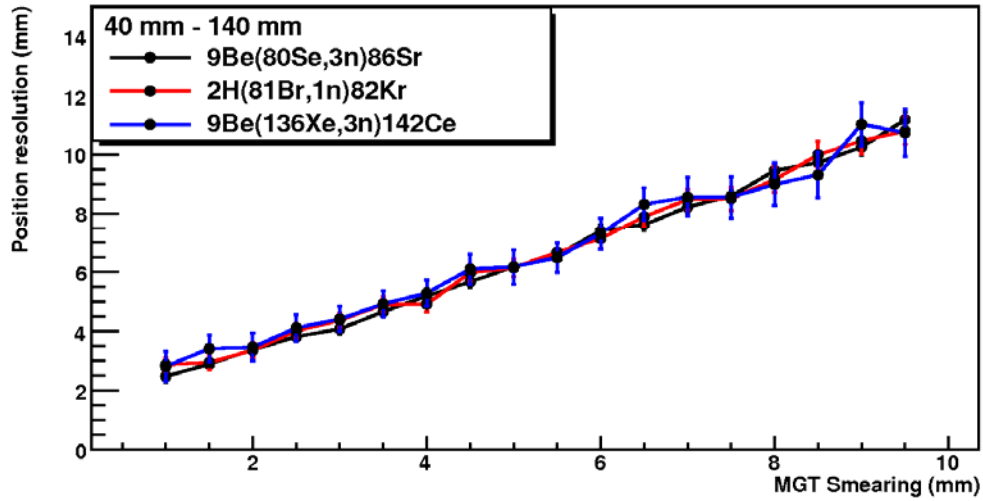


Fig. 4.11 Simulated position resolution as a function of the smearing parameter of the MGT tracking program for three fusion-evaporation reactions (see legend). An AGATA triple cluster detector was placed at 90 degrees relative to the incoming beam and at the two distances  $d_{close} = 40$  mm and  $d_{far} = 140$  mm. See text for further details.

## 5. Detector module: Crystal, cryostat and detector performance

The full AGATA spectrometer will comprise 180 asymmetric hexagonal shaped, electronically segmented, tapered, encapsulated HPGe detectors. Three slightly different asymmetric detectors are combined into a triple cluster detector unit. The AGATA array will consist of 60 identical cryostats, each housing three detectors with an individual semi-hexagonal shape. With this configuration, a 9 cm thick germanium shell will be realized with up to 82% of solid angle coverage. This configuration for AGATA was selected on basis of its modularity and symmetry as well as for its rather large inner radius of 23.5 cm (to crystal face) which allows the use of most ancillary detectors.

### 5.1. AGATA crystals and cryostats

#### 5.1.1. The AGATA crystals

All detectors are produced by the company Canberra, Lingolsheim (Strasbourg), France. The three types of detectors employed in AGATA are built out of 36-fold segmented coaxial HPGe crystals, and merely differ in their near-hexagonal shape (see Fig. 5.1).

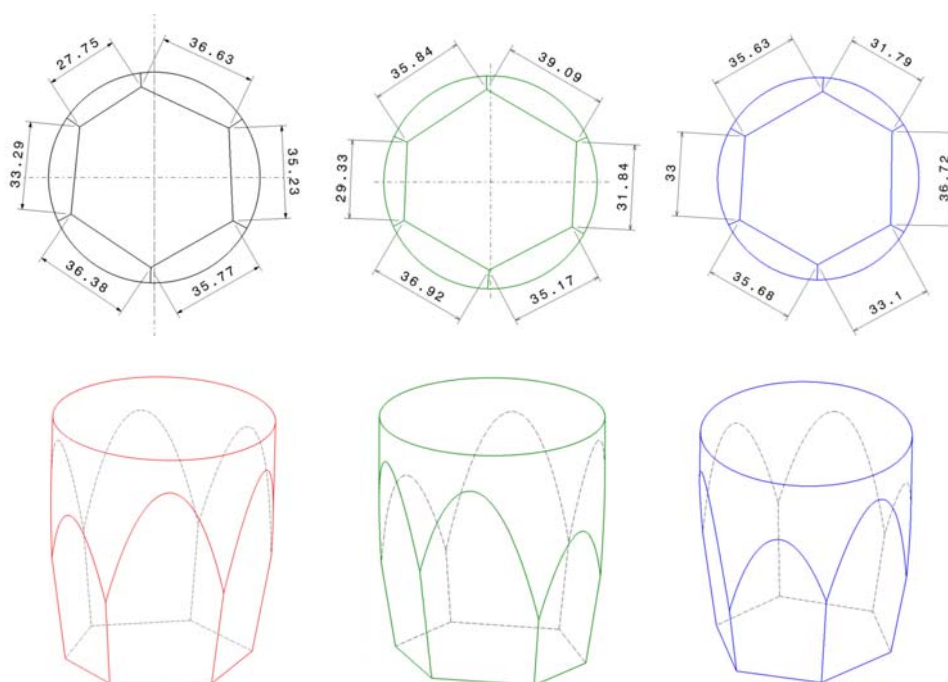


Fig. 5.1. Mechanical drawing of the three different crystal geometries. One of each type is present in each triple cryostat. Colour code and labelling complies with AGATA labelling convention.

The different geometries are assigned a letter and a colour: A/red, B/green and C/blue. The crystals each have a length of  $90 \pm 1$  mm and a diameter of  $80^{+0.7}_{-0.1}$  mm at the rear. At the front they are tapered to a hexagonal shape with an  $8^\circ$  tapering angle. The crystal's central hole has a diameter of 10 mm and extends to 13 mm from the front end. The 6-fold sector-wise segmentation goes through the middle of each flat hexagonal side. The 6-fold longitudinal segmentation forms rings of 8, 13, 15, 18, 18 and 18 mm starting at the hexagonal front face of the detector (see Fig. 5.2). The widths of the rings have been optimized by GEANT4 calculations for uniform distribution of the interactions and optimal pulse-shape sensitivity.

The AGATA labelling convention assigns the letters A to F to the six sectors around the detector axis, while the numbers 1 to 6 are used in conjunction with the six rings, with 1 being at the front end and 6 at the back (closest to the dewar).

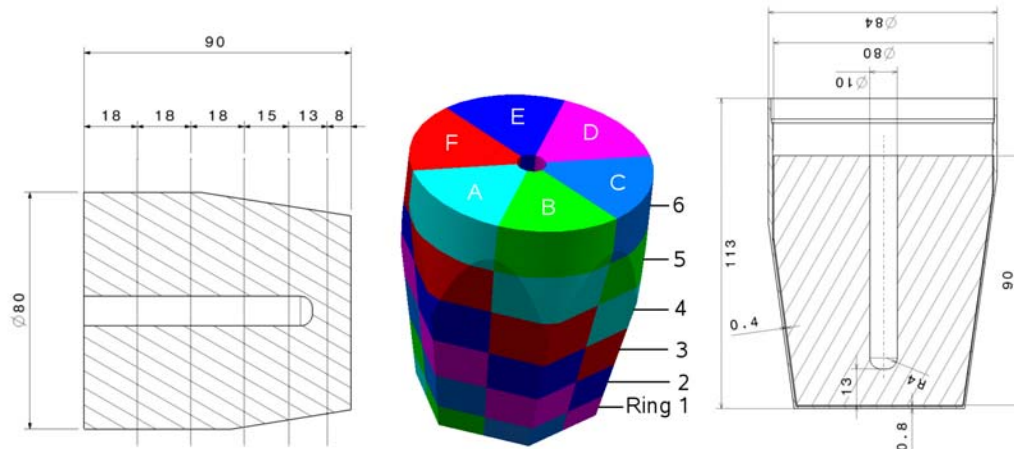


Fig. 5.2. Mechanical drawing of segmentation and encapsulation for an AGATA detector. (left) Dimensions of longitudinal segmentation (centre) Segment labelling (right) Dimensions of encapsulation and core.



Fig. 5.3. Pictures of the AGATA unsegmented crystals. (left) encapsulated crystal, (centre) encapsulated crystal with PCB (right).

A picture of a bare Ge crystal is shown in the left part of Fig. 5.3. The typical weight of Ge amounts to about 2kg (see table 5.1). All crystals are made of n-type HPGe material. The impurity concentration is specified to be between  $0.4$  and  $1.8 \cdot 10^{10}/cm^3$ . The surfaces of these crystals are very delicate, each crystal is encapsulated into an Al canister with a 0.8mm wall thickness. The encapsulation technology was developed first for the EUROBALL cluster detectors (2). The distance between capsule walls and crystal side faces is 0.4-0.7 mm. The 6x7 connector feed throughs provide access to each of the 36 segmented outer contacts. They are grouped per sector (centre part of Fig. 5.3). The core contact, which is used for applying the high voltage and to obtain the core energy signal, is isolated with ceramic.

A two-layered printed circuit board (right part of Fig. 5.3) is mounted in proximity of the segment feed throughs and acts as an interface for the cold part of the pre-amplifier electronics. The board allows to connect and dismount in a fast way detectors from the cryostat. Three detectors – one of each colour – are mounted in each cryostat. Tracking requires extreme care with positioning of these crystals. A narrow 0.5mm spacing is given between the Al capsules of the detectors (see Fig. 5.4(a)).

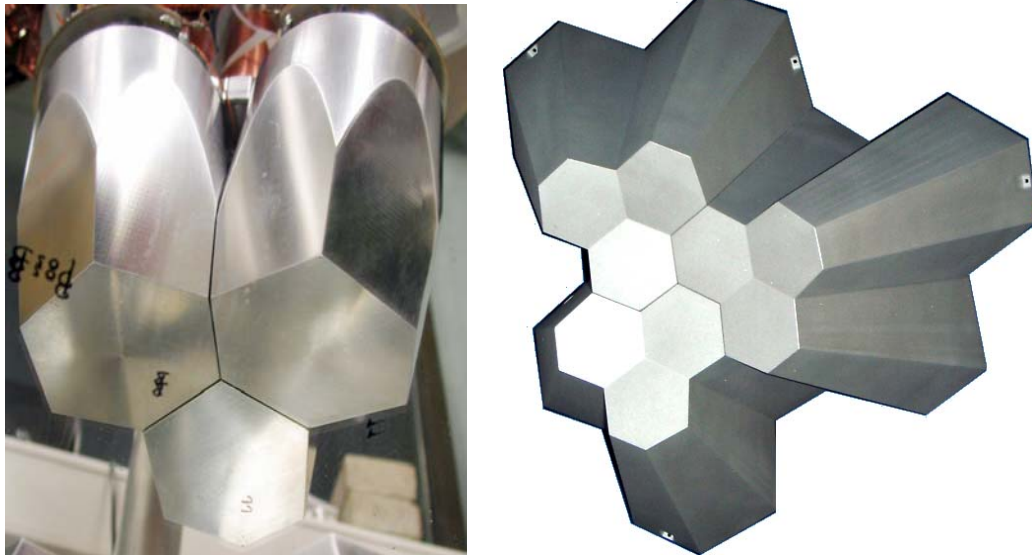


Fig. 5.4. Inside one end cap, only a gap of 0.5mm exists between the Al of the end caps and the detector capsules. Here very strict tolerances on positioning of detectors in the AGATA ball are required in order to avoid thermal conductivity.

### 5.1.2. The AGATA cryostats

The AGATA cryostats are manufactured by the company CTT, Montabaur, Germany. Some of the design concepts of the AGATA cryostats are based on the EUROBALL and MINIBALL cluster detectors. The preamplifiers are the only remaining analogue electronic part which exists in the whole electronic measurement chain. The preamplifiers of segment and core contacts are divided in two spatially separated parts. The cooled input stages of the preamplifiers are operated close to the Ge crystals at liquid nitrogen temperature. Cooling and mounting in close proximity of the detector is required to optimize noise performance. In addition a good electronic shielding between the input stages is required in order to minimize crosstalk contributions. The AGATA cryostats employ a separated cooling scheme for the encapsulated Ge detector and the cold part of the preamplifier electronics. While the Ge detectors are cooled to 90 K, the FETs are operated at temperatures near 130 K where their noise contribution is minimal. The other adjacent parts of the preamplifier electronics contribute less to the noise performance and are therefore situated outside the vacuum, where they are accessible at any time.

The electric connection between both parts is made by several hundreds of individual thin wires with low thermal conductivity. The thermal isolation is established by a vacuum with pressure values below  $< 5 \cdot 10^{-6}$  mbar. This pressure is maintained over long periods by the active getter materials build into the cryostat. A schematic picture of a fully connected triple cryostat is shown in Fig. 5.5. The end cap is rendered semi-transparent to show the alignment of the detectors relative to the end cap. The picture also demonstrates one of the challenges in the design and assembly of such a cryostat.

A single triple cryostat comprises 111 individual high resolution spectroscopy channels. A comparable number of channels are typically employed in a whole spectrometer operational today.

Although each individual FET has only an electric power consumption of  $\sim 20$  mW, the total consumption of the 111 FETs in a single AGATA triple cluster adds up to 2.3 W. Together with the enhanced thermal connection by the wiring inside the cryostat and the radiative heat absorption, a considerable cooling capacity is demanded. A schematic drawing of the LN<sub>2</sub> dewar is shown in Fig. 5.6. The dewar for the triple cryostat contains up to 4.5 l of liquid nitrogen. It has a length of 38 cm and an outer diameter of 24.7 cm. One dewar filling

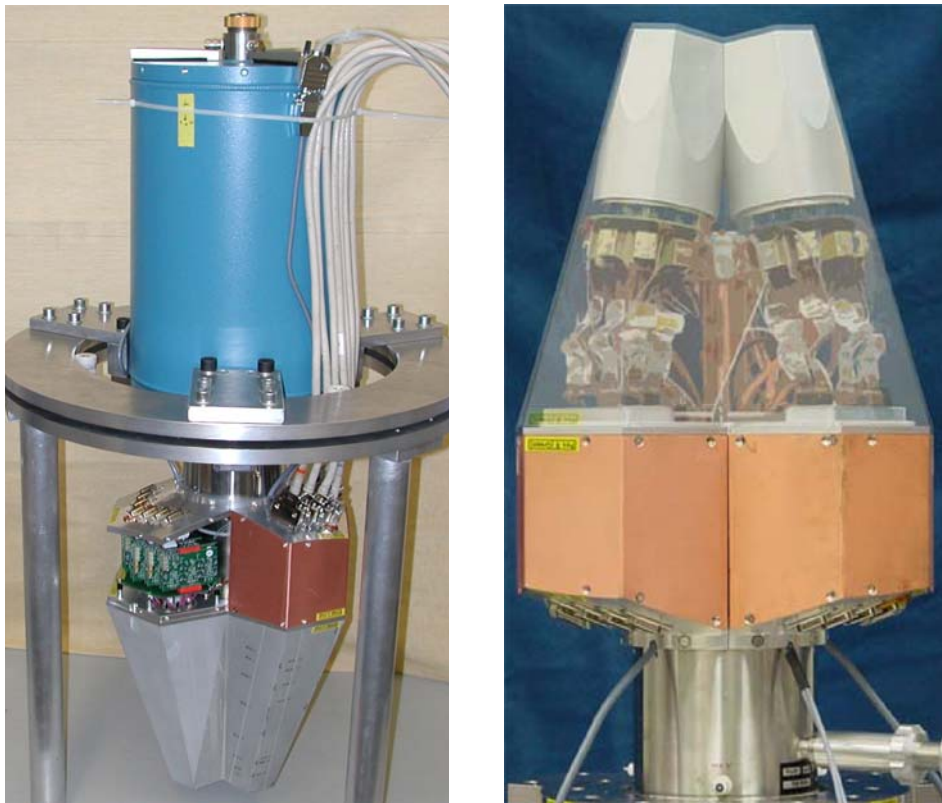


Fig. 5.5. (left, a) The first operational ATC: ATC1. (right, b) ATC2. The AGATA asymmetric triple cryostats (ATC). Fig. 5.5(b) was graphically edited to show the alignment of the detectors relative to the endcap.

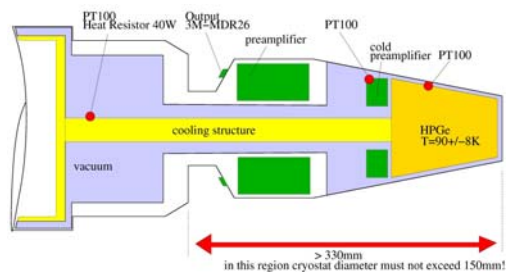


Fig. 5.6. Schematic of the cryostat

is sufficient for 12-14 h of continuous operation. The dewar allows for an electronic measurement of the LN2 filling level. Temperature is monitored over two platinum resistance thermometer (type PT100) readouts. A PT100 is positioned at the copper cooling finger, close to the dewar and another PT100 is sitting in close vicinity of the crystals. After cooling down the cryostat and the detectors with LN2 the triple detector a period of at least 24 hours at LN2 temperature is needed to guarantee that the measured temperatures apply also to the situation inside the encapsulated crystals. After this period HV can be applied safely to the three detectors. A typical cooling down cycle of the ATC is shown in Fig. 5.7. Temperature values are obtained from the PT100 closest to the Ge detector crystals.

The closed AGATA triple cryostat is shown in Fig. 5.5(a). Triple cryostats have a length of 92 cm and a weight of 38 kg without the Ge crystals. Very low tolerances are also demanded for the manufacturing of the cryostat end caps and the final spacing between detector side faces of different triple detectors. This is mandatory for precise and

uncompromised positioning of the detectors in the array. Finally a narrow mechanical margin of 0.5mm between end caps remains (see Fig. 5.4(b)).

The bending of the thin walls of the end caps were measured to stay within tolerances under vacuum. The pre-amplifiers for the AGATA detectors require, besides the traditional good energy and timing properties, also fast and clean transfer functions to register unperturbed signal traces for pulse shape analysis. In addition a high count rate capability was demanded in order to exploit fully the high efficiency.

New pre-amplifiers have been developed for AGATA by a collaboration of GANIL, the University of Milan and the University of Cologne (3; 4) which fulfil these requirements. A more detailed description of the new pre-amplifier is given in a separate part of this document. Three segment pre-amplifiers are integrated on one PCB. The core preamplifier includes an on-board precision pulse generator and allows for an extremely wide dynamic range using a built-in reset technique. Although the power consumption per channel was limited to 250mW by design, the 111 closely packed spectroscopic channels produce substantial heat. This is demonstrated in Fig. 5.8 which was taken with an infra-red camera. In closed condition, the temperature runs up to 55°C, which is below the considered limit for safe operation of 65°C. The preamplifiers have shown good gain stability between filling cycles. Differential signal output of the 111 spectroscopic channels is provided through 21 MDR connectors. The segment MDR connectors merge the 6 segment signals of each sector. The core pre-amplifier has an individual MDR connector for the pre-amplifier output signal and the pulser control signals.

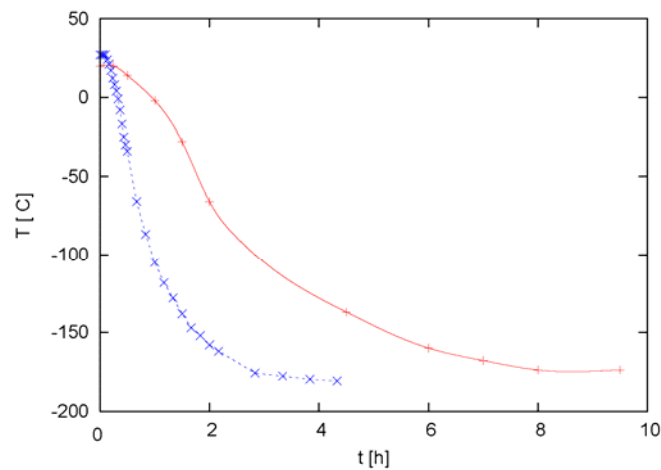


Fig. 5.7. Cooling cycle of ATC1 (in red) and a single test cryostat (in blue).

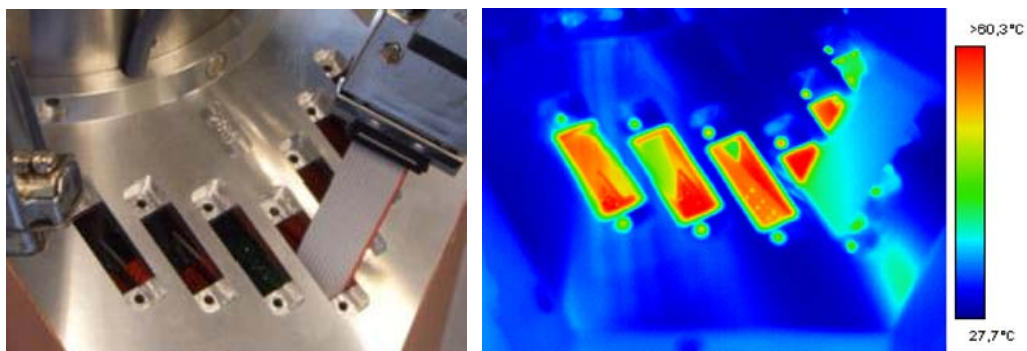


Fig 5.8. (a) preamplifier housing. (b) preamplifier housing in infra-red spectrum.

## 5.2. Detector and cryostat pool

In October 2008, all 15 crystals for the demonstrator phase were delivered by the manufacturer Canberra for customer acceptance test. However several of the crystals did not pass the customer acceptance test (CAT - see below) at the first time after delivery and were sent back to Canberra for rework. So far 3 A-type, red crystals, 3 B-type green ones and 4 C-type blue crystals have been accepted. The CAT measurements for detectors A004 and B004 were not completed due to administrative reasons and remain pending (status December 2008). A summary of all AGATA detectors is shown in table 5.1, including serial numbers, ownerships and detector specifications.

Prior to the delivery of the first asymmetric AGATA Ge detectors, three symmetric encapsulated AGATA detectors were tested (S001, S002 and S003) along with a dedicated symmetric triple cryostat (STC). These detectors have a 10° tapering angle. These prototype detectors were needed to study principal properties of the new 36-fold segmented detector type. Especially the triple cluster detector was essential for development of technical details and prototyping of various subsystem parts. This was done before the decision on the final AGATA detector configuration was made. The symmetric triple cryostat was operated in a first in-beam commissioning experiment at the tandem accelerator of the University of Cologne. The results of these experiments are shown in section 21 of this report.

Detector	Ser. Nr.	Owner	Delivery	Accepted?	HV [V]	Weight [g]
<b>S001</b>	73838	Cologne	01/04/04	yes	4000	-
<b>S002</b>	73821	GSI	01/04/04	yes	5000	-
<b>S003</b>	73839	Munich	01/12/04	yes	4000	-
<b>A001</b>	73952	France	01/06/06	01/08/06	5000	-
<b>A002</b>	74030	Padova	01/06/07	22/04/08	4000	1980
<b>A003</b>	74009	Liverpool	06/11/07	01/03/08	4500	2011
<b>A004</b>	74095	Ankara	01/07/08	pending	5000	1995
<b>A005</b>	73949	Stockholm	11/12/07	no	5000	1995
<b>A006</b>	74096	Padova	28/11/08	pending	5000	1995
<b>B001</b>	74034	Padova	06/01/07	no	5000	2042
<b>B002</b>	73979	France	01/08/06	01/11/06	5000	-
<b>B003</b>	74026	Liverpool	01/06/07	01/08/07	4500	2023
<b>B004</b>	74010	Ankara	05/06/08	pending	5000	1946
<b>B005</b>	74065	Stockholm	18/12/07	no	4500	2025
<b>B006</b>	74076	Padova	16/7/08	17/10/08	4000	2043
<b>C001</b>	73899	Padova	01/12/05	01/05/06	4500	-
<b>C002</b>	73951	France	01/06/06	01/10/06	5000	-
<b>C003</b>	74013	Liverpool	09/10/07	pending	5000	1992
<b>C004</b>	74036	Ankara	01/09/07	21/12/07	5000	2023
<b>C005</b>	74033	Stockholm	11/12/07	22/09/08	4000	1992

Table 5.1. Status of AGATA detector pool (15/12/2008). Weights were measured on naked HPGe crystals before encapsulation

Cryostat	Ser. Nr.	Owner	Pulser?
TestC1	Prototype	Cologne	No
TestC2	10033	Saclay	No
TestC3	10037	TU Munich	Yes
TestC4	10045	Daresbury	Yes
TestC5	10030	GSI	Yes
TestC6	10032	Padua	No
STC	-	Cologne/Padua	-
ATC1	10034	UK	Yes
ATC2	10036	-	Yes

Table 5.2 Overview of operational AGATA cryostats (15/12/2008).

Currently two asymmetric triple cryostats (ATC) are operational. Besides the AGATA triple cryostats, presently 6 single cryostats are available to the community. These so called test cryostats (TestC) can accommodate for a single crystal and are intended for CAT and characterization purposes. An overview of the cryostat pool is given in table 5.2, including serial numbers, ownership and whether the cryostat is equipped with pulser. Single cryostats have a length of 77.8 cm and their weight is 17.7 kg (with- out HPGe-crystal). The dewars of the single cryostats have a total length of 36.1 cm and an external diameter of 22.5 cm. Their fill volume for LN<sub>2</sub> amounts up to 2.7 l which allows for more than 12 hours of operation. The maximum operation time is slightly depending on the orientation of the cryostat. The first test cryostat was originally equipped with MINIBALL's PSC823 preamplifiers. After completion of the AGATA preamplifier development all cryostats were equipped with standard AGATA preamplifiers. Different end caps can be used on the test cryostats in conjunction with the different crystal geometries. Five types of end caps can be employed: round, symmetric and 3 asymmetric (A-, B-, and C-shape). Round end caps can be used for any Ge crystal shape. A close distance to the crystal is advantageous for characterization. Here the asymmetric end caps are used which are adapted to the shape of the encapsulation.

### 5.3. Customer acceptance tests

Before delivery to the AGATA collaboration, each Ge detector is subject of a factory acceptance test (FAT) done by the manufacturer. The results of these tests are provided by Canberra in form of an AGATA manual and relate to measurements performed using a CANBERRA test cryostat equipped with 37 cold input stages and using CANBERRA electronics.

Upon delivery, the specifications to meet are verified in a more extensive customer acceptance test which is performed by the AGATA detector working group. The tests are performed at IKP, Universitat zu Köln and CEA, Saclay.

For these measurements a single test cryostat is used which is equipped with 37 cold input stages. Standard analogue commercial electronics is used for energy resolution measurements. The cross talk properties are determined with a 37 channel coincidence electronics based on digital electronics. The CAT is supposed to be finished within two months after delivery. A CAT report is send to the detector owner with recommendations regarding the acceptance of the crystal. The requirements relate to core and segment energy resolution and crosstalk properties. Parts of the specifications are summarized in detail in table 5.3. Up to now crosstalk has never been the reason to reject a crystal. Several crystals failed due to the following reasons:

- leakage currents
- electron and hole trapping
- missing segment contacts
- segment energy resolutions out of specification

For the segment energy resolution, it can be observed that mainly front segments (ring 1) are affected. Even for accepted detectors, the tendency of a lower energy resolution is clearly present (see also Fig. 5.9). An overview of the detector performance is given in table 5.4 for all accepted detectors. Typical examples of crosstalk measurements with three symmetric AGATA detectors are shown in Fig 5.10. The data points of Fig 5.10 show peak energy shifts of the 1332.5 keV line from  $^{60}\text{Co}$  as a function of all possible 2 fold segment combinations. These values are obtained for the core energy and the segment sum energy under the condition that the full energy deposition is divided into exactly two segments. The major crosstalk effects of the segmented Ge detectors are the reduced segment sum peak energy. The energy difference of typically 2.0 keV is related to the coupling from the core signal to the segments. These energy shifts were investigated by utilising different core coupling capacitors. A detailed explanation and description of the underlying physics can be found in (5).

Energy variations around the calibration reference are observed for the core signal as a function of the 2 fold segment combinations. In comparison with the crosstalk model (5) these values are one order of magnitude higher than calculated and other effects cover the expected small energy shifts. In particular, electron trapping is put forward as an explanation for the major effects observed in the core: The energy differences vary systematically as a function of the radius of the Ge crystal, and the observed energy shifts are in agreement with calculations based on literature values.

<p><b>FOR THE CORE:</b></p> <p>Measurement of the FWHM for 1.33MeV (<math>^{60}\text{Co}</math>): <math>\leq 2.35\text{keV}</math>          Measurement of the FWHM at 122keV (<math>^{57}\text{Co}</math>): <math>\leq 1.35\text{keV}</math>          Peak shape : FWTM / FWHM: <math>\leq 2.0</math>          Measurement conditions: The source is positioned in front of the detector. Count rate <math>\leq 1000</math> counts per second, Gaussian shaping time: 6 <math>\mu\text{s}</math>.</p>
<p><b>FOR THE SEGMENTS:</b></p> <p>Measurement of the FWHM at 1.33MeV (<math>^{60}\text{Co}</math>): <math>\leq 2.30\text{keV}</math>          Mean value: <math>\leq 2.1</math> keV (not FAT)          Measurement of the FWHM at 60keV (<math>^{241}\text{Am}</math>): <math>\leq 1.3\text{keV}</math>          Mean value: <math>\leq 1.20\text{keV}</math>          Measurement conditions: The source is in front of each segment. Count rate <math>\leq 1000</math> counts per second, Gaussian shaping time: 6 <math>\mu\text{s}</math>.</p>
<p><b>EFFICIENCY:</b></p> <p>The efficiency of the detector at 1.33MeV is measured with a <math>^{60}\text{Co}</math> source at 25 cm distance from the Ge front end.</p>
<p><b>CROSSTALK (not FAT):</b></p> <p>The cross talk is extracted from a measurement of coincidences between the 36 segments using digital electronics. After adding the coincident signals of any pair of segments the variation of the position of the 1332.5 keV full energy peak will not exceed <math>\pm 0.65</math> keV.</p>

Table 5.3. Part of the AGATA specifications which are subject of the customer acceptance test (CAT).

Detector	Ser. Nr.	Core performance		Segments performance		Eff. [%]
		122 keV	1.33 MeV	60keV $\pm \sigma$	1.33MeV $\pm \sigma$	
<b>S001</b>	73838	1.16	2.20	1.14 $\pm$ 0.049	1.99 $\pm$ 0.077	71.6
<b>S002</b>	73821	1.19	2.08	1.07 $\pm$ 0.055	1.98 $\pm$ 0.067	70.2
<b>S003</b>	73839	1.10	2.13	1.03 $\pm$ 0.038	2.01 $\pm$ 0.082	70.0
<b>A001</b>	73952	1.34	2.33	1.079 $\pm$ 0.072	2.092 $\pm$ 0.156	84.4
<b>A002</b>	74030	1.26	2.31	1.031 $\pm$ 0.083	2.067 $\pm$ 0.108	83.1
<b>A003</b>	74009	1.22	2.28	1.142 $\pm$ 0.080	2.098 $\pm$ 0.128	85.8
<b>B002</b>	73979	1.29	2.27	1.094 $\pm$ 0.083	2.131 $\pm$ 0.105	87.2
<b>B003</b>	74026	1.28	2.23	1.062 $\pm$ 0.068	2.081 $\pm$ 0.106	79.2
<b>B006</b>	74076	1.01*	2.24	1.109 $\pm$ 0.076	2.041 $\pm$ 0.104	85.0
<b>C001</b>	73899	1.12	2.29	1.083 $\pm$ 0.083	2.113 $\pm$ 0.117	78.9
<b>C002</b>	73951	1.28	2.25	1.034 $\pm$ 0.079	2.027 $\pm$ 0.115	81.2
<b>C003</b>	74013	1.32	2.34	1.033 $\pm$ 0.083	2.084 $\pm$ 0.110	81.2
<b>C004</b>	74036	1.24	2.20	1.163 $\pm$ 0.076	2.207 $\pm$ 0.088	74.5
<b>C005</b>	74033	1.21	2.25	0.971 $\pm$ 0.083	2.042 $\pm$ 0.118	80.0

Table 5.4. Overview of detector performances. Results of the customer acceptance tests measured at IKP, Univ. Cologne are summarised for the accepted symmetric and asymmetric AGATA detectors. Standard deviations ( $\sigma$ ) include all segments. The reported efficiencies correspond to the values measured by Canberra. (\*value measured at 60keV)

#### 5.4. References

- [1] J. Gerl and W. Korten, AGATA - Technical Proposal for an Advanced Gamma Tracking Array for the European Gamma Spectroscopy Community " <http://www.agata.org/links> "
- [2] J. Eberth and J. Simpson, From Ge(Li) detectors to gamma-ray tracking arrays - 50 years of gamma spectroscopy with germanium detectors  
Progress in Particle and Nuclear Physics 60 (2008) 283-337
- [3] A. Pullia, G. Pascovici, et al., IEEE-NSSC3 (2004) 1411.
- [4] A. Pullia, et al., IEEE Trans. Nucl. Sci. 53 (5) (2006) 2869.
- [5] B. Bruyneel, P. Reiter, A. Wiens, J. Eberth, H. Hess, G. Pascovici, N. Warr, D. Weisshaar, Crosstalk properties of 36-fold segmented symmetric hexagonal HPGe-Detectors, accepted for publication in Nucl. Instr. And Meth. A (2008), doi:10.1016/j.nima.2008.11.011

#### 5.5. Performance of the first asymmetric AGATA triple module

The first asymmetric triple cryostat (ATC) was assembled by CTT, Montabaur, and successfully commissioned together with the AGATA detector working group at IKP, Univ. Cologne. The first ATC is housing the following accepted crystals: A001 (Serial nr. 73952), B002 (Serial nr. 73979) and C002 (Serial nr. 73951). The cluster detector was equipped with single core preamplifiers and 3x12 GANIL segment preamplifiers. All analogue energy resolutions were measured with a standard ORTEC 572 spectroscopy amplifier with 6 $\mu$ s shaping time and a PC based MCA system. All digital data were taken with 10 XIA DGF modules rev. E, (4 chan. digitizers with 14bit ADCs at 40Mhz sampling rate) employing differential to single end converter boxes.

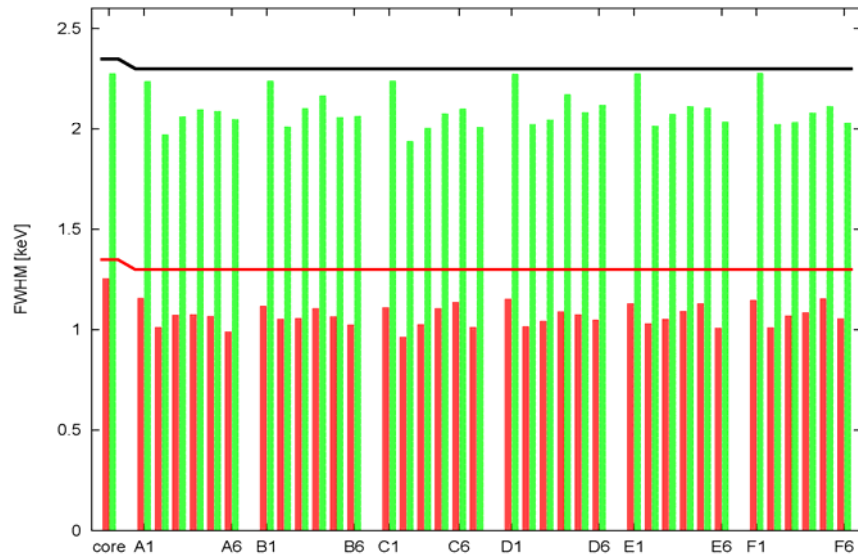


Fig. 5.9. Average resolution (FWHM) of core and segments, measured over all accepted detectors. The resolutions for the 60 keV line are shown in red. The resolutions for the 1.33MeV line are shown in green. The CAT specification limits are also shown.

Energy resolutions at 60 keV for all segments and at 122 keV for the cores were measured with analogue electronics. At higher energies of 1332.5 keV, the measurements were done with digital electronics. All segments which show energy resolution values above 2.3 keV at 1.3 MeV were measured again using analogue electronics. The results from the triple cryostat are compared in Fig. 5.11 and Fig. 5.12 with the measured performance of the same crystals in the single test cryostats. Values from the triple cryostat are shown in green, the performance in the single test cryostat is shown in red. The average values of the data are summarized in table 5.5.

The low energy resolution of the ATC is well within specification. The values obtained in the triple configuration are on average even better than in the single test cryostat. Since these resolutions are dominated by electronic noise, it demonstrates clearly the successful design and integration of the new AGATA triple cluster. Especially the electronic properties comprising the cold and warm parts of the new preamplifier assembly is causing low noise contributions in the triple cryostat despite the high integration density of 111 analogue channels. The following reasons are attributed to the improvements in the final assembly with respect to the single test cryostat: The test cryostat was equipped with PSC823 preamplifiers. The new AGATA preamplifiers were used for the ATC. An improved grounding was applied in the ATC as a result of various iterations. This reduces unwanted high frequency and noise components. A potential source for the microphonics effect was located at the core contact. Therefore the core contacts were glued in the ceramic feed through. The core energy resolution is slightly higher than in the test cryostat.

The resolution of the 1332 keV line is dominated by statistical noise and detector properties. The direct comparison with the values of table 5.4 should consider the different methods how the values were measured. Most of the averaged values in table 5.5 were obtained with digital electronics while the single test cryostat values are based on analogue electronics. Except for B002, which was entirely measured with analogue electronics. Also here the tendency in the energy resolution values, which were obtained with the test cryostat was reproduced in the triple cryostat. On average, B002 performed better in the ATC1 than in the test cryostat.

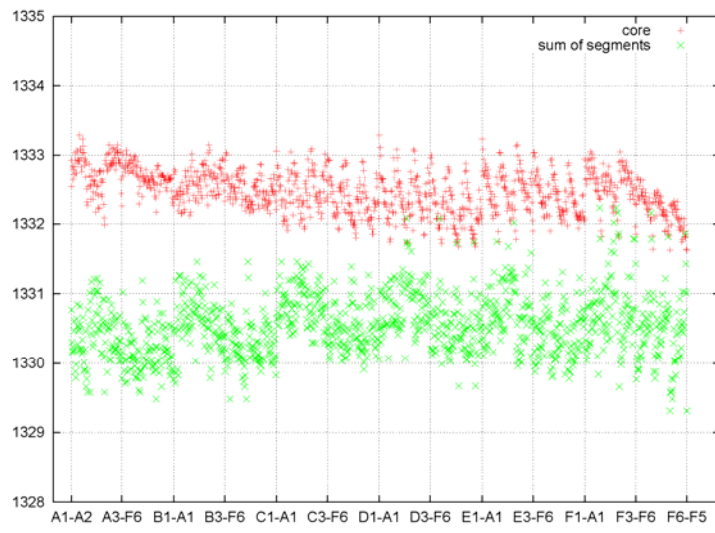
Detector	Ser. Nr.	Core performance		Segments performance	
		122 keV	1.33 MeV	60keV $\pm \sigma$	1.33MeV $\pm \sigma$
<b>A001</b>	73952	1.44	2.46	1.011 $\pm$ 0.053	2.19 $\pm$ 0.10
<b>B002</b>	73979	1.41	2.33	1.039 $\pm$ 0.070	2.10 $\pm$ 0.14
<b>C002</b>	73951	1.21	2.33	0.965 $\pm$ 0.063	2.11 $\pm$ 0.12

Table 5.5. Summary of the performance of detector ATC1; standard deviations include all segments.

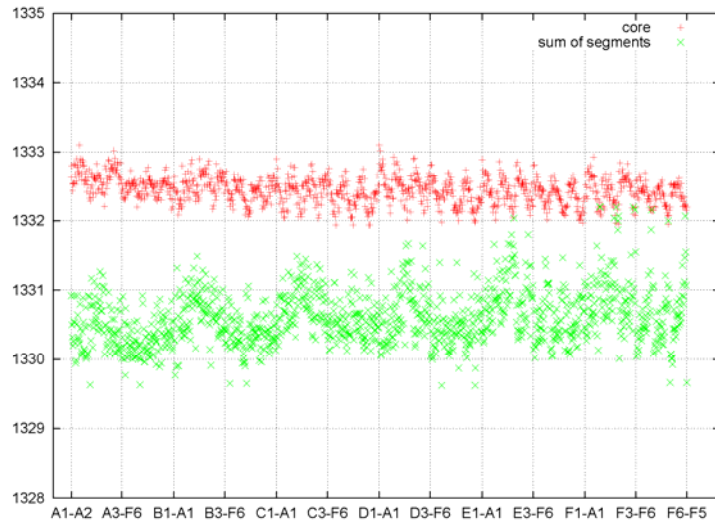
The crosstalk contributions were investigated by analyzing the coincident traces over a 7 $\mu$  sec long time period using the digital acquisition system on all three detectors. This technique, other than the technique and results shown in Fig. 5.10, analyzes crosstalk on the basis of much more abundant 1-fold events. After identification of the true energy deposition in exactly one segment the coincident and simultaneous baseline shifts are recorded which occur in all remaining 35 non-hit segments. This method allows determination of precise and absolute crosstalk matrix elements. The crosstalk pattern within each single detector is of the 0.1% level as shown in Fig. 5.13. The observed structure can be entirely attributed to the capacitive coupling between core and segments.

In contrast to first results obtained with the symmetric triple prototype cryostat, for the new asymmetric AGATA triple cluster detectors the crosstalk between the different three detectors is negligible. In ATC1, a major improvement on this part was achieved. The method applied to quantify this result is based on an extension of the 35x36 possible combinations shown in Fig. 5.10 for a single detector, to the full 110x111 possible crosstalk matrix elements within the full triple cryostat. Parts of this matrix are shown in Fig 5.14. For clarity only a limited sub set from the sectors A and F of each detector are shown.

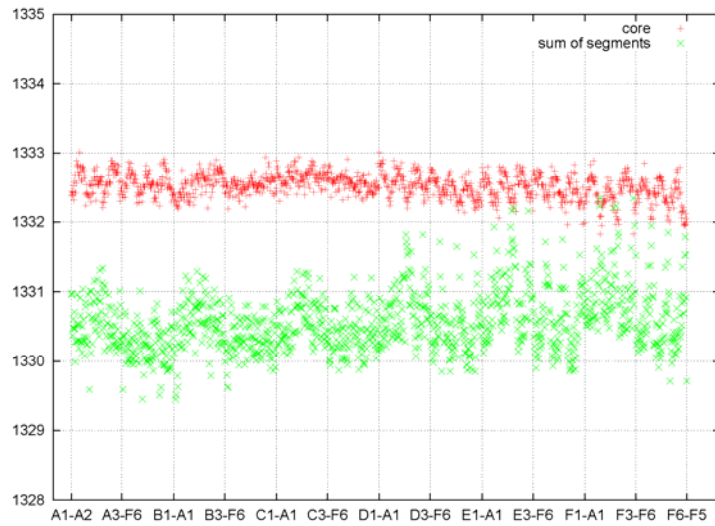
While on the diagonal graphs the same information is visible as in Fig 5.13, the crosstalk contributions between detectors would be shown in the off-diagonal graphs. However no crosstalk contributions appear between segments of different detectors. A small crosstalk component was observed between a firing detector and the core signal of a neighbouring detector. These contributions are on the 10<sup>-4</sup> level and well within the acceptable limits.



(a) A001

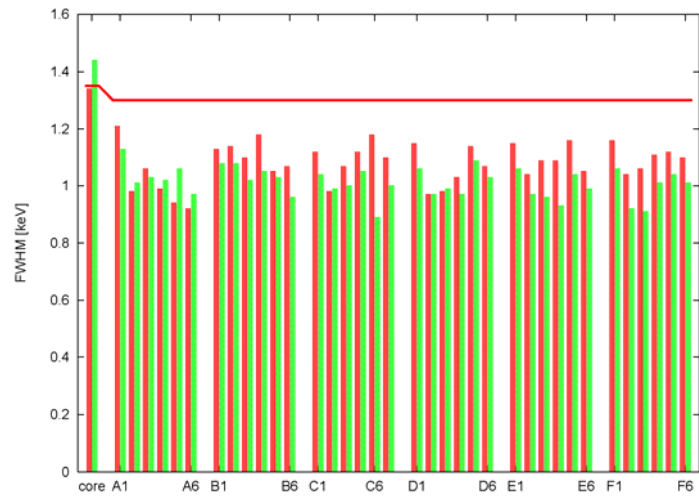


(b) B002



(c) C002

Fig. 5.10. Typical crosstalk measurement as performed for CAT. The crosstalk is observed through energy shifts in the centroids of the 1.33MeV line by gating on all 35 x 36 possible 2-fold combinations.



(a) A001



(b) B002

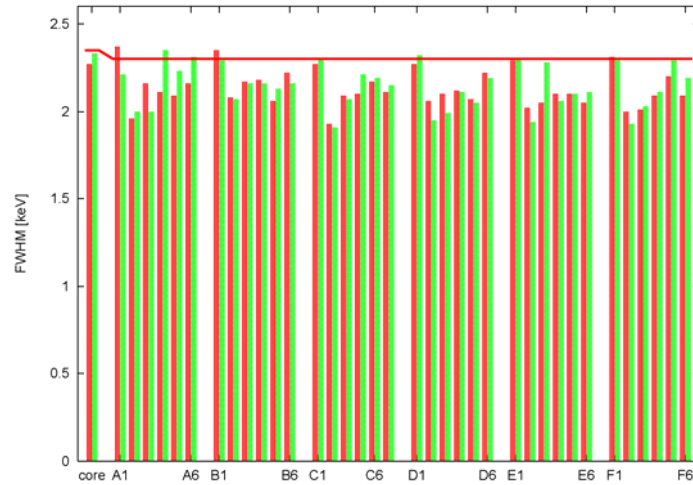


(c) C002

Fig. 5.11. Comparison of low energy performance of A001, B002 and C002 between single and triple cryostat. The performance of the Triple cryostat is shown in green. The crystals' performance in the Cologne test cryostat are shown in red. The low energy specification limit is shown by a red solid line.



(a) A001

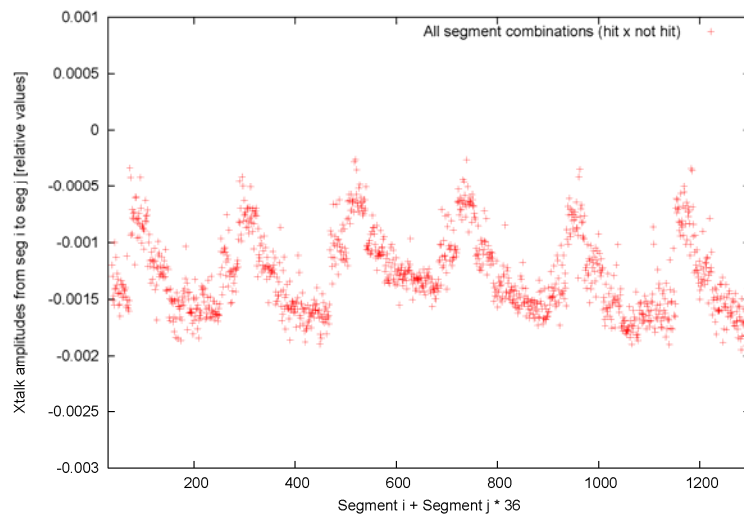


(b) B002

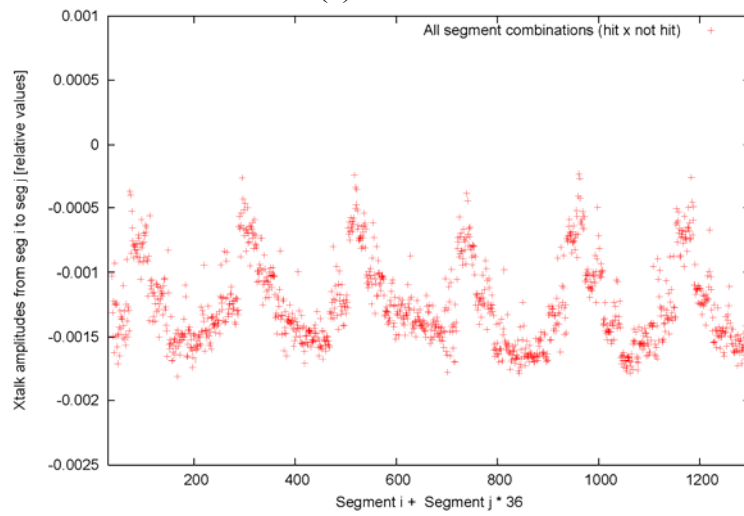


(c) C002

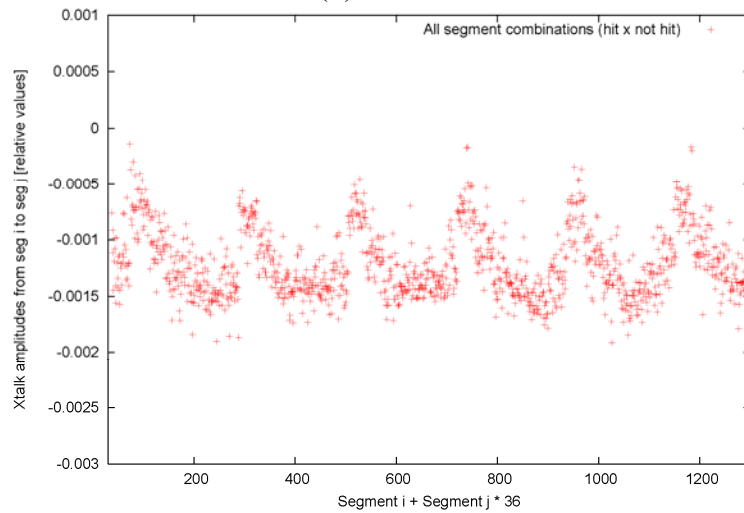
Fig. 5.12. Comparison of high energy performance A001, B002 and C002 between single and triple cryostat. The performance of the triple cryostat is shown in green. The results of the Cologne test cryostat are shown in red. The high energy specification limit is included (red solid line).



(a) A001



(b) B002



(c) C002

Fig. 5.13. Crosstalk amplitudes of all 35x36 crosstalk matrix elements in a single detector within the ATC1. The amplitudes were extracted from observation of baseline shift in onefold events.

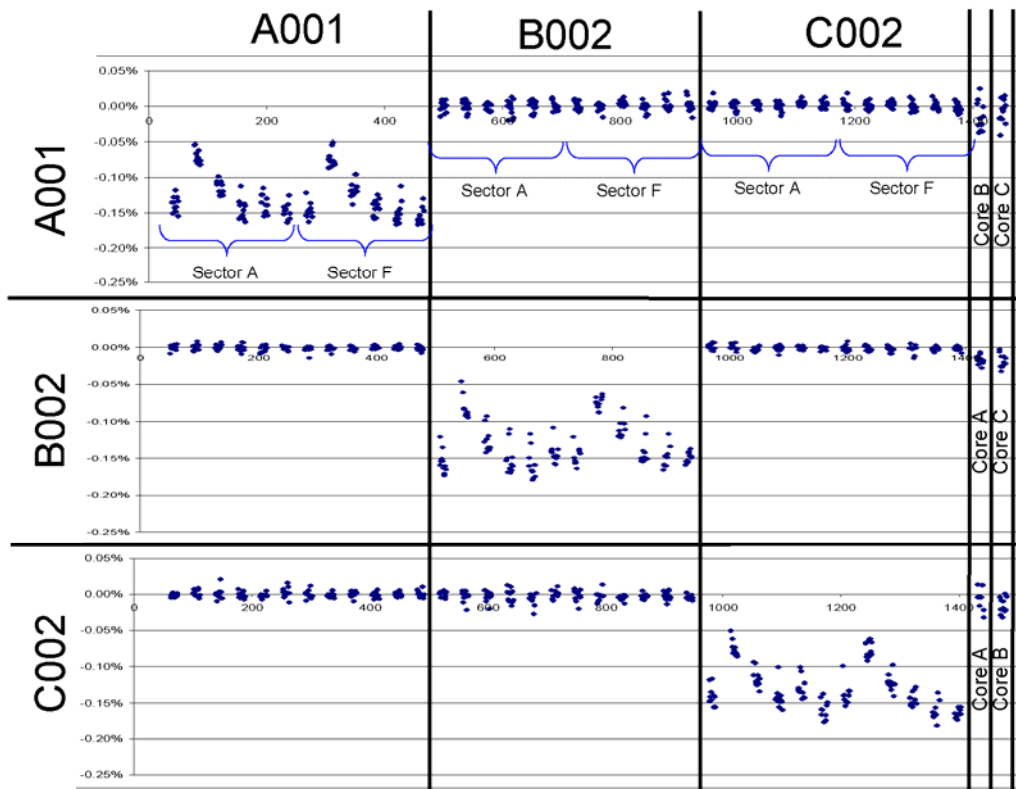


Fig. 5.14. Observed crosstalk amplitudes between detectors in ATC1. The amplitudes were extracted from observation of baseline shift in one-fold events.

## 6. Preamplifiers

### 6.1. AGATA Front-End

The segment and core signals of the AGATA detectors are read out simultaneously through advanced charge-sensitive resistive feed-back preamplifiers, employing a new “fast reset” technology for dead time and dynamic range optimization as well as an original circuit structure for maximizing the open-loop gain of the charge-sensing stage [1-11]. A custom programmable high-precision pulser located on the core-preamplifier board is used to inject calibration pulses to the core electrode itself as well as to all segment electrodes through the detector bulk capacitance, as shown schematically in Fig. 6.1.

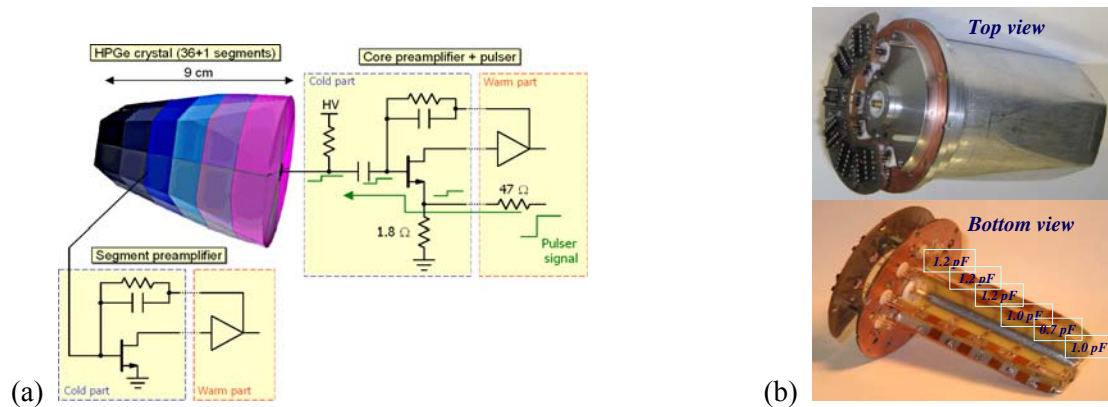
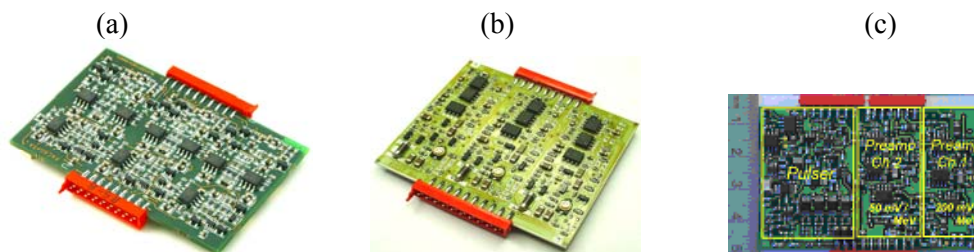


Fig. 6.1. (a) Scheme of the front-end of a segmented germanium crystal of AGATA. The signal path from the built-in pulser to the segments passes through a 1.8 ohm resistor installed in the cryostat, the input transistor of the core preamp, the High Voltage decoupling capacitor, and the detector bulk capacitance. (b) Photograph of the dummy detector realized at Koeln and used for front-end electronics developments.

The structure of the preamplifiers comprises a cold and a warm part. The cold part, located in close proximity to the detector electrodes, is operated at cryogenic temperatures and consists of a low-noise silicon Field Effect Transistor (FET), model BF862, a 0.8 pF feedback capacitance and a 1 GΩ feedback resistance. A peculiar shielding arrangement was developed for the cold preamplifier board for minimizing the inter-channel cross-talk. The warm part, operated at room temperature, is located outside the cryostat and comprises a low-noise transimpedance amplifier, a pole-zero stage, a differential output buffer, and a fast-reset circuitry. Fig. 6.2 shows photographs of the AGATA preamplifiers and their simplified schematic diagram.



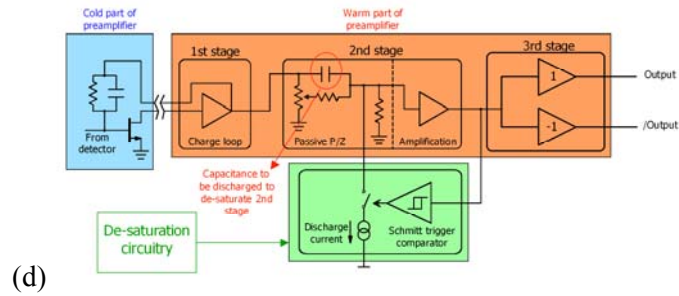


Fig. 6.2. Photographs of AGATA preamplifiers: (a) GANIL triple segment preamplifier, (b) Milano triple segment preamplifier, (c) Koeln-Milano dual gain core preamplifier with built-in pulser. (d) Simplified schematic diagram of the AGATA preamplifiers (the pulser is not shown).

The cold and warm parts are electrically connected through an optimized wiring scheme, utilizing a reduced count of feed-throughs and one ground wire per six preamplifying channels for local return currents. This ensures a good electrical grounding at low and high frequencies and a low enough thermal link between the cold and warm parts. A simplified scheme of the cold-warm preamplifier link is shown in Fig. 6.3(a).

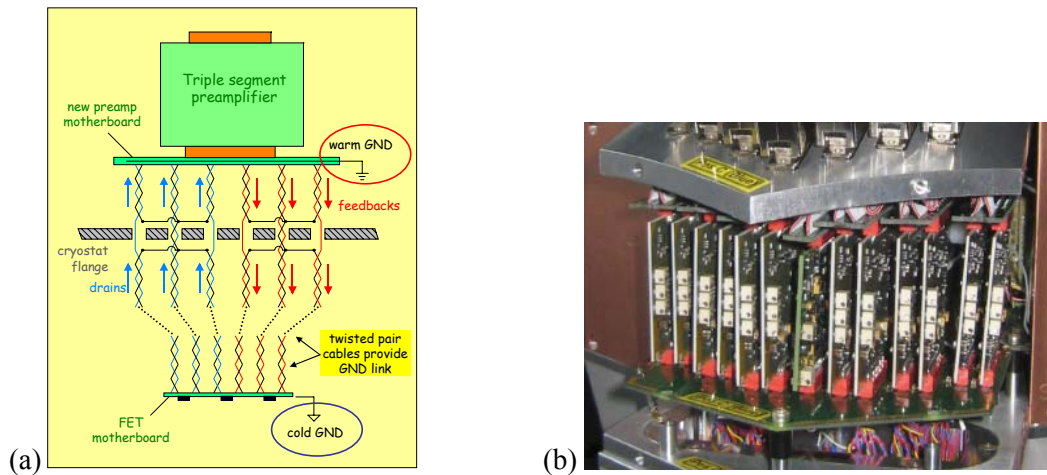


Fig. 6.3. (a) Scheme of the cold/warm preamplifiers connection. For the sake of clarity only one triple segment preamplifier is shown. (b) Photograph of a set of twelve triple preamplifiers and a core preamplifier as installed in the cryostat. The wires can be seen below the preamplifiers motherboard.

Two versions of segment preamplifiers, mainly developed at GANIL and Milano, have been realized and optimized using FR4 or alumina laminates. The average resolution over all 36 segments of GANIL and Milano preamplifiers as connected to an AGATA detector capsule is 1.15 keV fwhm at 122 keV and 2.15 keV fwhm at 1.3 MeV. No difference is observed in this regard and thus a half of the demonstrator array, under commissioning at LNL in 2009, is being equipped with GANIL preamplifiers and the other half with Milano preamplifiers. Two versions of core preamplifier with built-in pulser have been realized and optimized, as developed in a collaboration of the Koeln and Milano groups. The first version has a single amplification channel and uses TTL logic signals while the second has two amplification channels operated simultaneously (“dual gain”) for energy-range optimization, and uses LVDS logic signals. The core preamplifier uses a sophisticated compensation technique [1] to stabilize the cryostat/front-end system, which shows an eigenfrequency at  $\sim 120$  MHz. The energy resolution of the core preamplifier as connected to an AGATA detector capsule is 1.1 keV fwhm at 122 keV and 2.19 keV fwhm at 1.3 MeV. The spectral line provided by the built-in pulser over an acquisition time of 10 hours has a resolution of

1.005 keV fwhm, which is even better than that obtained with a commercial high-precision pulser for gamma ray spectroscopy. The specifications of the AGATA preamplifiers are shown in Table 6.1.

Table 6.1. Specifications of the AGATA preamplifiers.

Property	value	tolerance
Conversion gain for segments and single core	100 mV / MeV (terminated)	$\pm 10$ mV
Conversion gain for dual core	200 mV/MeV (Core Ch. 1) 50 mV/MeV (Core Ch. 2)	$\pm 20$ mV $\pm 5$ mV
Noise	0.8 kev fwhm (0 pF, room T)	
Noise slope	8 eV / pF	$\pm 2$ eV
Rise time	13 ns (0 pF)	$\pm 2$ ns
Rise-time slope	$\sim 0.4$ ns / pF	
Decay time	50 $\mu$ s	$\pm 2$ $\mu$ s
Integral non linearity	$< 0.025\%$ (D=3.5V unterminated)	
Output polarity	Differential, Z=100 $\Omega$	
Fast reset speed	$\sim 10$ MeV / $\mu$ s	
Inhibit output	Single Core: CMOS / Dual Core: LVDS	
Power supply	$\pm 6.5$ V, $\pm 12.5$ V	$\pm 0.5$ V
Power consumption of input jFET	$< 20$ mW	
Power consumption (except diff. buffer)	$< 280$ mW (840 mW for a triple)	
Supplimentary power for differential buffer in very high 'non saturated' counting rates	$\sim 700$ mW	
Mechanical dimension	$\sim 70$ mm x 50 mm x 7 mm (for triple segments and for dual core) $\sim 62$ mm x 45 mm x 7 mm (single core)	

## 6.2. Programmable Pulser Structure

The built-in programmable pulser is installed in a side of the core preamplifier board. It is a precision pulse generator designed to test the stability and linearity of the system, as well as to estimate the resolution of the segments. The output signal of the pulser is dc coupled to the source pin of the core input FET through a resistor divider consisting of a 48.5 ohm resistor and a grounded 1.8 ohm resistor. Thereafter the signal reaches each of the 36 detector segments as shown in Fig. 1. A block diagram of the programmable pulser is shown in Fig. 6.4

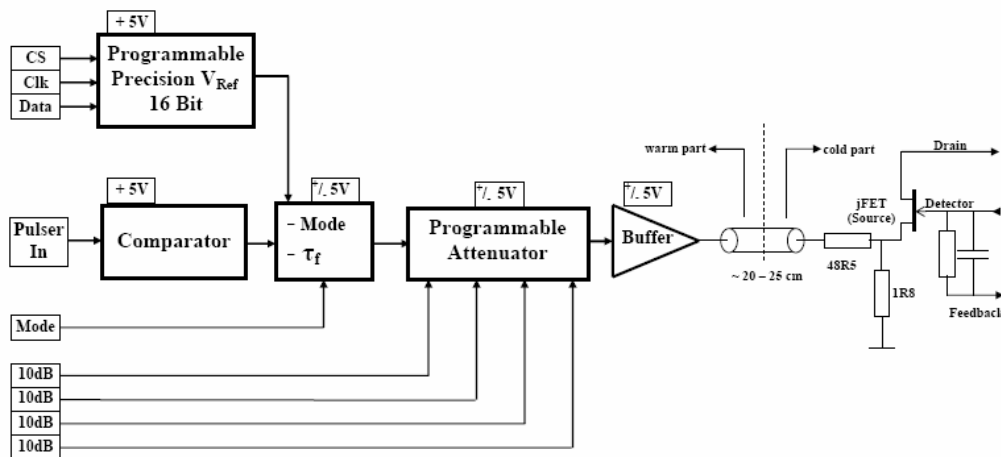


Fig. 6.4. Block scheme of the programmable pulser.

It uses fast CMOS electronic switches realizing a chopper which alternately transmits the reference voltage  $V_{ref}$  or the ground voltage to the output. The reference voltage is obtained through an ultra-stable band-gap generator circuit and is adjusted through a Digital to Analog Converter (DAC) acting as fine-gain controller. A “Mode” stage sets the shape of the output

waveform as a square wave or an exponential decay sequence. A programmable attenuator realized with CMOS switches acts as coarse gain controller.

### 6.3. Fast Reset Technology and ToT Measurements

All AGATA preamplifiers are equipped with the fast-reset device shown in the bottom block of Fig. 6.3d. A Schmitt-trigger comparator (LT1719) continuously senses the amplitude of the preamplifier output signal. When it exceeds an adjustable threshold the comparator commutes and turns on a temperature-stabilized current sink. Its current discharges capacitance  $C$  of the P/Z stage until the preamplifier output signal is brought back to the zero voltage floor. At this point the comparator commutes again and turns the current sink off. The comparator provides a digital signal (INHIB) which is high when the fast reset device is on and low when the fast reset device is off.

The preamplifier is therefore characterized by a mixed “continuous-pulsed” reset technique [7]. The continuous-reset mode is used for the typical signal amplitudes, up to a few MeV, which are covered by the Analog to Digital Converter (ADC) input range. The pulsed-reset mode works on larger signal amplitudes, either caused by individual events or by bursts of piled-up events, which cause ADC saturation. As compared to pure continuous or pulsed reset solutions, such operation mode provides an improved performance: it optimizes the pileup and the noise in the typical energy range and minimizes the dead time caused by amplitude saturation in the high energy range. In Fig. 6.5a the oscilloscope track of a large over-threshold signal (cosmic ray) is shown which activates the fast-reset mechanism. It can be seen that the preamplifier signal is quickly restored to the baseline value. In Fig. 6.5b a large signal is observed, which causes saturation of the sampling ADC. Note that the fast reset quickly desaturates the ADC. The corresponding digital output signal (INHIB) delivered by the comparator is also shown in the lower part of the figure.

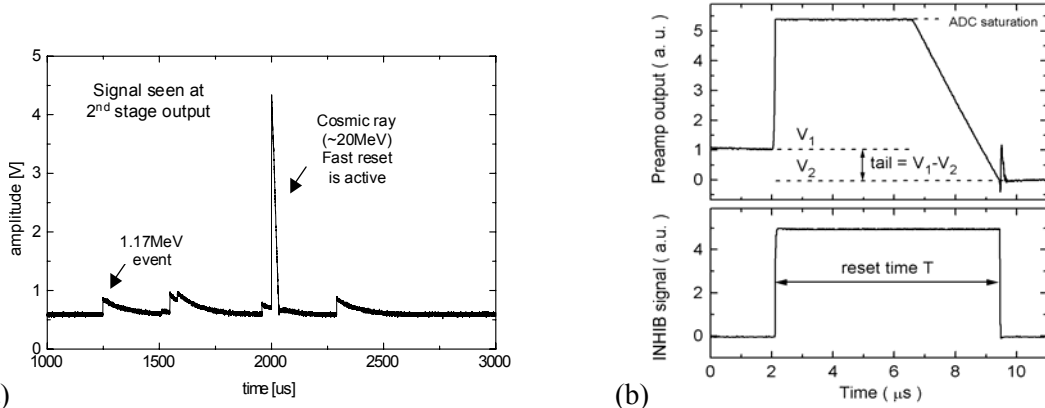


Fig. 6.5. Fast reset transients seen (a) on the oscilloscope, and (b) on the AGATA sampling ADC.

The “fast reset” technology allows pulse height measurement of large individual signals from the reset time, when the ADC overflow condition would give no possibility to make a direct measurement, as the upper part of the signal is lost. A quasi-linear relation holds between the reset time  $T$ , or Time over Threshold (ToT) of the preamplifier signal, and the amplitude  $E$  of the large signal. The exact time-to-energy relation has been mathematically derived as described in detail in [5]. Here we simply recall an approximate relation obtained as a second-order Taylor expansion of the original one, which is accurate enough for practical use:

$$E = b_1 T + b_2 T^2 - k_1 (V_1 - V_2) + E_0. \quad (1)$$

In Eq. (1) parameters  $b_1$  and  $b_2$  are the coefficients of the second-order expansion, while  $E_0$  is an offset term. The contribution to the reset time brought about by the tail of previous events is cancelled through the third term of Eq. (1). The tail is measured as the difference between the pre-pulse and post-pulse baselines  $V_1$  and  $V_2$  (see Fig. 6.5b), as estimated by averaging the baseline samples along a short time span.

We then applied the ToT technique to real gamma photons, using an AGATA capsule and an AGATA core preamplifier (first version), while collecting the spectrum from a 7-9 MeV Americium-Beryllium compound isotopic gamma-ray source [12]. This source is a compound system made of a long-lived Americium-Beryllium ( $^{241}\text{Am}+\text{Be}$ ) neutron source which produces fast neutrons in the 0-10 MeV range. These neutrons are moderated in surrounding paraffin and then absorbed into a natural metallic nickel target. The radiative capture of thermal neutrons in natural metallic Ni produces five prominent gamma-rays in the range 7.5-9 MeV, of which the 8.998 MeV line is the strongest by more than a factor of two. We were in particular interested in collecting the higher energy part of the spectrum, from 3 to 10 MeV, where the lines of C, Fe and Ni are located. At first we switched the reset device off and set the internal gain of the ADC so as to obtain an energy measurement range of 10 MeV. In this way we could collect the spectrum in standard “pulse-height mode”. The result is shown in Fig. 6.6(a). Then we let the reset device work and set the reset threshold at 3 MeV, so as to collect the same spectrum in “reset mode”, i.e. by applying the ToT technique on the stored digitized waveforms. The result is shown in Fig. 6.6(b).

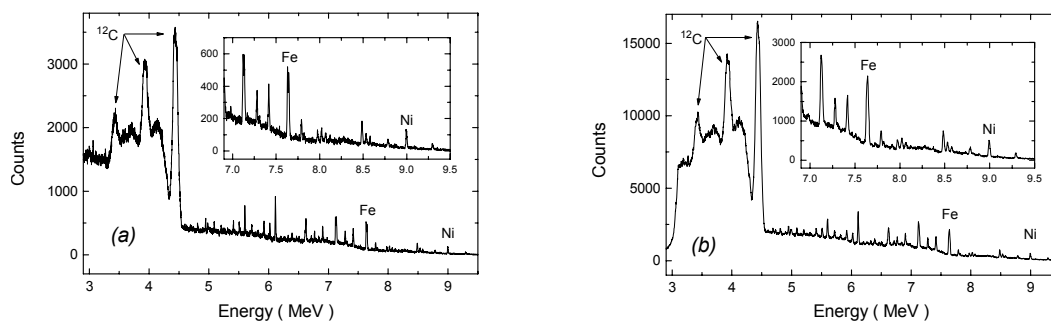


Fig. 6.6. Spectrum of the  $^{241}\text{Am}+\text{Be}$  source as acquired (a) in standard pulse-height mode, (b) in reset mode, i.e. by applying the ToT technique to the stored digitized waveforms

The excellent correspondence of the two spectra is evident, which proves the effectiveness of the reset-mode measurement technique. All the relevant peaks are identified by the ToT algorithm. It is worth pointing out that in this case the count rate did not vary during all the 12-hour acquisition session, as the source was extremely stable in flux. Therefore no issues arose concerning the peak shifts at increasing count rates. The obtained resolutions are shown in Table 6.2. The three Doppler-broadened lines due to  $^{12}\text{C}$  are perfectly reconstructed by the ToT technique, having the 4.44 MeV line the same resolution as obtained in pulse-height mode. This line is due to the first excited state of  $^{12}\text{C}$ , produced by a fusion reaction between Be and the  $\alpha$ -particles emitted by Am. As expected, all the other lines were found to show a slightly worse resolution with respect to the pulse-height mode spectrum. Anyway the obtained resolution in reset mode is better than 0.4 % over the full range. Moreover, at increasing energies, the resolution in reset mode approaches that obtained in pulse-height mode. The highest energy line at 8.9984 MeV, due to thermal neutron capture in nickel, shows a full width at half maximum (fwhm) of 15 keV in pulse-height mode and a fwhm of 19 keV in reset mode. In terms of percent resolution this means an increase from 0.17% to 0.21%. This was found to be an excellent result. The two Ni lines as obtained in the two modes are shown for comparison in Fig. 6.7.

Table 6.2. Resolution of the spectrum lines in the two different modes

Energy	Resolution (fwhm) in pulse-height mode		Resolution (fwhm) in reset mode	
	Energy	Resolution (fwhm)	Energy	Resolution (fwhm)
4.440 MeV ( $^{12}\text{C}$ )	104 keV	2.34 %	104 keV	2.34 %
~5.6 MeV	10.5 keV	0.14 %	18.8 keV	0.34 %
~6.1 MeV	15.1 keV	0.17 %	17.1 keV	0.28 %
7.6312 MeV (Fe)	11 keV	0.14 %	18.8 keV	0.25 %
7.6456 MeV (Fe)	11 keV	0.14 %	(29.4 keV for double-peak)	(0.38 keV for double-peak)
8.9984 MeV (Ni)	15 keV	0.17 %	18.9 keV	0.21 %

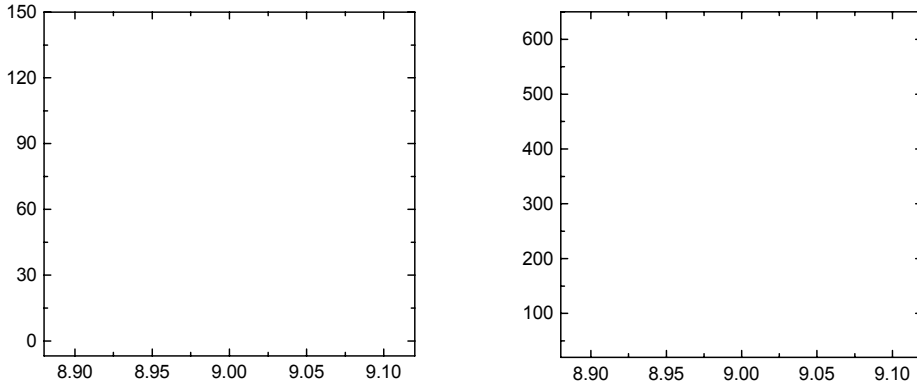


Fig. 6.7. Ni line as obtain (a) in pulse height mode, (b) in reset mode

The reset mode gets really successful at increasing energies and approaches the performance of standard processing, because the electronic noise becomes less important owing to the intrinsic broadening of the spectrum lines. For large volume germanium detectors this is due to the statistics of created charge carriers but moreover to the decreasing charge collection efficiency [13]. In this condition the shaping and filtering techniques on which the pulse-height mode spectroscopy is based become a less stringent requirement. Therefore, we can obtain energy information also through the ToT technique which is based directly on the signals provided by the preamplifier, i.e. before standard shaping and filtering. The purpose of the ToT technique is not that of replacing the standard pulse-height analysis, which will always give the best performance for a given energy range. The ToT technique is to be applied beyond the range of the ADC, where the saturated signals would be lost, so as to obtain an increase of the energy measurement range. In the shown measurements we tested the ToT technique on spectrum lines within the ADC range, because no other lines at higher energies were available. The  $^{241}\text{Am}+\text{Be}$  source was the only portable source of relatively high energy gamma-rays. Anyway, testing the ToT algorithm within the ADC energy range allows us to investigate the real performance of the fast-reset technique and make a fair comparison with standard pulse-height mode. In order to exploit the full potentiality of the ToT technique, the ideal acquisition chain consists of two read-out channels working in parallel with two different energy ranges. This is realized in the AGATA dual-gain core preamplifier shown in Fig. 6.2c. The first channel covers a relatively narrow energy range of 5 MeV, in order to optimize the resolution at low energies. The second channel covers a wider energy range, up to 20 MeV. The fast reset device operates in the first channel, with a reset threshold set at about 10 MeV. In this way we eliminate the issues connected to the transition region between pulse-height mode and reset mode, as this critical region is covered by the second channel. In addition, the overlap region between the two acquisition modes, from 10 to 20 MeV, is usable for a proper calibration of the ToT algorithm. Therefore the reset mode becomes useful beyond the range of the second channel, from 20 MeV on. At these high energies we reasonably think that the performance of the ToT technique reaches that obtainable with

standard pulse height analysis. As a result, we obtain an ultra-wide overall energy measurement range that optimizes the resolution in each region and with no discontinuities in the obtained spectra. In principle the upper limit of the obtained energy range is the saturation limit of the charge sensing stage of the preamplifier (which is not protected by the reset device) or about 150 MeV of equivalent energy. Actually, the ultimate limit to the measurement range would then be determined by the germanium detector efficiency in stopping the impinging gamma rays and no more by the saturation of the electronic chain.

#### 6.4. References

- [1] G. Pascovici, A. Pullia, F. Zocca, B. Bruyneel, D. Bazzacco, "Low noise dual gain preamplifier with built in spectroscopic pulser for highly segmented high-purity germanium detectors", WSEAS Transactions on Circuits and Systems, vol. 7, no. 6, pp. 470-481, June 2008
- [2] F. Zocca, A. Pullia, G. Pascovici, "Design and Optimization of Low-Noise Wide-Bandwidth Charge Preamplifiers for High Purity Germanium Detectors", IEEE Trans. Nucl. Sci., vol. 55, no. 2, pp. 695-702, 2008
- [3] A. Pullia, F. Zocca, G. Pascovici, D. Bazzacco, "Extending the dynamic range of nuclear pulse spectrometers", Rev. Sci. Instrum. 79 (3), art. 036105 pp. 1-3 (2008)
- [4] F. Zocca, A. Pullia, D. Bazzacco, G. Pascovici, "Wide Dynamic Range Front-End Electronics for Gamma Spectroscopy with a HPGe crystal of AGATA", 2007 IEEE Nucl. Sci. Symp. Conference Record, CD-ROM, paper N03-2, ISBN 1-4244-0923-3/07, Honolulu, Hawaii, USA Oct. 27 – Nov. 3 2007
- [5] F. Zocca, A. Pullia, C. Boiano, R. Bassini, "A Smart Reset Circuit for Low-Noise Preamplifiers of X-gamma Ray Sensor Signals", IEEE Trans. Nucl. Sci., vol. 54, no. 1, pp. 197-201, Feb. 2007
- [6] A. Pullia, F. Zocca, G. Pascovici, "An Advanced Preamplifier for Highly Segmented Germanium Detectors", IEEE Trans. Nucl. Sci. vol. 53 no. 5, pp. 2869-2875, Oct. 2006
- [7] F. Zocca, A. Pullia, C. Boiano, R. Bassini, "A mixed continuous-pulsed reset technique for digitised preamplifiers of radiation signals", 2005 IEEE Nucl. Sci. Symp. Conference Record, San Juan, Puerto Rico, USA 23-29 Oct. 2005
- [8] A. Pullia, F. Zocca, G. Pascovici, C. Boiano, R. Bassini, "Ultra-fast low-noise preamplifier for bulky HPGe gamma-ray sensors", 2005 IEEE Nucl. Sci. Symp. Conference Record, San Juan, Puerto Rico, USA 23-29 Oct. 2005
- [9] A. Pullia, F. Zocca "A low-noise preamplifier for gamma-ray sensors with add-on device for large-signal management", Nucl. Instr. and Meth. Sect. A, vol. 545, no. 3, pp. 784-92 2005
- [10] A. Pullia, C. Boiano, R. Bassini, G. Pascovici, "Active reset of digitized preamplifiers for ionizing-radiation sensors", IEEE Trans. Nucl. Sci., vol.51, no.3, pp. 831-5 (2004)
- [11] A. Pullia, G. Pascovici, B. Cahan, D. Weisshaar, C. Boiano, R. Bassini, M. Petcu, F. Zocca, "The AGATA charge sensitive preamplifiers with built-in active-reset device and pulser", 2004 IEEE Nucl. Sci. Symp. Conference Record, Rome, Italy, 16-22 Oct. 2004, vol. 3, pp. 1411-1414
- [12] J. G. Rogers, M. S. Andreaco, C. Moisan, and I. M. Thorson, "A 7-9 MeV Isotopic Gamma-Ray Source for Detector Testing", Nucl. Instr. and Meth, vol. A413, pp. 249-254, 1998.
- [14] G.F. Knoll, "Radiation Detection and Measurements", Third Edition, John Wiley & Sons, Inc., pp. 416-418



## 7. Detector characterisation

### 7.1. Introduction

The success of the AGATA project hinges on the ability to be able to reconstruct the trajectories of gamma rays scattered within the germanium detectors. The deposited energy and the location of the photon interactions can be extracted from the measurement and the analysis of the waveforms that arise on the segments during the charge collection. The pulse shape analysis algorithms currently developed use databases of calculated pulse shapes. These calculated pulses need to be validated with real pulse shapes taken at various points within a detector. For the development of tracking algorithms, it is also crucial to determine experimentally the position sensitivity in 3 dimensions in the whole volume of a detector.

The role of the detector characterisation working group is to perform a detailed analysis of the response function of the large volume high purity germanium crystals (HPGe) that will be utilised in the AGATA array. The work includes developing a theoretical basis data set which describes the detector response function and then validating this against the equivalent experimental data. Such knowledge will provide the project with the information necessary to enable Pulse Shape Analysis and Gamma-ray Tracking. The group has one operational experimental characterisation centre, based at the University of Liverpool in the UK and two centres being commissioned at CSNSM Orsay, France and GSI Darmstadt, Germany.

A schematic diagram outlining the Liverpool AGATA detector scanning system is shown in Fig. 7.1. The figure shows the mechanical configuration of the system, with the detector vertically mounted above the collimated source assembly. A 920MBq  $^{137}\text{Cs}$  source is mounted at the end of a 1mm diameter coaxial tungsten collimator of 120mm in length. The collimator is mounted in a lead collar and source housing assembly, which shielded the mounted source from the system operators. The whole assembly was mounted on a precision Parker x-y positioning table. The table was moved in precise computer controlled steps through the use of pacific scientific stepper motors and two Parker Automation axis indexers. The system has a position resolution of 100 $\mu\text{m}$ .

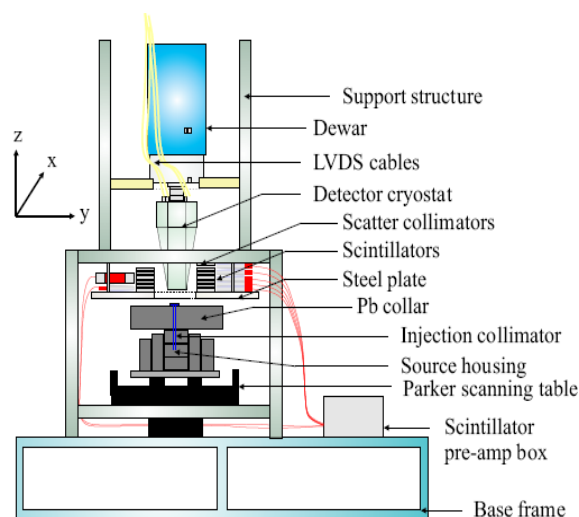


Fig. 7.1. A schematic diagram showing the Liverpool scanning table assembly.

Coincidence scanning utilizes the Compton scattering cross-section to define a single interaction position in x-y-z. Such a methodology demands that the gamma-ray photon Compton scatters through an angle of 90 degrees in the germanium detector, depositing the remaining energy in a collimated ring of coincidence scintillation detectors. This method is very precise but is a very slow procedure (typically 2 months per detector), due to the low coincidence rate between the germanium detector and coincidence scintillators. The

coincidence data has been utilised to validate the electric field simulation codes such as the Multi Geometry Simulation (MGS) toolkit. The precisely determined 3D interaction positions have allowed the comparison of experimental pulse shapes from single site interactions with those generated by the simulation. The data sets have also been utilised to validate the efficacy of the scanning procedure for producing comparable data sets for consecutive detectors. The absolute position sensitivity has been evaluated. A detailed analysis of singles and coincidence data for the prototype AGATA symmetric detectors can be found in work by Dimmock et.al. The scanning systems being commissioned at Orsay and GSI aim to utilise a faster procedure for precise coincidence measurements, which would significantly increase the number of AGATA detectors that could be experimental characterised. The detector characterisation group recommends a minimum of 3 of each shape of detector are measured.

In view of the time consuming characterisation process a second scanning system is being commissioned at CSNSM Orsay. A schematic view and a photo of the set-up are shown in Fig. 7.2. A 500 MBq  $^{137}\text{Cs}$  source is encapsulated by a stainless steel cylindrical container of diameter 4mm, height 6 mm and window thickness 0.4 mm. This container is then inserted into a collimator made of densimet (W-Ni-Fe alloy, density  $18.5\text{ g/cm}^3$ ). The gamma-rays emitted by the source are collimated by a 1.6 mm diameter hole 155 mm in length.



Fig. 7.2. Drawing (left) and photo (right) of the Orsay scanning system: 6 NaI modules of TOHR and mechanical support, the AGATA detector and the collimated intense  $^{137}\text{Cs}$  source.

Six modules of the TOHR (Tomographe à Haute Résolution [1]) detector are used to perform the coincidence measurements. Each module is made up of a stack of 40 triangular-shaped 200 mm thick W-plates. The plate separation is also 200 mm. The plates are pierced by a large number of 200 mm diameter holes positioned on a hexagonal lattice. At the back of the stack of plates, there is a NaI crystal for the detection of gamma-rays. The geometry of each stack of plates acts as a many slit ( $\sim 16000$ ) collimator with a focal distance of  $\sim 7\text{cm}$ . The 6 modules are positioned in a compact semi-circle at  $\pm 10.8$  degrees from the horizontal plane around the AGATA detector with the same focal point in the Germanium detector. The position of the common focal point can be changed by translating the TOHR array or by turning the AGATA detector about its symmetry axis thus allowing a full 3D scan of the AGATA detector.

From the simulations, the number of single interaction Compton scatter events at a given position can be determined:  $\sim 400/\text{hour}$  near the front face of the detector, and  $\sim 100/\text{hour}$  in the front third of the detector, but only  $\sim 10/\text{hour}$  at the back of the detector. These results are confirmed by the performed measurements.

## 7.2. Example activity

To date, three AGATA symmetrical segmented Canberra Eurisys (CE) prototype HPGe detectors have been tested at the University of Liverpool and one asymmetric production detector is presently being measured. A data set of the experimental preamplifier pulse

shapes observed as a function of the interaction position of a beam of gamma-ray photons was recorded. A highly collimated  $^{137}\text{Cs}$  (662keV) source was used to measure the detector response function and an automated x-y positioning table was used to move the source. Such a detector “scan” allows the experimental detector response function to be precisely measured, allowing comparison with a theoretical pulse shape database. Scan data can be collected in two modes of operation, Singles and Coincidence respectively. Singles data yields x-y position information on the interaction position of a gamma-ray photon. Such a measurement is relatively quick to collect however it suffers from the fact it produces an average detector response. The primary interaction mechanism for gamma-rays of 662keV in germanium will be Compton scattering, this will lead to uncertainties in the position of interaction. The singles data therefore has enabled the investigation of the detector response through the bulk crystal.

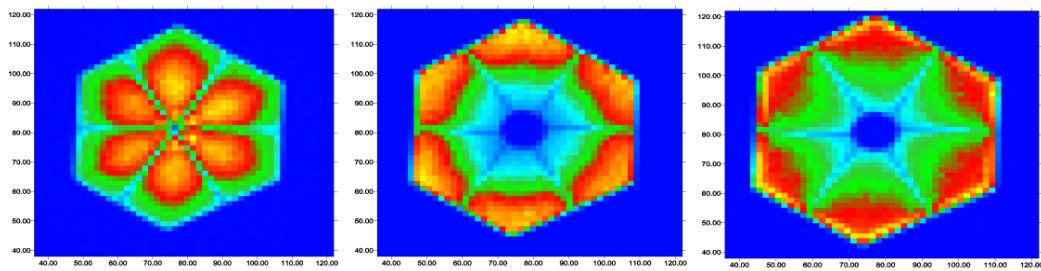


**Figure 7.3,** The distribution of intensity for 662 keV full energy deposition confined to a single segment. The blue colour corresponds to <50 counts, the yellow to >700 counts. The result for ring 1 (left), ring 2 (centre) and ring 3 (right) clearly show the segmentation pattern of the detector.

A scan of the front face of the asymmetric production detector C001 was performed, yielding  $\sim 800$   $^{137}\text{Cs}$  photopeak cps. Data were recorded on a 1mm grid for 1 minute at each position. The system was triggered using an external CFD with a threshold of  $\sim 650\text{keV}$  on the central contact in order to eliminate unwanted Compton scattered or background data. The resulting distribution of intensity for 662keV full energy deposition confined to a single segment in rings 1, 2 and 3 of the detector is shown in Fig. 7.3. The x and y axes represent the position of the scanning table, a range of 0 to 80mm. Regions of high and low intensity are indicated by yellow and blue respectively. The plots clearly show the segmentation pattern of the detector and the presence of the core hole for rings 2 and 3.

The average pulse shape recorded at each position was calculated and a 2D histogram of the core pulse shape rise time T30 (10-30% of max. amplitude) and T90 (10-90%) was plotted, the results are shown in Fig. 7.4. The results show a strong dependence in the charge collection time as a function of interaction position. In the AGATA detector, the electrons move towards the central anode while the holes move towards the outer cathode. Therefore, with increasing radius the electrons have further to travel (the opposite is true for hole transport). The T30 distribution clearly demonstrates the dependence of the electron drift time with radius, with a minimum T30 of  $\sim 30\text{ns}$  for small radii and maximum T30 of  $\sim 100\text{ns}$  for large radii.

The T90 curves are determined by the combination of both electron and hole transport. This gives rise to a distinctive minimum in the charge collection time at the distance of equal collection times. The maximum T90 values are therefore observed at both large and small radii for regions in the coaxial volume of the detector, yielding a maximum rise time of 200ns in ring 2 or 240ns in ring 3 where the radius is larger. The minimum rise time is  $\sim 100\text{ns}$ . For the front ring (1) of the crystal both the T30 and T90 distributions have a different character due to the more complex electric field distribution in this region of the detector. Minimum rise times are observed at small radii due to the quasi-planar nature of the electric field and hence associated short charge collection times through the 13mm distance

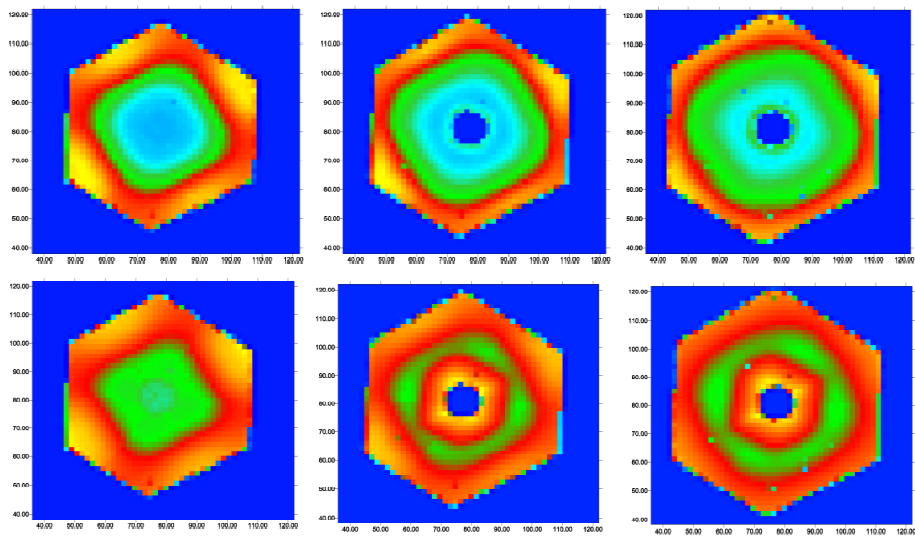


**Figure 7.4,** [Top] The core pulse shape rise time T30 (10-30%) distribution. The values obtained range between 30ns (cyan) and 100ns (yellow). The results for ring 1 (left), ring 2 (centre) and ring 3 (right) clearly show the crystallographic axis orientation. [Bottom] The corresponding T90 (10-90%) distribution. The values obtained range between 100ns (green) and 240ns (yellow).

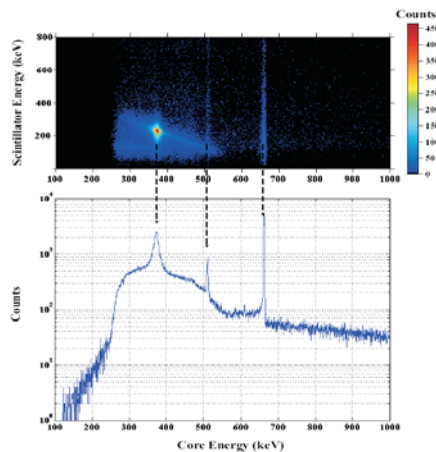


Figure 7.5 Matrix of the centre contact energy versus scintillation detector energy for all fold one events that triggered the acquisition. A fold one gate was also applied to the scintillation detector banks. The small circular shaped region of high intensity in the centre of the matrix corresponds to the 90o scatters. The diagonal line that extends through either side of this region corresponds to other scattering angles through which the gamma rays could pass between the collimation gaps. The 662keV photo-peak was the result of random coincidences with photons, emanating from the source, penetrating the lead shielding and interacting in the AGATA detector.

from the front face to the hole drill depth in the crystal. These plots also show the influence of the FCC crystal lattice orientation on the pulse shape rise times. For pulse shapes measured at the same radius a 30% effect is evident on the observed rise profile, this must be taken into account in the theoretical simulation if a reliable validation is to be achieved.

Coincidence scan data has yielded precise pulse shape response data from 2000 experimental interaction positions inside the AGATA detector volume. As an illustration of the quality of the coincident events a matrix of the centre contact energy versus scintillation

detector energy for all fold one events that triggered the acquisition is shown in Fig. 7.5. A fold one gate was also applied to the scintillation detector banks. The small circular shaped region of high intensity in the centre of the matrix corresponds to the  $90^\circ$  scatters.

Once the true coincident events have been selected, the arrays of pulse shapes were output in ASCII format for subsequent processing. Of the ten collimation depths probed, the first two in each rig were identical, thus the contributions were summed, leaving eight different depths in the study. The effective segmentation in the front of the detector meant that for interactions at depth of 17.9mm, the gamma ray could scatter from either the first or second ring, depending on the radius of the scanning table. The interactions at  $z = 17.9\text{mm}$  were split according to the ring in which they occurred, thus a total of nine depth categories were considered.

The ASCII file for each single site interaction position was read into an algorithm that processed the data and constructed the corresponding set of 37 average pulse shapes for that position. The algorithm utilised a series of functions, described in Fig. 7.6, to determine the best set of pulses for each average.

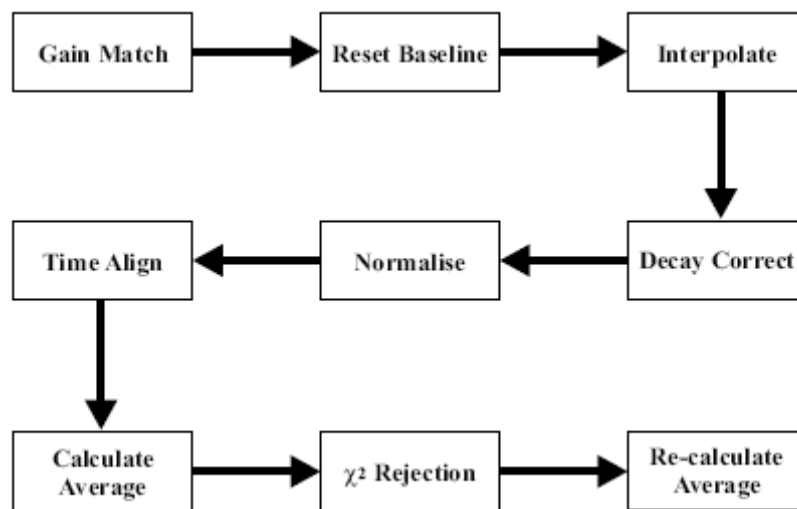


Figure 7.6: Flow diagram showing the analysis procedure for processing the array of pulse shapes at each precisely determined interaction position.

The functions are summarised as:

1. Gain Match - The 37 waveforms for each event in the array were scaled by their pre-calculated gain factors, derived from the  $^{152}\text{Eu}$  baseline difference spectra.
2. Reset Baseline - The average baseline for each waveform was calculated and set to zero.
3. Interpolate - Each pulse was interpolated from 12.5ns per sample to 2.5ns per sample to ensure accurate time alignment. The function performed a five-point linear interpolation followed by a three-point moving average.
4. Decay Correct - All 37 pulses were multiplied by a sample-by-sample factor that accounted for the average decay time constant of the preamplifier. Thus the resulting compensated real charge pulses had a constant flat top from the point of maximum rise.
5. Normalise - The maximum amplitudes of the real charge outer and centre contact pulses were averaged and normalised to one. The remaining 35 pulses were scaled by the same factor.
6. Time Align - As the GRT cards do not have a global clock, the pulses had to be aligned independently on an event-by-event basis. The  $t_{10}$ s of both the centre and outer contact real charge pulses were calculated per event. Each pulse was then

- shifted so that the t10 position was tracked to a pre-determined sample number. The remaining 35 pulses were shifted by the same coefficient as calculated for the core.
7. Calculate Average - The set of 37 average pulses was calculated by summing down the columns of the array of manipulated pulse shapes and dividing by the number of pulses in the sum.
  8.  $X^2$  Rejection - The  $X^2$  distribution for each position was calculated by comparing the centre and outer contact real charge pulses, and nearest neighbour image charge pulses of the average distribution to the individual pulse shapes that constituted the average.
  9. Re-calculate Average - The set of 37 average pulses was then recalculated, excluding those events for which the  $X^2$  was deemed too large. Figure 7.7 shows the average (red) and constituent (blue) pulse shapes for an interaction at  $x = 78.8\text{mm}$ ,  $y = 49.0\text{mm}$ ,  $z = 33.1\text{mm}$ , following the 2 rejection. The effect of the cancellation of the random noise across the pulses is clearly visible. The standard deviation of the baseline noise for the average pulses is  $0.9\text{keV}$ , as opposed to  $4.7\text{keV}$ .

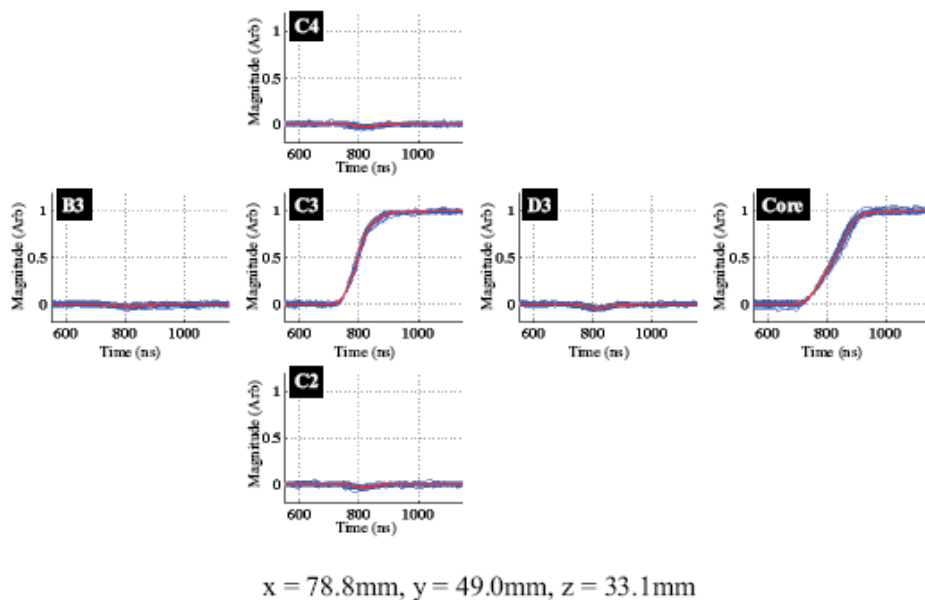


Figure 7.7: Average (red) and all constituent (blue) pulse shapes for an interaction at  $x=78.8\text{mm}$ ,  $y=49.0\text{mm}$ ,  $z=33.1\text{mm}$  in segment C3, following the  $X^2$  rejection,

Pulse shape databases have been generated from simulated and experimental data for the S002 and S003 AGATA symmetric prototype detector geometries. Each database contains sets of 37 pulses for each of the 2490 single site interaction positions. By performing a detailed comparison between the experimental and simulated data, it has been possible to quantify the agreement between the simulated and experimentally measured pulse shape response. The validity of the use of the MGS software to generate a basis for on-line Pulse Shape Analysis (PSA) has been assessed. The comparison of the equivalent experimental databases has also allowed the efficacy of the scanning procedure to generate reproducible data sets to be tested. The comparison with the optimised theoretical MGS basis data set is discussed in the next section.

## 8. Pulse shape calculations

### 8.1. Introduction

In order to realise the real-time localisation of the scattering sequence following a gamma-ray interaction inside an AGATA detector, the experimentally digitised pulse shapes will be compared with a basis data set. For online pulse shape analysis (PSA) to be implemented successfully, it has been estimated that in excess of 30000 basis sites per crystal for a 2mm Cartesian grid [8.1] are required. The basis can be obtained from either experimental or simulated data, however on average 2 hours of data collection are necessary for the generation of the thirty seven average pulses at each basis site. The time prohibitive nature of this work means a reliable methodology for generating a theoretical basis data set was required. The AGATA project has therefore developed electric field simulation codes such as Multi Geometry Simulation (MGS) package, the Java AGATA Signal Simulation (JASS) toolkit and the IKP Detector Simulation and Optimisation method, in order to facilitate the realisation of on-line PSA. These codes have been used to generate variants of a single crystal basis. In particular MGS was used to assess the performance of the competing PSA algorithms tested for several different basis configurations and the following description will therefore focus on its use. Two of these basis configurations are presented simultaneously in figure 8.1. The figure illustrates both a 5mm and 2mm Cartesian basis, as one would expect the finer basis was found to give the best position resolution, however the larger number points required resulted in longer interaction processing times.

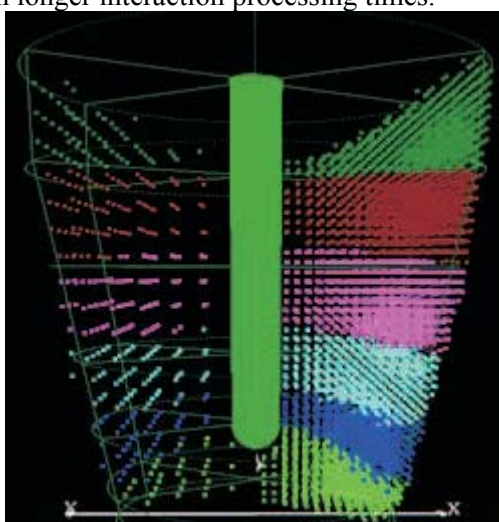


Figure 8.1: A schematic representation of the basis points for two contrasting equi-spaced grids that could be used for the AGATA prototype detectors. The number of bytes held in memory is related to the number of grid points. As such, the grid spacing must be a compromise between deconvolution accuracy and processing time. The figure is taken from [8.1].

### 8.2. Detector Pulse Shape Simulation

The Multi Geometry Simulation (MGS) [8.2] package was developed at the Institut Pluridisciplinaire Hubert Curien IPHC (previously Institut de Recherche Subatomique, IReS) in Strasbourg France. It utilises MatLab's matrix environment to derive the expected pulse shape response at the contacts of any geometry of HPGe detector. The stand alone package has been compiled for use with both Linux and Microsoft Windows operating systems.

Environments such as FEMLAB and DIFFPACK can also be adapted for providing an analytical solution to the complex electric field distribution inside the AGATA detectors. They utilise Finite Element Methods (FEM) for solving partial differential equations, such as the solution to Poissons' equation. MGS was developed as an alternative specialised solution to these commercial packages.

MGS utilises the multi-step algorithm, shown in block format in figure 8.2. The calculations are performed on a user specified 3D grid that maps a given detector volume. Results from each stage of the calculations are stored in matrices. The values at each point in the matrices are then recalled to generate the pulse shape response, as determined by the trajectories of the charge carriers through the weighting field.

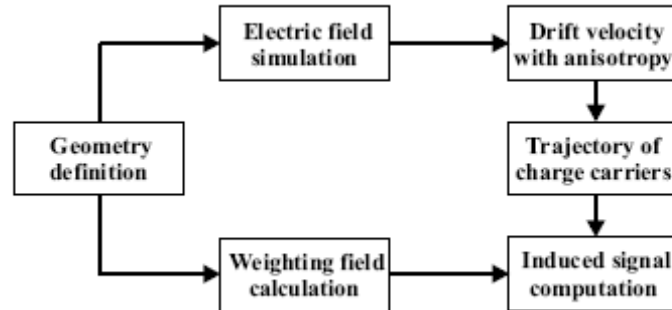


Figure 8.2: MGS data flow diagram for the simulation of the expected pulse shapes at the contacts of any arbitrary HPGe detector geometry. For a given detector, the crystal volume is divided into a cubic matrix of lattice sites. Values for the electric potential, electric field and weighting field are calculated at each position. The drift velocity matrices are calculated from the electric field matrix. The detector response for a given interaction site is calculated by tracking the trajectory of the charge carriers through the weighting field.

In order to compute the pulse shape response for a given interaction position in the detector volume, the following routines must be performed:

1. Specification of the detector geometry. This requires an input text file that contains the coordinates of the apices of the crystal. The user is then prompted to enter parameters relating to the operating bias voltage, impurity concentration, operating temperature, spacing between the crystal and the encapsulating medium, the properties of the bore hole (if the detector is coaxial), the segmentation and passivation.
2. Calculation of the electric potential surfaces and electric field lines, starting from the solution of the Poisson equation.
3. Implementation of charge carrier transport in a semiconducting medium. Data derived from work described by [8.3] and [8.4] has been incorporated to describe the anisotropic mobility of electrons and holes respectively.
4. Calculation of the trajectories of charge carriers for arbitrary interaction positions.
5. The application of Ramo's theorem [8.5], providing the resulting charge recovery at the contacts.
6. Weighting potential and weighting field resolution.

MGS has been used to simulate the both the symmetric prototype and asymmetric AGATA detectors. Figure 8.3 shows the symmetric prototype detector geometry generated by MGS. The central anode and outer cathode are coloured red and blue respectively. Figure 8.4 shows the Electric potential (figure 8.4a) and Electric field (figure 8.4b) values in the z-x plane at  $y = 51\text{mm}$  (centre of the crystal). The results show the decrease in potential and field strength as a function of increasing radius from the central anode. The figure clearly illustrates the complex nature of the electric field within the closed end coaxial geometry of the AGATA crystal.

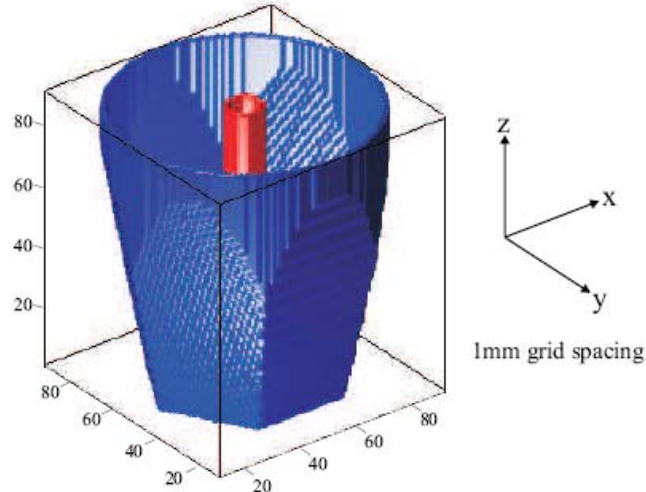


Figure 8.3: An MGS simulation of the AGATA symmetric prototype detector geometry.

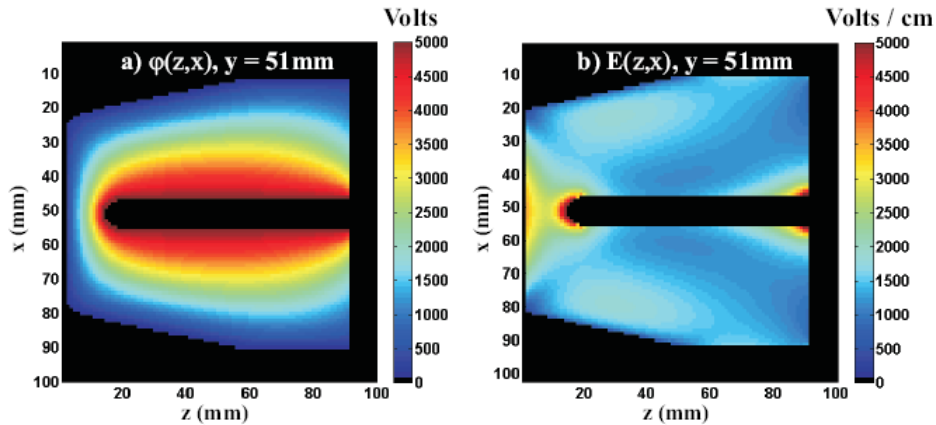


Figure 8.4: a) Electric potential and b) Electric field values in the z-x plane at  $y = 51\text{mm}$  (centre of the crystal). The results show the decrease in potential and field strength as a function of increasing radius from the central anode.

At high electric fields and low temperatures the charge carrier drift velocities in germanium become anisotropic [8.6]. They depend on the electric field vector with respect to the crystallographic lattice orientation. The electron drift velocities,  $V_e$ , are saturated at field strengths  $>3000\text{Vcm}^{-1}$  for the  $\langle 100 \rangle$  and  $\langle 110 \rangle$  directions, and at  $\sim 4000\text{Vcm}^{-1}$  for the  $\langle 111 \rangle$  direction. The hole drift velocities  $V_h$  are saturated for fields  $\sim 4000\text{Vcm}^{-1}$  along all three major crystallographic axes. The models for anisotropic drift of the electrons and holes in n-type HPGe detectors implemented in MGS have been derived from work presented in [8.3] and [8.4] respectively.

Before the induced current at each electrode can be calculated, the weighting potentials and weighting fields must be generated. The calculation is performed with a null space charge density and with +1V on the sensing electrode with all other electrodes grounded. For a given interaction position, the charge pulse response observed at any electrode depends on the trajectory of the charge carriers through the weighting potential of that electrode. In order to illustrate the reason for the shape of the real and image charge signals calculated for the AGATA geometry, a test example for two interactions in segment A4 of the detector is presented in figure 8.5. In this example position A is close to the centre

contact and position B is close to the outer contact. The green dashed lines show the path of the charge carriers to the electrodes. Figure 8.5a, figure 8.5d and figure 8.5g show the weighting potentials for the core, segment A4 and a neighbouring segment, A3. The weighting potential for the core shows a qualitatively similar distribution to that of the electric potential. It has a maximum value in the centre of the detector and decreases as a function of radius. Conversely, the weighting potential for segments A3 and A4 are strongest at large radii, and fall away quickly as the radius approaches the core. The weighting potential for each electrode extends throughout the volume of the detector and is related to the geometry of that electrode.

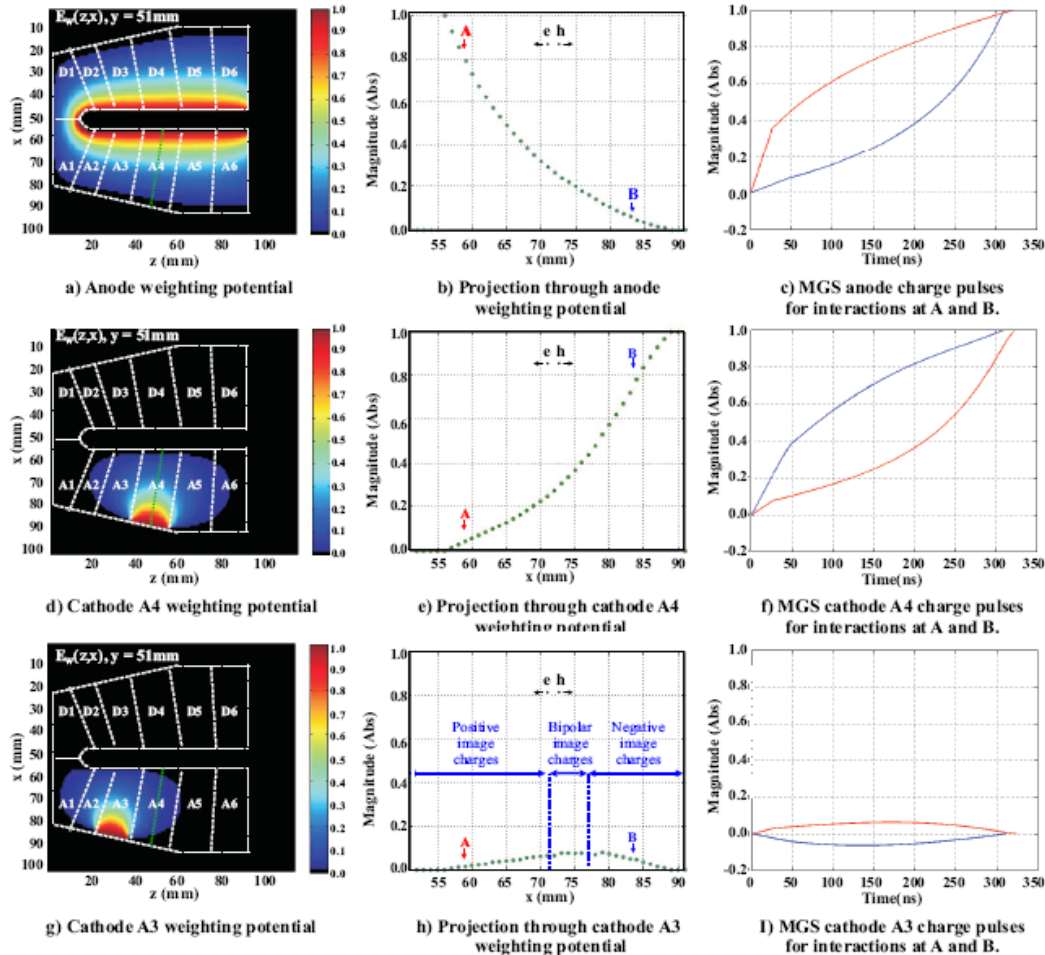


Figure 8.5: A figure showing how MGS calculates the charge pulse response from the trajectory of the charge carriers through the weighting potentials of the electrodes. Two interaction positions in segment A4 are considered. Position A is close to the centre contact and position B is close to the outer contact. a), d) and g) show the simulated core, A4 and A3 weighting potential distributions for the z-x plane at  $y = 51\text{mm}$ . The trajectory of the charge carriers is shown by the green dashed lines. b), e) and h) show the projections through the weighting potentials along these trajectories. c), f) and i) present the charge pulse response for interactions at A (red) and B (blue) for the core, segment A4 and segment A3 respectively.

Figure 8.5b, figure 8.5e and figure 8.5h show projections through the weighting potentials along the trajectory of the charge carriers for the central anode, segments A3 and segment A4 respectively. For each simulated interaction, MGS outputs the induced current as a function of time. The contributions from the electron and hole must be summed and integrated in order to obtain the charge pulse response. The remaining sections of figure 8.5 illustrate the resulting charge pulse shapes that are utilized in the basis data set. This simple integration does not account for the limited bandwidth of the charge sensitive preamplifier,

the low-pass Nyquist filter at the input stage of the digitiser cards, or the sampling of the 14bit 80MHz FADC used in the experimental data. In order to compensate for these experimental factors, several corrections have been applied to the data. The simulated data is adjusted to fit the experimental data as the correction factors can be applied independently of the noise.

The MGS code was used to generate a full basis data set of each shape of AGATA detector. Figure 8.6 illustrates the level of agreement between a coincidence experimental data set and the MGS basis for an interaction in the true coaxial region of the AGATA s002 prototype detector. The MGS code was validated using this experimental data and the MGS code parameters were adjusted to obtain the optimum agreement. The read should not there are still discrepancies observed.

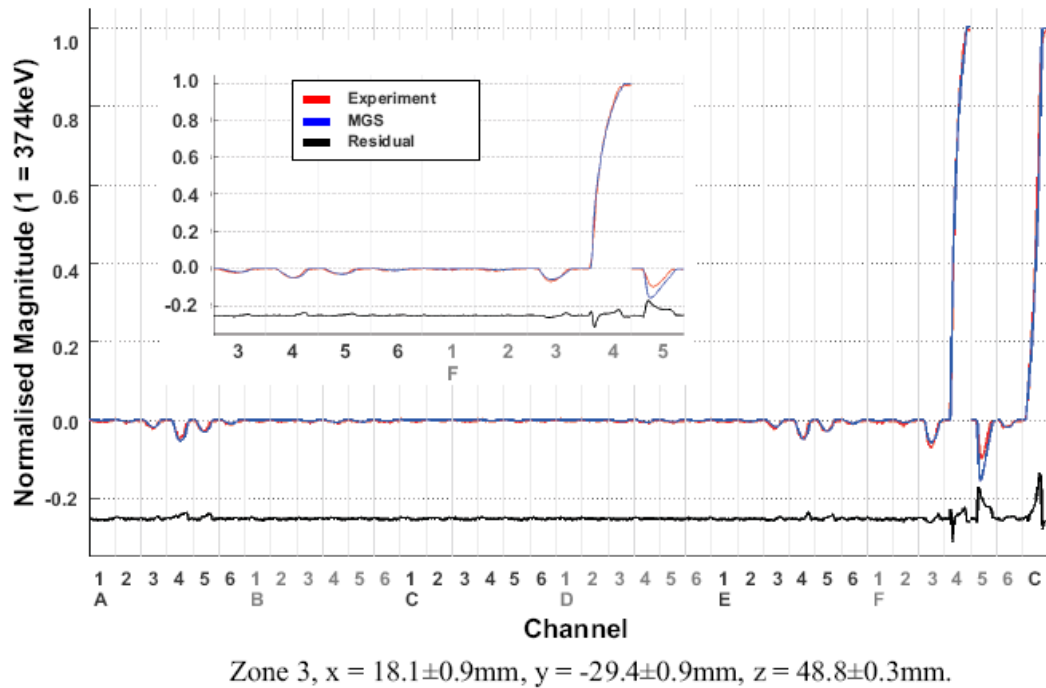


Figure 8.6: A figure showing the 37 charge pulses from the S002 prototype detector for an interaction in a “true coaxial” region of the detector at  $x = 18.1 \pm 0.9 \text{mm}$ ,  $y = -29.4 \pm 0.9 \text{mm}$ ,  $z = 48.8 \pm 0.3 \text{mm}$ . The average experimental pulses are shown in red, the MGS calculated responses are shown in blue and the difference in magnitude between the two pulse shape data sets is shown in black. The inset section of the figure shows the expanded region between pulse shapes E3 and F5

The coincidence scan data yielded precise pulse shape response data from 2000 experimental interaction positions inside the AGATA detector volume. This data was compared to the optimised theoretical MGS basis data set, the results from this comparison are shown in figure 8.7. The results show a general good agreement between theory and experiment with an average displacement of between 2.2 mm and 2.6 mm, 4.2mm and 48.8mm from the front of the detector respectively. This result has been independently corroborated by work performed at IKP by Bruneel et al. It is speculated that the reason for the apparent directionality of the arrows towards the front or centre of the segments is the influence of derivative cross talk between the segments, which influences the observed pulse shape rise time. A methodology for correcting for this has been developed and will be implemented for future work.

### 8.3. Summary

All the detectors have shown good energy resolution performance at low and high energy, yielding typically  $\sim 1.1 \text{keV}$  at  $60 \text{keV}$  and  $\sim 2.0 \text{keV}$  at  $1.3 \text{MeV}$ . The levels of cross-talk have been measured and quantified. Analysis of the singles data has allowed charge pulse rise time

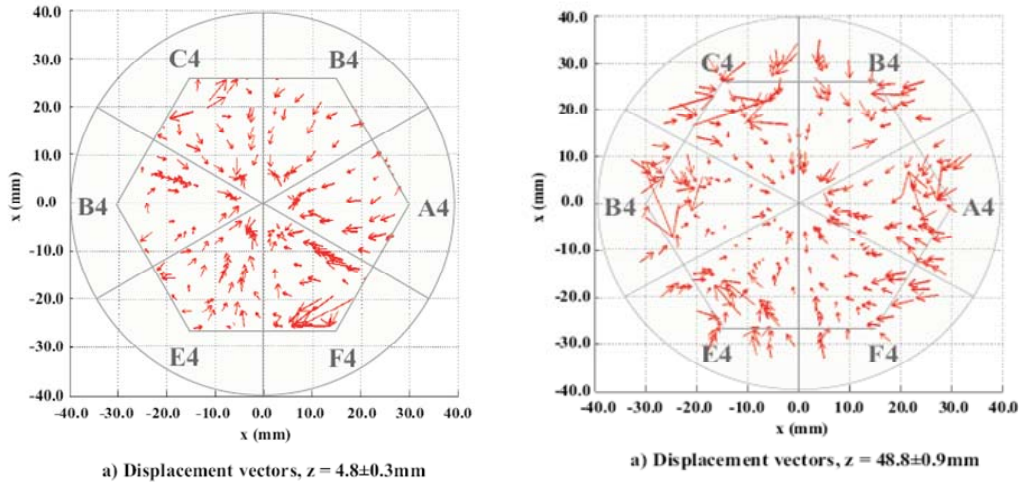


Figure 8.7 A vector displacement map where the arrows represent the difference between experimentally measured interaction positions and the site in the MGS basis that gives the best match.

and image charge asymmetry matrices to be generated. From these, the charge transport properties through the crystal volume have been studied. MGS has been calibrated from pulse shape comparisons at over 2000 interaction sites within the detector. An average displacement of 2.5 mm in x and y has been measured when comparing each of the average responses for the 2000 experimental interaction positions to a  $1.0 \text{ mm} \times 1.0 \text{ mm}$  MGS basis. Good agreement between the S002 and S003 experimental data sets has proven that the symmetric detectors respond in a similar manner and that the consecutive scans have been performed to a high precision.

Depth (mm)	Ring	Min Displacement (mm)	Max Displacement (mm)	<Displacement (mm)>
$4.2 \pm 0.3$	1	$0.1 \pm 0.4$	$11.9 \pm 0.4$	$2.2 \pm 0.4$
$15.7 \pm 0.3$	1	$0.2 \pm 0.6$	$17.3 \pm 0.6$	$2.7 \pm 0.6$
$48.8 \pm 0.3$	4	$0.1 \pm 0.7$	$17.0 \pm 0.7$	$2.6 \pm 0.7$

Table 8.1 A table showing the variation in the magnitude of the displacement vectors for 4.2mm, 15.7mm and 48.8mm from the front face of the detector crystal.

#### 8.4. References

- [8.1] Grid Search - A possible PSA algorithm for the AGATA demonstrator, R. Venturelli, Presentation, AGATA Week (2007)
- [8.2] A simple method for the characterisation of HPGe detectors, P. Medina, C. Santos, Di Villaume, Istr. Meas. Tech. Conf (2004).
- [8.3] The influence of anisotropic electron drift velocity on the signal shapes of closed-end HPGe detectors, L. Mihailescu, W. Gast, R.M. Lieder, H. Brands, Nucl. Instr. Meths. Phys. Res. A, Vol.447, p350 (2000).
- [8.4] Characterization of large volume HPGe detectors Part I: Electron and hole mobility parameterization, B. Bruyneel, Nucl. Instr. Meths Phys. Res. A, Vol.569 p764 (2006).
- [8.5] Review of the Shockley Ramo theorem and its application in semiconductor gamma-ray detectors, Z. He, Nucl. Instr. Meths. Phys. Res. A, Vol.463(2001)
- [8.6] Anisotropy of the conductivity of n-type germanium at high electric fields, M.I. Nathan, Phys Rev, Vol.130, p2202 (1963).

## 9. Pulse shape analysis and algorithms

### 9.1. Introduction

The performance of the gamma-ray tracking arrays strongly depends on the capability of the pulse-shape (PSA) and tracking algorithms. The task is to identify the individual interaction points, and the corresponding energy-deposits, of a gamma ray with a low percentage of error. The accuracy of the location has to be better than five millimeters. The location and energy determination must be performed by algorithms that are fast enough for real-time application, with the computing power available in the near future. In case of multiple interactions in a crystal or even in a segment the analysis effort strongly increases with the number of degrees of freedom. We have developed a set of different algorithms optimized for the different types of events. A first operational version of the pulse shape analysis code has already been implemented in the final NARVAL environment. After the first test experiments in Legnaro, the other fast algorithms, suited to more complex event structures, will be also implemented. Nevertheless it is expected that the performance of PSA will continually improve during the project due to refined algorithms and increased computing power.

### 9.2. Signal bases

The method of pulse shape analysis is based on a more or less direct comparison of the measured pulse shapes from all segments in a crystal and a so-called signal basis. The signal basis consists of a full set of pulse shapes using the digitizer resolution of 10 ns for each grid point inside the crystal, several time steps within the digitizer resolution and normalized signal amplitudes. The typical grid used here is 2 mm in each coordinate with time steps of 1 ns which fills a signal basis of roughly 1 Gigabyte.

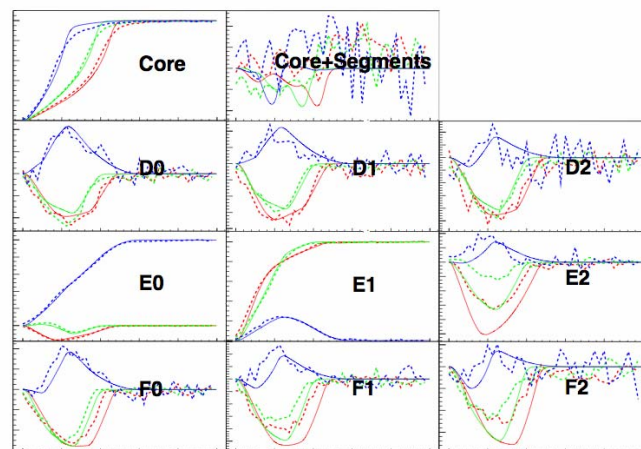


Figure 9.1 Comparison between AGATAGeFEM (solid) and experimental (dashed) signals from a symmetric AGATA detector.

It is very essential to use a basis of the detector response that is as precise as possible. This pulse shape basis can be obtained using a detector scanning system (the scanning tables developed by the Collaboration are described above) or a simulation code. Up to now, extensive but still only partial detector scans have been performed. More complete detector scans will be done in 2009 using new methods and electronics to get complete 3D regular scan of the different germanium crystals types used in AGATA. First pulse shape basis have been generated using the MGS simulation code [9.1]. Two other codes are being developed by the collaboration. Pulse shapes are calculated using the Schockly-Ramo method, different profiles of impurity concentrations inside the crystal and a 3 D Matrix of drift velocities for electrons and holes. The detector specific parameters used in the calculations have to be fitted to scanning table data. Unlike the MGS version, the new codes, called JASS and

AGATAGeFEM, have the possibility to work with precise geometries that deviate from the assumed shape of the crystal and the assumed positions of segmentation borders without the usual limitations of a grid size of  $> 1$ mm. Especially the deviations at the boundaries could be significantly improved by new interpolation methods developed here. Promising results have been produced, see figure 9.1.

In order to improve the quality of the simulations, it was necessary to understand the peculiarities of the charge collection process in germanium. The semi-conductors' band structure causes anisotropies in the drift of the charge carriers leading to a dependency of the pulse shapes on the crystal orientation. One can find adequate models, describing this behaviour in the literature. There are still some important practical issues remaining for which we have found new solutions. The Cartesian grid used in JASS for calculating all necessary potentials has a grid size of 0.5 mm. This reduces the relative error to values smaller than 1% in test cases with known analytical solutions. When the geometry of the crystals is only given with the precision of the grid one cannot avoid the charge carriers from drifting into non-physical regions and the possibility of a wrongful identification of a hit segment with an interaction location cannot be neglected. This is prevented by describing the geometry with numerical precision. Lastly we concentrated on improving the interpolation routine. This plays an important role not only in the calculation of the charge carrier trajectories but also in calculating the resulting pulse shapes. As both the electric as well as all the weighting potentials are only given at the points of the 0.5 mm grid a precise interpolation routine is of utmost importance. By default we use a Gaussian kernel with 2<sup>nd</sup> order interpolation. This kernel was the only one tested with uniform performance throughout the detector. With the new interpolation method, the mean path integral of the weighting fields, which is a measure for signal coupling to neighbouring segments, only deviates by 0.07 percent.

### 9.3. Decomposition algorithms

The coordinates of the interaction points are determined, by comparing the detected pulse shapes to the calculated basis, in real time. Indeed, the high experimental event rate multiplied by the data rate of the digitizer produces an information flux far beyond the disk storage capacities in terms of volume and recording speed rate. Hence, the data from a set of 37 x 100 data samples delivered by the digitizer are reduced to a few coordinates, energies, times and reliability information. A gamma ray will normally have a chain of interactions in the shell of germanium detectors (e.g. 3-4 at 1.3 MeV). There can be more than one interaction in one detector segment or/and the gamma ray can be scattered to another segment of the same crystal or to an adjacent detector, or even across the shell. Several fitting procedures have been developed in order to decompose the measured signals into the given basis signals, such as genetic algorithms, wavelet decomposition, and a matrix method. The choice was made at the fall of 2007, to concentrate on the Grid Search algorithm [9.2], as, due to its simplicity, it is the most robust among the signal decomposition codes. This code has been validated using the experimental data from the 2006 Köln experiment [9.3]. Though the data quality was not as good as expected from the AGATA digitizers, it has been shown that, in the case of single hit events, this code flavor gives already sufficiently Doppler correction. For all these reasons, the grid search was implemented in the NARVAL environment, and will be the first PSA code used on-line during the commissioning experiment.

The grid search algorithm is not well adapted to complex situations in which several hits occur in the same region. Thus, the implementation of more sophisticated algorithms is planned. Thus a dispatcher code, choosing the more adequate PSA algorithm for a given event, will also need to be implemented. This will sort the multiple hit cluster events to one of the two methods envisaged: the Fully Informed Particle Swarm [9.4] and the SVD matrix method [9.5, 9.6, 9.7, 9.8]. The former method is faster but the latter gives a better precision on the location of the hits. The following table gives an overview on the performance of different algorithms derived from tests using simulated data.

Algorithm	single interaction		multiple interactions	
	CPU time [ms/evt]	resolution [mm]	CPU time [ms/evt]	resolution [mm]
Grid search (GS) [9.2]	3	2	-	4 (only neighboring seg. hit)
Extensive GS [9.4]	8	1	3E5	4
PSO [9.4]	0,3	2	2-5	5
Matrix method [9.5, 9.6]	20	0.5	50	1.3 - 3
Genetic Algo. [9.9]	1E3	1	1E3	5
Binary Search	0,2	1	Not adapted	Not adapted
Recursive Subtraction [9.10, 9.11]	Not evaluated	3 (only radial coordinate)	Not evaluated	5 (radial coordinates)
Neural Network [9.4]	6	1.5	Not adapted	Not adapted
Wavelets	Not evaluated	2.3	Not adapted	Not adapted

#### 9.4. Signal alterations

After energy calibration in the front-end electronics, the experimental signals that are to be compared to the basis signals are still altered by different phenomena: noise, pedestal, time-jitter, cross-talk etc. The team has studied the influences of the two latter effects and their possible correction.

Concerning the time-jitter, different time-shift determination methods have been considered: supplementation of the basis with time-shifted signals, Neural Network determination [9.4], Kolmogorov-Smirnov determination [9.12], Taylor expansion and the substitution of residue minimization by chi-square minimization [9.13, 9.14]. The first method has the drawback of requiring larger signal bases, the latter method reduce the influence of the time-jitter but does not measure it. Using simulated data the Neural Network algorithm has shown to be very fast and providing a resolution better than 2 ns at computing times in the order of 10 $\mu$ s. Taking into account only the core signal, this algorithm seems to be very robust and hardly affected by noise and crosstalk discussed below. The Kolmogorov-Smirnov and Taylor expansion methods are purely algebraic. They also give excellent results in terms of computing speed, robustness and precision. The final choice between these methods will be made using the commissioning experiment data.

The cross-talk effect is present in any segmented detector. It induces strong energy shifts and decreases the hit location precision as it mixes the transient signals. Cross-talk contributions appear between segments of different detectors. Only negligible cross-talk components were observed between a firing detector and the core signal of a neighboring detector [9.15, 9.16]. The effects of cross-talk are described in details in the Section *crystal, cryostat and detector performances* of the present Report. Two quite similar correction methods have been used. The first one consists in including the cross-talk effect into the basis signal using a cross-talk matrix. The second one consists in correcting the measured signal by the cross-talk effect. Cross-talk corrections permit to lower the FWHM error on the position by about one millimeter.

Another difficulty in the interaction location arises due to the fact that the germanium crystal may be slightly displaced or tilted inside its capsule. It has been shown that this problem may be addressed prior to the experiment using the scanning tables (see below) or within the final set-up using radioactive source at fixed points and the gamma imaging method [9.17].

## 9.5. PSA implementation

Within the AGATA DAQ the kernel of NARVAL has the responsibility of moving data between the processes that do the work, the so-called actors. In order to facilitate the maintenance and development of algorithms used for AGATA two levels of abstraction are used for the PSA. The first is the AGATA Data Flow (ADF) library that is responsible for coding and decoding data in the data flow. The second layer of abstraction is a set of C++ classes which provide, via inheritance, simple means of “attaching” a PSA algorithm to the NARVAL DAQ. This system has been successfully tested with the grid search algorithm. Due to the fact that no cross correlations between the signals of different AGATA crystals had been found so far all the PSA relevant algorithms operate on the signals of each individual crystal in parallel on different machines. This also allows using several computers in parallel to analyze different events. Currently, it is foreseen to use two processors with 4 cores each to process the data of one crystal. Compared with the overall costs of AGATA electronics this is still a negligible cost contribution which could be easily extended to improve the PSA performance by a factor two to four.

Finally the events have to be reassembled according to their time stamps and a tracking algorithm is applied in order to disentangle the coincident interaction points and to determine the total energy and the emission direction of those gamma rays that have been fully absorbed in the germanium shell. Absolute positions of the individual crystals, tilting angles and target positions corrections only enter at this stage.

## 9.6. References

- [9.1] « A simple method for the characterization of HPGe detectors », P. Medina, C. Santos, D. Villaume, Instrumentation and Measurement Technology Conference, IMTC 04. Proceedings of the 21st IEEE, Vol. 3, p. 1828 - 1832 (2004).
- [9.2] R. Venturelli and D. Bazzacco, LNL-INFN (Rep) Vol. 204 p. 220 (2005).
- [9.3] « Result of the in-beam experiment performed in Cologne », F. Recchia, (in prep. for NIM A).
- [9.4] « Simulation and Real-Time Analysis of Pulse shapes from highly segmented Germanium detectors », M. Schlarb, PhD Thesis (München, 2008).
- [9.5] « Pulse Shape Analysis for the Gamma-ray Tracking Detector AGATA », A. Olariu, PhD Thesis (Orsay, 2007).
- [9.6] « Pulse shape analysis for the location of the gamma-interactions in AGATA », Olariu A, Désesquelles P, Diarra C, Medina R, Parisel C, Santos C, IEEE Transactions on Nuclear Science, vol. 53, issue 3, pp. 1028-1031 (2006).
- [9.7] « Real time pulse shape analysis for the gamma-interactions in AGATA », P. Désesquelles, Ch. Diarra, P. Medina, A. Olariu, C. Parisel, C. Santos, Real Time Conference, 2005. 14th IEEE-NPSS (2005).
- [9.8] « Matrix formalism and singular value decomposition for the location of gamma interactions in segmented HPGe detectors », P. Désesquelles, T.M.H. Ha, K. Hauschild, A. Korichi, F. Le Blanc, A. Lopez-Martens, A. Olariu, C.M. Petrache, on behalf of the AGATA Collaboration (submitted) (2008).
- [9.9] « A genetic algorithm for the decomposition of multiple hit events in the gamma-ray tracking detector MARS » Th. Kroll and D. Bazzacco, Nucl. Instr. and Meth. A 565, Issue 2, 691-703 (2006).
- [9.10] F.C.L. Crespi, PhD Thesis (Milano, 2008).
- [9.11] « A pulse shape analysis algorithm for HPGe detectors », F.C.L. Crespi, F. Camera, O. Wieland, G. Benzoni, S. Brambilla, B. Million and D. Montanari, Nucl. Instr. and Meth. A 570, Issue 3, 459-466 (2007).
- [9.12] « Kolmogorov-Smirnov method for the determination of signal time-shifts », P. Désesquelles, T.M.H. Ha, A. Korichi, F. Le Blanc, C.M. Petrache, on behalf of the AGATA Collaboration (submitted) (2008).
- [9.13] « Fast analytical methods for the correction of signal random time-shifts », P. Désesquelles, T.M.H. Ha, A. Korichi, F. Le Blanc, A. Olariu, C.M. Petrache, on behalf of the AGATA Collaboration, Nucl. Instr. and Meth. B (2008) doi:10.1016/j.nimb.2008.11.042

- [9.14] « NNLC: Non-Negative Least Chi-square minimization and application to HPGe detectors », P. Désesquelles, T.M.H. Ha, A. Korichi, F. Le Blanc, C.M. Petrache, on behalf of the AGATA Collaboration (submitted) (2008).
- [9.15] « Characterization of Segmented Large Volume, High Purity Germanium Detectors », B. Bruyneel, PhD Thesis (Köln, 2006).
- [9.16] « Crosstalk properties of 36-fold segmented symmetric hexagonal HPGe-Detectors », B. Bruyneel, P. Reiter, A. Wiens, J. Eberth, H. Hess, G. Pascovici, N. Warr, D. Weisshaar (accepted for publication in NIM A) (2008) NIM-A-D-08-00551.
- [9.17] « In-beam test and imaging capabilities of the AGATA prototype detector », F. Recchia, PhD Thesis (Padova, 2008).
- [9.18] « A novel technique for the characterization of a HPGe detector response based on pulse shape comparison », F.C.L. Crespi, F. Camera, B. Million, M. Sassi, O. Wieland and A. Bracco, Nucl. Instr. and Meth. A 593, pages 440-447 (2008).



## 10. In-beam Experiments with the first triple cluster

In this section the experimental results of the first in-beam performance test of the AGATA prototype triple cluster assembled from three symmetric germanium crystals (serial numbers 73821, 73838 and 73839) are presented. It will be shown that with the application of PSA algorithms it is possible to improve the effective energy resolution of the detectors from 35 keV to 4.8 keV FWHM for the 1382keV ground-state transition of  $^{49}\text{Ti}$ . This result corresponds to a position resolution of approximately 5mm, fully consistent with the specifications of the AGATA project.

### 10.1. Motivation

The performance of a gamma-ray tracking array like AGATA depends critically on the precision achieved in locating the photon interaction points. Therefore, once the prototype triple cluster of AGATA was available, it was soon decided to determine experimentally such value through an in-beam measurement which was performed in Summer 2005 at the Institute of Nuclear Physics (IKP) of Cologne, Germany. A very preliminary in-beam test with a cryostat mounting only a single crystal was actually performed previously by the Cologne group [1]. However, the experimental conditions were sub-optimal (no particle detector to define the kinematics) and the data were analysed following a simplified MINIBALL approach [2].

The main goal of the triple cluster experiment was to compare the performance of different pulse shape analysis algorithms under realistic experimental conditions. At this stage of the project, the speed of the PSA algorithm was not considered as an essential parameter for the comparison, and therefore the available algorithms were benchmarked essentially on the basis of the attainable position resolution. However, in the final implementation of AGATA, the algorithms will have to be fast enough to perform an on-line processing.

Incidentally, being the technology of encapsulated segmented HPGe detectors quite new, the in-beam test made it possible to gain experience in handling such complex devices under "realistic" experimental conditions. Inside the AGATA community, previous experience was present on the use of segmented HPGe detectors, namely with the 25-fold segmented MARS detector [3] and with the encapsulated 6- and 12-fold segmented MINIBALL detectors [4]. The new detectors of AGATA are however much more challenging from the technological point of view, given the high degree of segmentation combined with the process of encapsulation. It was therefore important to verify the behaviour of these detectors so that potential problems could be fixed in the subsequent production.

Another goal of this experiment was to check whether tracking of gamma-rays is already feasible with just three germanium crystals. The practical result is that tracking is quite problematic in such a closely packed configuration and therefore such a point will not be discussed further in this thesis.

### 10.2. Measurement of the position resolution

In order to have a "direct" estimation of the position resolution which can be obtained with the AGATA detectors, a dataset of collected signals is needed, corresponding to events in which a photon interacted in a single point of known position. With such a dataset, the result of a PSA algorithm applied to the data can be compared event-by-event with the known position of the interaction.

In order to collect such datasets, the signals from the detector must be recorded under controlled conditions, so that the position of the interaction point can be determined. A scanning table can be used to provide a basis of reference signals allowing the evaluation of the position resolution of the PSA algorithms. A major limitation of such methods is that the position of the interaction is defined with a precision of the order of the size of the collimator. In order to collect enough statistics in reasonably short times, the holes of the collimator cannot be too narrow and as a consequence a PSA algorithm will give a distribution of points

for each position of the collimator, the dispersion depending both on the PSA resolution and on the hole dimension. With the collimators used presently, the distribution will depend practically only on the collimation precision. Another limitation of this method is that only single interaction points are sampled, which is not the typical case in gamma-spectroscopy experiments, being multiple Compton scattering a highly probable process for gamma-rays interacting with a germanium crystal in the energy range 500-1500 keV.

A possible solution is the one of an indirect measurement, as done in the past for the MARS [5,6] and GRETA [7] detectors. The basic idea is that, when the gamma rays are emitted in-flight by a recoiling nucleus, the width of peaks in the Doppler-corrected spectra will depend on three factors, namely the intrinsic detector energy resolution, the error on the velocity vector of the emitting nucleus and the uncertainty on the photon direction. The last factor depends on the position resolution of the PSA algorithm used. If the other causes of Doppler broadening are known, the position resolution of the detector can be inferred from the observed energy resolution. This is not an easy task because all the direct and indirect sources of Doppler broadening have to be tracked down and, when not negligible, accurately quantified. Contrary to the scanning table events which are selected to correspond to a single photon interaction, in an in-beam measurement the conditions are the same as in the future use of the AGATA detectors.

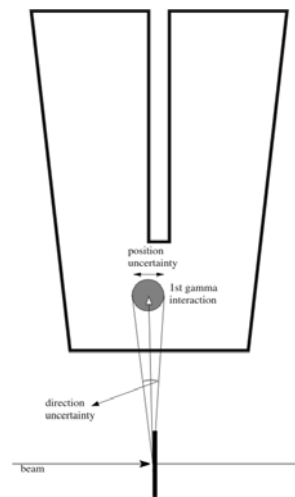


Figure 10.1. The finite position resolution attained from the AGATA detector is reflected in an uncertainty in the angle between the direction of the photon and the direction of the emitting recoil, resulting in a broadened peak in the Doppler-corrected spectra.

### 10.3. The experiment: choice of the reaction and setup

#### 10.3.1. Optimisation of the experimental conditions

In planning an experiment aiming to estimate the position resolution of the AGATA detector, one has to maximise the contribution to the error on the intrinsic energy coming from the position uncertainty of the first photon interaction.

From the physical point of view this means:

- to maximise the velocity module of the emitting nucleus. In this respect, the possibility to use an inverse kinematic reaction is a clear advantage;
- to place the detector at an angle of  $90^0$  with respect to the beam axis in order to have an angle between the recoil and the photon close to  $\theta = 90^0$ ;
- to place the detector as close as possible to the target. In fact a given position uncertainty translates into an angular uncertainty which is inversely proportional to the distance between the target and the interaction point.

It should be remarked that, in order to have the best estimate on the position resolution, all of the contributions to the intrinsic photon energy uncertainty which cannot be precisely estimated should be minimised.

The reaction chosen was  $^{47}\text{Ti} + d$  reaction at 85 MeV beam energy, using beam from the IKP Cologne tandem, and using a deuterated titanium target. Since the beam energy was far below the Coulomb barrier for a  $^{48}\text{Ti}$  target nucleus (which in the laboratory reference frame is of the order of 125 MeV), no contaminant  $^{47}\text{Ti} + ^{48}\text{Ti}$  reaction was expected. In this way it was possible to avoid the use of a gaseous target, which would have implied major technical challenges.

The choice of performing the experiment at 85 MeV beam energy was actually motivated with the attempt to enhance the cross section for direct reaction mechanisms with respect to the cross section for fusion-evaporation reaction, dominating at higher beam energies. This would somewhat simplify the required experimental setup, as discussed below. The Q-value for the planned reaction  $^{47}\text{Ti} (d,p) ^{48}\text{Ti}$  is 9.4 MeV.

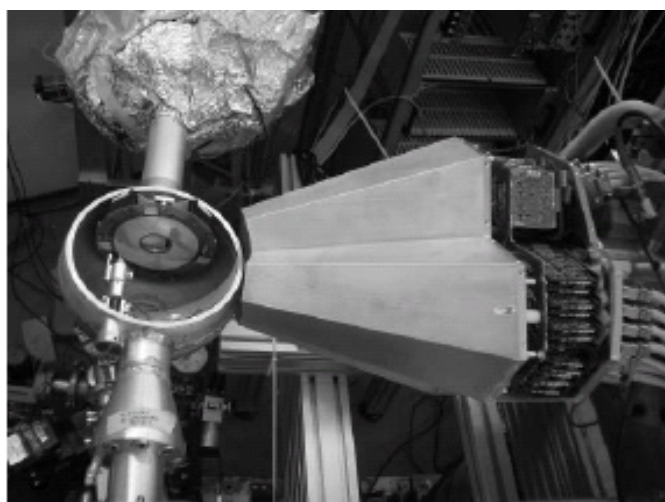


Figure 10.2. Photo of the experimental setup: the AGATA prototype triple cluster placed at  $90^\circ$  with respect to the beam axis and the DSSSD inside the open chamber.

For this experiment the full information on the recoiling nuclei was needed for an accurate Doppler correction. The velocity vector of the emitting nucleus was measured indirectly on an event-by-event basis by using a segmented silicon detector to detect the light charged particles emitted in coincidence with the gamma-rays. In the case of direct reactions, the velocity vector of the reaction partner can be extracted from the information on the position of the firing segment, by exploiting the two-body kinematics. Thus, there was no requirement to fully stop the particles inside the silicon detector, which would be needed in case the full particle energy had to be measured; the light charged particles were detected with a compact-disc shaped, 300  $\mu\text{m}$  thick double-sided silicon strip detector (in the following DSSSD) segmented in 64 radial sectors on one side and 32 annular rings on the other side, placed at 35~mm from the target position. With this detector, the uncertainty on the reconstructed direction of the recoiling  $^{47}\text{Ti}$  nucleus ranges from  $0.01^\circ$  to  $0.06^\circ$  depending on which ring of the silicon detector is hit. Such value is negligible with respect to the uncertainty of the photon direction. A 16  $\mu\text{m}$  thick aluminium absorber was placed in front of the silicon detector to avoid the elastically scattered titanium nuclei to reach the silicon detector.

In order to maximise the Doppler broadening, the minimum chamber size to fit the silicon detector was used in the experiment and the AGATA triple cluster was placed at a nominal distance of ~10~cm from the target, i.e. as close as possible to the chamber, at  $90^\circ$  with respect to the beam axis. A photo of the setup is shown in Fig. 10.2.

The gamma spectrum recorded by the AGATA cluster in coincidence with the DSSSD is shown in Fig. 10.3, where no Doppler correction was performed. A broad 984 keV

peak corresponding to the  $2^+$  to  $0^+$  transition of  $^{48}\text{Ti}$  is clearly visible, but there is also an unexpected strong 1382 keV peak which corresponds to the ground-state transition in  $^{49}\text{Ti}$ . Actually it turned out that it was not possible with the accelerator magnet to separate in the beam  $^{47}\text{Ti}$  from  $^{48}\text{Ti}$  which has a natural abundance roughly ten times larger. Therefore, it was decided to increase the beam energy and run instead the much stronger fusion-evaporation reaction  $d(^{48}\text{Ti}, ^{49}\text{Ti})p$  at 100 MeV beam energy. The problem with this reaction mechanism is that, since the centre-of-mass spectrum of the evaporated protons has a broad distribution, the direction of the proton is not sufficient to deduce the direction and the velocity of the  $^{49}\text{Ti}$  recoil on an event-by-event basis and a measurement of the full proton energy is needed. Unfortunately, as mentioned above, the DSSSD in use was 300  $\mu\text{m}$  thick, not enough to provide such information. This problem was taken into account by performing the simulations consistently with the experimental situation, i.e. ignoring the information on the proton energy. This procedure increases the uncertainty on the estimate of the position resolution.

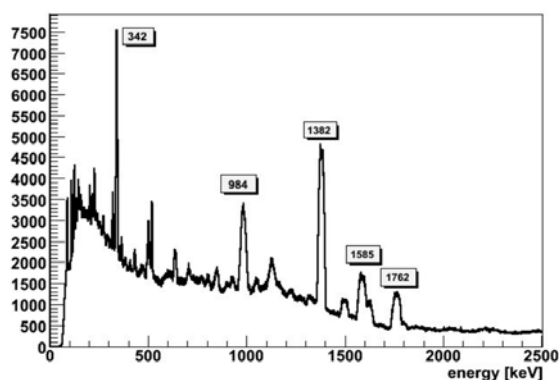


Figure 10.3. Raw gamma-ray spectrum recorded by the AGATA triple cluster in coincidence with the DSSD. Some peaks are labelled with their energies.

### 10.3.2. Electronics, DAQ and trigger

The electronics and data acquisition system was based on the Multi Branch System developed at GSI [8]. The core and the segment signals were digitised using XIA-DGF cards [9] with 14-bit FADCs and 40 MHz sampling frequency. The FPGAs mounted in these cards performed a digital trapezoidal shaping of the acquired signals to retrieve the information on the amplitude of the signal see [10,11]. With this configuration, the output for each channel of the DGF card consisted of 80 samples of digitised signal (i.e. a time slice of  $2\mu\text{s}$ ), the value of the amplitude and a timestamp. When a valid trigger was received by the digitisers, the signals from the core preamplifier and from all the segments of the detector were read-out and recorded. The synchronisation of the cards was performed by distributing a common clock through a star connection. This, together with the common trigger distributed by a daisy chain, was expected to guarantee a constant time difference between the signals digitised from different segments.

The signals coming from each of the 96 channels of the silicon detector were sent to a shaping and timing filter amplifier (STM 16 manufactured by Mesytec) and then digitally converted and readout by a VME Peak Sensing ADC (V785 manufactured by Caen) and a VME TDC (V775 manufactured by Caen). Since the scattered beam was stopped inside the absorber foil, the expected particle multiplicity was one particle per event, and therefore by combining the information from the rings and from the sectors it was possible to know without ambiguity the radial and azimuthal position of the interaction.

The trigger conditions required the coincidence between one of the three AGATA detectors AND one segment AND one ring of the silicon detector. In order to accept the events only when the digitisers were ready to process the signals, the "busy" signal from the digitisers has been used as a veto.

Since the data transfer of the DAQ was slow and the size of the event was of the order of 6 - 18 kByte (depending on the number of AGATA detectors firing), the trigger rate was dominated by the readout dead time, i.e. for most of the time the trigger was vetoed by the busy signal of the digitisers.

#### 10.4. Presort

In order to be able to perform the pulse shape analysis of the collected data a particular treatment has to be done on the recorded digitised signals. The event belonging to the channels of interest have to be selected. The fact that this experiment was performed coupling a thin DSSSD to the AGATA prototype triple cluster generated some difficulties in understanding the reaction channels and the mechanisms involved. In this section, the preliminary treatment of the experimental data will be briefly described.

##### 10.4.1. Quality and integrity of the data

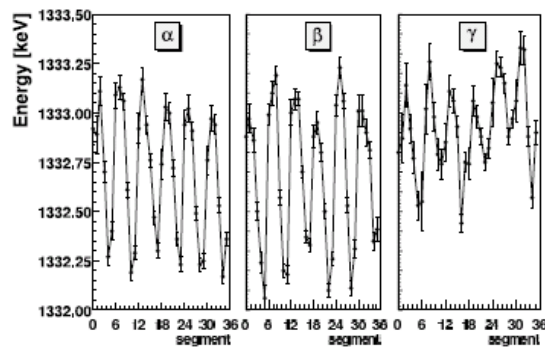


Figure 10.4 Energy measured by the core central contact as a function of the segment that is firing.

##### 10.4.1.1. Germanium detector: calibrations

Before and after the measurement, the germanium detectors were energy calibrated using a standard  $^{60}\text{Co}$  source. This operation is particularly critical with these detectors. In fact, differently from the standard non-segmented detectors, extremely long measurement times are required to gather enough peak statistics for the segments positioned in the back part of the crystal. Moreover, high statistics is needed to evaluate the crosstalk correction as first explained by Venturelli et al.[12]. This effect is expected to affect the resolution of the detector as a consequence of a variation of the gain depending on the pattern of firing segments. The signal amplitude of a segment has to be corrected according to a linear combination of the signal amplitudes of the other segments. This effect is known to be due to capacitive coupling between the high-impedance input and the low-impedance output of the FETs of two different preamplifiers [13]. Bruyneel in his PhD thesis [14] proposed an interpretation of this phenomenon based on an AC equivalent scheme of the detector.

Using the data of the calibration runs, it is possible to estimate the effect of proportional crosstalk for the coupling of the core with a particular segment, by constructing a dataset with the request that only one segment is firing (i.e. at segment multiplicity 1) and, for each detector, by incrementing 36 spectra of the core contact, each spectrum corresponding to the coincidence with a particular segment.

In this way, the proper recalibration coefficients have been estimated. Due to the lack of statistics in the calibration data it was not possible to determine the recalibration coefficients to correct the crosstalk for higher multiplicities. As a first approximation the coefficients found at multiplicity 1 have been applied also at higher segment multiplicities. Although the results are not perfect, the approximation seems to be reasonable since the crosstalk is expected to be more effective from the core to a segment, while the cross talk

from a segment to the core is of the order of 0.05%--0.2%. The energy measured by the core central contact as a function of the firing segment is shown in Fig. 10.4. The 6-segment period shows that the segment-central-contact crosstalk is similar for segments belonging to the same slice, or, in other words, having similar extension along the crystal axis.

#### 10.4.1.2. Germanium detector: synchronisation of DGF cards

The synchronisation of the digitisers is a relevant aspect of this kind of measurements. The digitised signals have to be processed with a pulse shape analysis algorithm, consisting in a comparison between the experimental data and the calculated signals stored in a database. A systematic delay of the signal from a particular segment will cause a mistake in the identification of the correspondence between the recorded and the basis signal. An even more complicated situation would arise if the delay of one channel with respect to another is changing event-by-event.

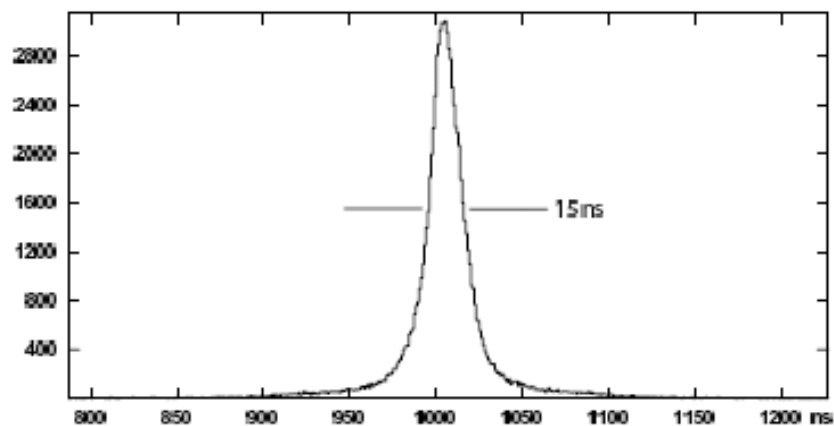


Figure 10.5. Time difference between the beta and gamma detectors for events in which both detectors fired. In this case a dCFD algorithm was used and the timestamp information was taken into account. The FWHM of the peak is 15 ns.

The trigger was sent via a daisy chain to each digitiser card and, as we will see, it turns out that the different distribution methods generated some inconsistency on the data. The use of a common clock, distributed via a star connection, in this configuration should ensure a constant delay between channels which can be measured and corrected for. In order to perform the alignment needed by PSA, the digitised data have been processed with an algorithm to extract the timing information. The algorithm used is essentially the same signal treatment as performed in an analogical constant-fraction discriminator [15,16], and is referred to as a *digital constant-fraction discriminator* (dCFD). If the timestamp is not accounted for several coincidence peaks are observed. When it is taken into account it is possible to obtain a good overall timing as shown in Fig. 10.5, where the difference of the times obtained applying the dCFD to the two signals of the central contact of the detectors is summed to the difference of their timestamps. Again the beta and gamma detectors are considered. The FWHM of the resulting time peak is 15 ns. As the sampling rate was 40 MHz, this result proves that subsampling precision is obtainable.

For the events in which only one segment is firing, the same good resolution has been obtained for most of the channels by performing the timing between a net-charge segment and the corresponding central contact.

The algorithm used to get timing information from the transient signals differs from

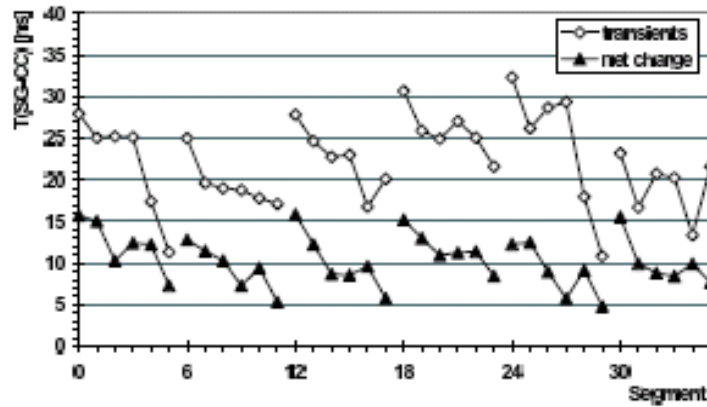


Figure 10.6. Comparison between the timing resolution obtained on transient and on net-charge segments. A threshold of 10 keV of equivalent amplitude is set on the transient signals.

the original one according to the relevant characteristics of these signals. Since the transient signal has a null integrated current, it is possible to skip the differentiation step. In addition, the transient signal can start with alternatively a positive or a negative slope, implying that the algorithm finding the zero-crossing should be sensitive to both the positive-to-negative and negative-to-positive transitions.

With these modifications to the timing algorithm, it was possible to have a good time resolution also for the transient signals. This resolution depends strongly on the signal amplitude. The timing resolution for the different transient segments is presented in Fig. 10.6, compared with the resolution for the net-charge signal. Only transient signals with equivalent amplitude of at least 10 keV have been considered.

#### 10.4.1.3. Germanium detectors: a posteriori positioning

In order to perform properly the Doppler correction, the position of the germanium detector with respect to the target should be measured with a precision of the order of a millimetre. In practice, such value could not be reached with the actual mechanical setup and the position of the detectors had to be inferred from the experimental data. More precisely we considered as the detector position the value giving the optimal Doppler shift. The accuracy of this "a posteriori" positioning will depend critically on the precision with which the position of the interactions inside the detectors are known. In principle, the positions provided by a PSA algorithm could be used, but in this case this procedure could lead to meaningless results. As a matter of fact, both the PSA algorithm parameters and the position of the detector are varied trying to minimise the width of the Doppler-corrected peaks. It is possible that the two concurring optimisation processes simply cancel mutually obtaining a good Doppler correction as a result of two biased procedures. For example, if the PSA algorithm systematically estimates in a wrong way the position of the interactions moving them towards the front face of the detector, the "a posteriori" positioning algorithm will correct for this effect by moving the whole detector in the backward direction. For this reason, it was decided to rely on a more robust method, although less sensitive, during the "a posteriori" positioning of the detector, by assuming that each interaction takes place in the centre of the firing segment, rather than using the more precise position provided by a PSA algorithm.

The position of a solid in a 3-dimensional space is uniquely identified by 6 parameters, for example by 3 coordinates and 3 Euler angles. In order to extract these parameters from the experimental data, our algorithm looks for the optimal Doppler

correction using an "inverse strategy", namely by transforming the known intrinsic energy of the photon to the laboratory reference frame. The transformation function will depend on the six parameters mentioned above, which can be extracted from the experimental data through a multidimensional fit for which the Minuit fitter from the ROOT suite [17] was used.

In principle, one would like to perform the multidimensional fit on a cube having on the three axes respectively:

- germanium segment firing [36x3 = 108 bins]
- silicon pixel firing grouped in 4x4 squares [64\*32/(4x4) = 128 bins]
- energy of the gamma-ray as measured by the central contact, without applying Doppler correction; a broad gate around 1382 keV was set [16384 bins]

The resulting cube has too large a size (108x128x16384) for a direct fit to be feasible, hence we had to reduce the problem to a fit of smaller bi-dimensional matrices.

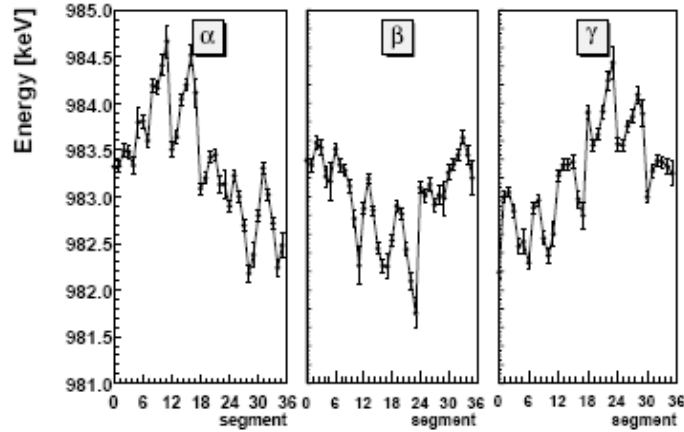


Figure 10.7. Position of the peak at 983.5 keV as a function of the segment firing. In case of perfect alignment all the points should be at 983.5 keV

The matrix which was actually fitted is a 2D matrix "A" having on the two axes:

- germanium segment firing [36x3 = 108 bins]
- silicon pixel firing grouped in 4x4 squares [64\*32/(4x4) = 128 bins]

The content of this matrix "A" at channel  $(g_{e_i}, s_{i_j})$  was a weighted average of the energy spectrum seen by germanium segment  $g_{e_i}$  in coincidence with silicon pixel  $s_{i_j}$ :

$$\langle E_\gamma \rangle_{ij} = \frac{\int_{E_\gamma} E_\gamma \cdot n(E_\gamma) \cdot dE_\gamma}{\int_{E_\gamma} n(E_\gamma) \cdot dE_\gamma} \quad (1)$$

where in our case the integrals were transformed into discrete sums running on the channel number. The uncertainty associated to channel  $(g_{e_i}, s_{i_j})$  was taken as the content of the 2D matrix "B" obtained by projecting the original cube on the third axis, that is the number of times that germanium segment  $g_{e_i}$  was firing in coincidence with silicon pixel  $s_{i_j}$ .

The function used to fit matrix "A" takes the position of the particle interaction on the silicon detector to calculate the direction of the recoil; the direction of the photon, depending on the six parameters mentioned above, is used to transform the intrinsic photon energy from the centre-of-mass to the laboratory reference frame.

Using the 6 parameters (3 coordinates and 3~Euler angles) extracted from the experimental data as discussed above, Doppler correction was performed by deducing the direction of the photon from the centre of each segment. Unfortunately, the position of the peaks turned out to be slightly dependent on the specific segment, implying that our "a posteriori" positioning is affected by an unknown systematic error. For instance, the distribution of the positions of the 984 keV peak as a function of the firing segment is

reported in figure 10.7. A dispersion of the points around the "true" value is apparent, with a FWHM  $\sim 1$  keV. It should be remarked that further attempts were performed in order to improve the "a posteriori" positioning, both based on automated or on manual procedures, however the alignment could not be improved.

### 10.5. Monte Carlo simulation

The main goal of the measurement was to estimate experimentally the position resolution attainable with the available PSA algorithms. This estimate is obtained from the quality of the Doppler-corrected spectra, namely from the broadening of the peaks. Actually, the resulting peak width originates from several contributions, many of which cannot be evaluated consistently. Therefore, it is not possible to construct a parametric model and the expected peak width should be obtained with a Monte Carlo simulation taking into account all of the relevant effects.

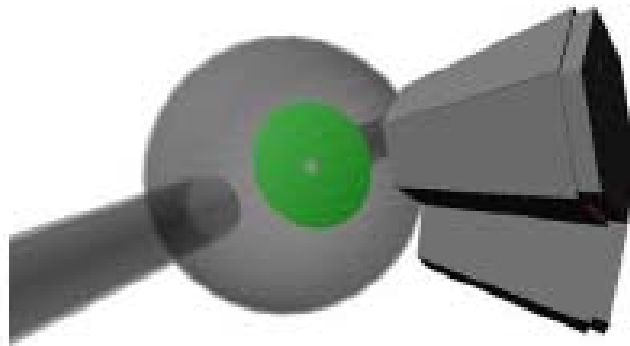


Figure 10.8. Pictorial view of the setup used for the GEANT4 simulation of the present experiment.

In this work, the Monte Carlo code developed for the optimisation of the geometry of AGATA was used [18]. The description of the DSSSD (including the aluminium absorber) and of the symmetric triple cluster were implemented. A pictorial view of the simulated setup is shown in Fig. 10.8.

In order to reproduce the experimental conditions, it is important to include a "realistic" treatment of the reaction kinematics. For this reason the AGATA Monte Carlo code allows the user to provide an input file containing an event-by-event description of the particles that have to be fired. An event generator program has been written in order to produce such input for the simulation. This program takes the cross sections from a calculation made with the parametric fusion-evaporation code CASCADE [19] and chooses a residual nucleus accordingly for each event. The particles needed to populate the residual nucleus are evaporated by the compound nucleus assuming the centre-of-mass spectra calculated by CASCADE. The photon cascade corresponding to the residual nucleus is generated using the GAMMAWARE package [20] in accord to the known discrete level spectrum and branching ratios.

The angular and energy dispersion of the beam, resulting from the beam emittance and the straggling inside the target, were evaluated through a Monte Carlo calculation performed with the SRIM code [21]. Since such values are relevant for the final peak width evaluation, they were fed to the AGATA code.

The Monte Carlo code gives an output similar to the data recorded in a real experiment. The single interaction points inside the AGATA detector are provided together with the energy deposited in the DSSSD detector. All of these values are given with arbitrary precision, i.e. the finite resolution of the detectors is not taken into account. For this reason the simulated data have been further processed by applying a smearing in the energy of the interactions, i.e. the exact values given by the Monte Carlo simulation have been changed

according to the energy resolutions of the detectors measured during the calibration runs. It should be remarked that these values depend on the specific crystal.

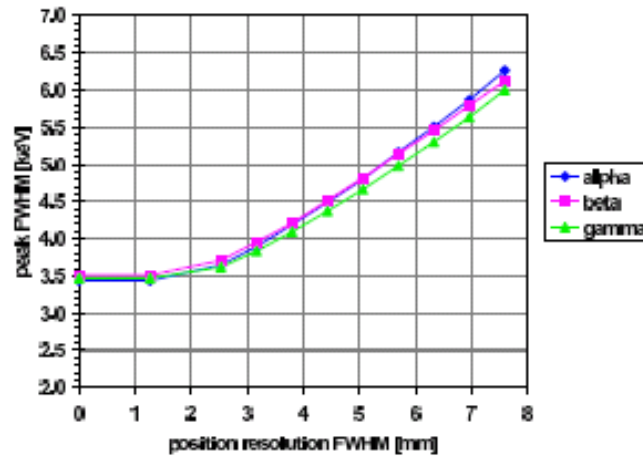


Figure 10.9. Simulated width for the 1382 keV peak of  $^{49}\text{Ti}$  as a function of the positional smearing,  $\text{FWHM}_0$ , without conditions on the segment multiplicity. See text for details.

In order to mimic the behaviour of the PSA algorithm used to analyse the data (see the following section) the interaction points within a same segment were packed into a single point corresponding to their centre-of-gravity. An energy corresponding to the sum of the individual energies was assigned to such point. An energy-dependent position smearing was then applied, using a 3-dimensional gaussian distribution having FWHM:

$$\text{FWHM} = \text{FWHM}_0 \sqrt{\frac{E_0}{E_\gamma}} \quad (2)$$

where  $E_0=1382$  keV and  $E_\gamma$  is the energy of the interaction point. This expression could result in very small values of FWHM which are not likely, therefore a minimum value  $\text{FWHM}_{\min}=2\sim\text{mm}$  was considered.

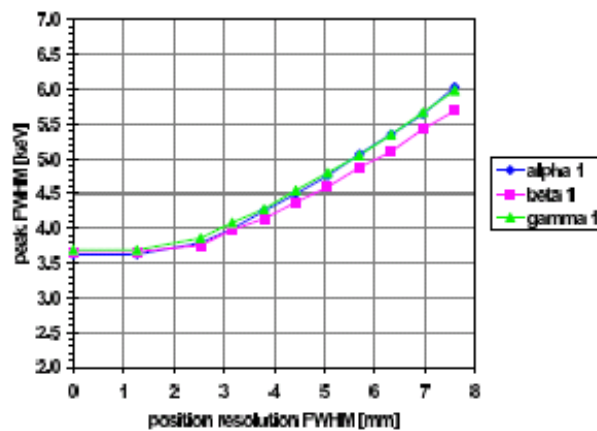


Figure 10.10. Simulated width for the 1382 keV peak of  $^{49}\text{Ti}$  as a function of the positional smearing, FWHM. Only the events with 1 segment firing have been considered (see text for details).

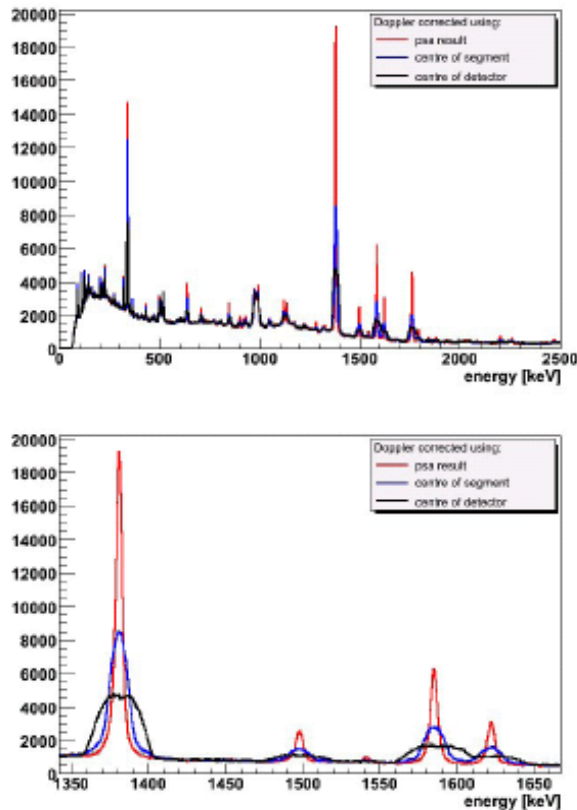


Figure 10.11 Doppler-corrected spectra for the full cluster, deducing the direction of the photon respectively from the centre of the detector, centre of the segment and from the PSA information. All of the segment multiplicities have been considered. The bottom spectrum is obtained by expanding the top spectrum around the energy region of interest.

The simulated data were Doppler-corrected by deducing the recoil vector velocity from the DSSSD information in a way consistent with what was done for the experimental data, namely by deducing the vector velocity of the recoiling nucleus from the direction of the firing ring/sector of the silicon detector. The resulting FWHM for the 1382 keV of  $^{49}\text{Ti}$  is shown in figures 10.14 and 10.15 as a function of the smearing FWHM<sub>0</sub>. In the plot of figure 10.14, all segment multiplicities are considered, while in figure 10.15 only segment multiplicity 1 is taken into account. It should be remarked that the resulting peak width is slightly larger at multiplicity 1 than at higher multiplicities. Actually, at this photon energy, it is unlikely that the photon undergoes direct photoelectric absorption and the most probable sequence is (multiple) Compton scattering followed by photoelectric absorption. Assuming that the whole scattering sequence takes place in the same segment, the centre of gravity of the interaction point could differ considerably from the first interaction point, resulting in a worsening of the Doppler correction.

## 10.6. The grid search PSA algorithm

Several PSA algorithms have been developed and tested so far within the AGATA collaboration. In the present work, the grid search method [22] by Roberto Venturelli was used, which was originally developed and tested on the experimental data from the MARS in-beam experiment. The original implementation was modified to cope with the new data format and it was further optimised as well. The algorithm is based on the comparison between measured net and transient signals of the segments and calculated signals from a fine grid of points in the crystal.

## 10.7. Results

As explained in the previous sections, the position resolution provided by the PSA algorithm can be deduced from the quality of the Doppler correction. The pre-sorted data, corresponding to events with the AGATA triple cluster firing in coincidence with the DSSSD detector, were processed with the grid-search PSA algorithm in order to extract the individual interaction points within the crystal. The basis of signals considered for the pulse shape analysis was calculated with the MGS code [24] over a cubic lattice having 2~mm step and 5~ns sampling rate. As discussed in section 10.6, only one interaction point per segment was considered. In case of more segments firing in coincidence, the first interaction point of the photon was assumed to lie within the segment having the largest energy deposition. Doppler correction was performed by inferring the photon direction from the first interaction point and by deducing on an event-by-event basis the velocity vector of the recoiling nuclei as discussed in section 10.4

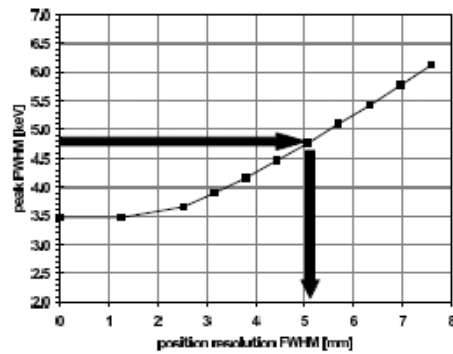


Figure 10.12. Width of the simulated 1382 keV peak as a function of the position smearing for the full triple cluster. Individual crystal energy resolution have been considered. All of the segment multiplicities are taken into account. The horizontal arrow indicates the experimental width.

The results of this procedure are shown in figure 10.11, together with the spectra obtained by Doppler correcting at detector or segment level. The improvement in quality of the spectra is apparent. For the 1382 keV peak of  $^{49}\text{Ti}$ , FWHM=4.8 keV is obtained following the PSA algorithm, which should be compared with 14 keV and 35 keV at segment and detector level respectively. The resulting position resolution is extracted quantitatively by comparing the experimental peak width to the simulated value using the curves shown in Figs. 10.9 and 10.10 In this case the simulated data from the three individual crystals were summed up, obtaining the curve plotted in Fig. 10.12.

A contribution of 1 keV was summed quadratically to the simulated peak width in order to cope with the systematic error originating from the imperfect positioning of the triple cluster, discussed in section 10.4. The observed peak FWHM = 4.8 keV corresponds to a smearing  $\text{FWHM}_0=5.1$  mm, or equivalently the observed position resolution at 1382 keV is 5.1mm.

It should be observed that the value deduced in this way is actually an average of position resolution values measured at different energies, since the detected 1382 keV could correspond to a single segment in which 1382 keV are released or to more segments in which the same energy is partitioned, each of them thus having lower energy deposition and worse position resolution. This originates ultimately from signal-to-noise considerations which affect especially the transient signals. Thus, from this point of view, events in which a single segment is firing with a net-charge signal should produce narrower peaks. Furthermore, at segment multiplicity 1 there are no segments in which net-charge and transient signals superimpose, thus resulting in an overall better performance of the PSA algorithm. On the other hand multiple Compton scattering is the most probable interaction process for photon energies around 1 MeV and in this case the PSA algorithm will only provide the centre of

gravity of the actual interaction points, which could lie at large distances (of the order of 1cm) from the first interaction point. This added uncertainty in the direction of the photon results in a broadening of the peaks which could partially compensate the improvement in position resolution.

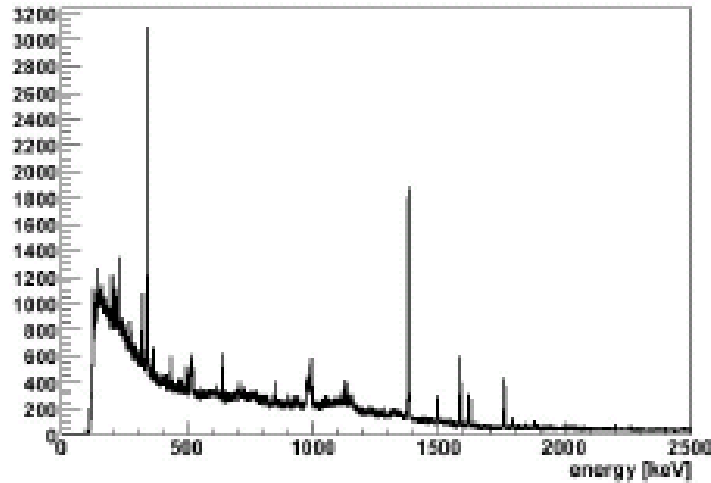


Figure 10.13. Doppler-corrected spectrum for the third detector "gamma", deducing the photon direction from the PSA information and considering only segment multiplicity 1.

The experimental data have been further analysed by selecting only events with segment multiplicity 1. For instance, the Doppler-corrected spectrum for the third detector "gamma" is shown in figure 10.19, where the photon direction was provided by the PSA algorithm. In this case the width for the 1382keV peak of  $^{49}\text{Ti}$  was  $\text{FWHM}=4.3\text{keV}$ , slightly better than the value obtained for the full cluster without conditions on the segment multiplicity. The comparison of the peak FWHM with the simulated data, shown in Fig. 10.14, suggests that in this case the position resolution correspond to a smearing  $\text{FWHM}_0=3.8\text{mm}$ , hence better than the value obtained for the full cluster.

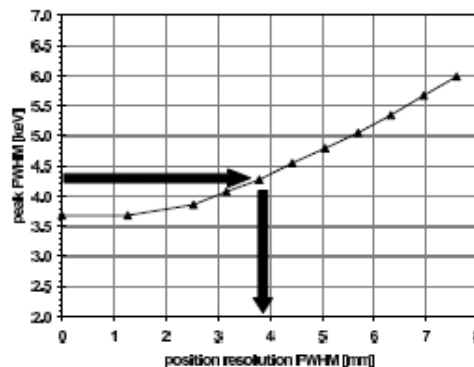


Figure 10.14. Width of the simulated 1382 keV peak as a function of the position smearing for the third detector "gamma". Only segment multiplicity 1 is considered. The horizontal arrow indicates the experimental width.

It is not easy to attribute an uncertainty to the present estimates of position resolution. Considering the approximations made with the Monte Carlo simulation, where part of the parameters can only be defined in a rough way, and the statistical errors, we estimate that the uncertainty on the present measurement of position resolution is of the order of 1 mm.

Other groups within the AGATA collaboration have analysed the same data using different PSA algorithms, which can therefore be compared on the basis of the quality of the

resulting Doppler correction. Applying the Matrix method [25] and the MINIBALL algorithm [2] the peak width of the 1382 keV transition is respectively 6.2 and 6.4 keV [26], therefore in both cases the position resolution is poorer than that obtained using the grid search method. The peak width obtained with the Recursive Subtraction method [27] is instead 7.3 keV [28]. In this last case the result should be considered quite a preliminary one since the present version of the algorithm only considers the net-charge signals. Revised versions of the algorithms are continually under development.

## 10.8. References

- [1] T. Steinhardt, D. Weisshaar, J. Eberth, O. Thelen, H. Hess, A First In- Beam-Experiment with the 36-fold Segmented AGATA-Detector. 3<sup>rd</sup> AGATA week Strasbourg, 21-25 November 2005.
- [2] D. Weisshaar, MINIBALL: Ein neuartiges Gamma-Spektrometer mit ortsauflösenden Germaniumdetektoren, Ph.D. thesis, IKP Köln (2002).
- [3] T. Kröll, D. Bazzacco, Simulation and analysis of pulse shapes from highly segmented HPGe detectors for the  $\gamma$ -ray tracking array MARS, Nuclear Instruments and Methods in Physics Research A 463 (2001) 227–249.
- [4] N. Warr, J. Eberth, G. Pascovici, H. G. Thomas, D. Weißhaar, MINIBALL: The first gamma-ray spectrometer using segmented, encapsulated germanium detectors for studies with radioactive beams, European Physical Journal A 20 (2003) 65–66.
- [5] T. Kröll, D. Bazzacco, R. Venturelli, B. Quintana, C. A. Ur, M. Bellato, R. Isocrate, C. Manea, R. Menegazzo, P. Pavan, C. R. Alvarez, E. Farnea, A. Gadea, D. Rosso, P. Spolaore, F. Camera, B. Million, E. Musso, A. Pullia, O. Wieland, G. Casati, A. Geraci, G. Ripamonti, M. Descovich, Gamma-ray Tracking With The MARS Detector, in: P. Fallon, R. Clark (Eds.), Frontiers of Nuclear Structure, Vol. 656 of American Institute of Physics Conference Series, 2003, pp. 357–364.
- [6] T. Kröll, D. Bazzacco, R. Venturelli, M. Nespolo, B. Quintana Arnés, C. Ur, M. Bellato, R. Isocrate, C. Manea, R. Menegazzo, P. Pavan, C. Rossi Alvarez, E. Farnea, A. Gadea, D. Rosso, P. Spolaore, B. Million, A. Pullia, O. Wieland, A. Geraci, G. Ripamonti, M. Descovich, In-beam experiment with the  $\gamma$ -ray tracking detector MARS, Nuclear Instruments and Methods in Physics Research A Article in Press.
- [7] M. Descovich, I. Y. Lee, P. Fallon, M. Cromaz, A. O. Macchiavelli, D. C. Radford, K. Vetter, R. M. Clark, M. A. Deleplanque, F. S. Stephens, D. Ward, In-beam measurement of the position resolution of a highly segmented coaxial germanium detector, Nuclear Instruments and Methods in Physics Research A 553 (2005) 535–542.
- [8] H. Essel, N. Kurz et al., The GSI Multi Branch System. See also <http://www.gsi.de>, Tech. rep.
- [9] B. Hubbard-Nelson, M. Momayezi, W. K. Warburton, A module for energy and pulse shape data acquisition, Nuclear Instruments and Methods in Physics Research A 422 (1999) 411–416.
- [10] V. T. Jordanov, G. F. Knoll, Digital synthesis of pulse shapes in real time for high resolution radiation spectroscopy, Nuclear Instruments and Methods in Physics Research A 345 (1994) 337–345.
- [11] A. Georgiev, W. Gast, Digital pulse processing in high resolution, high throughput, gamma-ray spectroscopy, IEEE Transactions on Nuclear Science 40, Issue: 4, Part 1-2 (1993) 770–779.
- [12] R. Venturelli, D. Bazzacco, M. Bellato, A. Pullia, T. Kröll, Folddependent energy correction in segmented germanium detectors, LNL-INFN(REP) 198 (2003) 156–157.
- [13] B. Bruyneel, P. Reiter, G. Pascovici, Characterization of large volume HPGe detectors. Part II: Experimental results, Nuclear Instruments and Methods in Physics Research A 569 (2006) 774–789.
- [14] B. Bruyneel, Characterization of Segmented Large Volume, High Purity Germanium Detectors, Ph.D. thesis, Cologne University (2006).
- [15] R. L. Chase, Pulse Timing System for Use with Gamma Rays on Ge(Li) Detectors, Review of Scientific Instruments 39 (1968) 1318–1326.

- [16] Z. H. Cho, R. L. Chase, Comparative study of the timing techniques currently employed with Ge detectors, *Nuclear Instruments and Methods* 98 (1972) 335.
- [17] R. Brun, F. Rademakers, ROOT - An object oriented data analysis framework, *Nuclear Instruments and Methods in Physics Research A* 389 (1997) 81–86.
- [18] E. Farnea, F. Recchia, D. Bazzacco, N. Marginean, O. Stezowski, Results from the Monte Carlo simulations for the AGATA array, *LNLINFN(REP)* 204 (2005) 218–219.
- [19] F. Pühlhofer, On the interpretation of evaporation residue mass distributions in heavy-ion induced fusion reactions, *Nuclear Physics A* 280 (1977) 267–284.
- [20] O. Stezowski, <http://agata.in2p3.fr>.
- [21] J. F. Ziegler, SRIM-2003, *Nuclear Instruments and Methods in Physics Research B* 219 (2004) 1027–1036.
- [22] R. Venturelli, D. Bazzacco, Adaptive grid search as pulse shape analysis algorithm for  $\gamma$ -tracking and results, *LNL-INFN(REP)* 204 (2005) 220–221.
- [23] A. Görge, The position sensitivity of the AGATA prototype crystal analyzed using a database of calculated pulse shape., <http://irfu.cea.fr/Sphn/Deformes/Agata/local/files/report.pdf>.
- [24] P. Medina, C. Santos, D. Villaumt, A Simple Method for the Characterization of HPGe Detectors, in: *Proc. of Instrumentation and Measurement Technology Conference*, 2005.
- [25] P. Désesquelles, C. Diara, P. Medina, A. Olariu, C. Parisel, C. Santos, Real Time Pulse Shape Analysis for the  $\gamma$ -Interactions in AGATA, *Real Time Conference*, 2005. 14th IEEE-NPSS.
- [26] J. Ljungvall, *5th AGATA week Orsay*, 15-19 January 2007.
- [27] F. C. L. Crespi, F. Camera, O. Wieland, G. Benzoni, S. Brambilla, B. Million, D. Montanari, A pulse shape analysis algorithm for HPGe detectors, *Nuclear Instruments and Methods in Physics Research A* 570 (2007) 459–466.
- [28] F. Crespi, *5th AGATA week Orsay*, 15-19 January 2007.



## 11. Tracking

### 11.1. Introduction

The aim of tracking algorithms is to reconstruct the trajectories of the incident photons in order to determine their energy and direction. To do this, the algorithms must disentangle the interaction points identified in the Agata detectors and establish the proper sequences of interaction points. Tracking algorithms can be divided into 2 classes: algorithms based on back tracking [1] and algorithms based on clustering and forward tracking [2]. Both are inspired from particular properties of the interaction of photons with matter.

For photon energies of interest (tens of keV to 20 MeV), the main physical processes that occur when a photon interacts in Germanium are Compton scattering, Rayleigh scattering, pair creation and the photoelectric interaction. Since Compton scattering is the dominant process between 150 keV and 10 MeV (c.f. Figure 11.1), all tracking algorithms are based on the properties of this interaction.

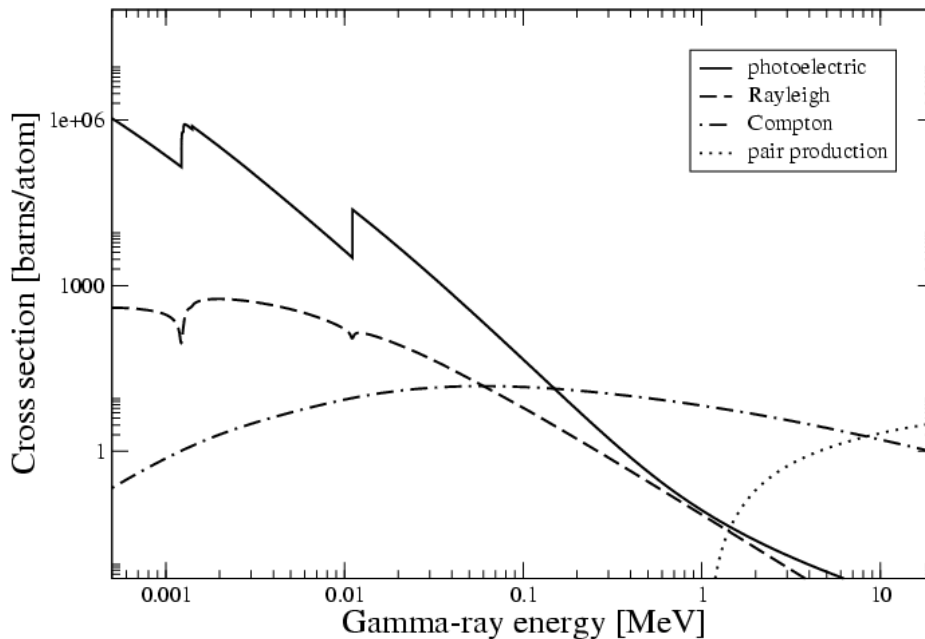


Figure 11.1: Cross section of the main physical processes for photons in Germanium as a function of photon energy.

Scattering angles can be obtained from conservation of energy and momentum but also from the geometrical positions of the interaction points. In either the forward-tracking based algorithms or the backtracking algorithms, the tracking procedure is based on the comparison of these 2 different scattering angles with the added complication that the correspondence between these 2 angles is blurred by physical (properties of the interaction of photons and electrons in Germanium) and technical (threshold and noise of the electronics and uncertainties of the pulse shape analysis (PSA)) effects.

Within the Agata project, tracking activities have mainly been devoted to the development and optimisation of tracking algorithms. Tracking has also been used to evaluate the performance of PSA. Another part of the work related to tracking has been the use of tracking techniques to investigate the background suppression capabilities of other experiments. Finally, a considerable amount of work has been devoted to include tracking into the data acquisition architecture of Agata and to make tracking algorithms and information regarding tracking available to the community.

### 11.2. Development of tracking algorithms

The development of tracking algorithms and the improvement of existing ones is an ongoing process. Realistic simulated data sets, produced with the GEANT4 Agata code [3] have been systematically used to test, compare and improve the performance of tracking algorithms. The primary photons are tracked in the detectors as they undergo various electromagnetic interactions. However, since the actual energy release is performed by the secondary electrons, the default option of the code is to track all the secondary particles. The output of the simulation code is a list of interaction points with their corresponding positions  $(x_i, y_i, z_i)$  and energies  $(e_i)$ . These correspond to the ideal situation, as given by Geant4, where all the interaction points are detected with infinite position and energy resolution. In order to produce more realistic data, the interaction points separated by less than  $d_{res}=5$  mm are packed together, the positions of the interaction points are randomly shifted in all direction (x,y and z) by sampling a Gaussian energy-dependent uncertainty distribution and an energy threshold of 5 keV is applied to all the interaction points.

### 11.2.1. Clustering Techniques

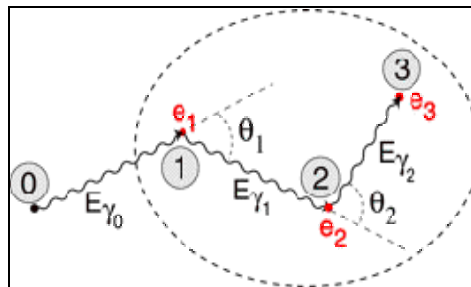


Figure 11.2: Schematic representation of the total absorption of a photon of energy  $E_{\gamma_0}$  via 2 Compton scatterings (at points ① and ②) and a photoelectric interaction (at point ③).

It has been shown that forward-tracking algorithms are more efficient than back-tracking ones [4]. This is because back-tracking algorithms rely on the identification of the last (photoelectric) interaction point in a scattering sequence (interaction point ③ in Figure 11.2), which generally loses its original characteristics after PSA: it is poorly localised and/or packed with other interaction points.

In forward-tracking algorithms, the first step of the procedure is to group interaction points into clusters in  $(\theta, \phi)$  space. The second step is the actual tracking routine: A figure of merit is computed for all the possible sequences of interaction points in each cluster on the basis of scattering angles, photon ranges and interaction probabilities and using the position of the target as the starting point of every sequence. A cluster is then accepted if the figure of merit of the best sequence lies above a certain threshold, which maximises efficiency and P/T. What distinguishes the various algorithms is the quality of the clusters, which are examined and validated by the tracking routine.

As part of their contribution to the AGATA project, Romanian physicists have developed a new tracking algorithm, which is based on fuzzy logic. For the clustering part of the algorithm, a well-known fuzzy logic algorithm (the Fuzzy C-Means) was tested. This algorithm is an objective function based numerical algorithm suitable for identifying well-separated groups of points in a multidimensional space. Because of the decreasing photon path with decreasing energy, it is assumed that all the interaction points belonging to a certain photon will be grouped together in 3D space, making this approach feasible

The algorithm is an iterative one, at each step a new set of positions for the groups and a new set of membership degrees being computed. The objective function of the algorithm is generally based on the least-squares formula, but including as a weighting factor the degree of membership of the points. After running the algorithm, the optimal positions of the centres of the clusters and the degree of membership of each point to each of the clusters are obtained. The next step in the code is the *defuzzification*, which makes the move to

Boolean logic (moving from the “each point belongs to a certain degree to every cluster” to “each point belongs to one cluster”), making possible the use of standard validation procedures. For the validation of the clusters the forward-tracking technique was used. Another clustering method has been developed at IPHC of Strasbourg. This method, called "deterministic annealing", comes from information theory and its principle is described in analogy to statistical physics.

The clustering problem is to perform the minimization of a cost criterion, here referred as the distortion D:

$$D = \sum_{i=1}^N \sum_{j=1}^n p(v_i, c_j) \cdot d(v_i, c_j)$$

where  $p(v_i, c_j)$  represents the probability that an interaction point  $v_i$  belongs to the cluster  $c_j$  and  $d(v_i, c_j)$  is the squared Euclidean distance between the point  $v_i$  and the centre of the cluster  $c_j$ . The optimal solution of the problem is obtained by minimization of the free energy inspired from the annealing process in statistical physics.

This work will be submitted to the Nuclear Instrument and Method journal and will be followed by a development of the probabilistic tracking method [5] that enables to reconstruct gamma rays without on-line PSA. This could be of interest for studies at very high counting rate.

The forward-tracking algorithm (OFT) developed in Orsay [4] has been improved in several ways. Inspired by the MGT tracking program [6], the clustering routine has been adapted to the event multiplicity. In the OFT code, points are grouped into clusters in  $(\theta, \phi)$  space according to their relative angular separation: For a given value of the allowed angular separation and given a first interaction point  $i$ , interaction point  $j$  is assigned to the same cluster if:

$$\left| \cos^{-1} \left( \sin \vartheta_j \sin \theta_i \cos(\varphi_j - \varphi_i) + \cos \theta_i \cos \theta_j \right) \right| \leq \alpha$$

The procedure is then repeated with interaction point  $j$  and the next potential member of the cluster, and so on.

When the number of incident photons is large, a large clustering angle may result in a bad peak-to-total and reduced photo-peak efficiency since interaction points belonging to more than one photon can be assigned to the same cluster. On the other hand, a small clustering angle may lead to incomplete clusters.

By introducing a dependence of the maximum allowed value of  $\alpha$  on the number of interaction points in the event, the efficiency and peak-to-total for low and medium gamma-ray multiplicities could be increased, while slightly improving the tracking performance at high multiplicities.

The detection efficiency and peak-to-total obtained by the above-mentioned algorithms for 1 MeV photons emitted at the centre of Agata are resumed in Table 11.1.

Algorithm	Efficiency (%)	Peak-to-Total (%)
MGT	28(43)	49(58)
OFT	24(37)	54(68)
Fuzzy C-Means	27	46
Deterministic Annealing	26(36)	47(69)

Table 11.1: Simulated photo-peak efficiency and peak-to-total of Agata for cascades of 30 (and 1) 1 MeV photons. In all the cases, the data is packed and smeared in the standard way and a 5 keV energy threshold has been applied.

### 11.2.2. Calculation of Effective Distances

In all tracking philosophies (forward tracking and back tracking), the photon trajectories are tracked with the help of the Compton scattering formula and with the ranges and cross sections of the photoelectric, Compton and pair production interactions. To compute the appropriate ranges of photons in Germanium, the effective distances in Germanium between interaction points as well as between the interaction points and the source need to be computed. The problem can be solved analytically if the detector geometry is approximated to a  $4\pi$  Germanium shell (this is illustrated in Figure 11.3). This approximation was checked with the GEANT4 simulation code, Agata [3]. In this code, the exact geometry of Agata is defined, i.e. the shape of the crystals, encapsulations, cryostats, the empty spaces and the distances between all these elements.

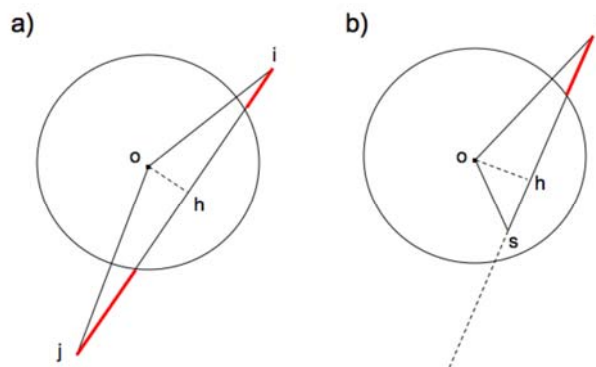


Figure 11.3 Representation of the distances (in red), which need to be calculated by the tracking algorithms: a) distance between interaction points *i* and *j* and b) distance between the source *s* and the interaction point *i* (the source of the gamma rays is not necessarily at the centre of the shell).

The routine `DistanceInGe()` was especially added to the `DetectorConstruction` part of the package in order to calculate the length of Germanium material separating 2 points. By launching the tracking code within the Agata simulation code, the routine `DistanceInGe()` can be called directly each time distances need to be computed. In this way, the performance of the tracking code with exact distances can be compared with the one assuming a solid  $4\pi$  Germanium shell.

The conclusion of this work, made possible by E. Farnea and M. Palacz, is that the approximation of a Germanium shell is valid. This result means that no lookup table of the geometry needs to be used to run the tracking algorithms in the AGATA acquisition system. This is a considerable simplification and frees a lot of computing memory and time.

### 11.2.3. PSA and Front-End Electronics

Tracking codes have been developed incorporating the fact that the PSA identifies the positions and energies of the interaction points with a certain error. This error depends on the actual position of the interaction points in the crystal and also on the amount of energy deposited at the position. To mimic this effect, tracking codes generally smear the position and energies of simulated interaction points. It is also systematically assumed that the interaction points, which are separated by less than a given distance, cannot be resolved and are treated as one interaction point carrying the sum of the individual energies and situated at the energy-weighted barycentre. This is called the packing procedure.

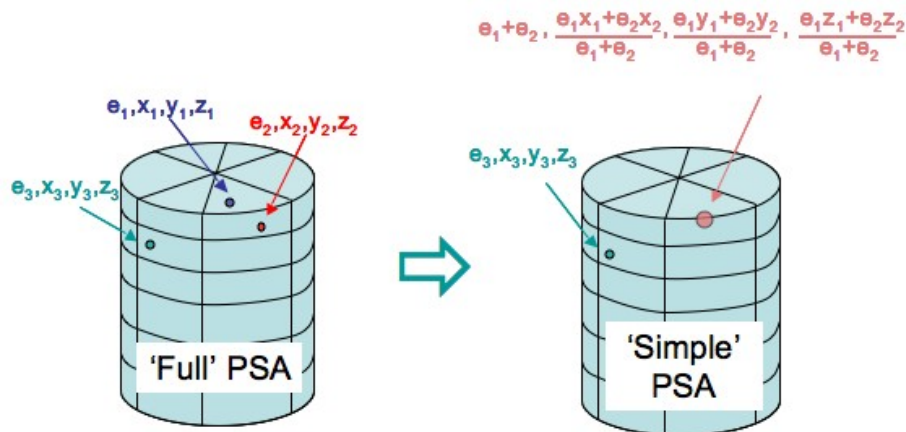


Figure 11.4: Schematic representation of the difference between the "full" PSA, in which events with more than one interaction point per segment are considered and the "simple" PSA, in which only 1 interaction point per segment is assumed.

It has recently become clear that PSA algorithms have difficulties in dealing with events in which there is more than one interaction point per segment. This is because the parameter space to search becomes very large and because the properties of the response function of the detector can lead to more than one solution. Although algorithms to determine the number of interaction points in each segment have been developed and have shown encouraging results in the coaxial part of the crystal [7], the effect of systematically assuming only one interaction point per segment has been investigated in Padova and Orsay.

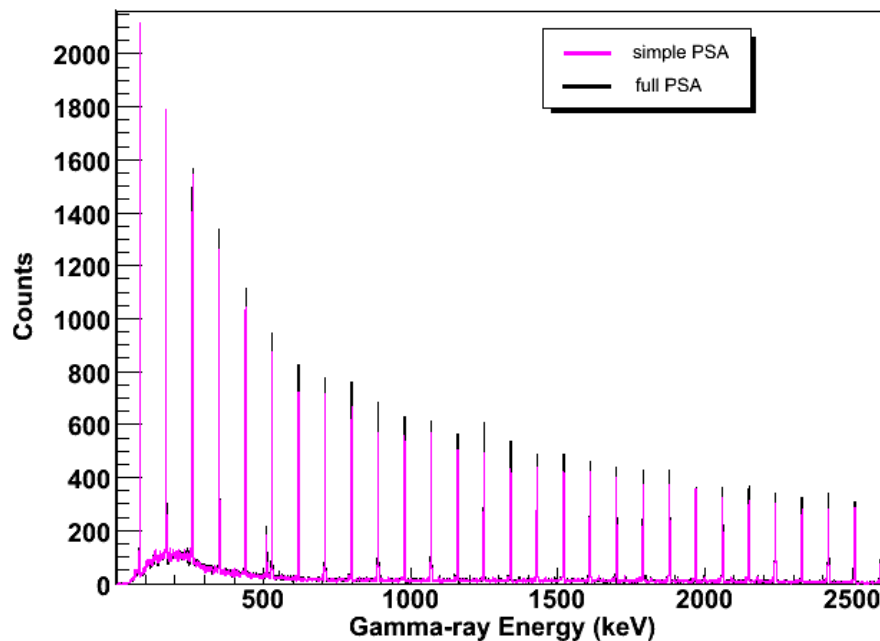


Figure 11.5: Tracked energy spectra of a 30-photon rotational band following "simple" and "full" PSA.

The interaction points of events simulated with the Agata code [3] were packed and smeared in the usual way to yield a first data set. The second data set was obtained by packing the interaction points situated in the same segment (an example is shown in Figure 11.4). Tracking was then performed on the two sets of data. No drastic drop in performance is observed (c.f. Figure 11.5), not even when the recoil velocity is 50% of the speed of light, which yields a higher concentration of interaction points because of the Lorentz boost.

This result is understandable since the average of the distribution of the number of interaction points per segment is close to 1 and varies only slightly with incident photon energy.

Up to now, the uncertainty in the position of interaction points is taken to be equal in all directions (x,y and z) and dependant on the deposited energy  $e$  (the smaller the energy, the larger the uncertainty). The FWHM of the uncertainty distribution (in cm) is given by the following expression, where  $e$  is in MeV:

$$FWHM(e) = 0.5 \sqrt{\frac{0.1}{e}}$$

One still needs to investigate the effect of a varying uncertainty within the Agata detector.

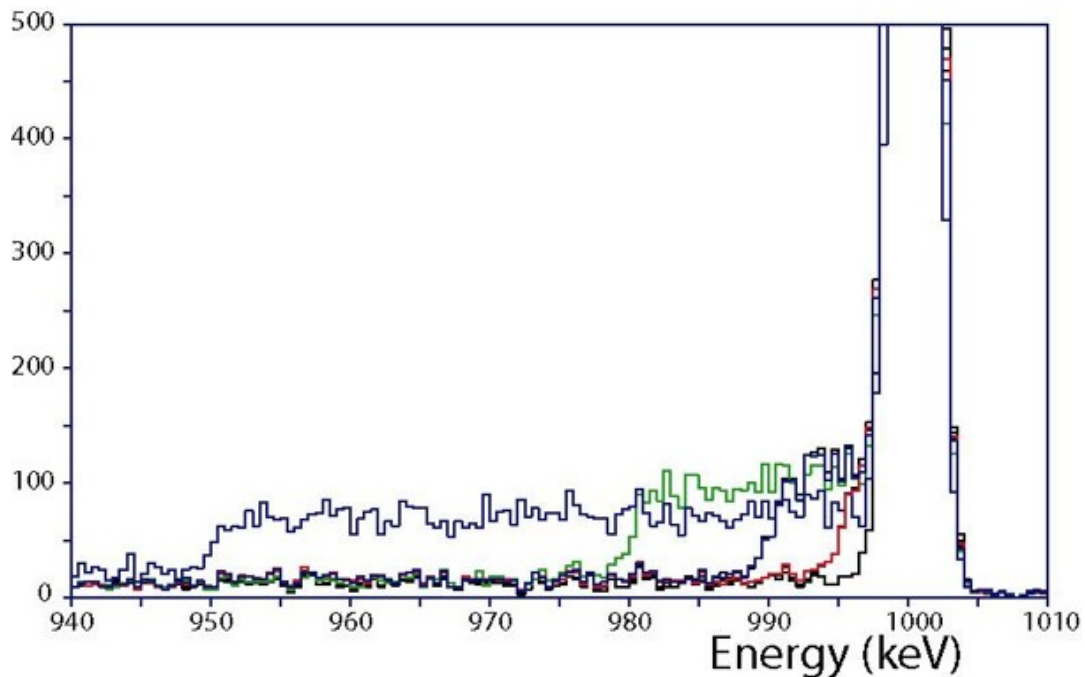


Figure 11.6: Tracked energy spectra corresponding of 1 MeV photons assuming various detector energy thresholds (see text for details).

Signals corresponding to a deposited energy below a certain value will not be detected in Agata. The effect of this energy threshold on the tracking efficiency has been looked into in Padova. The results are shown in Figure 11.6 in the case of 1 MeV photons and detector energy thresholds of 1 (black), 5 (red), 10 (blue), 20 (green) and 50 keV (dark blue) thresholds. The loss in photo-peak efficiency with respect to the 1 keV threshold case is found to be 1% (5 keV threshold), 8% (10 keV threshold), 13% (20 keV threshold) and 29% (50 keV threshold).

#### 11.2.4. Neutrons

The effect of neutron damage on PSA has been studied at Berkeley and the conclusion is that a measurable effect on position resolution is never reached before annealing is required for energy resolution. However, the influence of the elastic and inelastic interactions of neutrons on tracking performance has been found to be significant for low to medium gamma-ray multiplicities especially on the peak-to-total [8] (this is clearly visible in Figure 11.7). Ways of discriminating neutron-induced from gamma-induced interaction points need to be found in order to recover a good peak-to-total for gamma-ray multiplicities ranging from 1-15. As far as pulse shapes are concerned, it has been shown that neutrons and gammas yield similar

signals even though the interaction mechanisms are different [9]. Distinguishing neutrons and gammas by time of flight methods requires a timing resolution better than 5 ns, which will be hard to achieve in the case of low-amplitude signals.

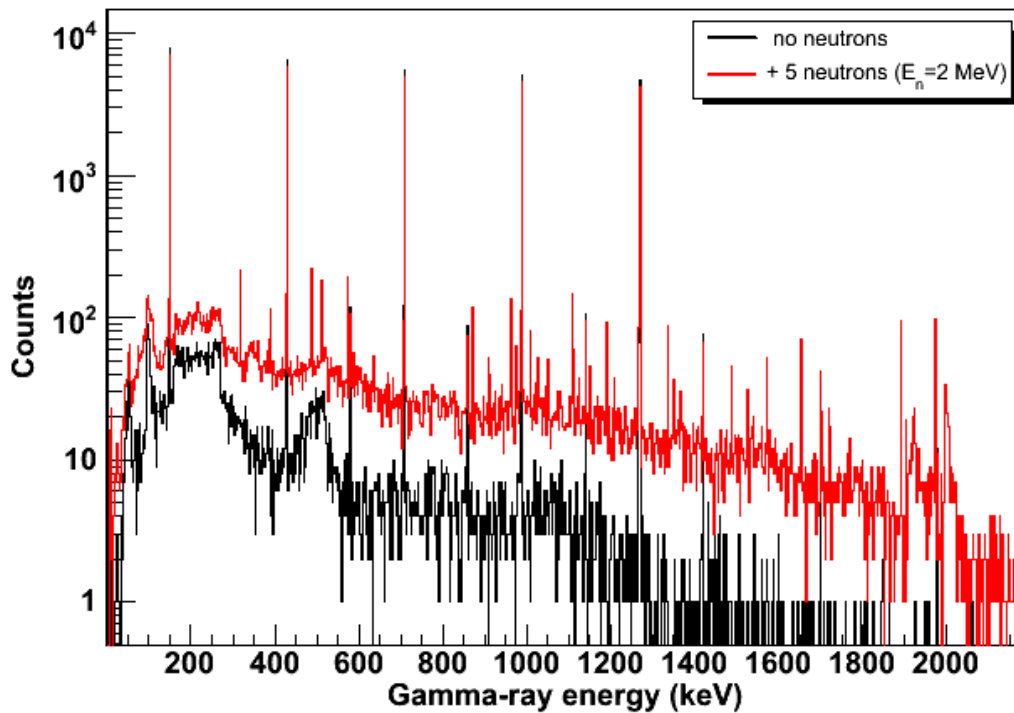


Figure 11.7: Tracked energy spectra of a 5-photon rotational band when no neutrons are present in the events and when 5 neutrons are emitted in coincidence with the gamma rays.

Physicists at Ankara and Uppsala Universities have recently re-addressed the issue of neutrons in Agata. The aim is to reduce the background in the gamma-ray spectra due to neutron interactions in the detectors. Such a neutron-induced background may become a serious problem especially when using neutron-rich radioactive heavy-ion beams at the future facilities such as SPIRAL2 and NUSTAR/FAIR. Simulations using the Geant4 Agata code [3] and the MGT tracking program [6] were carried out by emitting neutrons and gamma-rays from the centre of Agata and fingerprints of the neutron interaction points were identified.

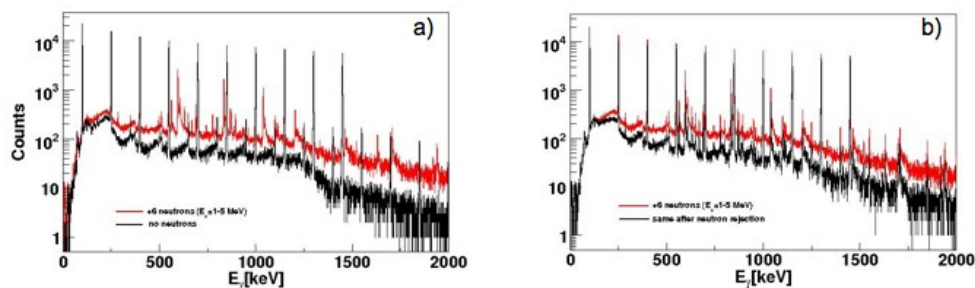


Figure 11.8: a) Tracked energy of a 10-photon rotational band when no neutrons are present in the event and when 6 neutrons are emitted in coincidence with the gamma rays, b) tracked energy of the same 10-photon rotational band plus 6 neutrons before and after neutron rejection.

In a simulation with simultaneous emission of 6 neutrons and 10 gamma rays, the peak-to-background ratio was improved by a factor of 2.5 at a gamma-ray energy of 1.0 MeV

after neutron rejection, see Figure 11.8b. The same neutron rejection procedure reduces the full-energy peak efficiency at 1 MeV by a factor of 1.2 (16%) while the 1039.5 keV transition due to inelastic scattering on  $^{70}\text{Ge}$  is reduced by a factor of 2.1 (53%). Figure 11.8a shows the background caused by the inelastic scattering of neutrons in comparison to a spectrum where there are no emitted neutrons.

### 11.2.5. Background Rejection

The background rejection capacity of the MGT and OFT algorithms was checked by tracking events emitted 1 meter away from the centre of a  $4\pi$  germanium shell and comparing the resulting tracking efficiency and peak-to-total to those obtained when the photons are emitted from the centre of the shell. To reduce the simulation time and the amount of useless data in the case of the off-centre source, only photons emitted into a specific cone are considered (this is illustrated in Figure 11.9). The tracking efficiencies obtained in both cases (centred and off-centred source) are given in Table 11.2 for incident energies ranging from 200 keV to 1 MeV.

Algorithm	$E_g=200$ keV	$E_g=500$ keV	$E_g=1$ MeV
MGT centred	95%	94%	93%
off-centred	57%	74%	79%
OFT centred	83%	73%	72%
off-centred	1.1%	25%	30%

Table 11.2: Tracking efficiency for 200, 500 and 1000 keV photons emitted from the centre of a  $4\pi$  shell and 1 m away obtained with the MGT and OFT tracking algorithms. In both cases tracking is performed assuming the source is at the centre of the shell.

The MGT tracking algorithm is more efficient at tracking gamma rays emitted into a  $4\pi$  Germanium shell than the OFT algorithm, however this is at the expense of a poor background rejection.

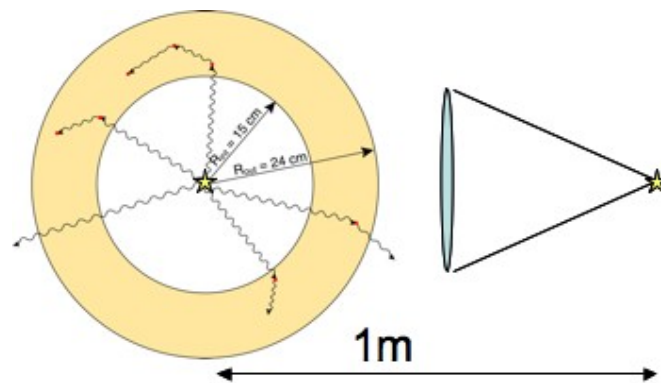


Figure 11.9: Schematic illustration of photons emitted from the centre of a Germanium shell and 1 metre away from it.

### 11.2.6. Scattering Materials

The effect of the crystal encapsulation and of the presence of other dead materials on the tracking efficiency of Agata has been checked in Padova. The materials, which are in between the source and the Germanium crystals absorb and scatter photons. The absorption yields a drop in efficiency at low energies, as it is the case in “standard” detector arrays but the scattering also affects the tracking efficiency at higher energies. As can be seen in Figure 11.10, the addition of a reaction chamber or an ancillary device inside Agata makes the performance of the array drop considerably. This calls for a very careful design of ancillary devices.

### 11.3. Imaging

The performance of PSA is generally tested by checking how well experimental spectra can be Doppler-corrected since this procedure directly depends on the attainable precision in locating each interaction point. In practise, the 1<sup>st</sup> interaction point in the scattering sequence is chosen on the basis of energy considerations and the angle of emission, which is needed for the Doppler correction, is obtained from the reaction kinematics and the position of the 1<sup>st</sup> interaction point. The width of the Doppler-corrected gamma-ray lines is then converted into position resolution. This technique was applied for the first in-beam test performed with an Agata triple-cluster and a ~5 mm FWHM position resolution was obtained.

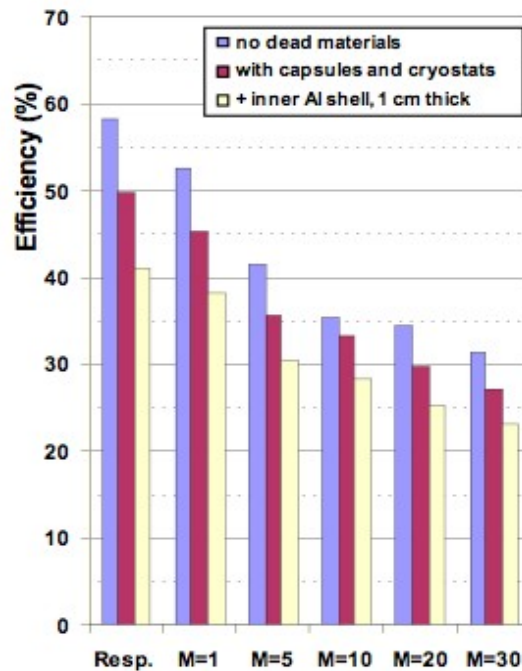


Figure 11.10: Response function and tracked photo-peak efficiency of Agata for 1 MeV photon events of multiplicity 1 through 30 in the presence of various materials and a schematic ancillary device.

Another method has recently been devised by physicists from Padova, Bucharest and Turkey. It relies on Compton-imaging, which does not need any beam nor complex experimental set-up. Instead it is assumed that the quality of the image reconstruction obtained through the knowledge of the Compton scattering sequence in the detector can provide information on the position resolution. The position and energy of the interaction points were extracted using the grid search algorithm [10] assuming only 1 interaction point per segment. Since the incident energy is known, the 1<sup>st</sup> scattering angle can be extracted by selecting events according to their total energy and number of interaction points. This angle defines a scattering cone in 3D space. If more than one event is analyzed, all the cones should overlap in a single point corresponding to the source of the gamma rays. Placing the source far away from the detector reduces the problem to the forming of a 2D image on the surface of a sphere, which can be represented in a  $(\theta, \phi)$  plane. Comparison of the experimental and simulated  $\theta$  and  $\phi$  image profiles of a <sup>60</sup>Co source has yielded a position resolution of about 5mm [11].

Monte Carlo simulations for the DEcay SPECTroscopy (DESPEC) project have shown that the imaging capability of segmented Germanium detectors provides an efficient rejection of uncorrelated gamma rays originating from background sources i.e. not originating from the target area. So far, suppression factors of 10 to more than 100 have been achieved with single gamma-ray events [12]. Further work is under way to evaluate the performance in

the case of higher gamma-ray multiplicity events; in particular what is the compromise that has to be made between background suppression efficiency and full-energy efficiency.

#### 11.4. Integration into the Data Acquisition System

Tracking will be performed at the end of the Agata data flow on 1 or 2 nodes of the PC farm of the data acquisition, which will be running the NARVAL system. Work is in progress to make all the existing algorithms NARVAL-compliant following the interface established by J. Cresswell and X. Grave.

```

Example : Tracking code

int main(int argc, char * argv[]) {
    ... // Variable declaration

    process_config (".", &error_code);
    carac_process = process_register (&error_code);
    process_initialise (carac_process, &error_code);
    ... // recuperation of the data

    if (!error_code) {
        process_block (carac_process,
            input_buffer, size_of_input_buffer,
            output_buffer, size_of_output_buffer,
            used_size_of_output_buffer,
            &error_code);
    }
    free (carac_process);
    return (error_code);
}

```

The code is annotated with three pink curly braces on the right side:

- Initialization**: Brackets the lines `process_config`, `process_register`, and `process_initialise`.
- Process**: Brackets the `process_block` function call.
- End**: Brackets the `free` and `return` statements.

Figure 11.11: Example in C of online algorithm code.

This means that the stand-alone algorithm codes need to be modified so that they may be compiled as a shared library, which respects the interface required by NARVAL. The interface with the NARVAL system is ensured by specific functions. The mandatory functions are *process\_config*, *process-register* and *process\_initialise*, by which NARVAL initialises the algorithm and *process\_block*, by which NARVAL processes the data. Other functions such as *process\_reset*, *process\_start*, *process\_pause*, *process\_stop* inform the algorithm of the state of the acquisition. An example of program structure is shown in Figure 11.11.

In order to facilitate the integration of algorithms into NARVAL, a special library called Agata Data Flow (ADF) has been developed by O. Stezowski. The goal is to make the data format transparent to the algorithms, i.e. ADF allows each algorithm to access the data it needs without knowing the structure of the data flow. It also provides a virtual NARVAL environment in which to test and debug algorithm codes in stand-alone mode.

The OFT is currently the only tracking algorithm, which has been integrated into the NARVAL architecture. Its performance in terms of calculation speed has been optimised with the help of N. Dosme and meets the specifications for the AGATA demonstrator: a complex event of 30 1 MeV photons emitted into 4p is tracked in under 2ms with a 1.7 GHz Opteron. Further programming is needed in order to adapt the code to the newest version of ADF. Also, since it has been decided that the tracking algorithms must perform the transformation from the crystal to the AGATA reference frame, this routine needs to be written and implemented.

For more information, the web site of the Agata Tracking Team can be found at the following URL: <http://www.csns.in2p3.fr/-Tracking-Team-.html>

### 11.5. References

- [1] J. van der Marel and B. Cederwall, NIM A 437 (1999) 538
- [2] G. Schmid *et al.*, NIM A 430 (1999) 69
- [3] E. Farnea and D. Bazzacco, LNL-INFN(REP) 202 (2004) 158
- [4] A. Lopez-Martens *et al.*, Nucl. Instr. and Meth. A 517 (2004) 454
- [5] I. Piqueras *et al.*, NIM A 516 (2004) 122
- [6] D. Bazzacco, MGT code developed within the TMR “Gamma-ray tracking detectors”.
- [7] F.C.L. Crespi *et al.*, Nucl. Instr. Meth. A 570 (2007) 459
- [8] J. Ljungvall and J. Nyberg, Nucl. Instr. Meth. A 550 (2005) 379
- [9] J. Ljungvall and J. Nyberg, Nucl. Instr. Meth. A 546 (2005) 553
- [10] R. Venturelli, D. Bazzacco, LNL-INFN(REP) 204 (2005) 220
- [11] F. Recchia *et al.*, LNL-INFN(REP) 222 (2008) 193
- [12] S. Tashenov and J. Gerl, Nucl. Instr. Meth. A 586 (2008) 224



## 12. Electronics

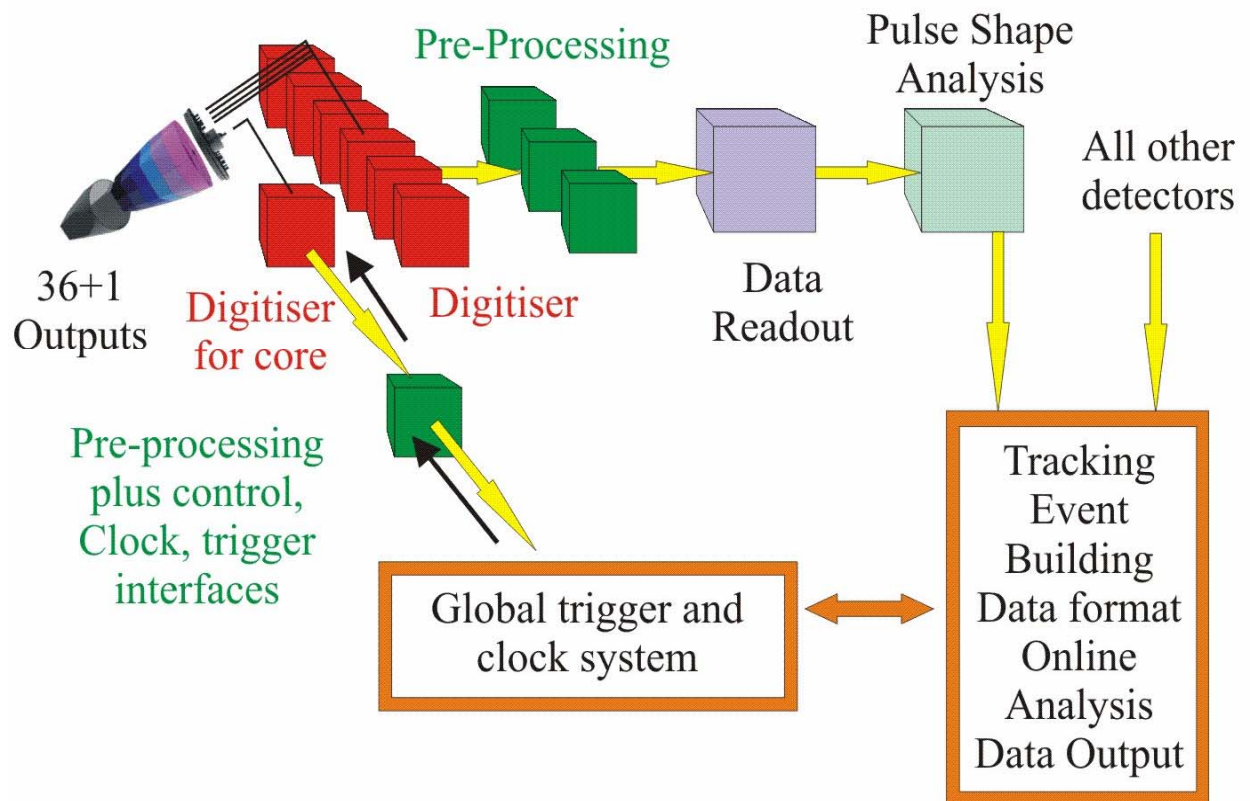
### 12.1. Overview of the AGATA electronics

The objective of the AGATA electronics is to digitise the signals from each crystal, perform some online calculations on the data in real time to establish when the crystals detected a gamma ray (local trigger) and the amount of energy deposited by the gamma ray in each segment (as well as the total energy in the detector observed by the core). The position of the gamma ray interactions is calculated in the PSA farm and so the AGATA electronics must supply a short trace including the digitised leading edge of each pulse observed on each detector segment along with the energy and timestamp.

In order to achieve these aims it is necessary to ensure that each digitising ADC is aligned with all the others and that time-stamped data based on a common clock are generated. It is also necessary that the system throughput is capable of being controlled (slowed) by data selection using triggering as well as operating in a free-running configuration where data about each gamma ray interaction detected in a crystal is sent to the PSA with no preselection.

Various architectures and physical implementations of these basic requirements (including commercial as well as self-build) were discussed and as a result the following architecture has been implemented by the AGATA collaborators.

### *Schematic of the Digital Electronics and Data Acquisition System for AGATA*



The overall design philosophy treats each crystal (one core plus 36 segment outputs) as a separate entity. Within that entity the core is treated differently to the segments. The core signal is formed by the superposition of the charge released in all the interactions in all 36 segments of the detector. So it can be used as a trigger for the whole crystal.

The AGATA electronics for each crystal comprises:

- one digitiser using custom mechanics to house 8 cards (6 for segments, 1 for core and 1 for power) in a standalone box
- two pre-processing cards containing 8 PMC mezzanines on an ATCA carrier with PCI Express readout to the PSA farm (6 cards per triple-cluster; 2 triple-clusters per crate)
- A connection to the Global Trigger and clock System (GTS)

To maintain good electrical isolation, all connections between the electronics components are fibre optic connections unless copper cables are unavoidable (e.g. connections from the detectors).

A special VME card was designed for connecting ancillary detectors to the specialised AGATA clock and timestamp system. This is the AGAVA module which responds with the AGATA timestamp to a trigger signal from an ancillary detector system.

The following sections describe in more detail the implementation of the digitisers, and the pre-processing. The GTS and the AGAVA interface are described in the following sections (DAQ).

## 12.1. The digitiser

### 12.1.1. Introduction

The objective is to create the best design ensuring good quality of the data to be sent to the preprocessing card, and enabling easy maintainability of the system during the experiment and in an electronics workshop.

The Digitiser Team is constituted from the technical groups of 3 Laboratories:

- **Institut Pluridisciplinaire Hubert Curien [IN2P3 / CNRS]**
- **Daresbury Lab Nuclear Physics Group, [STFC]**
- **University of Liverpool Nuclear Physics Group [Electronic Design group]**

### 12.1.2. OVERVIEW OF THE DIGITISER

#### 12.1.2.1. System description.

The principal goal of the digitiser card is to make the interface between the detectors and the preprocessing module.

The Digitiser will do the following tasks:

- Receive the signals from 1 crystal, (36 segments + 1 core).
- Digitize the input signals at a rate of 100 MHz, with 14 bit ADCs.
- Send the signals coded by optical fiber by group of 6.
- Send the Core CFD logic signal to the pre-processor for Ancillary detector using fiber-optic link.
- Provide spare channels and inspection lines for maintainability.
- Provide an interface for re-programming, and control in an electronics workshop and detector workshop.
- Provide an interface for slow control during experiments.
- To be mounted a less than 5 m from the Detector Preamplifier.

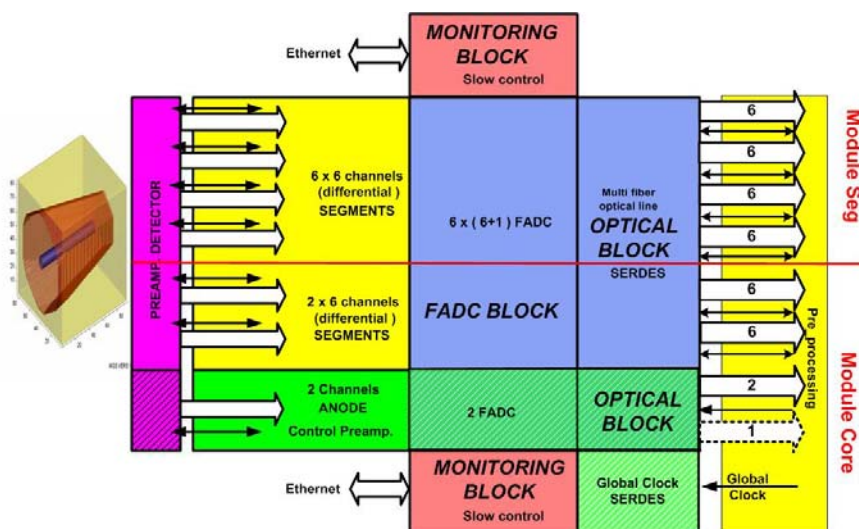


Fig. 12.1 Block diagram

The FADC cards contain 100 MHz ADCs producing 14 bit wide data plus other signals needed by the pre-processor.

The Monitoring block provides control of the spare channels and inspection lines via a slow control link to the GUI system control software. The temperature of the various parts of the digitiser electronics will be accessible by the slow control.

The FADC card outputs pass through a serializer circuit permitting the use of fiber-optic links between the ADCs and the pre-processing cards to give flexibility for future upgrades of pre-processing electronics and maximum electrical isolation.

The serializer will be integrated into the VIRTEX2 FPGA (Rocket I/O). One 12 channel fiber-optic transmitter will be used to each group of 6 segment channels. One optical interface with a low data rate will be used for offset control from pre-processing card for each group of 6 channels.

One 8 channel fiber-optic transceiver ( 4 RX, 4TX )link will be used to connect to the pre-processing card, the core FADCs data, the timing and the control. The transmitted channels will be used for the core 100Mhz FADC data (two channels), the core CFD logic signal (one channel), and the Global clock calibration feedback path( one channel ). The receive channels will be used for the Global clock signal, the Synchronization signal, and the offset controls for the core electronics.

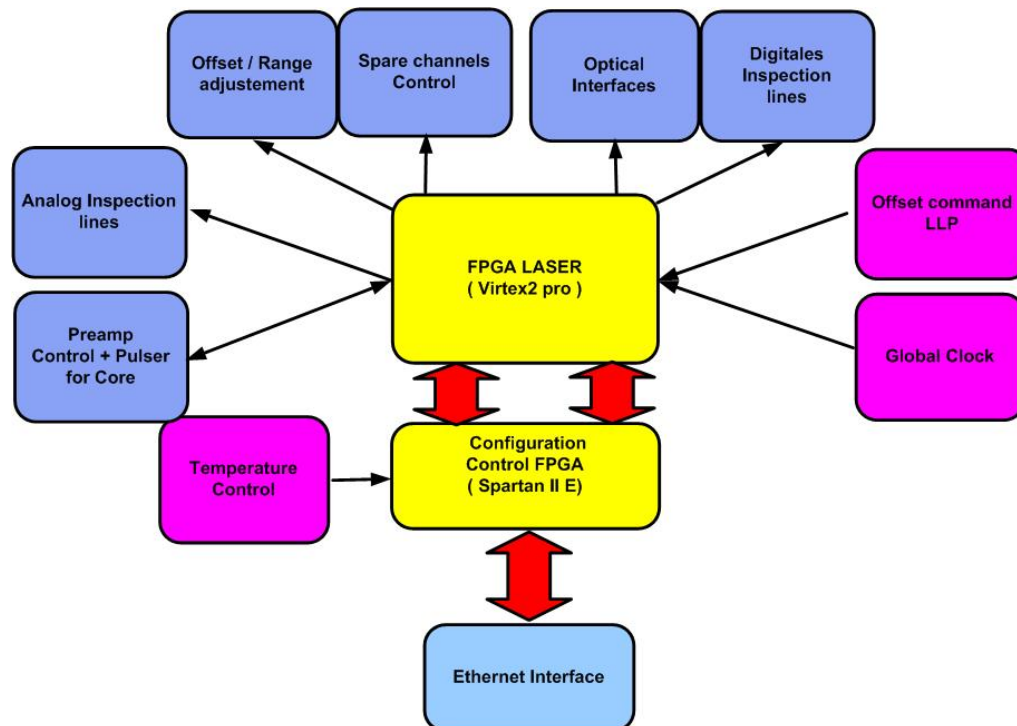


Fig 12.2 Block diagram for Control

**a) Temperature Control.**

This part will have to manage the monitoring of the temperature of both the digitiser box and FADC and if necessary its regulation. For the final modules one could envisage simplifying it but not for the first prototypes. The values of the temperatures will be recorded in a FIFO in order to enable their inspection over time. These temperature values will be available for external monitoring via the slow control interface.

**b) Preamplifier Control and Pulser for Core.**

This part will manage the control interface for the Core and Segment preamplifiers and the pulser for the Core

**c) Analog inspection lines.**

Each analog channel from the detector can be inspected before and after coding. Two analogue lines will exist per group of 6 segments channels. These inspection lines will be disabled in an experiment.

**d) Offset adjustment and Range monitoring.**

The offset value required will be computed by the pre-processing or the digitiser card to obtain the maximum use of the ADC dynamic range. The adjustments are made by a DAC on each channel. The monitoring block has to control each DAC. There is one DAC per channel. Two input ranges exist for each channel but only one can be selected at a time for each group of 6 channels.

**e) Spare Channel control.**

One spare FADC input for each group of 6 inputs is available. The FPGA will switch the spare channel to the channel to be replaced.

**f) Optical interfaces.**

The FADC output (14bits + overflow) and the Inhibit signal ( Pion measurement ) give a bus with 16 bits. This will be serialised by the Rocket I/O of the Virtex2 Pro FPGA. To transfer this data a data rate of 2Gbits/sec is needed .To simplify the Digitiser will use a Parallel Optical Link Transmitter with 12 channels of which only 6 will be used for the serialised data.

One 8 channel fiber-optic transceiver ( 4 RX, 4TX )link will be used to connect to the pre-processing card the core FADCs data , timing and control The transmit channels will be used for the core 100Mhz FADC data (two channels), the core CFD logic signal (one channel), and the Global clock calibration feedback path( one channel ). The receive channels will be used for the Global clock signal, the Synchronisation signal, and the offset controls for the core electronics.

For the segment offset control we'll use a 100MB/s optical interface as proposed by Agilent in the "Inexpensive 20 to 160 MBd Fiber-Optic Solutions" Application note 1123. All the optical interfaces include a monitoring function for the laser diodes, these monitors will be available using the slow control.

**g) Digital Inspection Lines.**

The output of an FADC can be routed, within the FPGA, to one of two DACs with buffered outputs available at the front panel. This will assist in commissioning and fault finding in the electronics lab.

**h) Offset command LLP.**

The Offset command link will operate via this interface. For the segment offset control we'll use a 100MB/s optical interface as proposed by Agilent in the "Inexpensive 20 to 160 MBd Fiber-Optic Solutions" Application note 1123.

One line will control a group of 6 segment channels.

**i) Global Clock.**

The Global Clock function will have to reconstruct a high quality clock with a very small jitter (<7pS). This clock will be received through one optical receiver within the core transceiver. When used in an electronics workshop the digitiser will have to provide its own clock signal for coding (independent of an external system of clock).

**j) Ethernet Interfaces.**

For slow control an Ethernet Interfaces module will be integrated in the Digitiser. The data rate is slow but good enough for this application. The Ethernet enables the Virtex2pro to be re-programmed without disassembling the digitiser module, and is used to slow control the experiment. This interface will respect the galvanic isolation.

### 12.1.3. HARDWARE DESCRIPTION.

#### 12.1.3.1. FADC BLOCK

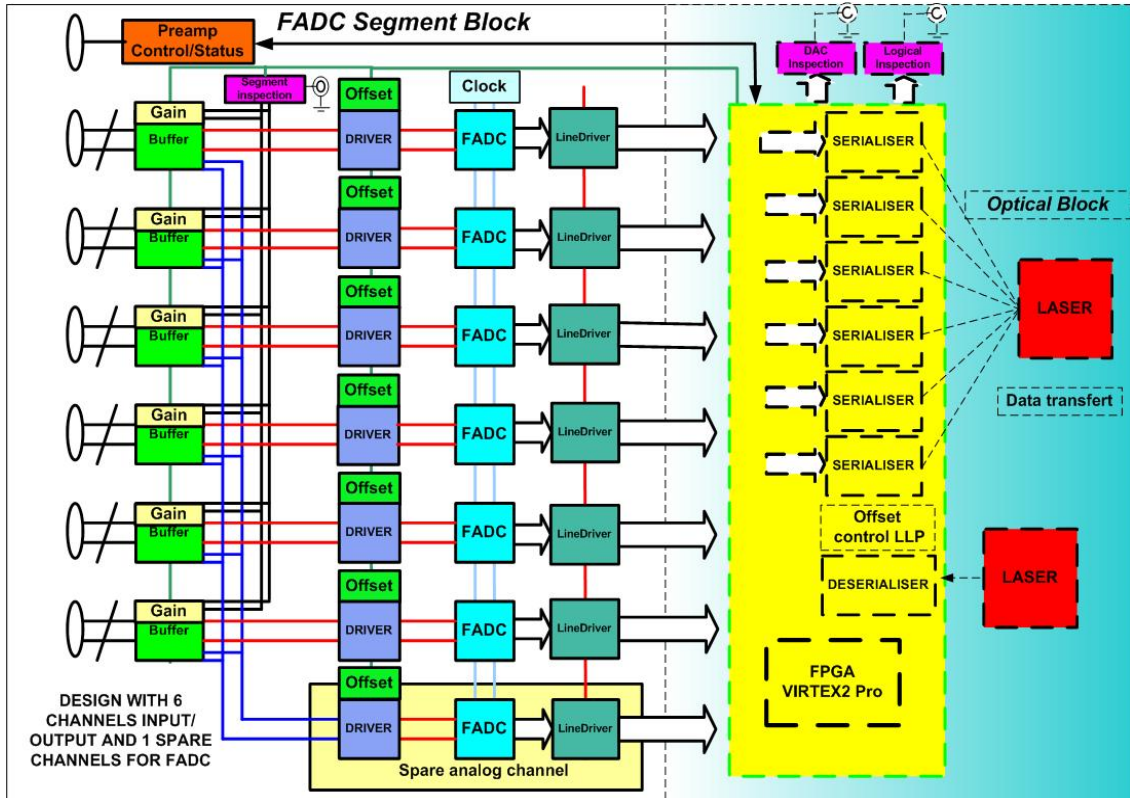


Fig 12.3 Diagram for segment

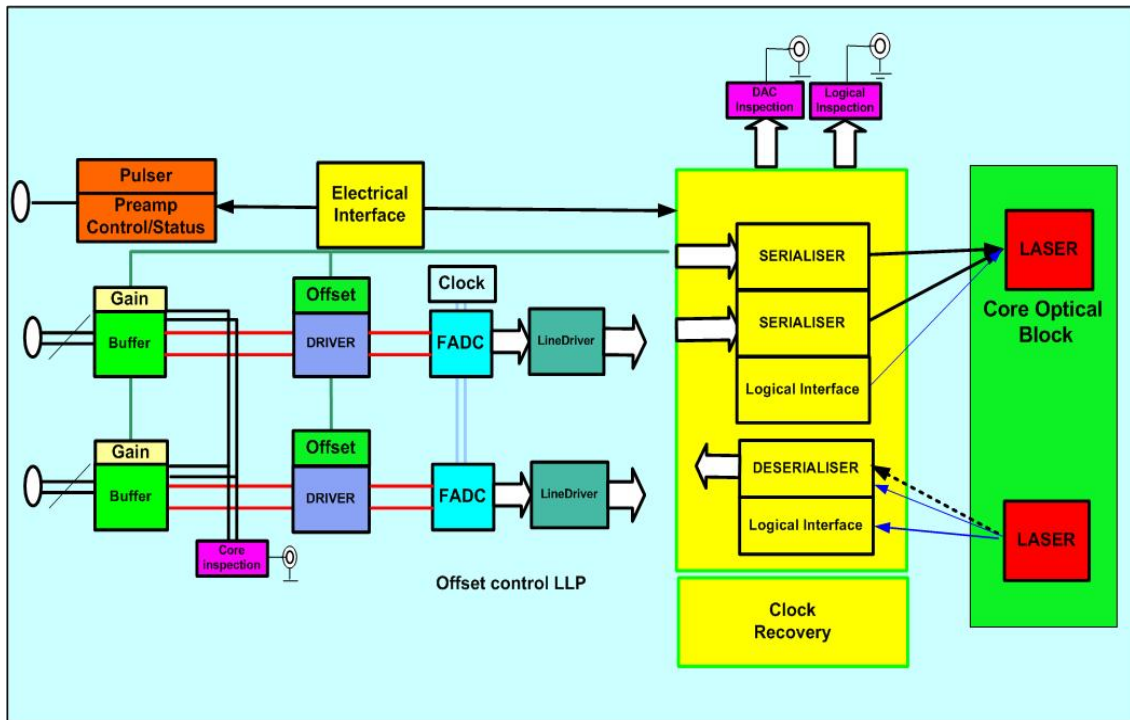


Fig. 12.4 Diagram for Core

**a) Buffer**

The Buffer module provides impedance matching and routing of the input signals between the FADC, and inspection lines. The input signals are differential. The buffer module includes the range selector.

**b) Offset**

The offset value required will be dynamically computed by the pre-processor or the digitiser to extend the ADC dynamic range.

**c) Driver**

The driver adds the offset signal. The anti-aliasing filter is included in the Driver before the FADC. All the offset DACs are based on the same chip: PCM56. We have a great deal of experience with the performance of this device. It has a low noise level, is bipolar and has a serial control interface. The output will be connected to two buffers one with a gain of one, and the other with a gain of -1. Will used Texas ultra low noise buffer OPA692.

**d) FADC**

The ADC must have 14 bits at 100 Mhz, 16 data bits are sent to the FPGA; bits 0 to 13 are data, bit 14 is the FADC overload and bit 15 could be used as a synchronization pulse. The overload bit could be also transmitted to preamplifier for the pole zero reset through the FPGA. The ADC is the AD6645 100 Mhz from Analog Device.

**e) Line Driver**

It avoids capacitive loading of the data bus of the FADC, and allows the FADC data bus to be transmitted to the Virtex

**f) Clock**

The clock module receives the clock of the Global Clock and transmits it to the FADCs with minimal jitter.

**g) Preamp Control / Status**

This part implements the optical isolation between the Digitiser and the Preamplifier for control and status signals, and the Pulse module signals.

**h) Serialiser**

The serialiser is needed to send the data to the optical interface. The Virtex2 Pro has a specific hardware module dedicated to this function called ROCKET I/O. They have been designed to be compliant with the optical fiber interface devices. The data rate transfer will be 2 Gbit/s.

The Rocket I/O serialiser has a latency which changes each time the FPGA is power-cycled or reset. To use all the channels in parallel we must be able to determine the latency of each of them. So a synchronization protocol between the pre-processor and the digitiser must be defined.

The quality of the clock used in the serialisers has a direct influence of the bit error rate.

**i) Laser Interface**

To implement the optical interface between the Digitiser core Module and the Pre-processor a Parallel Fiber Optic Link Transceiver will be used.

The transmitter module converts parallel electrical input signals via a laser driver and a VCSEL array into parallel optical output signals at a wavelength of 850 nm. The modules are pluggable, and are each fitted with an industry-standard 100 pin MegArray socket for connection to the host.

**j) DAC Inspection.**

A dual 14bit DAC (or 12 bit) will be used to inspect signals after digitization. These DACs will be disabled if not needed.

**k) Logical Inspection.**

Two lines will be use for electronic workshop or debugging.

**l) Clock recovery**

This is one of the more fundamental parts of the Digitiser. The clock is send to all FADCs on the digitiser board. For a good SNR with a high frequency signal input the clock must have the smallest jitter possible.

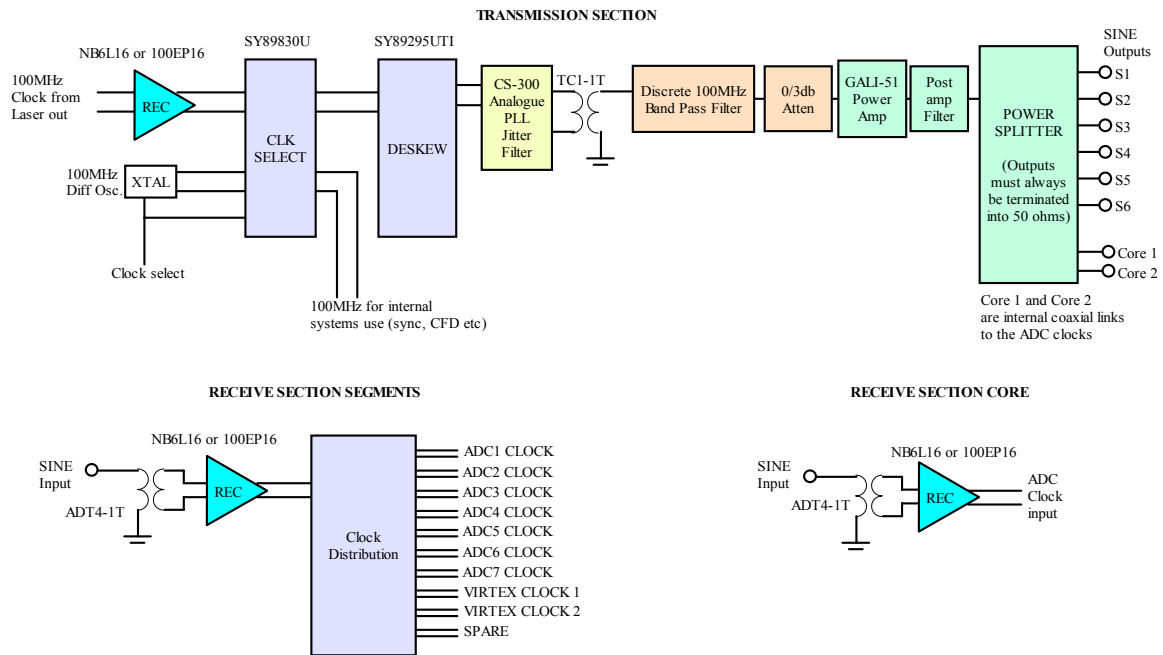


Fig. 12.5 Block diagram for Clock

The above diagram shows the proposed clock distribution scheme, which is used. The clock is received as 100MHz from the LASER output using a high gain high bandwidth buffer. The output is fed to a device which will allow an internal clock to be used in the absence of the external 100MHz from the LASER (Testing etc.). The internal clock is disabled and stopped when not required to reduce interference. The selected clock then passes to a CS-300 Phase Lock Loop device which is intended to remove as much jitter from the input clock as possible. The differential output from the CS-300 is fed via an RF transformer to a 100MHz band pass filter, centered on 100MHz with a high Q.

The filter output is attenuated if required and fed to a RF Power amplifier. This amplifier may add some harmonics to the signal so it is followed with a small ceramic filter with an 80MHz cut off (low pass). The resultant good quality sine signal is fed to a power splitter which distributes the clock to all its outputs with minimum skew. These outputs are taken to SMA connectors either on the front panel or internally for the Core ADCs.

Each segment ADC card has an SMA connector which receives the 50ohm cable carrying the sine clock from the power splitter. This is fed via a transformer to the differential inputs of a line receiver and then to a clock distribution chip which provides 10 differential clock outputs with low skew.

The Core ADCs have the same transformer followed by either a single line receiver of type 6NB16, or a single input dual output type, 6NB11. Only one coaxial connection will be required in the case of the 6NB11 device. The coaxial cables for the core can be routed internally to the unit.

In order to have the same delays for the segment and core it may be wise to include the 10way distribution chip in the core as in the segments so that both circuits are identical.

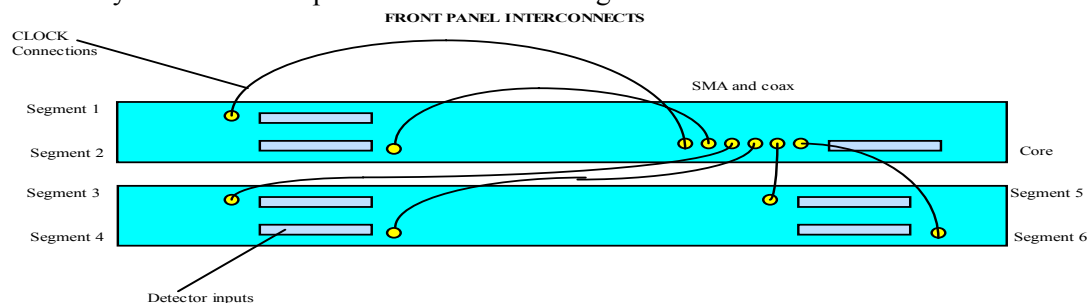


Fig. 12.6 Block diagram for Clock

The above diagram shows the clock interconnections on the front panel of the two digitiser modules.

### 12.1.3.2. Digitiser Control bus Overview

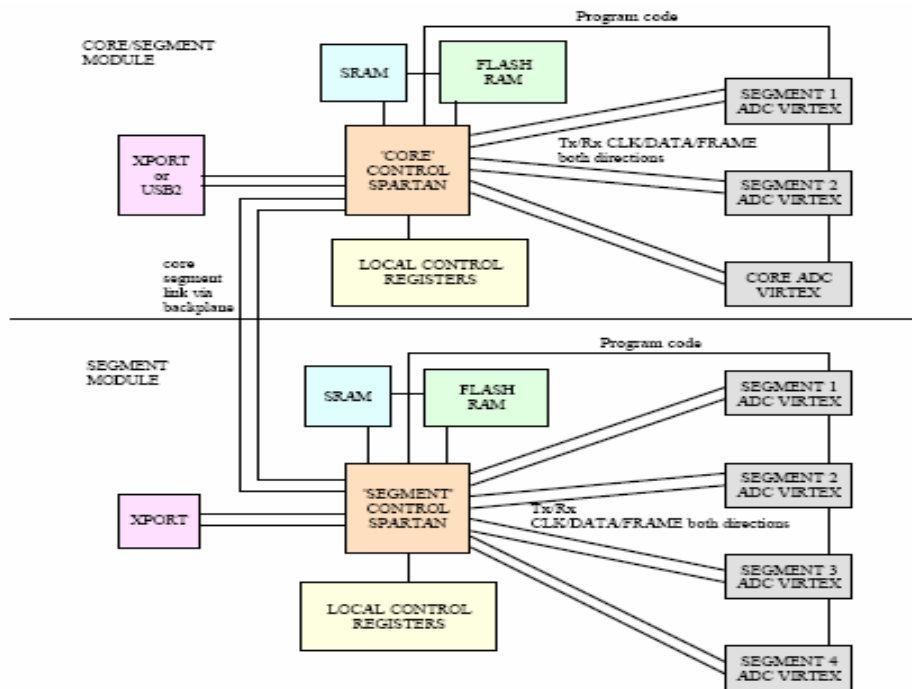


Fig. 12.7 Block diagram for slow control

The diagram above shows an overview of the communications within a single AGATA Digitiser box. The box consists of two Modules as follows:-

Core/Segment Module which contains the Core electronics and the 2 cards with 7 segment channels per card (6+1 spare each card). This gives the Core and 12 usable Segment channels in this module.

Segment Module contains 4 PCBs each with 7 channels of segment ADC (6+1spare). This gives 24 usable Segment ADC channels. The communication between all the devices internal to each module and also between modules is serial with 5 wires in each direction. 2 differentials CLOCK, 2 differential DATA and a single FRAME. The FRAME signal has two functions.

- 1) To show the start and end of a data transfer. Only data and clocks within a FRAME will be accepted.
- 2) To act as a handshake line from Rx to Tx during data transfers to prevent buffer overruns at the receiving end.

### 12.1.3.3. DC supply distribution

The DC supply has to be compatible with the integration. Tree distributions are complex to take care about all the different voltage needed by the FPGA and the analog part. To reduce the noise level and the power dissipation it has been decided to use as first module a DC-DC converter from Vicor. Because of the noise due to this type of module an EMI filter will be connected at the input interface. The input voltage will be 48 Volts DC @8 Amps.

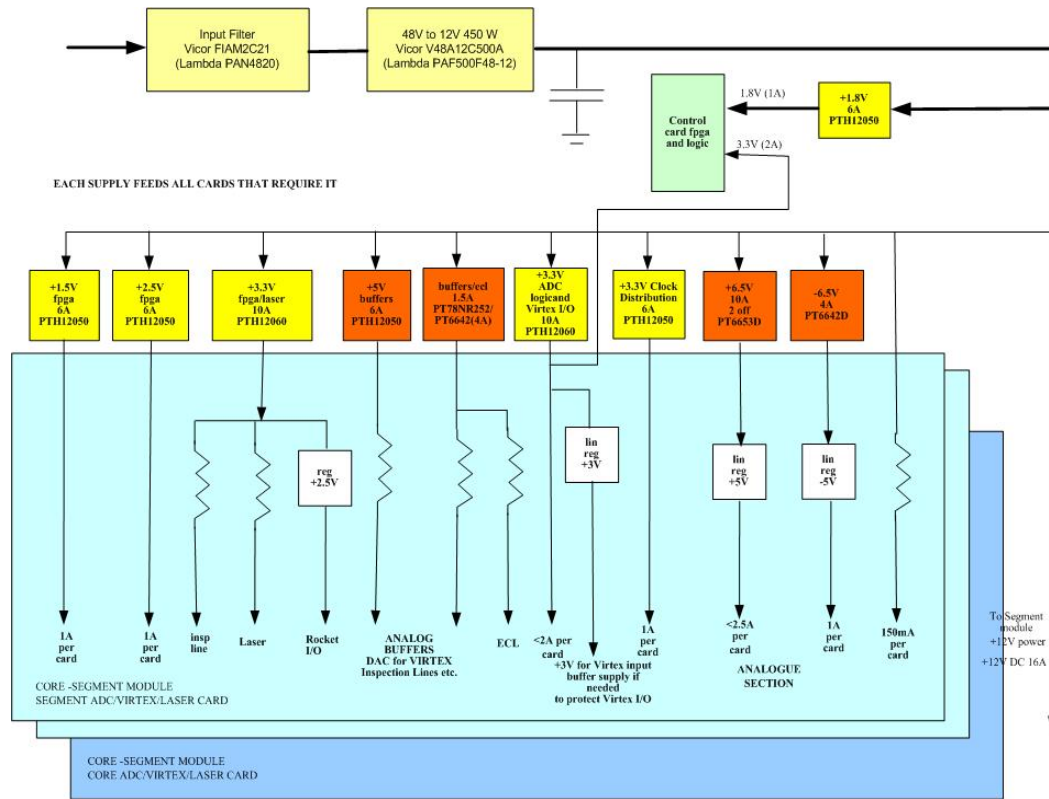


Fig. 12.8 V1 Core DC supply

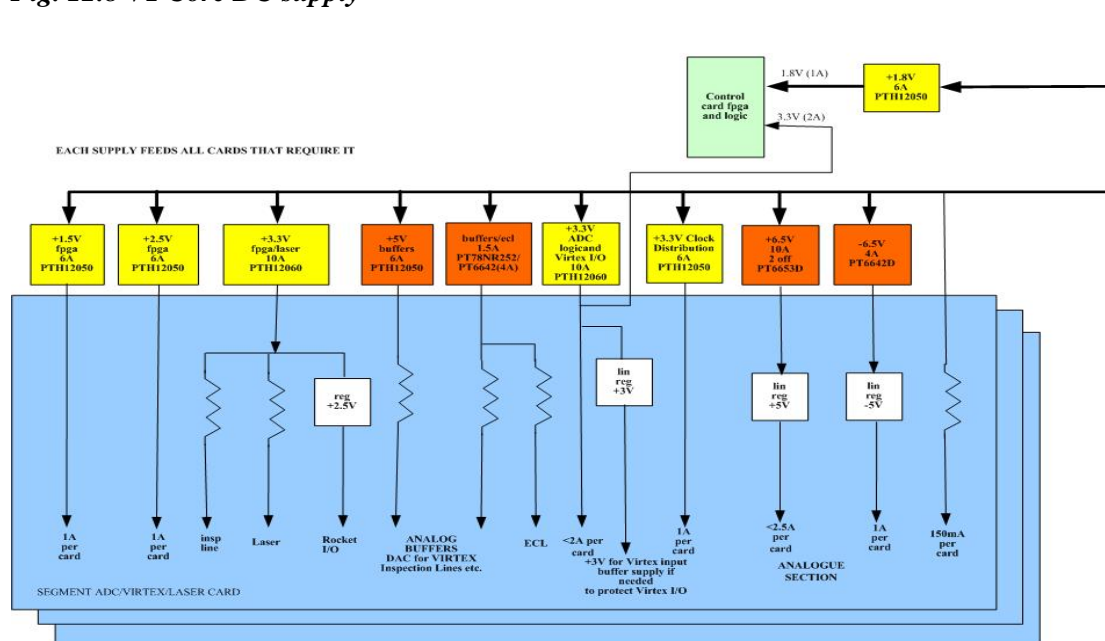


Fig. 12.9 V2 Segment DC supply

#### 12.1.3.4. Mechanical description

##### One Module called CORE MODULE with:

- DC supply input and Local Power supply
- Core FADC and Laser Interface.
- 2 Boards of 6 channels each Segment FADC and Laser Interface
- Master Control & Monitoring.

##### One Module called SEGMENT MODULE with:

- 4 Boards of 6 channels Segment FADC and Laser Interface.
- Control & Monitoring.
- Local Power supply

##### The Mechanical Housing:

- Input for water cooling.
- Back plane PCB for communication between boards.

Good thermal contact to the plates of the cooling block and easy module insertion and extraction is a pre-requisite of the mechanical design. The top and bottom plates will be pulled onto the module external surface by spring tension spread over the outside of the box. It is envisaged that a lever and plate mechanism will be provided to open up the space between the top and centre (or bottom and centre) cooling plates for the removal of a module. This is currently under investigation.

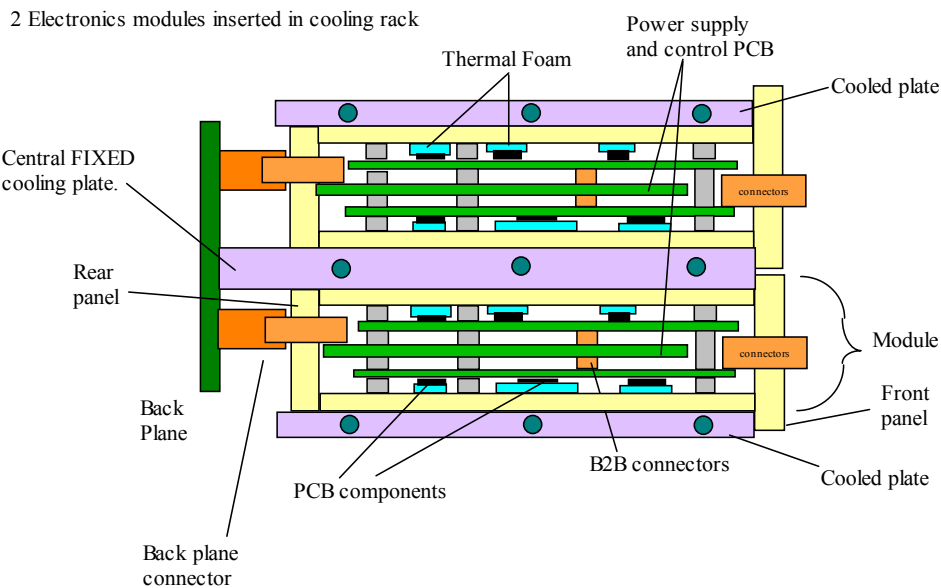
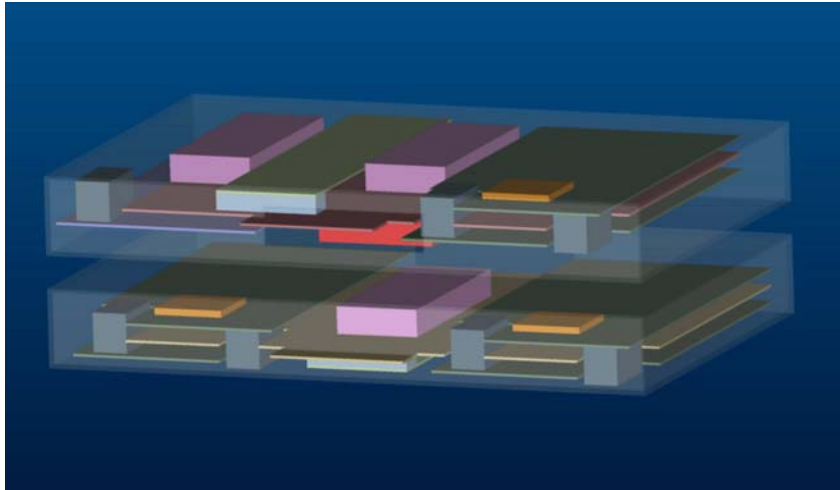


Fig. 12.10 Section through electronics module after insertion in cooling rack.



*Fig. 1-11 Global assembly*

### 12.1.3.5. REALISATION

Actually 8 digitisers have been delivered at IPHC plus the prototype



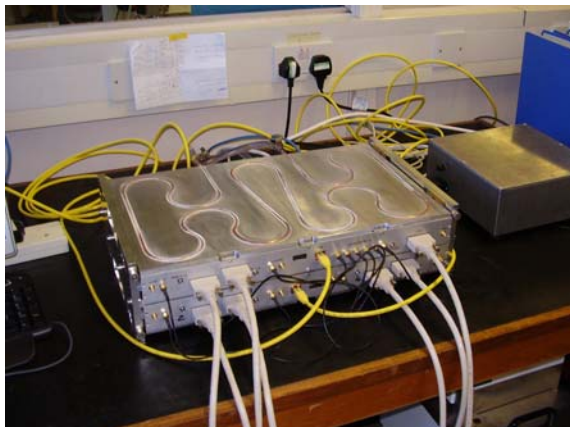
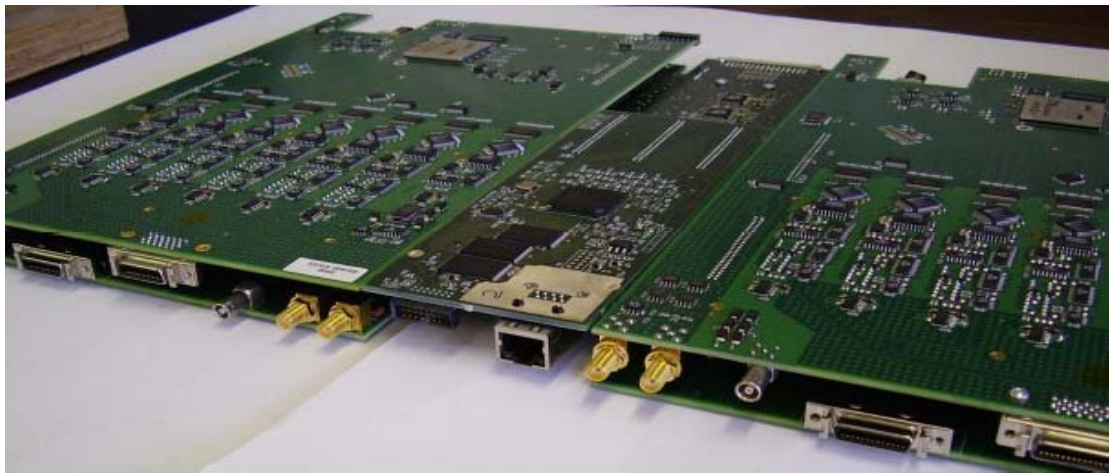


**Fig. 10.12 Global description**

**12.1.3.6. TESTS**

**12.1.3.6.1. Tests in situ**

- Different types have been done at:
- IKP Cologne (Agata detector)
- Liverpool ( Agata detector )
- Legnaro ( Agata detector + pulser)
- Orsay ( optical link tests )
- Padova ( optical link tests)

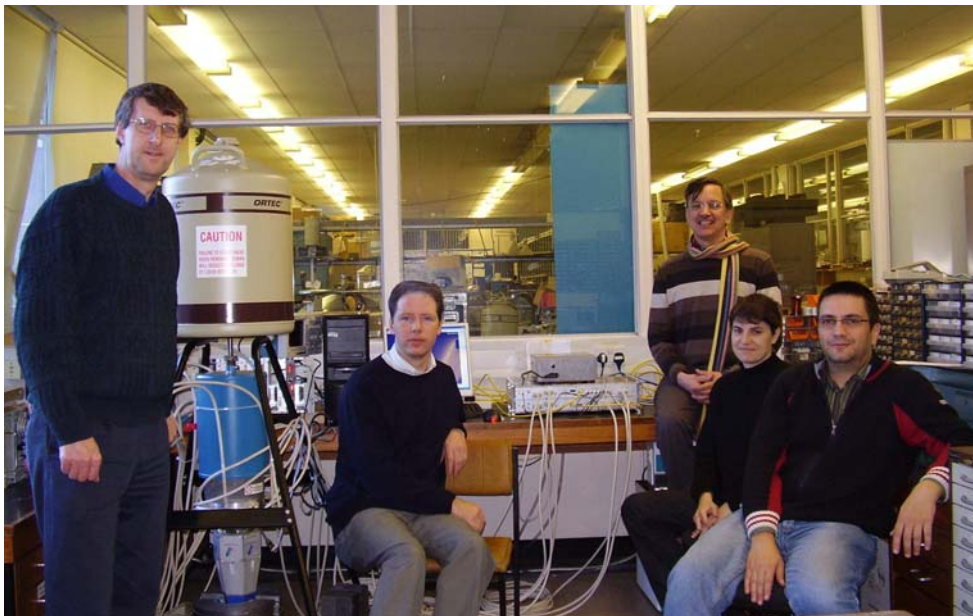


Fig. 12.13 Tests in Liverpool December 2006. (J. Thornill, D. Wells, P.J. Colman-Smith C. Parisel and P. Medina)

**12.1.3.7. Characterization**

The digitiser has been characterized for the noise level noise:

	<b>ENOB</b>	<b>SNR (dB)</b>
<b>Digitiser1</b>	12.29	75.74
<b>Digitiser2</b>	12.30	75.78
<b>Digitiser3</b>	12.33	75.90
<b>Digitiser4</b>	12.32	75.92
<b>Digitiser5</b>	12.29	75.73
<b>Digitiser6</b>	12.30	75.81
<b>Digitiser7</b>	12.31	75.87
<b>Digitiser8</b>	12.30	75.83
<b>General Average</b>	12.30	75.82

ENOB is the Effective Number of Bits

**12.1.3.8. Digitiser in “stand alone mode”: SAM**

During some electronic workshop or some detector workshop, for development, diagnostics, tests and maintenance purposes, the digitiser is also able to work without the preprocessing part. The digitiser is able to work as a multi channel Analyzer (MCA) and is able to calculate the energy for a group of 6 channels in same time. Some diagnostics tools have been implemented inside the digitiser. (ramp generator (DNL), noise calculation).

Additionally, some tools have been developed to work with the digitiser to simulate the detector or to be used as a “data recorder” : Snapshot & PSG ??

For the SAM operating needs in order to manage all communications with a digitiser sub-part, the CORE and SEGMENT modules, some specific PC software has been designed and developed : SAMWISE.

Switching to the SAM (by uploading some specific code into a module sub-part which is called CORE card or Segment card) enables these features:

- The digitiser can register the shape of 6+1 channels at the same time by implementing some triggering features: one of 6 channels for a SEGMENT card and one of 2 channels for the CORE card.
- The digitiser can calculate the energy (like a MCA) for 6+1 channels at the same time (same channel distribution as above).
- The digitiser can run some diagnostic mode for noise / DNL measurement.
- The digitiser can run some ‘PoleZero-time decay constant’ estimation mode for each detector channel (37).
- The digitiser is used to test new energy algorithm.
- Monitoring of all analog and FPGA’s temperatures

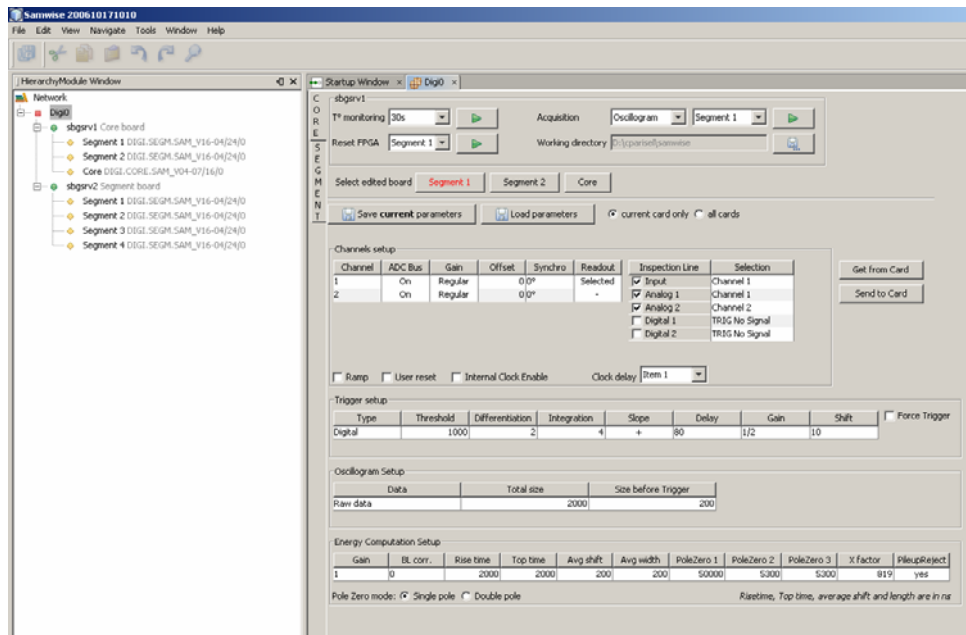
All communications goes through some XPort component which basically encapsulate a basic serial COM RS-232 I/O port into Ethernet socket frames, but the primary speed/transfer rate still remain the one of a RS-232 which is very low /slow but sufficient for SAM context.

#### 12.1.3.8.1. SAMWISE

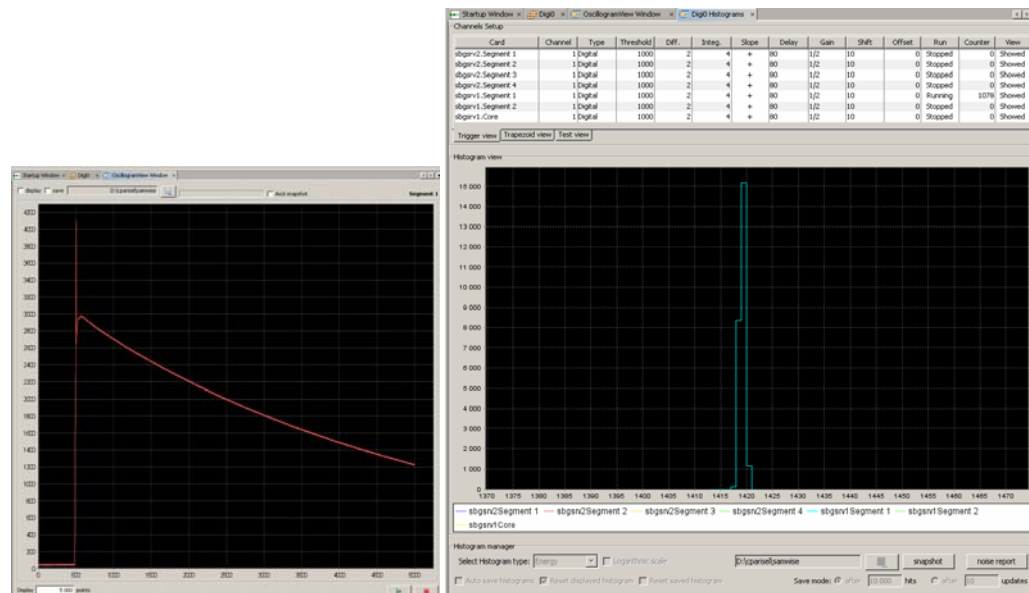
SAMWISE is the PC software designed in order to operate a digitiser in Stand Alone Mode (for electronic or detector workshop).

It is some java written software and is build on top of the netbeans platform (<http://www.netbeans.org/features/platform/index.html>).

NetBeans refers to both a platform for the development of applications for the network (using perl, php, python, ruby, java, c and c++), and an integrated development environment (IDE) developed using the NetBeans Platform.



**SAMWISE Main screen: parameters and run/stop actions**



**SAMWISE screens: oscillogram and energy histogram**

## 12.1.3.8.2. VHDL for SAM

### 12.1.3.8.2.1. Functionalities

Some functions are exclusively used for the testing of the cards:

- The ramp generator in the oscilloscope mode in order to verify that the RAM memory is correctly addressed.
- The ‘ADC histogramer’ mode in order to calculate SNR off-line.
- The ramp generator into the offset controller: to verify that the PCM56 offset circuit is turning well and to compute the DNL.

The others functions used to test the detector are the following:

- The ‘Oscilloscope mode’ for observing sampled data traces of the input signals and internal signals. A trigger function is implemented to detect the arrival of a pulse. Many types of trigger are possible for the user.
- The ‘Energy histogramer’ mode to store the computed gamma-rays energies. Some trapezoidal shaping (Moving Window Deconvolution) is done with original exponential pulses provided by the detector. A baseline restorer and some trapezoidal flat top averaging are implemented.
- Pole-Zero computing which is a tool useful to compute the decay time of the exponential pulse. All the SAM tasks are performed around the FPGA Virtex2Pro 2VP30FF896 which has these main characteristics:

<b>Virtex2Pro “2VP30FF896”</b>	
<b>Logic cells</b>	<b>30,816</b>
<b>Slices</b>	<b>13,696</b>
<b>I/O Max</b>	<b>556</b>
<b>RAM</b>	<b>136*18kbits</b>
<b>DCM</b>	<b>8</b>
<b>Xtreme Mult. 18*18s</b>	<b>136</b>
<b>MGT 3.125Gbits</b>	<b>8</b>
<b>PPC 405</b>	<b>2</b>

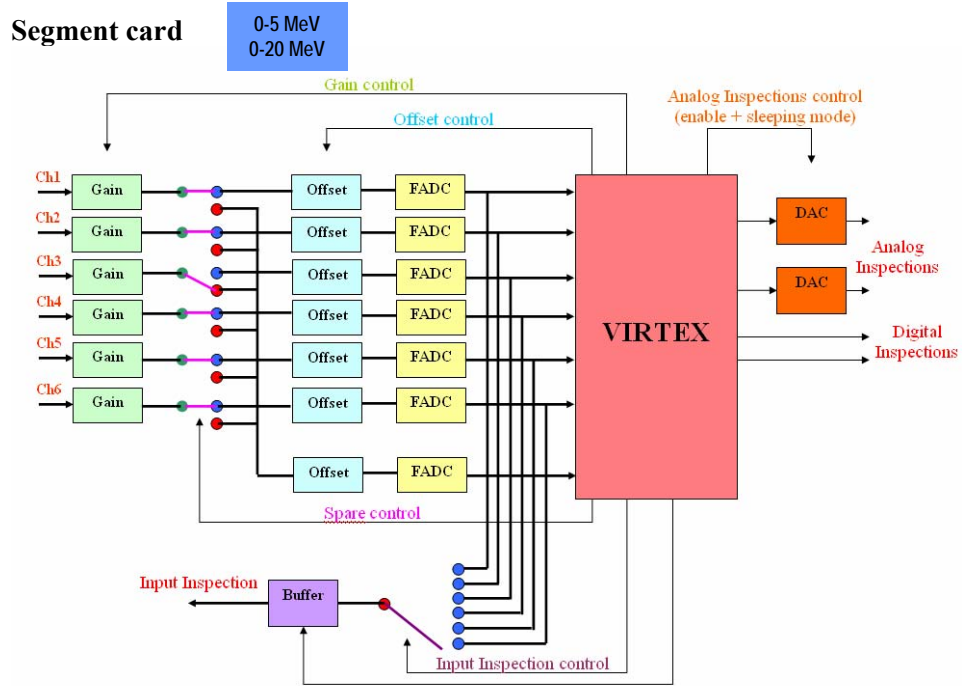
Table: Virtex2Pro FPGA Details

The MGT (Rocket IO) are only used to transmit data by optical fiber for the digitiser in global mode.

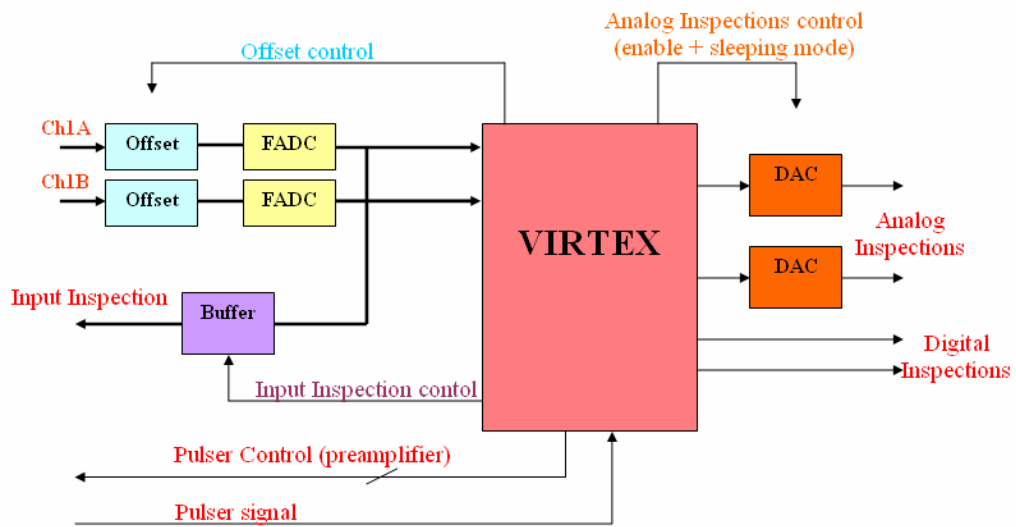
In Stand Alone Mode, the FPGA is able to perform two main tasks:

- Global control of the card (segment or core) useful to modify the main characteristics of the exponential pulses (gain, offset) and to diagnose the shape of the signals via the inspections lines.
- Digital measurements useful for the characterization of a detector or for the characterization of the card itself: sampled data memorization (oscillograms), energy calculation, noise characterization, etc.

## Global control

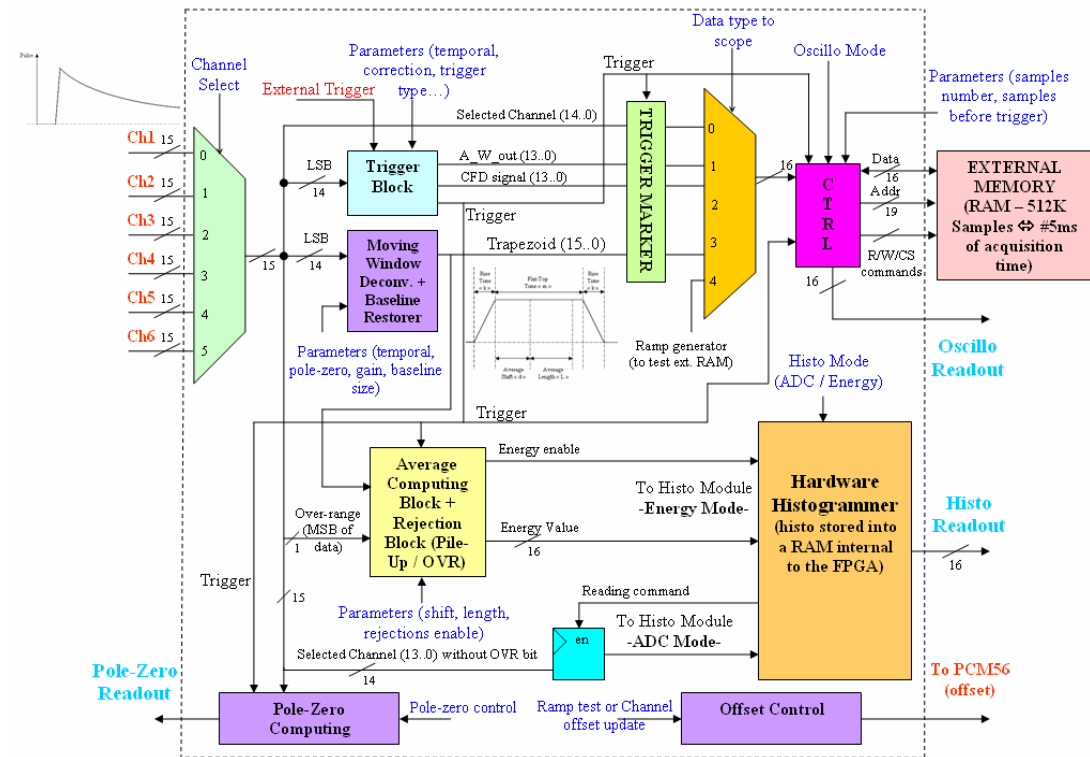


## Core card



## Measurements

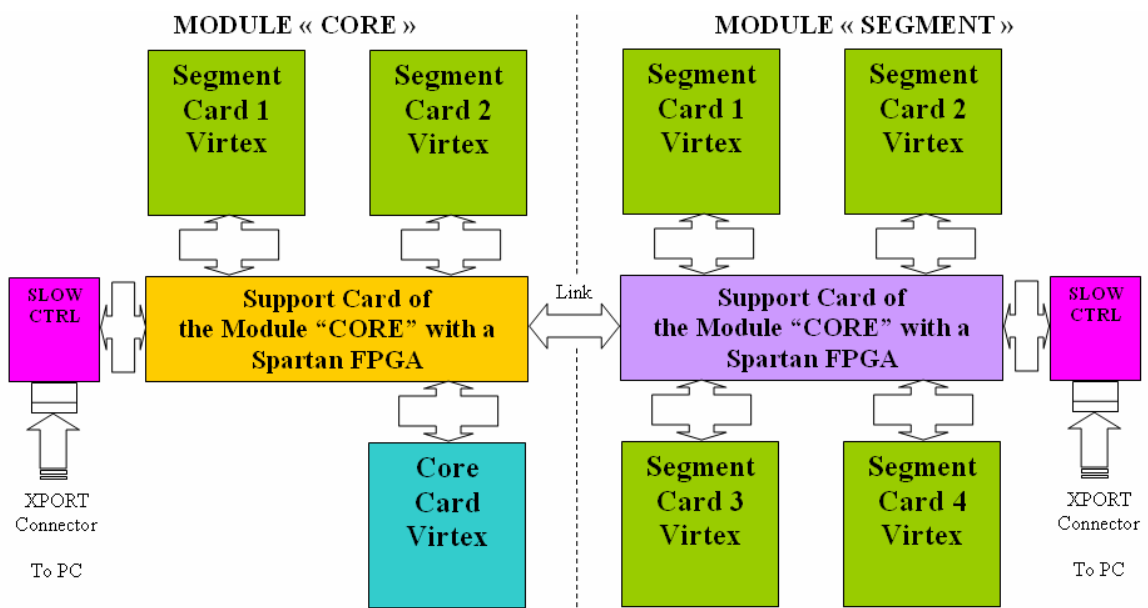
Many digital functions are implemented to well characterize the performances of the card and to test the detectors. They are listed in the figure below.



For the core card, only two channels are connected to the inputs.

### 12.1.3.8.2.2. SAM communications

The communication between the Virtex of each card and the user PC computer is explained in the figure illustrating all the digitiser.



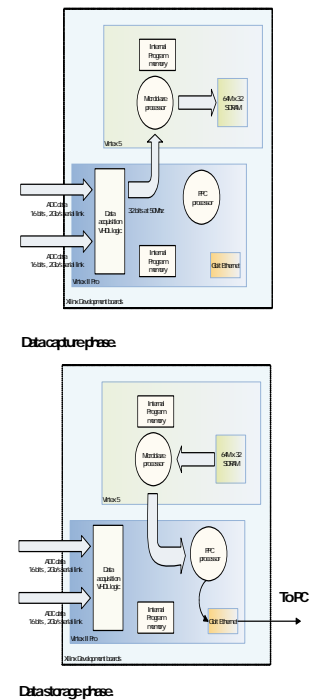
The link to the PC is ensured by a Xport Connection (Ethernet). The data rate is relatively slow (some kB/sec) but is it widely sufficient for the digitiser in Stand Alone Mode. The support card of each module assures the data transfer between the Xport connection and the Virtex of each female card via a serial transmission with a protocol well defined.

#### 12.1.4. Snapshot system for the digitiser

The snapshot system is connecting to a digitiser. It provides Clock and Synchronization pulses. It useful to collect 64Msamples of data forms any 2 ADC channels. It forwards the data to a PC for storage.



**Fig 12. 14 Tests in Padova**



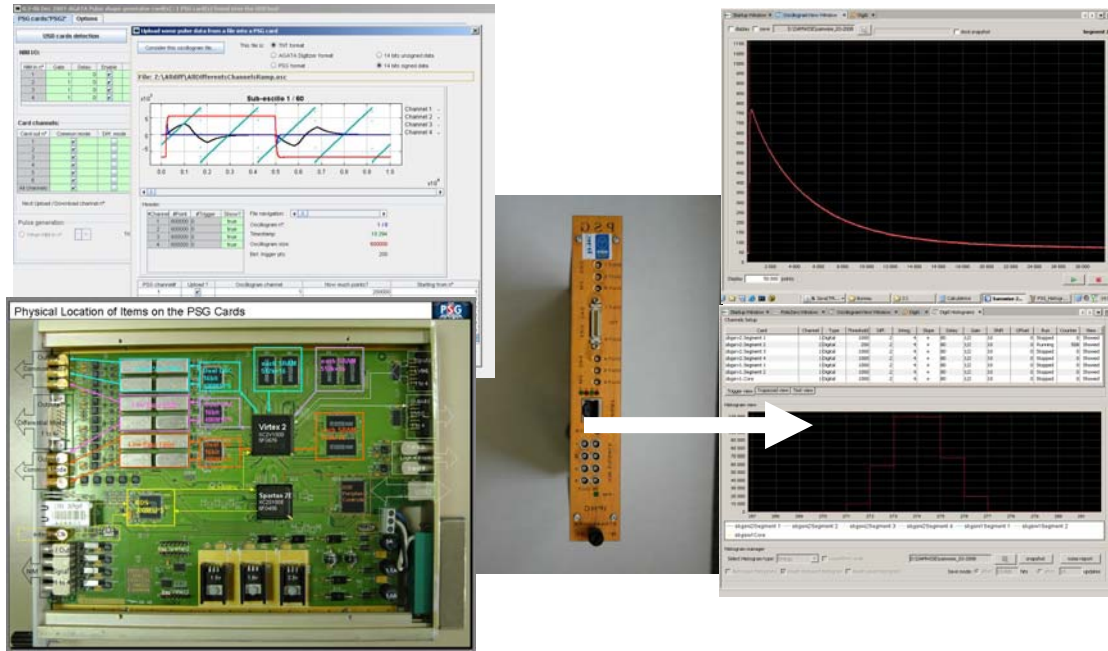
#### 12.1.5. Waveform Generator (PSG)

The 6 channel PSG card can be used to simulate one Crystal (using 6+1 PSG cards together). It is constituted by 6 x 16 bits 400 MHz. Each channel has 5 ms of memory.

A PSG channel memory can be uploaded with

- Some TNT2 oscillogram file
- Some oscillogram generated by a Digitiser card in SAM mode
- Any MCA card if the sampled points can be saved in some basic ASCII format
- Any simulation/mathematical software (ex: MGS or any matlab / scilab software) that is able to construct a waveform and to export it to some simple ascii file)
- Some memory download of a PSG card

An output MDR26 connector compatible with Agata cable allow the PSG to be connected to Digitiser module in order to simulate one Crystal.



PSG store previous sampled data  
And is able to generate associated analog data

Digitiser process PSG data...  
(SAMWISE screens)

Fig. 10.15 PSG mode

One PSG card has 6 channels, so with 6 +1 cards => we can consider all channels of a full crystal.

### 12.1.6. CONCLUSION

All the digitiser parts have been delivered and work as mentioned in the specification documents. The design of the digitizer is a success because of very good collaboration between the 3 labs. Evolutions are discussed now but not define in details (TOT for example). But the actual digitizer can be produced for AGATA.

## 12.2. Pre-Processing

### 12.2.1. The Team

The pre-processing team comprises engineers from the laboratories in CSNSM Orsay, IPN Orsay, INFN Padua and STFC DL and RAL:

IPN Orsay

- Carrier VHDL design (FPGA2- trigger distribution)
- Carrier VHDL production code
- Carrier commissioning (production run of 34 cards)
- Original carrier design

INFN Padua

- Carrier rework (prototype and pre-production)
- Carrier VHDL (release 0 for initial tests)
- Carrier VHDL (FPGA 0- data readout)
- Delivery of 6 tested carriers for October tests
- GTS Mezzanine

CSNSM Orsay

- Segment mezzanine (hardware and VHDL)
- Core mezzanine (hardware and VHDL)
- Production run of core and segment mezzanines

IPHC Strasbourg

- Supply of MWD code for use in core and segment mezzanines in “black box” format

STFC RAL and LPC CAEN

- VHDL code for carrier readout (PCIe and propriety “FASTER” protocols)

Team size

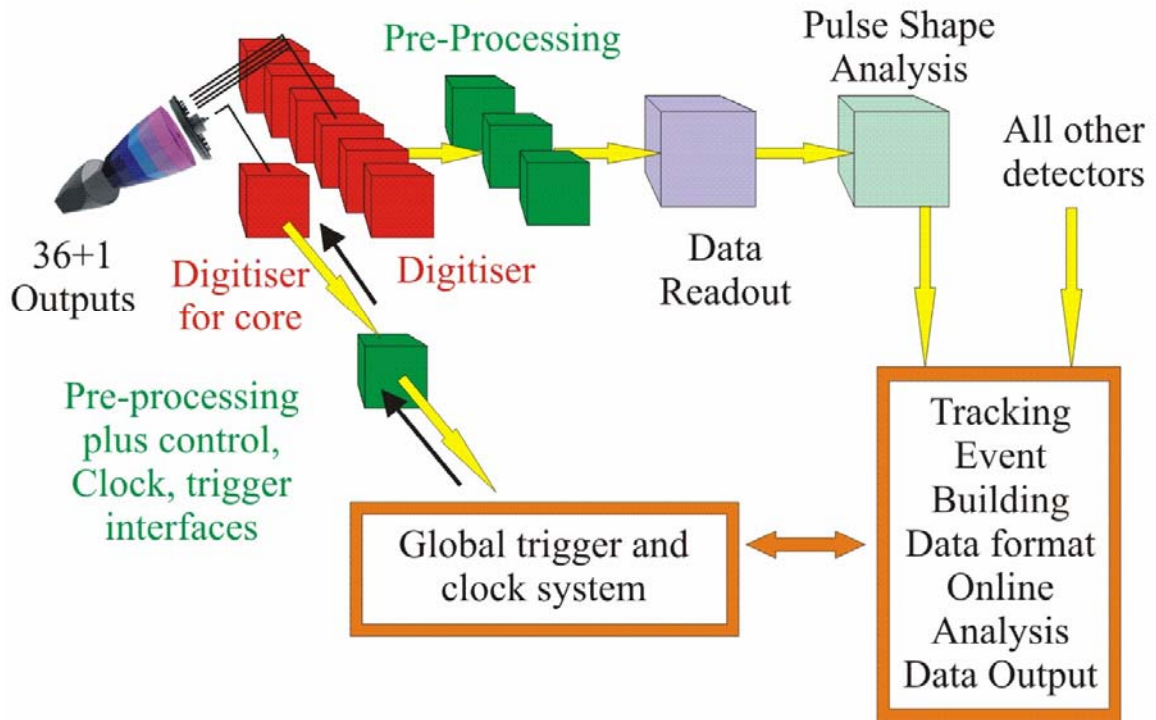
On average between 10 and 15 people are working on this project in this team.

### 12.2.2. Introduction

In essence the role of the pre-processing system is to take data from the digitiser system, extract all the useful data which can be calculated on a per-channel basis in real time, and pass on these parameters, along with the leading edge of the digitised trace from the incoming pulse, to the Pulse Shape Analysis (PSA) system. The pre-processing also interfaces with the Global Trigger and Clock system (GTS) from which a clock for the digitiser and the timestamp information is derived. In some cases the front end data rate might exceed the processing capacity in the PSA, or one of the following data acquisition systems (tracking, event building or tape server). The global trigger mechanism can be used to reduce the front end data rate in these cases by pre-selection based on criteria such as multiplicity (number of active crystals) or coincidence with ancillary detectors or coincidence with beam pulses.

A schematic diagram is shown below. The local level processing hardware elements (digitiser, pre-processing and PSA) are shown and also their interfaces to global level processing. The pre-processing electronics is shown in dark green.

## *Schematic of the Digital Electronics and Data Acquisition System for AGATA*



The counting rate in the core contact is much higher than that in any of the segments; to a first approximation it is 36 times higher (without taking into effect the segments affected by induced charge from neighbouring segments). Since the segment electronics is triggered by the core, the rate at which the segments collect data traces is the same (high) rate as the core contact. The processing rate for traces in the segments will, therefore, be the same as in the core, although many of the traces will contain no data and could be rejected by a zero suppression algorithm (currently there is no plan to implement zero suppression because the PSA wants access to all the data including the apparently empty channels).

The need for triggering in the core requires special interconnections with the segment electronics and also with the global triggering system. Since this connection is already made for the triggering, it is used also as the interface point for receiving the clock and timestamps. So the core contact electronics is the master and the segments are controlled from it.

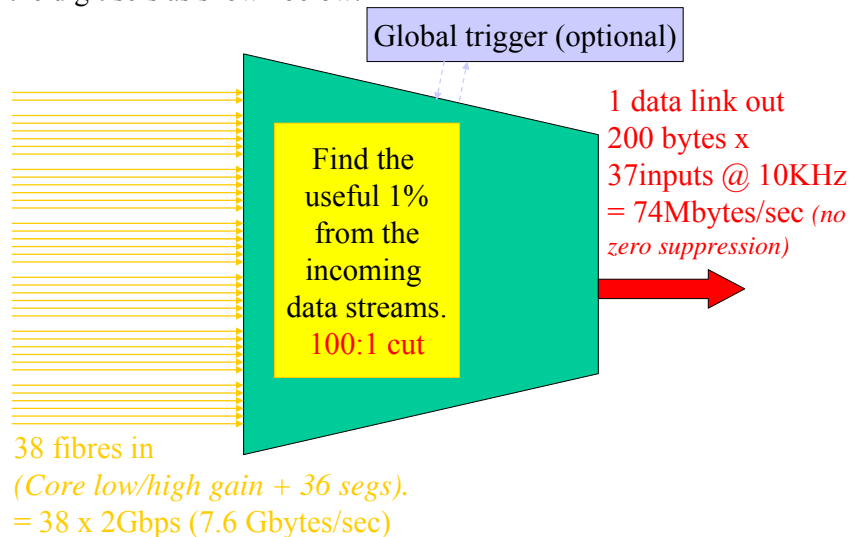
The fibre links from the digitiser electronics are mainly unidirectional (transferring data from digitiser to pre-processing). However, the core contact fibre are bi-directional (full duplex) so that clocks and control signals can be sent to the digitiser. Examples of control signals are the offset for the baseline compensation DAC and synchronisation test pulses. One slow fibre is provided for each group of 6 segments to control the offset DAC at the digitiser segment inputs (and any other parameters requiring a feedback path from the pre-processing - the necessity for this link will be reviewed after the prototype tests).

The pre-processing hardware takes the incoming data streams and store traces started by the crystal level trigger information derived from the core contact (and optionally validated by the global trigger system too). The traces are processed to extract parameters such as energy, time and, in the future, preamplifier time over threshold (pion overload energy, based on the preamp “inhibit” signals sent on the top (D15) data bits from ADCs). It then passes the leading edge of the pulse trace to the PSA, along with these parameters.

The digitising speed is 100MHz, so the pre-processing hardware also uses 100MHz clock rates for incoming data (some internal clocks are 200MHz).

The Global Trigger and clock System (GTS) interface provides the system clock and a trigger system. The trigger system can be used to reduce the counting rate, for example by a multiplicity filter or by a coincidence requirement with an ancillary detector or with beam pulses. Where rate reduction is not required, the pre-processing runs in triggerless mode which means that all the processed data are sent on to the PSA stage. In this case a software trigger is performed downstream, after PSA and tracking. The maximum delay (latency) which can be accommodated in the pre-processing hardware while the GTS trigger decision takes place has implications for the amount of storage required in the pre-processing. It is estimated that up to 20µs of trace length could be needed for processing and therefore the maximum trigger latency is 20µs. Lower values can be configured, but coincidences with more than 20µs delay will be detected in software triggers.

Another way to understand the pre-processing’s role is this: to find the useful 1% in the data flow from the digitisers as shown below.



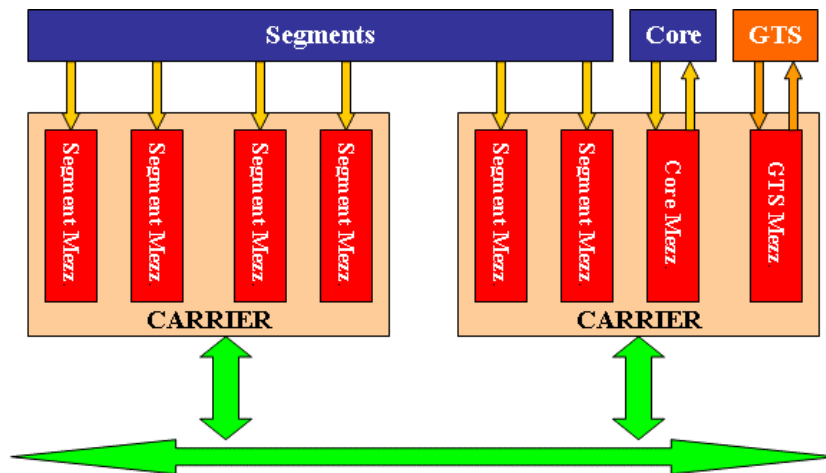
### 12.2.3. Inputs

- Digitiser Interface
  - 36 digitised segment ADC signals in groups of 6 with 6 additional fibres whose use is described below (12 way multifibre per group of 6 segments)
    - Transmitted over unidirectional multifibre connections.
    - Data is converted to/from serial format before/after transmission using Xilinx MGT’s.

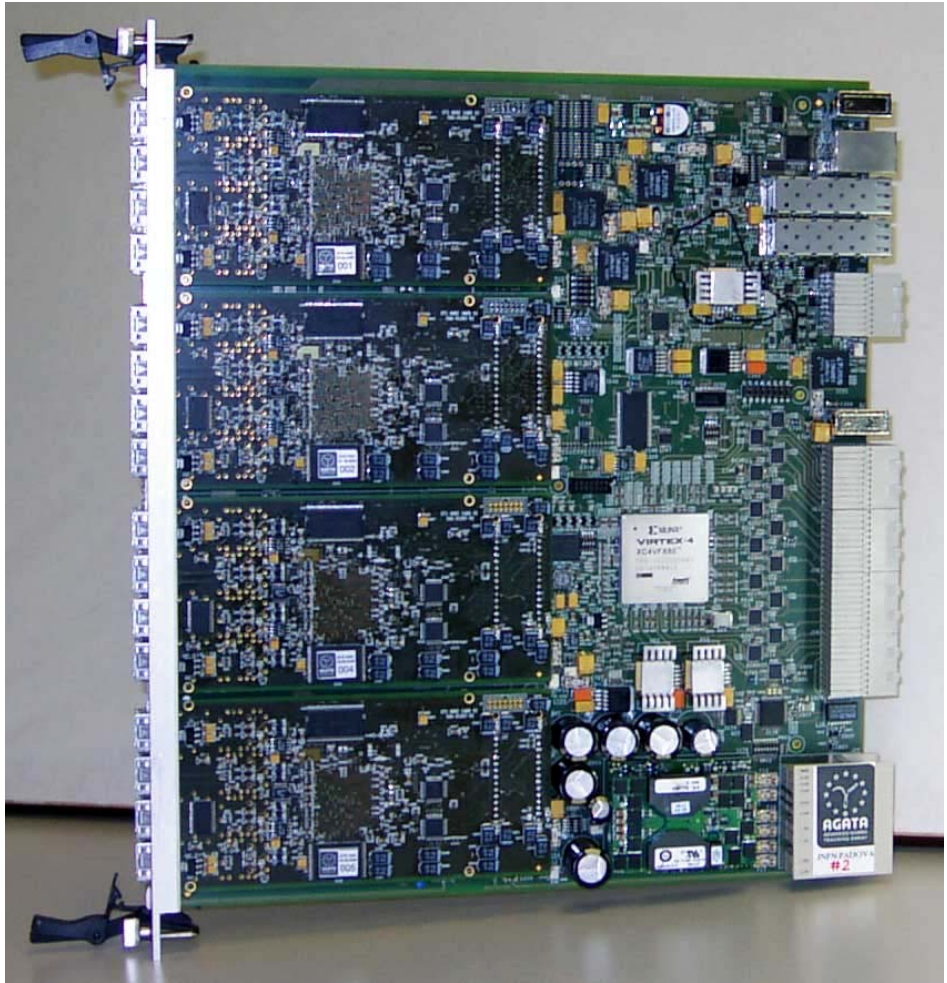


- Leading edge of the trace (600ns)
  - Energy word, and confidence/quality factor word
  - Other parameters with quality/confidence factors
- Output to Digitiser
  - Control commands received from Global Clock/Trigger system
  - Separate fibre for pure 100MHz Clock for digitisers- no associated commands are sent on this fibre and no clock recovery is needed in the digitiser (The clock itself is recovered from the incoming GTS command serial bit stream by the GTS mezzanine)
  - A fibre for the sync pulse (used to line up all the clock in all channels)
  - Offset correction values (*sent via shared low rate (10Mbits/sec) fibres 1 per 6 segments and via a dedicated high speed (1Gbit/sec) fibre for the core*)

#### 12.2.5. Implementation.



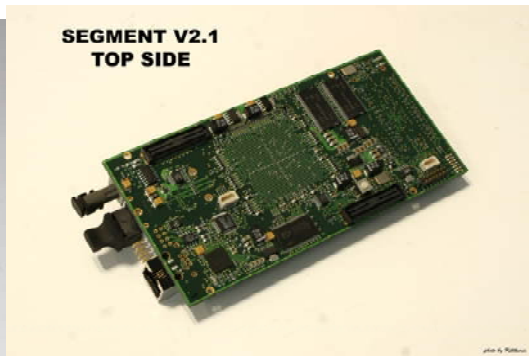
The design has been implemented using a mezzanine based approach, using CMC form factor. The mezzanines are mounted on ATCA carrier cards which accommodate 4 CMC mezzanines on each carrier.



Carrier card equipped with 4 mezzanines



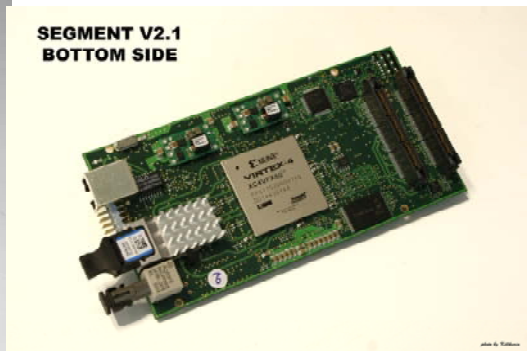
CORE V2.0  
TOP SIDE



SEGMENT V2.1  
TOP SIDE



CORE V2.0  
BOTTOM SIDE



SEGMENT V2.1  
BOTTOM SIDE

Core and Segment Mezzanine cards

The role of the pre-processing is to take the continuous data stream from each of the digitiser's ADCs and extract useful information to be passed on to the PSA.

The useful information is, as a minimum, a set of traces corresponding to a gamma-ray's interaction in the detector. So, the first task is to decide which part of the incoming data stream is useful- this is achieved by running a digital trigger algorithm on the detector's core contact data stream. When this trigger finds a pulse in the data it extracts a data trace and generates a local trigger output which indicates to all the segment electronics that they should also extract a trace from the data stream. Traces are stored locally, within each pre-processing channel.

At this point there are 2 options for how the pre-processing behaves. If the AGATA system's data handling bandwidth can handle the full data from all gamma rays generated during the experiment then the pre-processing will just go ahead and put the traces in an output buffer. However, for reasons of either financial constraints in the AGATA EDAQ or over-ambitious raw gamma ray count rates it may be necessary to make a judgement on the usefulness of the pulses detected by the pre-processing, saving only the best ones. In this case the pre-processing enquires via the GTS about whether other detectors were also active in coincidence with this one and whether the GTS system's criteria for saving the data are met. In this mode of operation the traces are held in each channel's local memory for up to 20us while the GTS makes a decision. Either an event reject or an event accept response is generated for each local trigger based on the GTS decision. If the EDAQ bandwidth matches the gamma ray rate then no GTS trigger decision is made and the event accept signal is generated for all detected pulses.

For events which are accepted, the pre-processing stores a trace of the digitised leading edge of the pulse from the core and all 36 segments in a buffer waiting to be sent to the PSA.

In addition to selecting useful portions of the incoming data stream using a trigger algorithm, the pre-processing will also apply other algorithms to the data streams.

The first of these algorithms is the Moving Window Deconvolution (MWD) algorithm to determine the gamma ray energy by filtering the incoming pulse digitally.

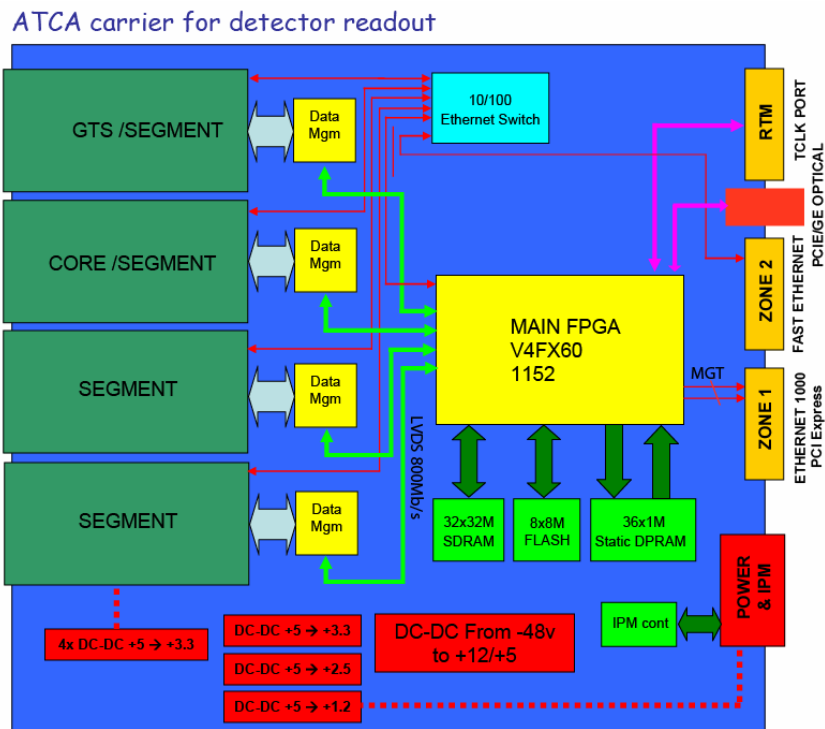
The second algorithm is associated with the preamplifier's inhibit signal. The inhibit is activated when the preamp is saturated by a pion (much higher energy than the gamma rays). The preamplifier recovers by injection of charge from a constant current source, so the length of the recovery time (i.e. the width of the inhibit pulse) is directly proportional to the energy deposited by the pion. The Inhibit from the preamps is sent from the digitiser in the previously unused to ADC data bit (D15). The width of the inhibit pulse is counted by the pre-processing ( $n \times 10\text{ns}$ ). The ADC baseline value immediately prior to the pion is known by the MWD algorithm and so it can be subtracted from the calculated pion energy to improve the accuracy.

#### 12.2.6. Carrier Implementation.

The carrier houses the mezzanines which read data from the core and segment cards in the digitiser and a GTS mezzanine which communicates with the clock and trigger system (GTS). The GTS receives the global clock, aligns it locally within the pre-processing and then uses a dedicated data path in the core mezzanine to align the clock in the digitiser too. It is also used to accept or reject local triggers. The core and segment mezzanines receive data from the digitiser and process it as described later.

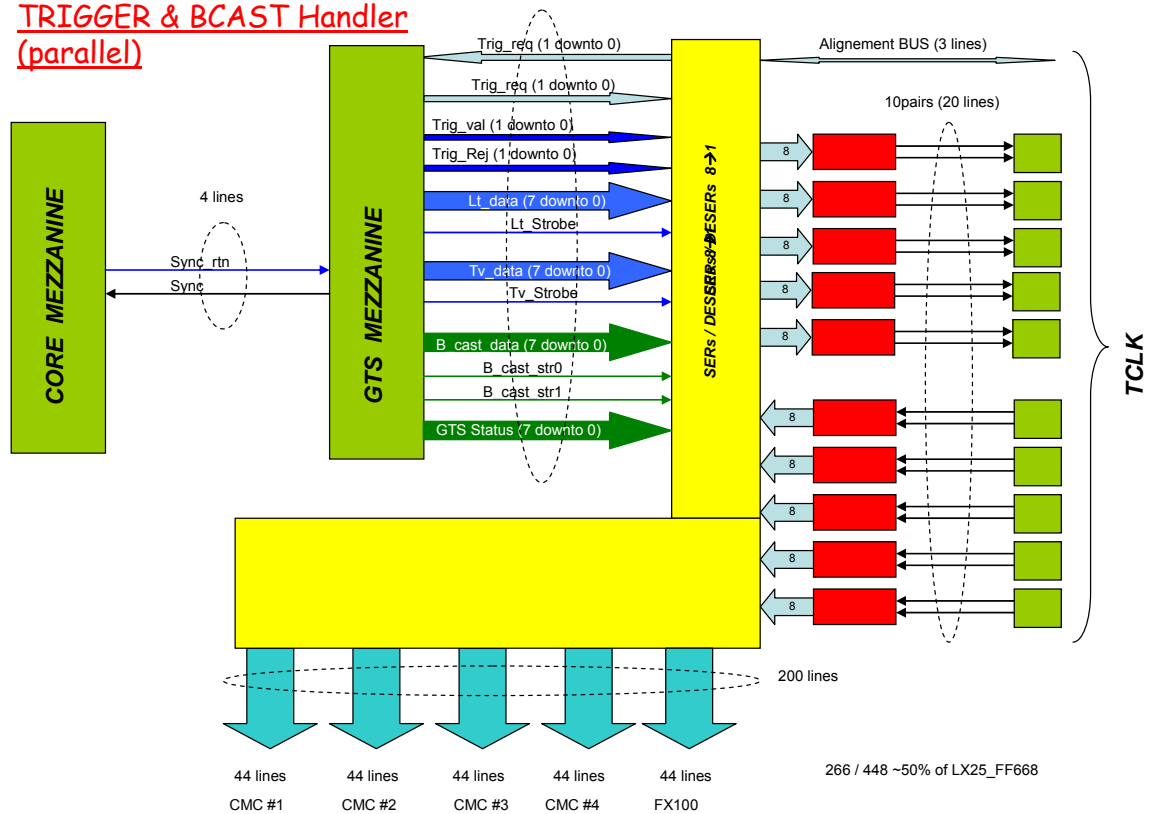
Segments are read out via the carrier, all data being concentrated into a single FPGA per carrier before transmission via PCI express to the PSA farm on demand by the PSA. The carrier reads each mezzanine at 100Mbytes/sec.

## Diagram of Carrier



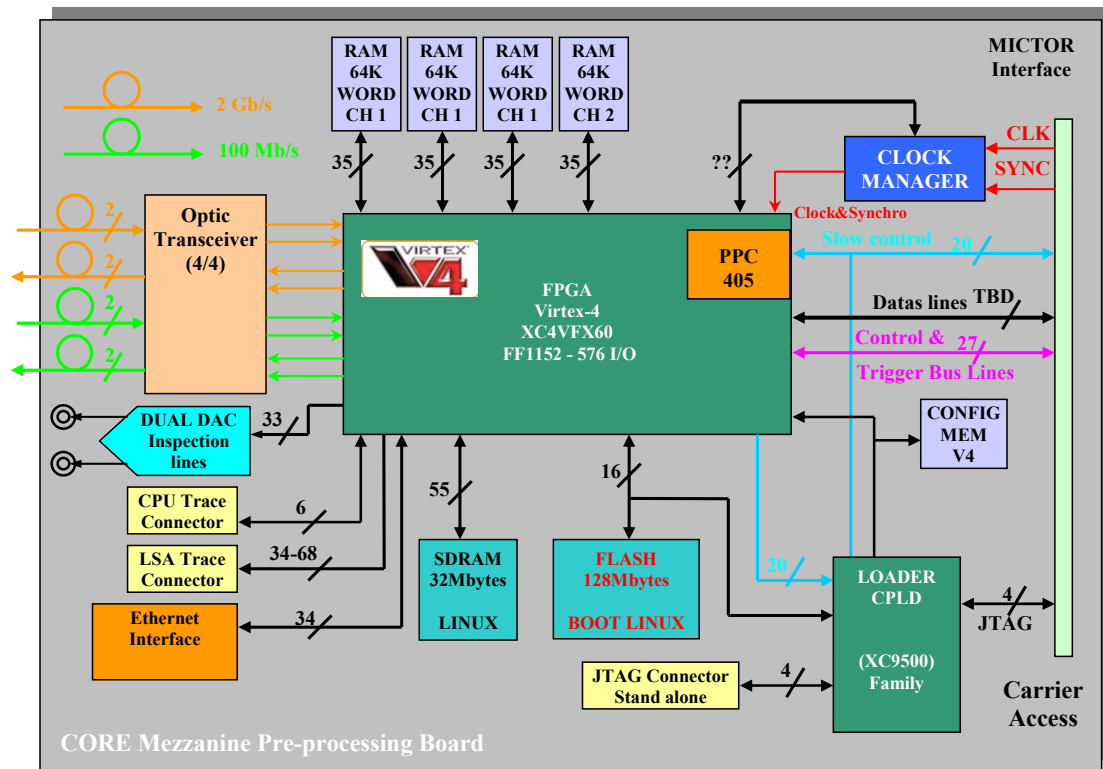
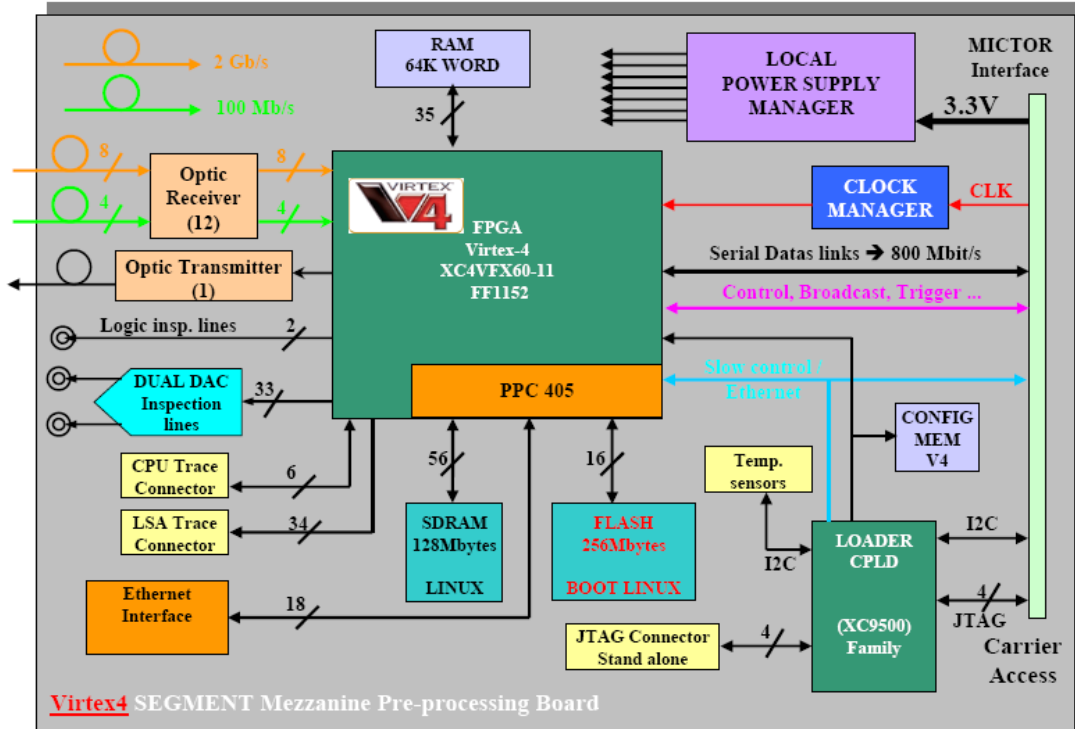
A different FPGA (shown below) handles the trigger interconnections within the carrier. Trigger connections between the 2 carriers handling one crystal use a dedicated TCLK backplane link.

### TRIGGER & BCAST Handler (parallel)



### 12.2.7. Mezzanine Implementation.

The following paragraphs describe the implementation of mezzanines in more detail. There are 3 types of mezzanine- the core, segment and GTS cards. Core and segment are very similar, differing only in detail such as the input fibre receiver footprint and the extra processing for finding triggers in the core. The GTS mezzanine is completely different, interfacing with the GTS system rather than the digitiser.



### 12.2.7.1. Mezzanine Size.

The ATCA carrier cards accept 4 CMC format mezzanines. Connection between CMC and carrier card is achieved by two connectors, each 114 pins (Manufacturer Mictor, distributor: Tyco).

### 12.2.7.2. Core and segment Mezzanines.

#### 12.2.7.2.1. Core and segment Mezzanine card input stage:

The input to the segment mezzanine from the digitiser is via 12 fibre multi-fibres with 6 used for data transmitted from the digitisers. The other 6 inputs are connected at both the digitizer and pre-processing ends, but have not yet been allocated a use. They are reserved for future use. (6 way multi-fibres are not available, so we get these spare lines for free). The fibre data receivers produce one LVDS data stream for each input. The core mezzanine uses almost the same PCB as the segment mezzanine but with a different subset of components mounted, different layout for fibre receivers/transmitters and a different program in the FPGA. The fibre link between core mezzanine and digitiser comprises a quad transceiver (8 fibres) of which 2 receive ADC data, generating LVDS data streams after deserialisation and 6 are used to transmit and receive control signals at 100 Mbits/s from and to the digitizer part, for example the 100MHz clock, a Synchronisation pulse, ADC input offset and the output of the digitiser's CFD algorithm.

#### 12.2.7.2.2. Core and segment Mezzanine card processing:

The LVDS serial data streams are deserialised using Rocket i/o ports in Xilinx Virtex4 FPGAs. Data are clocked into FIFO memories using the recovered clock from the serial link. At the FIFO output the clock can be either the global clock as received from the Global Trigger System (GTS) or that recovered from the incoming data. The FPGAs not only receive but also process the data, using the MWD algorithm to calculate energy on all 38 input signals. The core signals are also examined using a CFD algorithm to look for triggers.

#### 12.2.7.2.3. Mezzanine to carrier interface:

In each of the 114 pin Mictor connectors, 10 pins are used for power supplies and their grounds, leaving 104 pins for signals:

- Data readout path,
- Trigger path ( Timestamp, local trigger...)
- Slow Control (Ethernet)
- GTS clock
- Communication signals between mezzanines(“Message” and “Broadcast”)

Full details of this (and much more) are in the published pre-processing specification (latest version is 10a).

### 12.2.8. Slow control:

On the carrier the Ethernet connection (RJ45) is connected to a media converter and then, using Media Independent Interface (MII), connected to a software switch in the FPGA power pc on the carrier card. From the carrier card, MII links connect the Ethernet to the other mezzanines. In this way the high current external interface for Ethernet is only done once. 4 signal pairs per mezzanine are reserved for Ethernet connected to the power PC (PPC) embedded in one of the on-board Virtex4 chips which will act as master. A direct Ethernet connection is also provided on the mezzanines for standalone testing.

#### 12.2.9. Self Test and diagnostics:

A JTAG port is provided for boundary scan data path testing and also for FPGA programming on both the carrier and the mezzanines. Extensive self test and diagnostics are built in to enhance the system reliability and fault detection/correction performance. Temperature monitoring is provided. On the mezzanines, DACs are connected to the FPGAs to allow visualisation of data as analogue signals to help debugging. The resulting inspection line(s) are available on the front of the mezzanines via Lemo 00 connectors.

The segment and core mezzanine provide external memory that can be used, for example, to store long traces. For the segment card, six 64k-bloc memories are embedded allowing a 3.9ms trace for one channel or 650 $\mu$ s for 6 channels. Concerning the core board, three 64k-bloc memories are available.

#### 12.2.10. Data readout from mezzanine to carrier:

The mezzanines are read through the Xilinx Chipsync architecture using 8 high speed parallel links running in a synchronised way to provide a 400Mbytes/sec data link (8 links running at 100MHz).

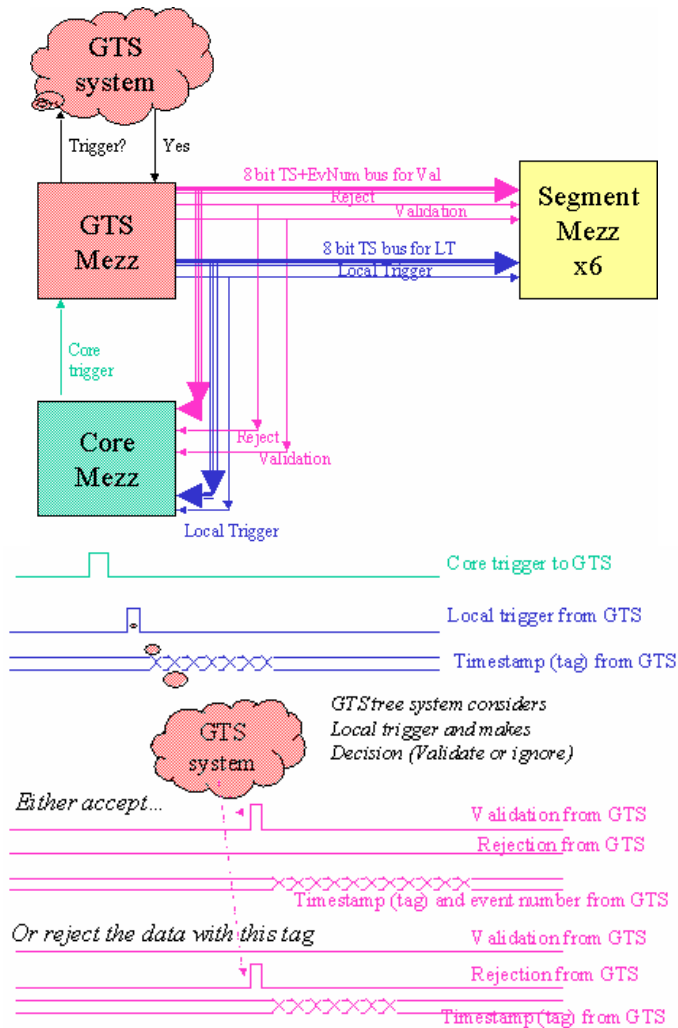
#### 12.2.11. GTS mezzanine:

The GTS mezzanine is described later in the GTS section.

#### 12.2.12. Trigger/Control Sequence:

The mezzanine connected to the core contact handles the triggering and control. When it detects a possible event it generates a local trigger request which is sent to the GTS mezzanine. In response to this request the GTS mezzanine will generate a local trigger and latch a timestamp which are distributed to all the mezzanines (via the local GTS port in the GTS mezzanine). The GTS mezzanine also sends a trigger request to the GTS through the GTS hierarchy and if the trigger condition is met, it receives a trigger validation from the GTS within 20 $\mu$ s. The trigger validation (or rejection) is passed to the carriers and back to the other mezzanines along with a timestamp identifier (matching the timestamp of the original local trigger from GTS). When running in triggerless mode the trigger validation is automatically generated by the core contact mezzanine a fixed delay after the local trigger.

The timestamp will not be continuously broadcast by the GTS mezzanine. Instead it will be used as a data label and sent with the local trigger (and again with the validation or reject signal). Note that the centralised decision mechanism means that explicit rejections are sent for events which are not validated. An event number is required by the software so will be sent with validations as well as the timestamp value. The system is sketched below.



The core and segment mezzanines don't have to keep track of time. They can only measure time indirectly by using the local trigger as a time reference and measuring relative to the local trigger. A consequence of this is that the local trigger must be distributed to all mezzanines with low skew and a fixed relationship to the 100MHz system clock.

The actual value of the timestamp is captured by the GTS with low jitter, but distribution to mezzanines of the timestamp value is not time-critical because the essential time information is carried in the local trigger signal. To avoid contention when events overlap there are 2 different 8 bit buses from GTS to the other mezzanines for the local trigger timestamp and for the validation timestamp.

The time between triggers is limited by the physics of charge collection in the Ge to at least 1µs. So we have time to transmit a timestamp (6 bytes) + event number (4 bytes) within the shortest inter-trigger gap.

### 12.2.13. Status:

The prototypes of all cards have been built and tested. Pre-production cards have been built and tested. At the time of writing (12/08) the full production is just being launched.



## 13. Data acquisition and GTS

### 13.1. Global DAQ architecture

Since the data acquisition is interacting with almost all the AGATA elements, it is at the heart of the array. As illustrated in Fig. 13.1, the DAQ elements shown in grey receive data from the detectors, process them and interact with the electronics.

The AGATA DAQ has basically two functions.

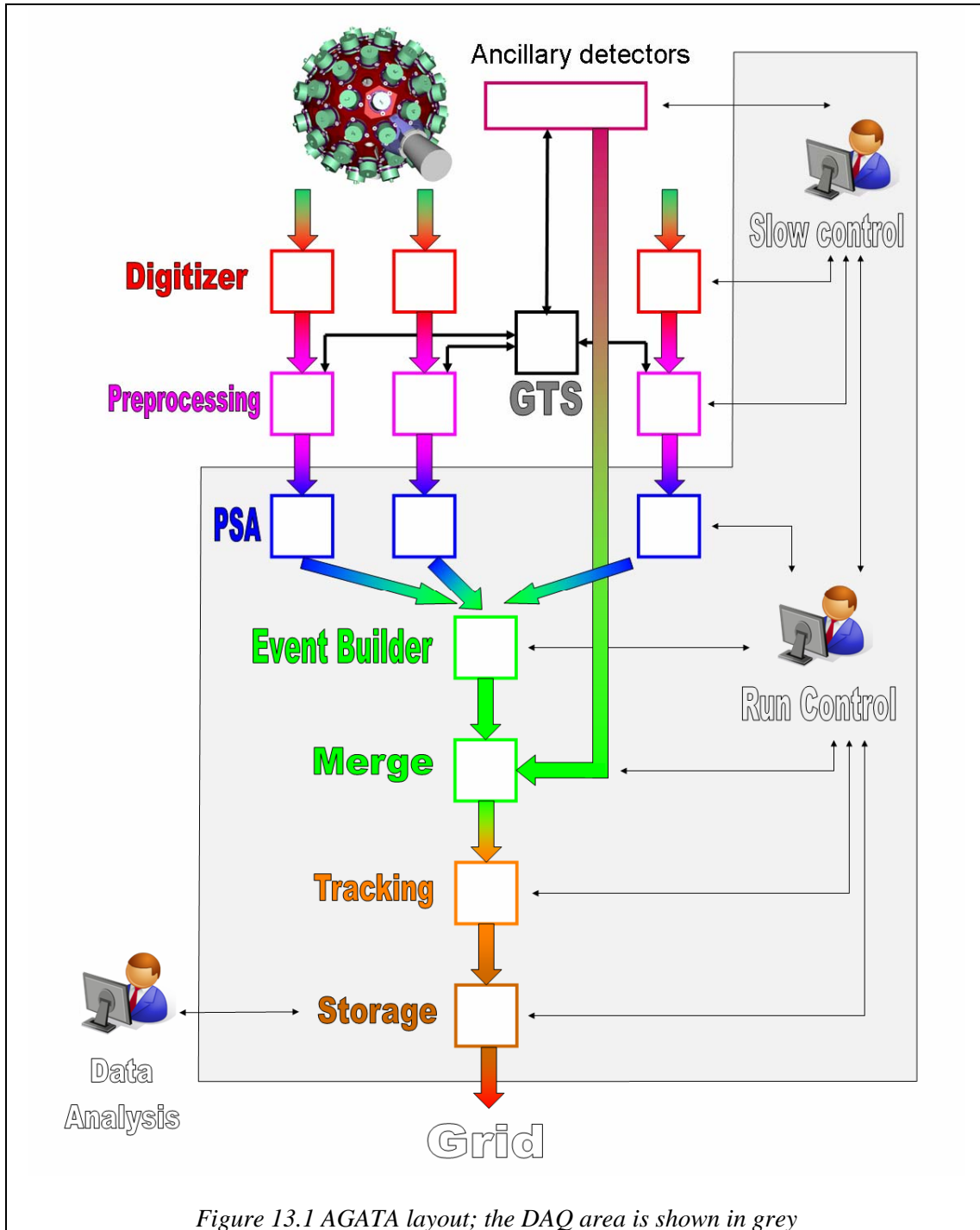
The first one is to transport and process the data flow from the detectors up to the data storage. Data sources are the AGATA detectors after their front-end electronics (see section 12) and ancillary detectors such as the Legnaro Prisma spectrometer. The data flow integrates the algorithms needed to process the hits. At the end of the chain, data have to be provided to the physicists in a understandable and user-friendly way thanks to the AGATA Data Format library. After the Pulse Shape Analysis, data from all crystals are merged together taking into account the physics correlations provided by the pre-processing electronics. Additional detectors coupled to the AGATA array are then assembled to the data flow. A next step consists to run the tracking algorithm who reconstructs the photons trajectories in the array from each interaction provided by PSA algorithms. Finally, data are stored on a large local disk array before being eventually sent to a Grid Tier1 computing centre. It is also possible to sample pieces of the data flow at each step of the process for control, monitoring or analysis purposes.

The second function is to control and monitor the whole system including the detector electronics. The task of the Slow Control is to setup the electronics, control and monitors the electronics: digitizers, carrier cards, segment core and GTS mezzanines. The Run Control centralizes information from different sub-systems of AGATA: electronics, data flow and additional detectors. Basic actions like setup, start acquisition, store data ... are performed through the Run Control. It also collects messages and errors from the sub-systems, provides a logbook to the users ... A Graphical User Interface is provided with the Slow and Run Controls. Spectra and rates provided by the DAQ actors, including those embedded in the electronics could be displayed with this interface.

The system first implemented for the AGATA demonstrator has been designed to be scalable to cope with the full array specifications, easily movable between different host sites and easily maintained by the DAQ working group. The software is deployed on a processing farm based on 1U "pizza boxes" servers. One 1U server is attached to each crystal to meet the demonstrator specification of 1 kHz counting rate per crystal. Other 1U servers are devoted to the event-builder, tracking, run control, disk server... but also data analysis. Networking is obviously an important issue having in mind the large rates foreseen in forthcoming AGATA phases: for the full AGATA array, the DAQ will cope with over 6000 channels each with rates up to 50 kHz. Procedures to install the machines, monitor CPU activities and network have been implemented for an easy and remote administration and management.

In such a large project involving actors from different countries, documentation is of utmost importance. Therefore, special attention has been paid to the documentation with a DAQ web site [web] and wiki documentation server.

Details of all the DAQ components are given in the next paragraphs.



## 13.2. Main Data Flow

### 13.2.1. NARVAL

#### 13.2.1.1. Introduction

NARVAL runs across a network and acts like a unique program taking data out of the electronic up to providing data to physicist (storage, histogramming display, ...). It can be therefore considered as the AGATA DAQ backbone.

NARVAL stands for Nouvelle Acquisition temps Réel Version 1.6 Avec Linux [nar,narw]. It is a highly distributed acquisition system. It is developed in Ada (but actors can load C/C++

shared library) and makes huge use of Ada 95 Annex E (a software bus in Ada 95 language, equivalent to CORBA or Web Services) for inter-processes configuration.

NARVAL is (and was) already used in many experiments near different physic facilities:

- Orsay's Tandem : Multi-detector triggerless acquisition, VXI Comet6X board (TDC + DSP readout); RECIF, CompactPCI based acquisition system; LAG64, 8x8 detector with VME TDC readout
- ISOLDE: PARRNE, with Comet6X boards
- Heidelberg University : LAG64
- GANIL : AZ4PI, RECIF based DAQ, NARVAL slave of GANIL's system
- Los Alamos, GANIL, Orsay's Tandem : CHACO, VME bus with TDC, QDC boards
- Research and Development : FASTER
- AGATA CSNSM scanning table

### 13.2.1.2. NARVAL Architecture

NARVAL can run many acquisitions in parallel. Each acquisition has a unique name in the NARVAL domain. The set of processes (actors) running an acquisition is named a subsystem. In order to control and coordinate an acquisition all information about topology, configuration, state machine, are stored in a process named "subsystem coordinator". All subsystems are registered in a list handled by the "NARVAL Naming Service". This gives us a three layers architecture as shown in Fig. 13.2.

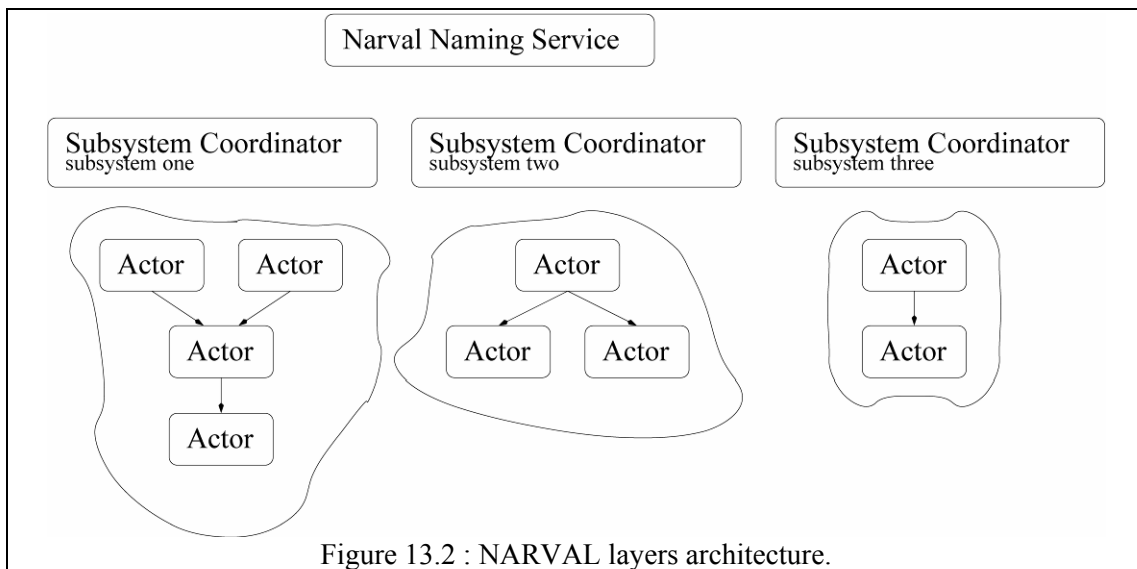


Figure 13.2 : NARVAL layers architecture.

An actor is mainly a process that takes part of handling the acquisition's data flow. There is four kind of actors:

- producer : injects data in a NARVAL subsystem,
- intermediary : acts like a  $N \times M$  switch or filter data,
- consumer : end of line actor, typically used for storage,
- standalone: exception to the rule, this actor don't handle any data but is aware of the subsystem state machine.

Data transfer between actors is handled through TCP/IP or Infiniband.

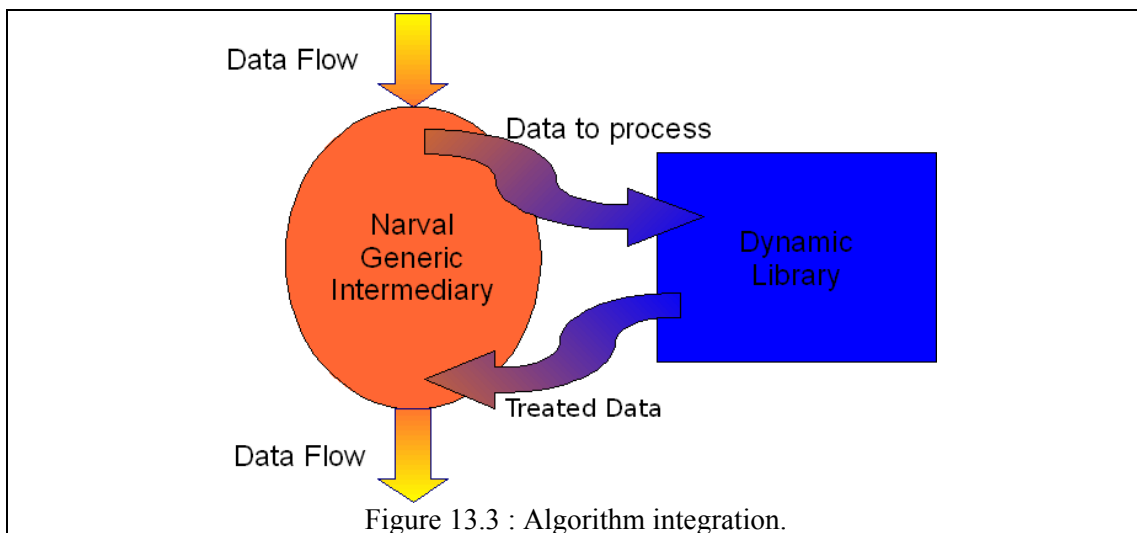
### 13.2.1.3. AGATA implementation

For AGATA, NARVAL will be used to drive the main data flow of the experiment from the front end electronic to the storage according to the layout shown in Fig. 13.1.

### 13.2.2. PSA and Tracking algorithm integration

As has been explained, the design of NARVAL is based on the actors concept. Actors are separate processes that receive from and send data to the data stream. These actors are unaware of the topology of the larger system(s) and therefore they can be developed separately as long as they provide the interface layer used by the NARVAL to load, control, and communicate with actors. This interface is defined in the document "AGATA PSA and Tracking Algorithm Integration" [cre].

For PSA and Pre-processing algorithms C++ based classes have been developed providing a simple mean to connect a working algorithm with the data flow of the AGATA DAQ: see Fig. 13.3. The base classes have also been used to integrate PSA into the NARVAL DAQ. A tracking algorithm has also been integrated. To further facilitate this separation between data transport and algorithm development, i.e. algorithms for PSA or tracking, the ADF framework (AGATA Data Format) has been provided: see next paragraph.



### 13.2.3. AGATA Data Format

In order to allow the development of algorithms (PSA, tracking), NARVAL provides facilities to load C/C++ code in Actors. It is the charge of any actors to scan the data flow and to extract the part it should process.

To simplify the access to the dataflow [flo], a library ADF (for AGATA Data Flow), written in C++, has been developed [adf]. It has been designed to be used in different frameworks, NARVAL being the one for online processing. As a consequence, it is a standalone library without any dependencies. The ADF library provides a virtual interface (see Fig. 13.4) to NARVAL that permits to develop / debug / test / optimize, outside NARVAL, algorithms suitable for online processing.

The main component is a Frame object which encapsulates the data delivered to or produced by an algorithm. A Frame is composed of two parts: a Key contains global information concerning the Frame (length, messages concerning the content of the Frame, event number or timestamp) and the data part specific to an algorithm. A Frame could be itself composed of other Frames (CompositeFrame) in case it is required i.e. to build an event that groups all the Frame having the same event number (or timestamp).

To ensure the portability in different frameworks, a weak coupling between the data and algorithm is proposed. Thus, an algorithm registered to a FrameIO manager through a Trigger that contains a description of the Frame(s) needed by the process. The FrameIO manager notifies the algorithm once the condition is fulfilled on the data flow and returns the interesting frame(s). Once the processing of the input data is over, the output data are packed in a Frame and recorded. Because algorithms are likely to change during AGATA's lifetime, Key and Frame have version numbers. The consistency of the whole system is ensured by factories (singleton in object-oriented approach) in charge of allocating Key and Frame. Configuration Frames are also defined and read / written from / to the data flow. The FrameIO manager is aware of such specific frames which contains the modification of the data flow structure: it has then the charge to take all the required actions so that the algorithm can keep on processing without interruptions or crashes.

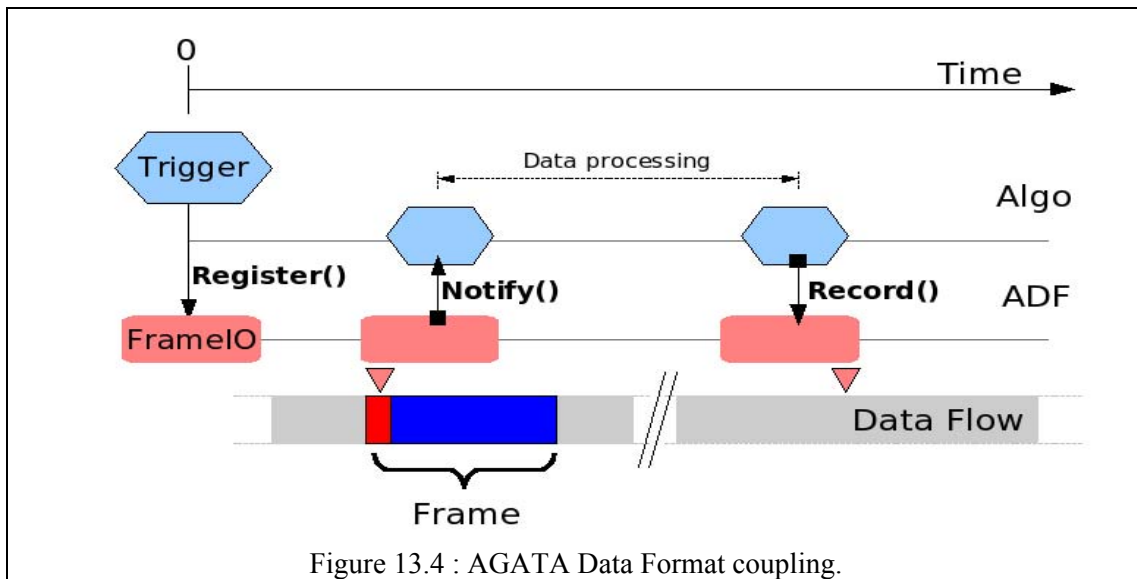


Figure 13.4 : AGATA Data Format coupling.

The whole code is under subversion (a version control system) and comes with an html documentation automatically generated from the sources using Doxygen. Simple examples are provided in the package to illustrate how to develop an algorithm suitable for AGATA processing.

#### 13.2.4. Event-Builder and Merge algorithms

The task of the event builder is to assemble hits from the different crystals into correlated events. The merger correlates AGATA event with those from the various ancillary detectors. Various scenarios have been defined by the ancillary detector working group and are described in [anc1]. Both algorithms can be based on event number or time-stamp correlations, depending on which AGATA trigger mode is used.

In a first phase, only event-number correlations will be implemented. Algorithms based on time stamp will be implemented in a second phase for trigger-less experiments.

The ADF library provides an interface to ease Event Building from a NARVAL point of view:

- access to event size
- access to event number
- access to time stamp

#### **13.2.4.1. Event Builder**

The actor implementing the Event Builder will have as many inputs as there is PSA output (i.e. the number of crystals). The main loop will have a local event number and will scan these inputs to find incoming data with the same number. If the event number is equal to the local event number, the sub event is selected, if it is greater, the input is not selected, if it is smaller an error is triggered and the sub event is discarded. All the selected pieces are then merged in an AGATA event.

#### **13.2.4.2. Merger**

The number of input for the Merger actor is two: one data flow is coming from the AGATA Event Builder the other one is coming from an ancillary detector. A similar algorithm as the Event Builder one will be used. Various ancillary detector data format may be merged. Therefore, a high-level interface library equivalent to the ADF one has been proposed to get basic knowledge of ancillary detectors hits (such as event number, time ...) [anc1].

#### **13.2.4.3. Trigger-less building and merging**

While running such experiments, building should be done using a moving time window. One has indeed to select data from each input with some local buffers in order to avoid side effect each time there is a new input buffer. The depth of the local buffer will be based on timestamp, which means that the algorithm should “memorise” enough sub events to fill the time window used for building coincidence.

#### **13.2.5. Spy/Watcher interface**

In order to survey the data acquisition system, NARVAL provides a spy mechanism. Every NARVAL actor (producer or intermediary) embed a system that enables it to distribute data on a NARVAL buffer basis. The spy is available to any client connected to the DAQ services network. In particular, physicists will be able to spy the data flow from their laptop.

In order to ease development of this server and enabling multi client without creating tasks (that will slow down the main data flow) a new TCP connection is opened for each client and closed after the data buffer is sent according to server and client sequences.

#### **13.2.6. Ancillary detectors readout interface and integration (PRISMA)**

For every ancillary detector, the integration with the “main AGATA DAQ” is accomplished by a chain of two or more NARVAL actors, starting with a producer acquiring data from the ancillary detector's readout system and ending with a filter actor called “merger” that will merge these data stream with the AGATA one.

The producer needed to get the ancillary detector's data stream inside the NARVAL DAQ system is basically a NARVAL actor containing a TCP/IP server. In the ancillary detector's readout system a client able to send data to the producer's TCP/IP server is needed.

The application layer protocol between the client and the server is very simple: the client once connected to the server, will send one (4 bytes) integer containing the number of bytes ready to be sent, the server will get it and then will acquire the exact number of bytes declared by the client. The process will be repeated (within the same connection) as many time as the client is ready to send one of its buffers. As long as the server go on to receive data, it will store it inside its NARVAL buffer, filling it and then freeing it sending its content to the next actor connected in the chain.

In the chain there could be as many filter actors as needed by the ancillary detector, their main purpose is to pre-process data to obtain the events in the right format (using ADF) to be merged with the AGATA ones.

The merger will eventually encapsulate one or more events, coming from the ancillary detectors' chains, in the corresponding AGATA event frame, according to the event number or to the timestamp.

An ADF format for the frame of every ancillary detector event has to be assigned in order to have one merger that could easily manage all the frames coming from every ancillary detector.

In the Fig. 13.5 is depicted a sketch of the chain for the PRISMA detector.

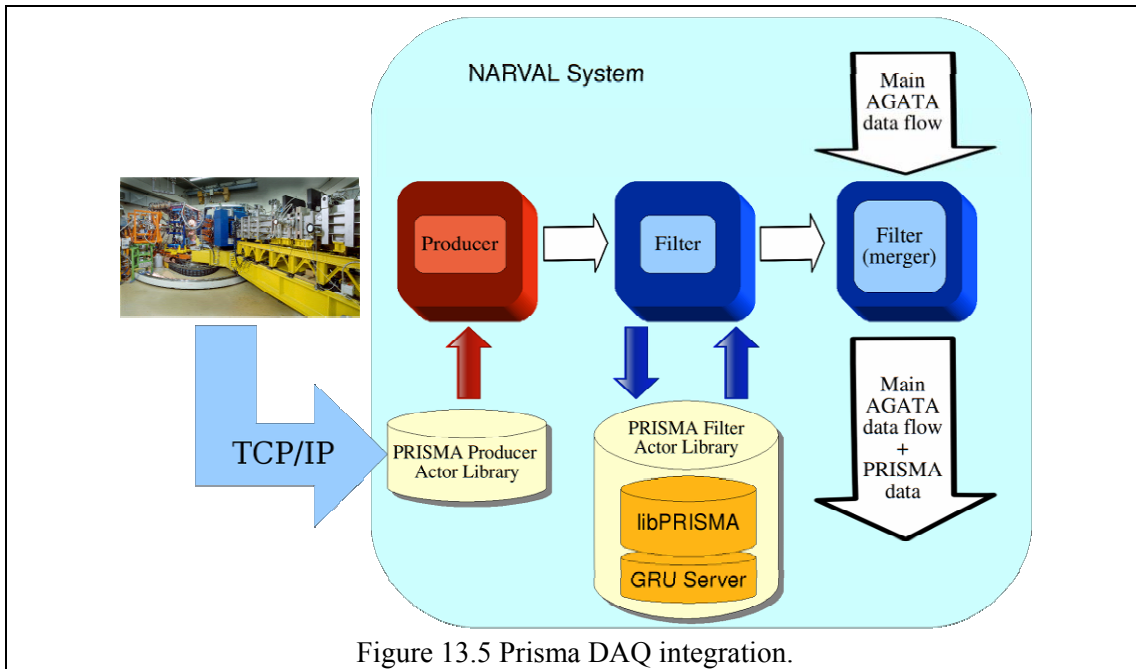


Figure 13.5 Prisma DAQ integration.

### 13.3. Services

#### 13.3.1. Run Control

The Run Control has the main purpose to control and monitor the DAQ components. It coordinates the several activities necessary to put the AGATA detector and its data acquisition system into operational state. Actions like initialization, setup of the several components, start and stop of the data acquisition, are performed by the operator through the Run Control system.

The Run Control interacts with the Slow Control system, which is in charge to control the hardware devices, in order to assure the correct configuration and setup of all the electronic devices, before a data taking is started.

The Run Control also provides the monitoring of the data acquisition (input rate, buffer occupancy, error rate, event dump, etc.), error report and handling functionalities, and logging capabilities.

The main tasks are outlined here:

- Access to the AGATA data acquisition system (login)
- Configure the DAQ
- Select the partition to run (i.e. a GTS partition, enable/disable ancillary detectors, etc.)
- Run multiple partitions (e.g. calibration mode)
- Synchronize other sub-system (e.g. slow control, trigger, ancillary, etc.) to be configured
- Control the overall system (e.g. start, stop, etc.)
- Handle all the information (e.g. generic log) and error/state messages

- Show (e.g. alarms)
- Archive (history)
- Handle the error in some automatic way to help to fix malfunctioning
- Monitor the DAQ (e.g. data rate, error rate, etc)
- Provide access to the GUIs
- Provide tools to help the cooperation for people in shift (e.g. logbook, etc.)

The run control we intend to use is based on the middleware produced by GridCC, an European funded project [gridcc]. The project aims to the control and to the monitor of remote complex instrumentation, including physics experiments. It is built around the concept of Instrument Element (IE), a set of coherent services used to configure, control and monitor remote instrumentation. In the case of a physics experiment, the instrumentation is basically the data acquisition system and the front-end electronics.

The GRIDCC middleware has been adopted by the LHC CMS experiment at CERN. The Run Control and Monitoring System of CMS (RCMS) is in advanced production. It has been used for all the important data acquisition tests with cosmic rays and was operating when the first LHC beam circulating on 10<sup>th</sup> of September 2008 [rcms].

### 13.3.1.1. Run Control layout

The run control for AGATA is designed according to the above specifications. Fig. 13.6 shows a top-level layout of the control system.

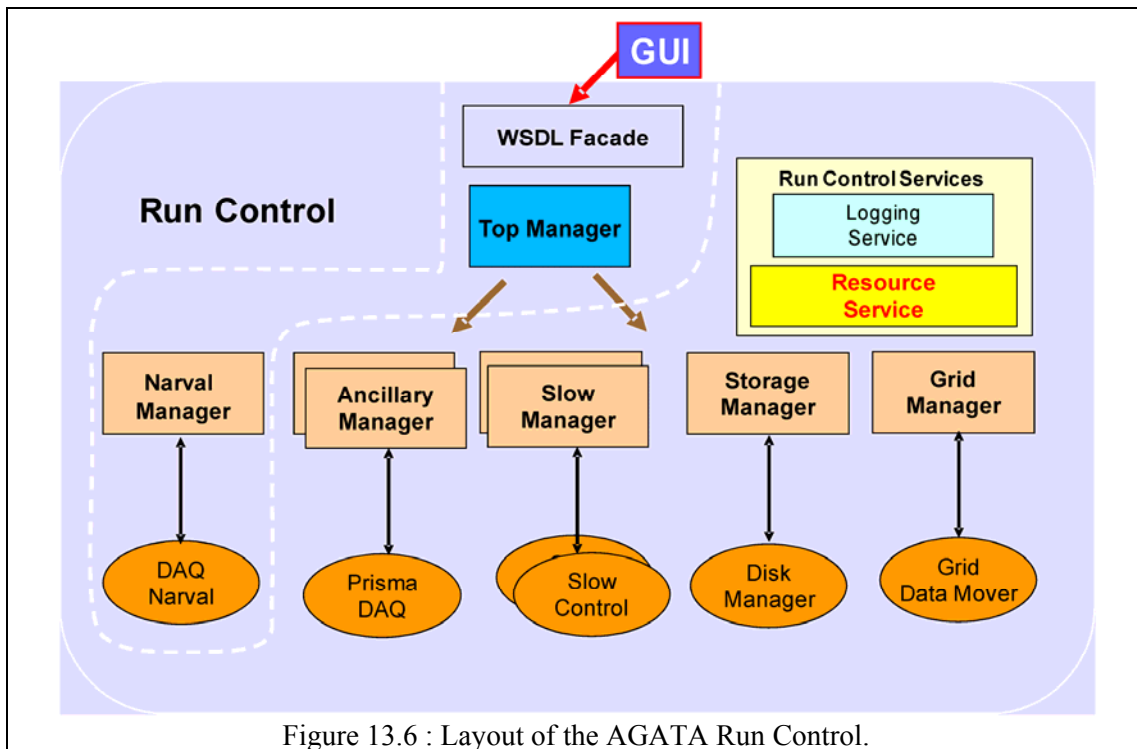


Figure 13.6 : Layout of the AGATA Run Control.

The Run Control provides the services to configure the system (Resource Service), to monitor the DAQ behaviour, and to log information and error messages (Logging Collector). The interaction with the several components of the system is performed through the Instrument Managers (IMs).

The Instrument Manager framework provided by the GridCC project is a Java based controller with a clear and well-defined interface to customize its behaviour. Control actions are performed on an event-driven basis. Events are generated by the operator (control commands) or by the controlled components (error or information messages coming from NARVAL actors, etc.). Events trigger custom procedures defined in the specific IM, for

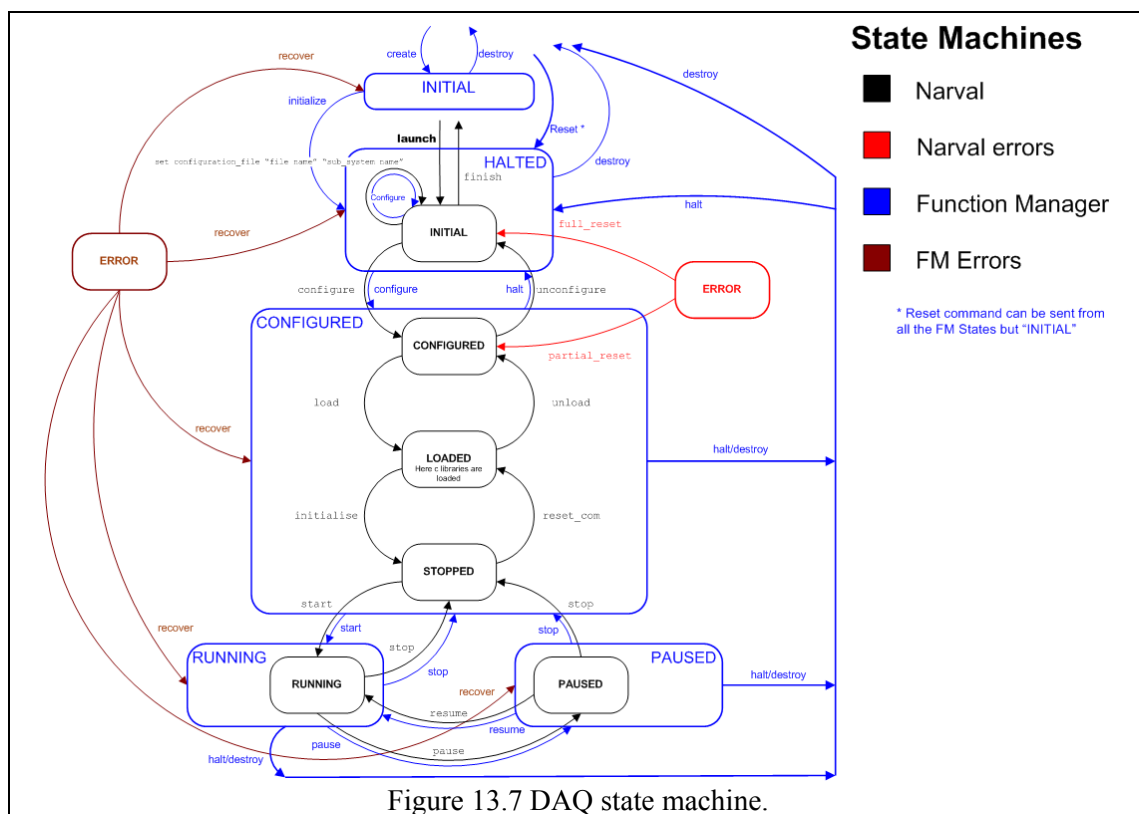
control, error handling and problem solving capabilities. A customizable Finite State Machine engine is used to define the basic behaviour of the Instrument Manager.

For AGATA a two level hierarchy of Instrument Managers has been chosen (see Fig. 13.6). The complexity of the detector and of the DAQ has been divided in a number of “sub-systems”, each one having its own Instrument Manager. A Top Instrument Manager then orchestrates the whole system. The GUI interacts with this Top IM thanks to a well-defined WSDL (Web Service Description Language) interface.

The sub-systems identified so far, each one having its own Instrument Manager, are the following:

- NARVAL (DAQ)
- Ancillary Detectors
- each ancillary is a separate sub-system
- Slow Control
- one per kind of slow controlled sub-system
- Storage
- Grid

In order to easily integrate the control and monitor of the several subsystems the same Finite State Machine (see Fig. 13.7) will be used in all the Instrument Managers.



Moreover, each subsystem must provide the proper channels for managing Control, Information, Error and Monitoring data flows. Each subsystem must then specify the way to configure itself.

### 13.3.1.2. Configuration

The Run Control system provides the Resource Service (RS) to configure the resources under its control. RS is basically a DataBase (DB) where different configurations of the system

(Instrument Managers, their URLs and topology, resources linked to a given IM and related URLs, etc.) are stored. In this DB there is also place to store the configuration of the controlled resources (for instance the topology of the NARVAL sub-system).

The configurations can be partitioned in a number of smaller configurations. The assembly of these smaller configurations (usually one per subsystem) generates the overall configuration of the system for a given data taking. The overall global configuration is identified by a simple name (like “Physics”, “Calibration”, etc.) that should not generate any confusion in the DAQ operator. Only a limited small number of global configurations will be available to the DAQ operator.

Some high level configuration, like enabling or disabling ancillary detectors, will be available to the main Graphical User Interface (see section 13.3.2).

### **13.3.1.3. Control flow**

The control flow of the experiment is originated by the GUI and in particular by its graphical control panel. GUI interacts with the TOP IM that, in turn, is directly interfaced to the subsystem IMs. Each subsystem IM then interacts with the resources belonging to the specific subsystem dispatching the control commands.

### **13.3.1.4. Log data collection**

The Apache log4j standard has been chosen to collect log information and a Log Collector service is provided. The Log Collector can receive log4j messages formatted both using a Java binary serialization or the XML standard.

The service can route the messages to different channels, even concurrently:

- TCP/IP sockets
- DB (both Oracle and MySQL)
- JMS (Java Message System), a publish/subscribe messaging system used to distribute the information
- A local file system with the log objects written in XML

The logs can be then viewed directly on the TCP/IP sockets using a chainsaw viewer [cha] and/or browsing the DB with the GridCC DBViewer that provides access to the log DB both on-line and off-line.

In the case of AGATA the final topology of the log collection will be decided according to the log collection rate. In case of low rate a single Log Collector will be used and all the sub-systems will write their log into this collector. If the rate will be high we will deploy a Log Collector for each sub-system, providing then a Top Log Collector. The topology will then follow the IM one. In both possibilities persistency (DB) and log viewers are provided

While the Log Collector is in charge of collecting several kind of information, its purpose is limited to the monitoring of the system. Log4j messages are not meant to change the behaviour of the system; in other words they do not trigger any action on the main control components, the Instrument Managers.

### **13.3.1.5. Errors, Status and Monitor data handling**

Information that needs to be processed online by the run control (the Instrument Managers) will follow specific data channels.

Errors generated by subsystems in asynchronous way will be propagated from subsystems to the Top Instrument Manager using a well-defined XML data format. A dedicated component, named Error Handler, inside the subsystem Instrument Manager will implement error recovery procedures.

A similar mechanism is in place for status information. Other information, like monitor parameters can also be retrieved in a synchronous way by the Instrument Manager by querying the subsystem components (pull mode). The processing of the retrieved information can trigger automatic actions in the Instrument Manager.

Moreover, the GUI will allow to:

- View the monitor parameters for a given DAQ component (for instance a NARVAL actor).
- Select the parameters one wants to retrieve and select the way the parameters will be updated (e.g. one shot, fixed interval time, etc.) .
- View the monitored parameters.

#### **13.3.1.6. NARVAL (DAQ) Run Control**

The NARVAL subsystem provides a web service WSDL interface (`aws_shell`), with all the meanings needed to implement the NARVAL Instrument Manager procedures. These include the sending of configuration and control commands, and the retrieval of monitoring parameters.

NARVAL Instrument Manager acts as a client of such a web service. Through the WSDL NARVAL actors can provide the list of monitoring parameters. The GUI allows to select the interesting parameters, visualize and eventually update them.

NARVAL is also capable of sending log4j messages to the Run Control logging collector, and asynchronous error messages to the Instrument Manager, for error handling purposes.

#### **13.3.1.7. Run Control – Slow Control interface**

A standard WSDL interface for all the slow control components has been defined (see paragraph 13.3.4). The Run Control acts as a web service client of such a WSDL. A Slow Instrument Manager for each component will be implemented, coordinated by the Top Instrument Manager.

#### **13.3.1.8. Ancillary detectors Run Control**

AGATA will be coupled to several other detectors. The integration at the Run Control level of the ancillary detectors is provided by the depicted run control structure, where an Instrument Manager is dedicated to each detector.

As previously explained, in order to be controlled, each subsystem must provide the necessary hooks for control and monitoring.

The first ancillary detector that will be coupled with the AGATA detector is the Legnaro's Prisma spectrometer. The Prisma DAQ is developed using the XDAQ [xdaq] framework. XDAQ provides a well-defined SOAP (Simple Object Access Protocol) interface for control and monitoring purposes, and the GridCC middleware already provides the code to interface to XDAQ applications. XDAQ also adopts the log4j standard and the error format previously mentioned to notify the IM.

For other ancillary detectors that will not use XDAQ the custom control code must be developed and integrated in the specific Instrument Manager.

#### **13.3.1.9. Electronic Log Book**

Between the several collaborative tools that can help the running of a complex detector, the electronic logbook is probably the most important one. It allows people to put information online in a chronological fashion in the form of short text messages.

For AGATA we have decided to use Elog [elog], a product widely used in the high-energy physics community (e.g: CMS and Atlas LHC experiments).

Developed at PSI (Paul Scherrer Institute - Switzerland) it presents several nice features:

- easy installation and maintenance,
- simple and flexible configuration,
- entries are separated in several groups (like Shift, Run Control, NARVAL, etc.),
- simple web interface,
- no DB backend needed,
- good support for pictures and HTML entries,
- email notification support.

In the present deployment, a self-registration mechanism is used. Registered users can submit messages, while all the other users (guests) can read the posted messages.

### 13.3.2. Graphical User Interface of the AGATA DAQ

#### 13.3.2.1. GUI as a stand-alone program

It is obvious that a data acquisition system should have the Graphic User Interface (GUI) – which allows performing commands such as loading the configuration, starting and stopping the system, etc. All the possible states of the DAQ state machine (mentioned in section 13.3.1.1) are reflected in the GUI by set of buttons allowing to perform particular actions. Some of them are enabled, some other disabled – depending on the current situation. This is obvious for everybody, who ever used any DAQ.

However in case of AGATA, there are some new features. The GUI is not a part of the NARVAL DAQ program. It is an independent program which communicates with NARVAL through the web services. It can be even run on any laptop connected to the computer network.

To give commands to the DAQ, the GUI should communicate with the part of the DAQ called a Subsystem Coordinator of NARVAL. However, we realized that it would be more efficient to have one step more: kind of “spokesmen” called the top instrument manager (mentioned in section 13.3.1.3): see Fig. 13.8.

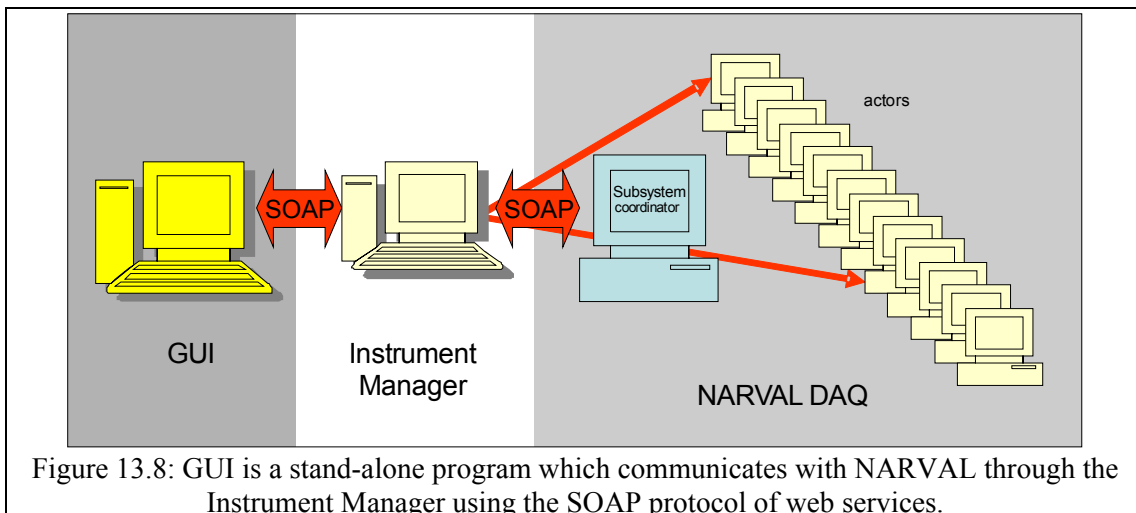


Figure 13.8: GUI is a stand-alone program which communicates with NARVAL through the Instrument Manager using the SOAP protocol of web services.

#### 13.3.2.2. Diagram of the data flow

Except commanding the DAQ to start or stop, we should be able to monitor its work. However, we should remember that NARVAL DAQ is not just one program, like it used to be in old days. NARVAL DAQ is more like a big society of processes (“actors”) running parallel

on many processors (computers). The configuration and relations in this society can be different, depending on the currently loaded “configuration” description.

It seems to be essential that GUI shows the current topography of the NARVAL actors. To be able to show this, the GUI communicates with the DAQ and asks some questions about the relations between actors. As the result, the GUI displays the graph showing all the actors and the connections between them: see Fig. 13.9 as an example. If the system is currently “running”, it also displays the data flow, marking the connections between actors with the lines of particular width and colour. By this we can quickly notice if some of the connections are “dead” or work worse than they should.

It is obviously important that this graph is made “on the fly”, so it reflects the real, current topology.

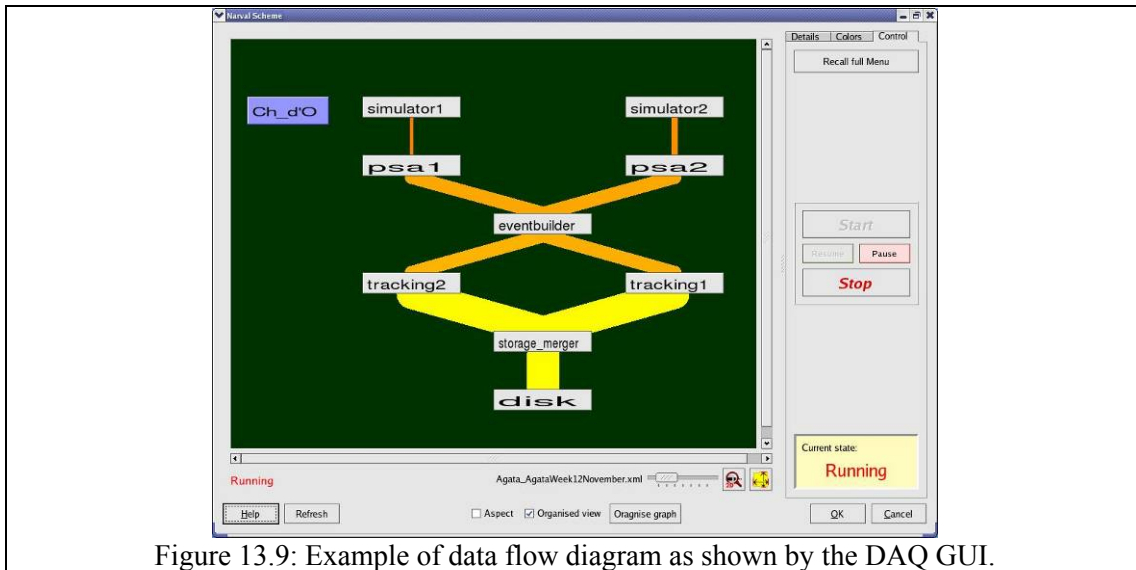


Figure 13.9: Example of data flow diagram as shown by the DAQ GUI.

### 13.3.2.3. GUI spectrum viewer

The GUI of AGATA can monitor the data flow in the whole distributed system. However, very soon we can expect a need for looking at the quality of the data.

The quality of data can be judged by observing the spectra. As mentioned earlier, each actor can load the dynamic library containing an algorithm in C++. Simply speaking: each of actors can load and run a small “user’s” program. With this program one can make some operations on the incoming data, but can also create (and accumulate) a set of spectra. These spectra can help us to see how good or bad is our incoming data, or how good are parameters of our algorithm.

Spectra are collected inside of an actor, and obviously, it would be good to have a chance to watch them from time to time. The GUI will allow this.

At first, the GUI gathers the information about all possible spectra currently accumulated in all the actors of NARVAL. The GUI presents it as the long list of spectra names.

Note that in NARVAL we can have many actors of the same kind, so their spectra will have the same name. This is why all of them will have as a prefix the name of the actor which is the owner of the particular spectrum (for example `name_of_actor :: name_of_spectrum`).

The GUI will help the user to watch some of these spectra on the screen. To make this possible the GUI will connect to the desired actors (more precisely, their so-called GRU spectra server described in 13.3.3). Using fast semi-TCP/IP protocol they will be imported to the GUI and instantly shown on the screen. As long, as the user is watching them, they will be updated every certain time (for example every 3 seconds), so on the GUI screen they will “grow”.

This feature of the GUI has already been implemented successfully. Fig. 13.10 shows the spectra created by one of the actors during the test of the Pulse Shape Analysis algorithm.

We can notice the shape of the crystal, which is being tested. As mentioned, these spectra are “alive” so the user can watch them growing during the time of the test.

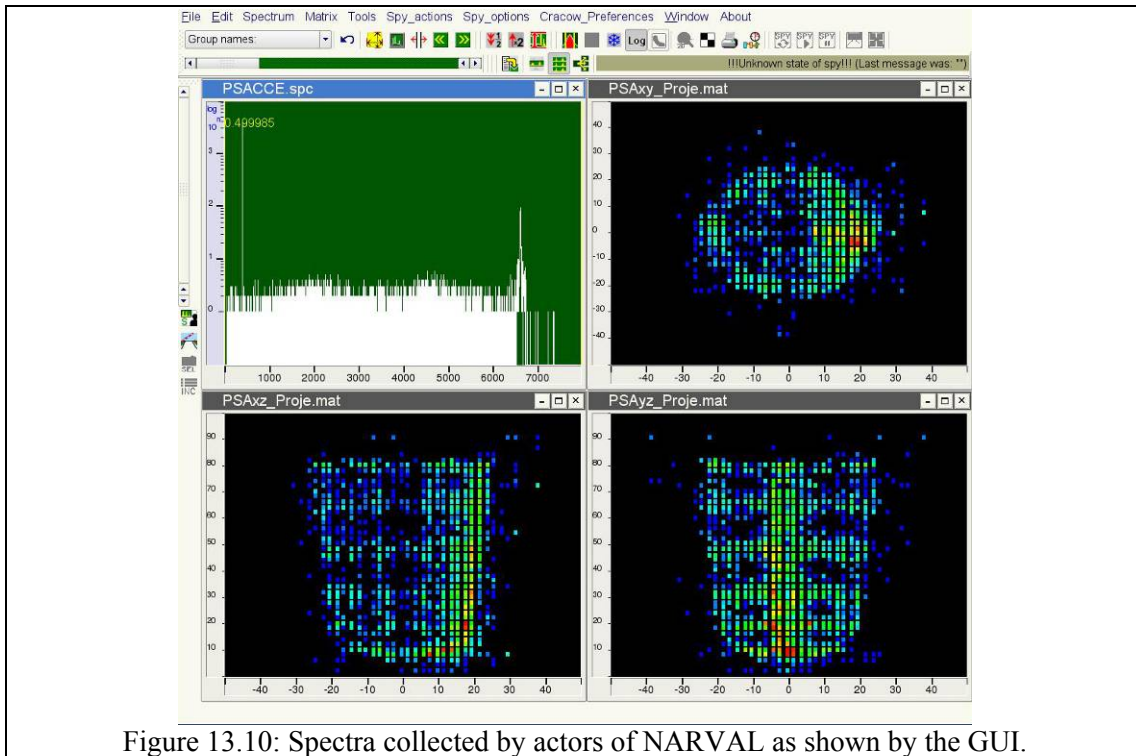


Figure 13.10: Spectra collected by actors of NARVAL as shown by the GUI.

### 13.3.3. Spectrum server

The different algorithms implemented in the DAQ will provide spectra or matrices. As an example, crystal core or segment spectra can be incremented in the PSA algorithms. Codes embedded in the front-end electronics may also increment spectra for monitoring or tests. In order to collect histogram from the various AGATA sources, the GRU spectrum server developed at GANIL, Caen has been implemented.

GRU (Ganil Root Utilities) is software to analyse Ganil data. GRU possesses a TCP/IP network histograms server and its associated client’s classes that can be used for other applications (ex: NARVAL actors). An application which wants to use the histograms server just has to be linked with ROOT libraries [root,rootw] and the GRU library.

In practice, a histogram Database is defined to manage and sort histograms. Then, the server is defined with the database as parameter. When a root histogram is added in the database, it is immediately available on the network. Histograms can be sorted in families or sub families that can be considered as folders.

Several options are available to get a histogram. The first one is to use Vigru, a graphical software to visualize a large number of histograms produced by several remote servers running on several computers. The second one, implemented in the GUI described in section 13.3.2, consist to create a client using the GRU library.

Detail of the GRU package are available in reference [leg].

### 13.3.4. Slow control

The Slow Control is the software system which enables to setup all the electronics (digitizers, pre-processing, GTS and ancillary electronics) and to monitor some key parameters of this hardware (e.g. temperatures). The main functionalities the Slow Control system has to provide are:

- define which electronic boards are present in the system,

- initialize the different boards with the correct values (write registers, execute initialization procedures ...),
- save (onto disk) all the setup parameters of the whole electronics or a part of the electronics,
- restore a previously saved setup,
- monitor some key parameters of the different boards (temperatures ...),
- handle error/alarm events and pass them to the Run Control,
- accept some simple commands from the Run Control (setup, go, stop, get state ...).

The different pieces of electronics the AGATA Slow Control system has to take into account are:

- digitizers,
- GTS Trigger Processor,
- ATCA carrier boards,
- GTS mezzanines,
- Core and Segment mezzanines.

The Slow Control system is designed with a client/server approach and a partitioning according to each type of hardware. As a matter of fact there is one slow control subsystem for each type of hardware, i.e. one slow control subsystem for digitizers, one for carrier boards, one for core/segment mezzanines, one for GTS and one for ancillary electronics (depending on ancillaries ...).

It has been decided that each piece of hardware should embed as much intelligence as possible and should be accessed by a network interface. Boards equipped with a Xilinx Virtex FPGA containing a PowerPC core embed a command server running under an operating system offering network services (UDP/IP, TCP/IP, HTTP, Web Services like SOAP). Digitizers can only be accessed via Xport/Ethernet by the Digitizer Slow Control Gateway, but ATCA carrier boards and core/segment mezzanines possess a Virtex with PowerPC and are therefore able to support much more advanced network protocols.

Details of the digitizer, segment and core mezzanines slow control are given in sections 13.3.4.1 and 13.3.4.2, respectively.

The carrier, GTS mezzanines and trigger processor slow control are under development and needs to be coupled with a higher-level interface.

The Save/Restore system is based on a text file implementation with self-describing path names, inside a SOAP server providing a simple set of SOAP messages to save or restore parameters [puc1].

#### **13.3.4.1. Digitizer slow control**

The AGATA digitizer Slow Control is a component of the global slow control for AGATA. It therefore implements the AGATA Slow Control SOAP procedures in addition to providing access to enable configuration and diagnostics to be carried out by system administrators and systems engineers.

The AGATA digitizer hardware has an embedded Ethernet interface which permits connection to an Ethernet segment. However, the commercial interface device used (Lantronix Xport) has limited firmware which permits only a single network connection (TCP) stream. Additionally the FPGA which controls the Ethernet interface also has limited resources available. It is hence not possible to implement the AGATA Slow Control protocols within the digitizer modules themselves.

For this reason, a Linux based workstation acts as a gateway between the rest of the AGATA system and the Digitizer modules. The AGATA digitizer Slow Control software runs within this workstation and communicates over a private Ethernet segment using private protocols with the firmware running in the digitizer hardware. No direct access is possible to the digitizer hardware. Fig. 13.11 presents the digitizer slow control layout.

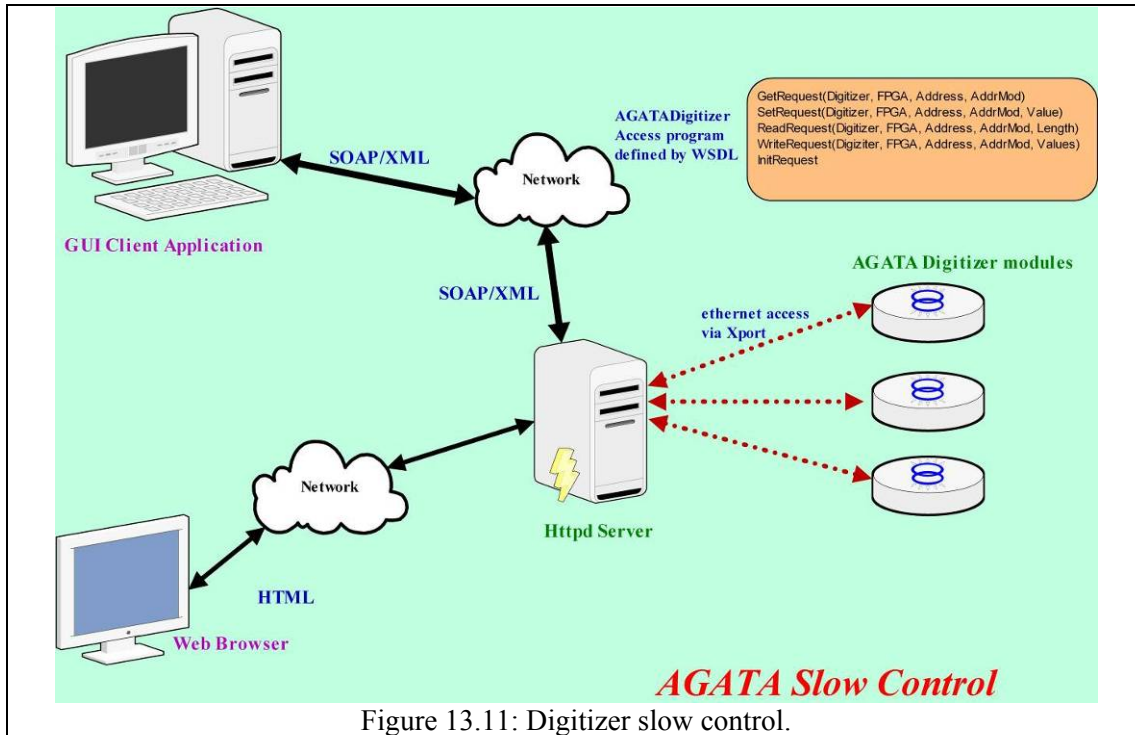


Figure 13.11: Digitizer slow control.

### Operation

In normal production use, the Digitizer Control will be done via the global AGATA control system. There are relatively few settings within the digitizer which need to be adjusted on a per experiment basis. Once the digitizer modules have been configured a single command via the AGATA Slow Control can be used to setup all digitizers and they are then ready to acquire data.

### Graphical User Interface

The AGATA digitizer Slow Control includes a Web interface which can be accessed from any standard Web Browser which has JavaScript enabled. No further software needs to be installed in the client system.

The GUI provides the following features:

- Setup of one or all digitizer modules (see Fig. 13.12).
- Setup of the software offsets
- Control of the core module preamplifier pulser
- Diagnostic access to the registers controlling data flow between the digitizer module and the front end readout electronics
- Monitoring of the temperature sensors within the digitizer modules
- Low level diagnostic access to the internal registers of the digitizer modules
- Configuration of the gateway software

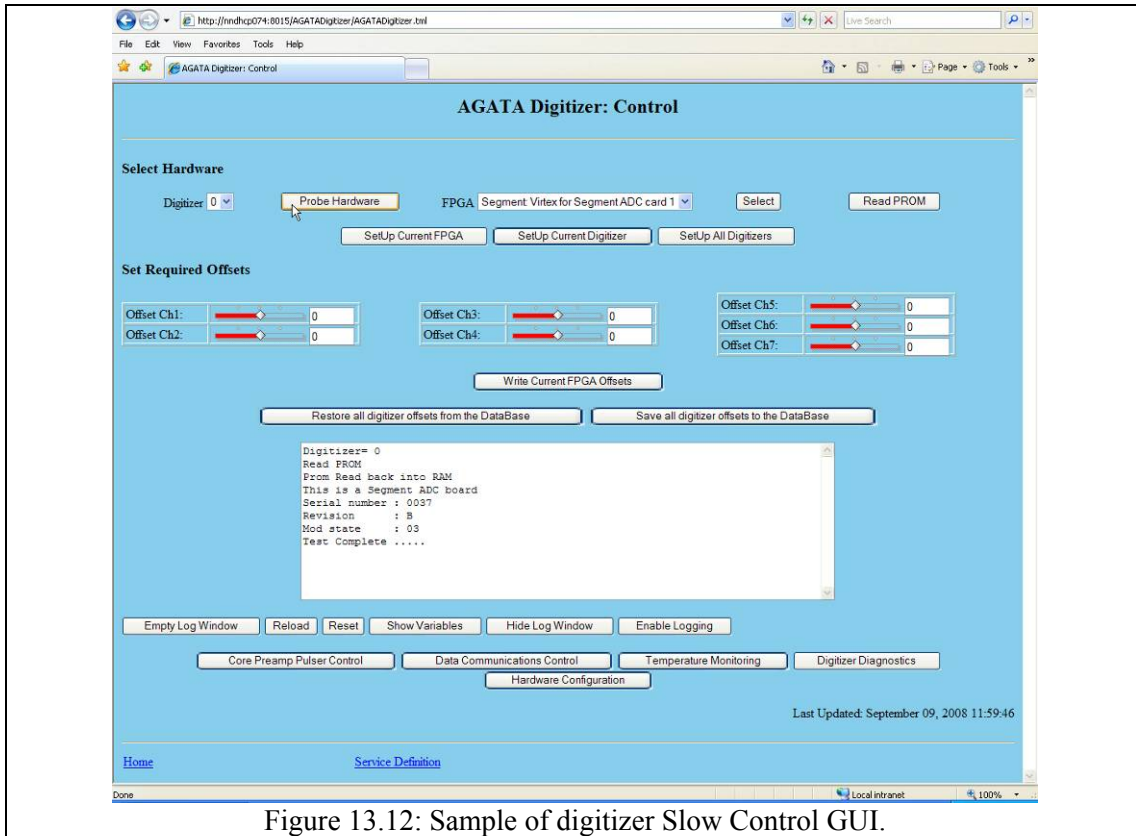


Figure 13.12: Sample of digitizer Slow Control GUI.

### **Implementation**

The network protocol used by the AGATA digitizer Slow Control is based on SOAP which is the foundation layer of the web services protocol stack. The web service is described by its WSDL definition file.

Additionally the AGATA Slow Control protocol is implemented which is also a Web Service and is defined by a WSDL file.

ENX and the segment and core mezzanines slow control

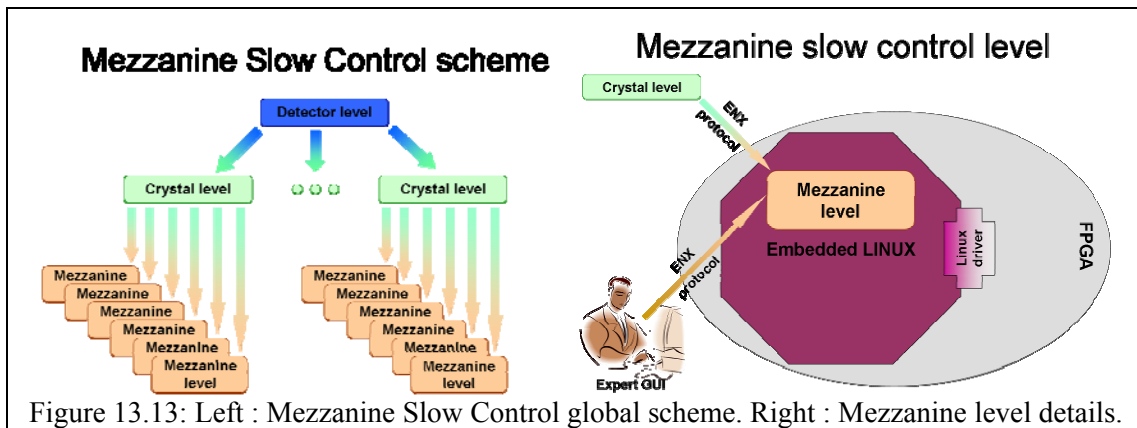
For the AGATA experiment, the slow control of the core and segment mezzanines cards is based on the ENX software [enx].

The Linux operating system will be installed on core and segment mezzanines, with the ENX embedded server on the PPC inside each of the Xilinx FPGA V4, which communicates, by SOAP/XML with the outside. One unique high-level ENX server running on a workstation will federate all the mezzanines, communicating with them by SOAP/XML, and will therefore provide a unique SOAP/XML entry point for a future « mezzanine » graphical user interface, as well as for the Run Control (for setup / go / stop / get state commands). To ease the configuration of the AGATA detector and to be compliant with others slow control parts (digitizer for example), two access levels have been implemented: crystal and detector views as explained below.

To summarize, the slow control comprises three distinct levels as shown in Fig. 11.13-left:

- Mezzanine: Lower level.
- Crystal: Intermediate level.
- Detector: Higher level.

The design of the slow control is therefore mapped to the real hardware architecture of the experiment.



Each of the levels can be controlled via a SOAP command:

- ENX protocol: for all levels,
- AGATA slow control protocol: at detector level only.

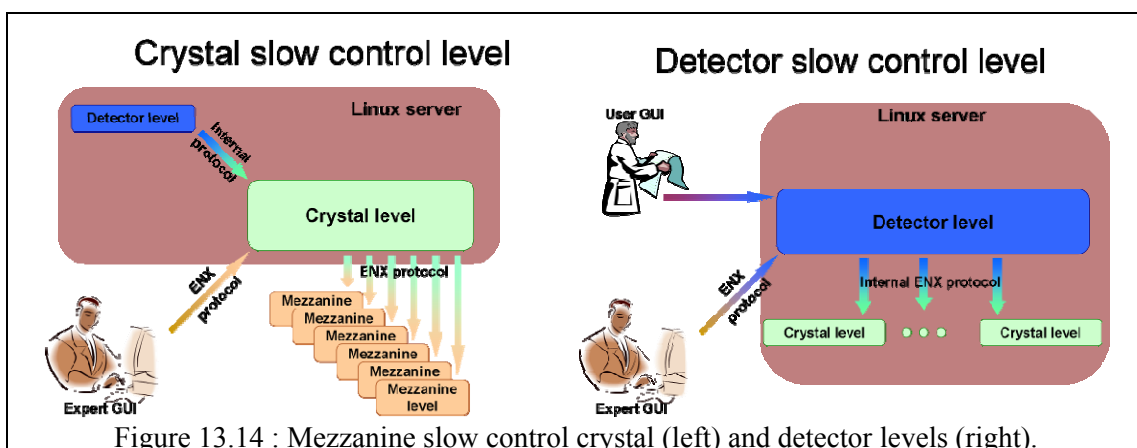
The different levels are implemented by an ENX driver.

### Mezzanine level

The mezzanine is the lowest level of the ENX slow control scheme. It is the ENX driver which handles the hardware: see Fig. 13.13-right. At this level, ENX is installed in the PowerPC 405 embedded on the FPGA of each mezzanine card. As ENX needs an OS to be used, a Linux based on micro kernel distribution has been installed on each mezzanine card. This ENX driver can be accessed via the expert interface and the crystal driver.

### Crystal level

At this stage, the ENX crystal driver is installed on a server of the AGATA experiment: see Fig. 13.14-left. Actually, this is a virtual machine. The crystal driver handles the mezzanine attached to this crystal. In the AGATA configuration, one crystal driver should manage 7 mezzanines (6 segment mezzanines and 1 core mezzanine). This driver can be accessed via the expert interface and the detector level.



### Detector level

This is the highest stage of the structure. The ENX detector driver is installed on the same server as the ENX crystal driver: see Fig. 13.14-right. The detector driver handles the crystals attached to this detector. In the AGATA configuration, one detector driver could manage up to 180 crystals. Obviously, it is possible to create multiple instances of this driver to define different virtual detectors. In such a way, it is easy to manage crystals in calibration phase and

others in-beam experiments running in parallel. This driver can be accessed via the expert interface and the global slow control interface defined for the AGATA experiment.

## 13.4. Hardware and infrastructure

### 13.4.1. The DAQ Box

The design of the DAQ needs to fulfil some requirements: AGATA is a mobile experiment and will be hosted in several laboratories in different countries. On the other hand, people working on this acquisition platform will not be necessarily present in the host laboratory. On the hardware side, there is a big need for computing power to run algorithms hosted by the data acquisition (PSA, Event Builder, merge, tracking). For the demonstrator phase, each crystal needs at least to be attached to one PSA process running on one dedicated computer. This process generates a large data flow which must be stored at very high rate.

The AGATA DAQ must be as much as possible independent of the host laboratory. Its hardware (servers, disk, local network ...) and software should be seen from the host laboratory as a “black box” provided by the collaboration. Therefore the DAQ computing facility is seen as a “black box” called the DAQ box: see figure 13.15. The communication between nodes is organized around two different networks, one for data acquisition called DAQ network and the other for network services called DAQ services network (see also section 13.4.2). Each acquisition node is connected to these two networks through a dedicated interface. External networks (host lab, internet) are accessed through a gateway controlled by a firewall. In order to reduce the dependency with respect to the host laboratory, basic network services are provided in the DAQ box (DHCP (Dynamic Host Configuration Protocol), DNS (Domain Name System), software distribution ...). The external users (developers, system administrator...) can access the DAQ box through a Virtual Private Network (VPN): OpenVPN. This free software running equally on Linux, Windows or Mac OSX, can be configured easily and offers secure and robust connections. In case where external users cannot use a VPN, they can ask for a login and password to access the DAQ box through a Secure Shell (SSH) connection.

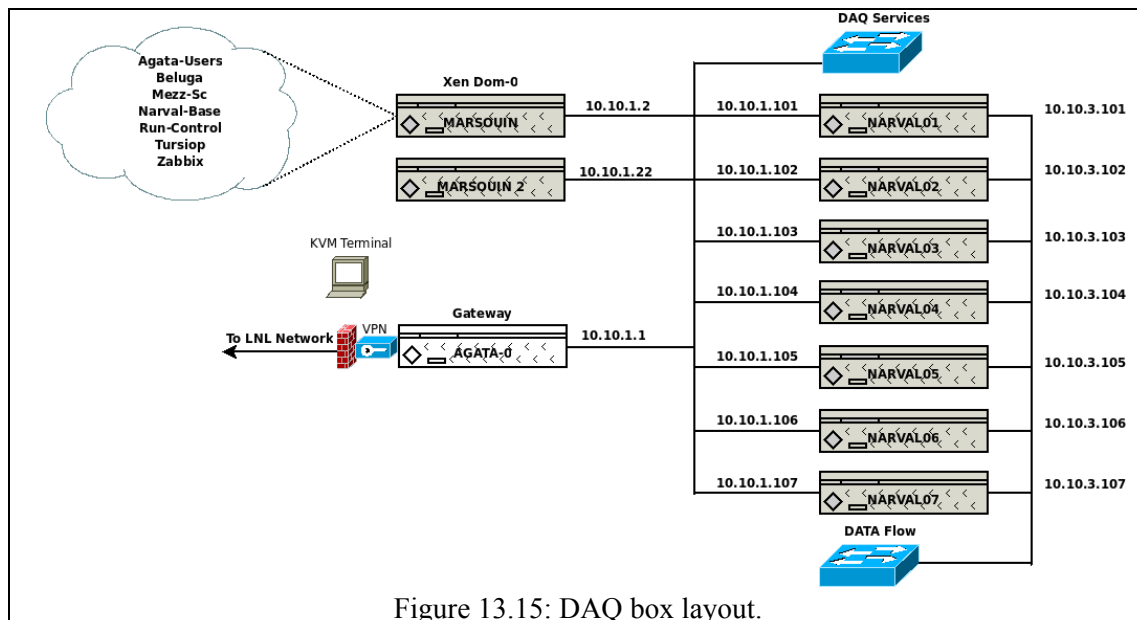


Figure 13.15: DAQ box layout.

To handle the processing power needed by the algorithms, the DAQ box includes one server per crystal for the PSA, 1 for event building, 1 for merging with ancillaries, 1 for tracking, 3 for General Parallel File System (GPFS) disks servers, 2 for slow control, 2 for

DAQ box control, and 2 for data analysis. In addition, workstations will be available in the AGATA control room for general purpose.

All servers are identical to ease the hardware maintenance. The model chosen is the IBM x3550 1U server, with 2 quad cores CPU (12Mb cache per CPU) and 16Gb RAM. Disks servers are attached to a 6540 fiber channel SUN storage and share data using GPFS clustered file system. All the DAQ box nodes use Debian GNU/Linux 4.0 as the operating system. On system administration point of view this distribution has some advantages: easy maintenance, small disk and memory footprint, adaptability, good community support, large software base.

The big number of machines in the DAQ box implies the need for an “industrial” installation system. Such an installation system guaranties identical software configuration on the acquisition nodes. For this purpose the SystemImager tool is used [SyI]. The installation is an order magnitude faster (5 minutes for a node) compared to “manual” technique; the installed node is identical to the other ones and the procedure can be done by a non-expert person. SystemImager can save multiple configurations of the nodes installation and rollback to an older configuration can be performed in case of problem. Software updates can also be handled.

Access provided to the DAQ box servers for software maintenance by OpenVPN and ssh are normally sufficient. However for local maintenance or when operating system can't start on these machines, access to the console can be provided by four KVM (Keyboard, Video, Mouse) switches. These KVM switches are stackable and one of them can be used over TCP/IP granting access to the others switches.

Many services are needed to handle the DAQ box: Monitoring, documentation, network control, installation server... These services are not CPU intensive, so there are gathered on one single server called “marsouin”. To separate cleanly the different functions, each service is hosted on a virtual Xen [xen] machine. Since this “marsouin” node is very sensitive, it has a raid 1 system disks installed and is cloned on a second server called “marsouin2”. One of these virtual Xen machine is the server “tursiops” which gives access to the Wiki DAQ box documentation. This Wiki is daily replicated on an external server reachable on the main DAQ web site: <http://csngwinfo.in2p3.fr/mediawiki/>.

One virtual server is dedicated to hardware monitoring. Zabbix [zab] is used for this purpose. Zabbix is an open source application able to monitor applications, network and servers. What makes it attractive for AGATA is that it is an all in one application, easily configurable through a web interface and that it natively stores monitored values in a database. Data can be visualized easily using a web browser: see Fig. 13.16 as an example. Zabbix can render them as table data values or as graphs. So far, data on network traffic, memory and CPU utilization are collected.



Figure 13.16: Zabbix DAQ hardware monitoring screen shot.

### 13.4.2. Network implementation at LNL

The AGATA's networking reaches all the parts of the experiment including the full readout chain, the front electronics, the main control room and the detector test rooms. The AGATA network is an isolated Local Area Network (LAN) within the LNL LAN with some gateways provided to allow external users to access the experiment. Fig. 13.17 depicts the layout.

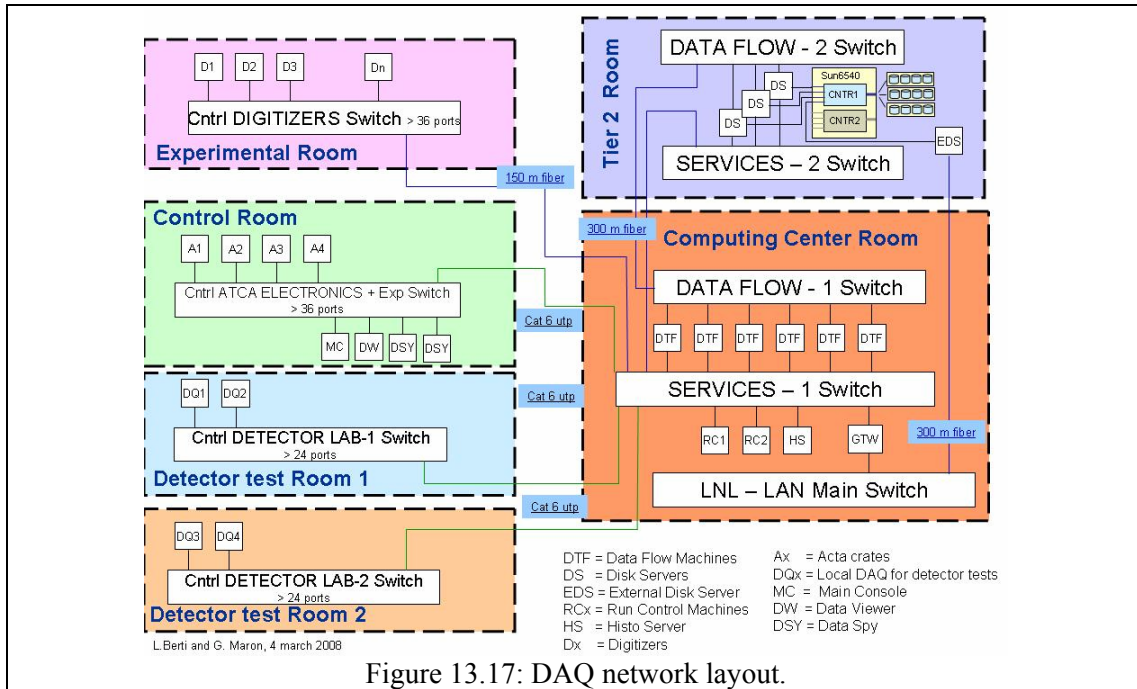


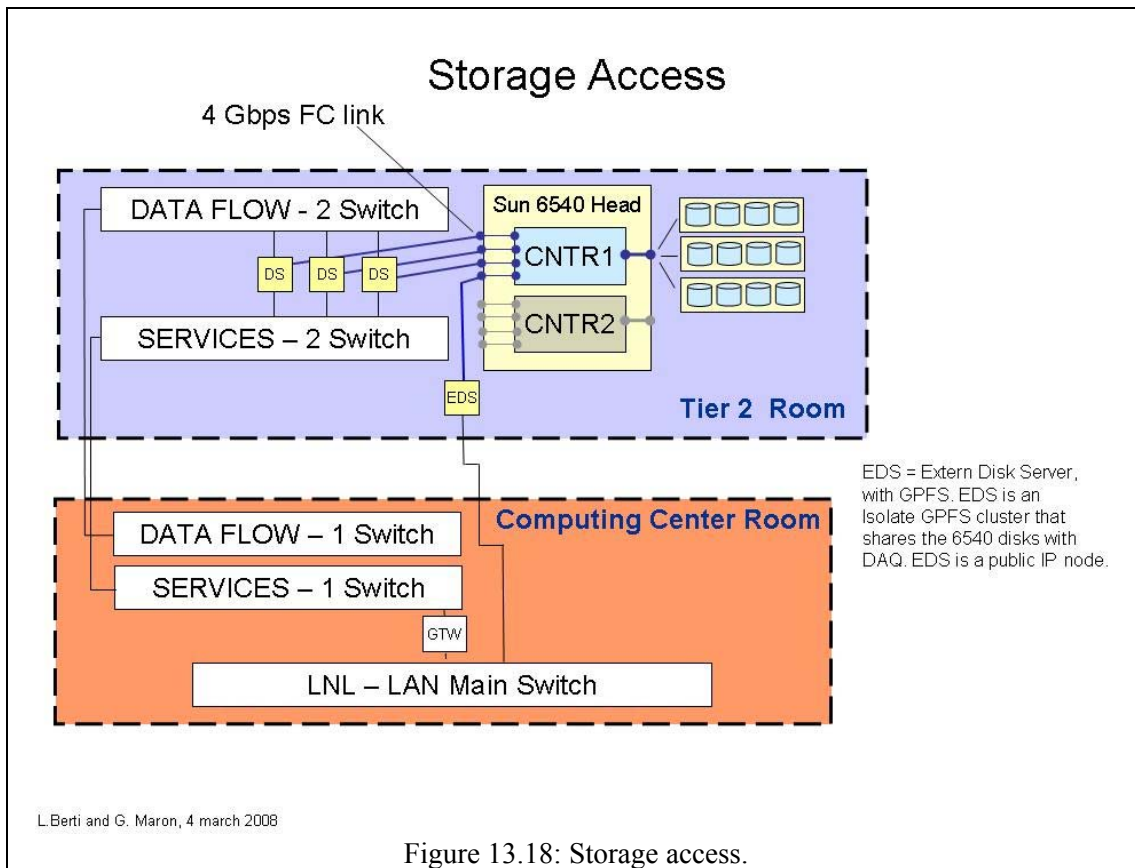
Figure 13.17: DAQ network layout.

A central service switch (SERVICE – 1 switch) connects all the rooms and labs where the experiment is located. Cat 6 UTP connections are used when the connection is less than 100 m while fibers are adopted for the longer connections (about 300 m).

The data acquisition has a own LAN (DATA FLOW switches) to avoid any type of interferences during data taking. For electrical power and cooling reasons data acquisition and storage devices have been hosted in different buildings. The LNL Computing Center Room, located in the Tandem building, hosts all the data flow machines (DTF) that includes PSA processors, event builder and tracking processors while disk servers and storage are located in the LNL LHC Tier2 Room within the LNL experimental hall number 3.

The DATA FLOW machines have a double network interface to allow the SERVICE network to reach them. SERVICE network reaches even the Digitizers controllers, the ATCA controllers, the Run Control machines, the histogram servers, the auxiliary machines devoted to the detector tests and the machines dedicated to the console of the experiment, to display data, to spy, etc. etc.

The disk servers (DS) access the Fiber Channel (FC) disk array controller (Sun 6540) with a fiber channel connection. To allow external access to the disks an External Disk Server (EDS) node is used. Such node will mount, as the other DSs, the GPFS file system and will be an isolated GPFS cluster sharing the Sun 6540 disks with the data flow servers. Fig. 13.18 shows this scenario.



Access to the experiment will be achieved in different way according where the accessing machines is connected to.

- For those machines connected to the AGATA SERVICE network there will be no restrictions as they are connected to a controlled network.
- For those machines attached to the LNL network it will be necessary to access the gateway first. A VPN software is used in this case. SSH tunnelling is even provided.
- Experiment access via the LNL wireless network is even possible, accessing first to wireless portal and then to the AGATA Network.
- Data movement will be performed through EDS and, when the transfer is limited to the LNL LAN, via Gateway (GTW).
- External interactive access will be possible using SSH connections.

#### 13.4.3. LNL Local infrastructure

The data acquisition infrastructure is hosted, as mentioned above, in two different rooms located in two different buildings.

The LNL computing centre room, located in the Tandem building, hosts the data flow machines (PSA, event builder, tracking farm) and DAQ services: see Fig. 13.19-left. This room has about 30 kW of power and an adequate cooling power. 10 kW are dedicated to the AGATA machines. An UPS is covering the electrical power interruptions no longer than 10 minutes. No generating set is available for this case.

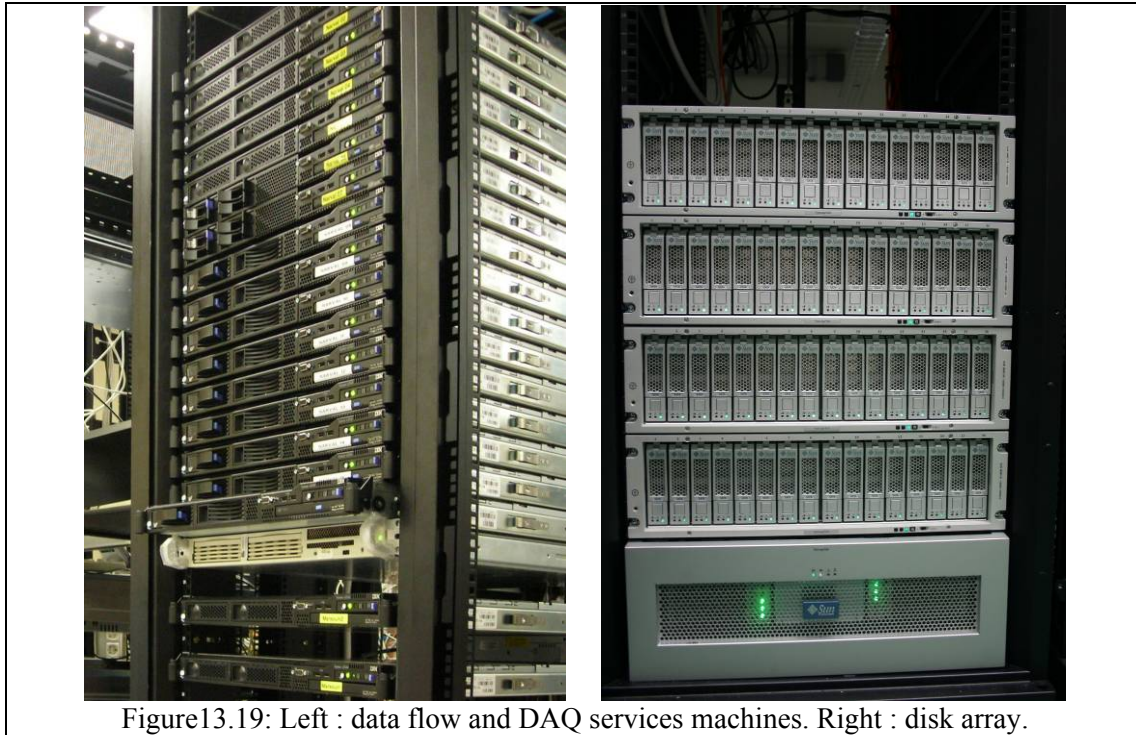


Figure 13.19: Left : data flow and DAQ services machines. Right : disk array.

The LNL LHC Tier 2 computing center, located in the experimental hall number 3, hosts all the disk servers, the disk arrays (see Fig. 13.19-right) and GRID services needed to the AGATA data mover. The room provides about 220 kW of power and adequate cooling power. Two cooled racks are reserved for the AGATA experiment. Possibility of expansions is foreseen. Fig.13.20 shows the room layout, the installed racks and the ones that will be installed end of 2008. AGATA has one rack in the already installed rack row, while a second one is foreseen in the rows that are being installed. UPSs with redundancy n+1 and a generating set up to 630 kW are use to assure the power continuity of the computing equipments and of the cooling system.

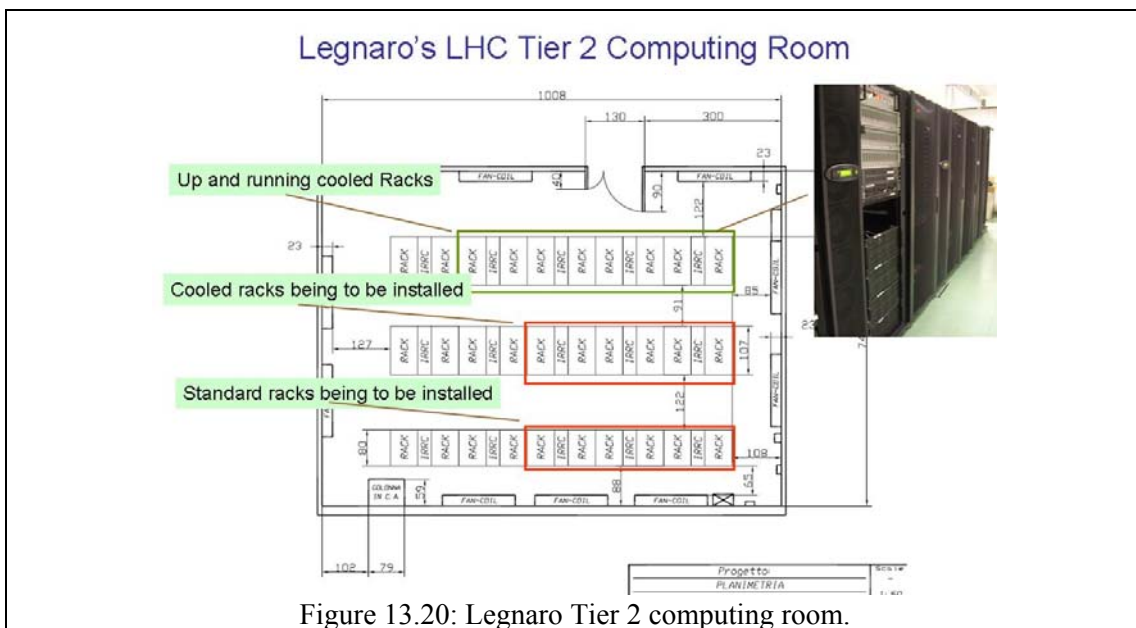


Figure 13.20: Legnaro Tier 2 computing room.

The Legnaro site is connected to the wide area network with a 2 Gbps link. An upgrade to 10 Gbps is foreseen for the year 2010.

### 13.5. Data archive and data mover

The AGATA on-line storage system is providing a well redundant storage for several tens of days of run, but it does not provide any form of permanent archive and/or tape based backup. Acquired data will be available on the on-line disks, but after a while they will be removed to make room to the data of the new incoming experiments. It is then clear that the AGATA collaboration needs a permanent archive that should provide both the official experiment reference data archive and the repository from where the AGATA users can copy the archived data into the own storage resources at home.

The basic requirements for a such historical archive system is about 10-20 TB/year of permanent storage and the availability of user-friendly procedures to copy data from the online system to the archive first and then from the archive to the home institute. The Tier 1 centres of the LHC have the technology and the expertise to store petabytes of data per year, so it seems quite natural to ask to one of them if they could hosts the AGATA data.

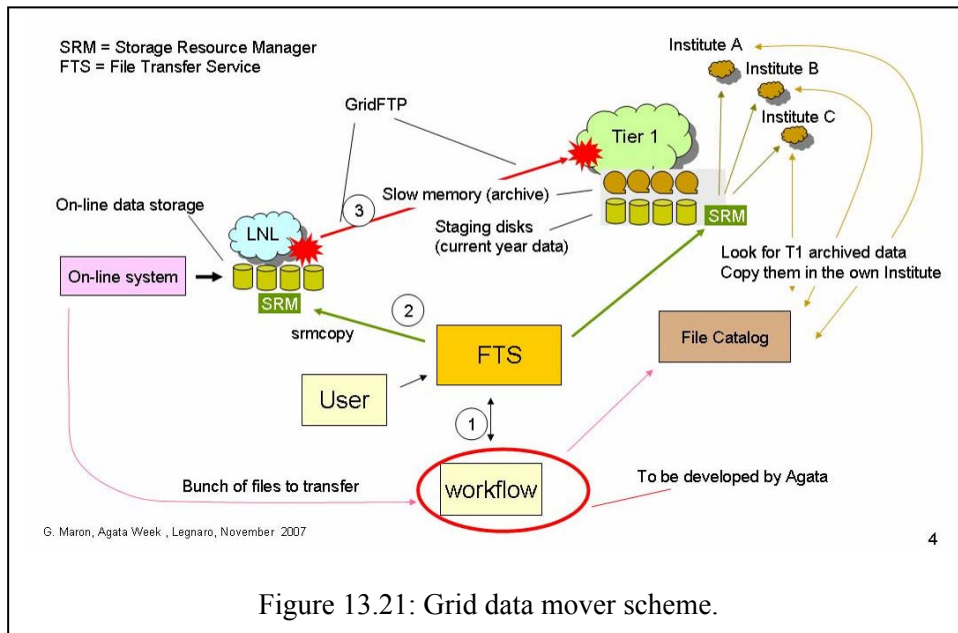


Figure 13.21: Grid data mover scheme.

As known, Tier1 speaks only a GRID language, so AGATA should be able to move the own data according to the GRID flavour.

A slow access data storage (typically tape based libraries) can be used for the permanent archive, as the speed is not an issue in this case. This allows to reduce of a factor of ten the costs of the storage.

The Italian T1 centre of CNAF-INFN has shown interest to host the AGATA data, providing of course the funds necessary to acquire the tapes.

Fig. 13.21 shows how a complete AGATA data mover could appear. The Storage Resource Manager (SRM) is the lower level of the system and provides the web service end points to start the copy operation of the data. The protocol used to move data is GridFTP. A workflow engine is necessary at this level to synchronize the copy of the data automatically. Higher level and more sophisticated approaches are available using the Tier 1 FTS (File Transfer Service) and/or a file catalogue that provides the list of the files that have been moved to the Tier1.

A basic data mover test has been successfully performed moving data from Legnaro T2 to the CNAF T1 using SRM endpoints and GridFTP protocol enabled for the AGATA Virtual Organization (VO).

Referring to the Fig. 13.17, only the machine EDS (External Disk Server) will have the responsibility to move data from/to the Tier 1 and then it will need to install the GRID middleware. All the other DAQ machines will be unaffected by the GRID operation.

### 13.6. The General Trigger System (GTS)

#### 13.6.1. Introduction

Data synchronization is an important aspect in the operation of the trigger and readout systems of the AGATA experiment. A high increase in efficiency with respect to current spectrometers is expected in AGATA by means of online gamma ray tracking and pulse shape analysis (PSA). Tracking and PSA require the concurrent digitization of preamplifier signals of the 36 fold segmented Ge crystals composing the array. Therefore, the design of the front-end readout and level-1 (L1) trigger in AGATA follows a synchronous pipeline model: the detector data are stored in pipeline buffers at the global AGATA frequency, waiting the global L1 decision. The L1 latency must be constant and shall match the pipeline buffer length. The whole system behaves synchronously and synchronization at different levels and in different contexts has to be achieved and monitored for proper operation of the system. In order to fix definitions, we list in Table 13.1 the various synchronization types that we refer to.

<i>Type</i>	<i>Description</i>
Sampling Synchronization	Synchronization of the detector signals with the clock phase
Serial Link Synchronization	Recovery of parallel data words from the serial bit stream.
Trigger Requests Alignment	Alignment of trigger data at the input of the trigger pipeline processor
L1 Validations Synchronization	Synchronization of L1A signal with data in the readout pipelines
Event Synchronization	Assignment of global clock and event number to data fragments in the DAQ path

Table 13.1: Synchronization types.

In AGATA each crystal is considered as a separate entity and from the point of view of the Data Acquisition System (DAQ), the whole detector may be considered as the aggregation of synchronized data supplied by individual crystals, possibly disciplined by a global trigger primitive.

Each crystal is composed of 36 segments and a central core contact, all individually readout. The data from the core contact are processed for event detection and hence, a level 1 trigger request or local trigger generation. The choice between the two behaviors is done upon configuration, the former corresponding to an effective way to reduce front-end data rates in cases where anyone of the stages of the readout chain is unable to perform at the actual data throughput.

#### 13.6.2. GTS Functionalities

From the logical description of the front-end operation given above it turns out that a certain number of global time referenced signals are needed. Among them:

1. common clock
2. global clock counter
3. global event counter
4. trigger controls:

- i. Throttling of the L1 validation signal
  - ii. Fast commands (fast reset, initialization, etc.)
  - iii. Fast monitoring feedback from the crystals
  - iv. Calibration and test trigger sequence commands
  - v. Monitor of dead time
5. Trigger requests
  6. Error reports

In AGATA, the transport medium of all these signals is shared by use of serial optical bidirectional links connecting the front-end electronics of each crystal with a central global trigger and synchronization control unit in a tree-like structure, thus actually merging together the three basic functionalities of synchronization distribution, global control and trigger processing.

More in detail:

*1: Common clock*

This is a 100 MHz digital clock supplied by a central timing unit (possibly GPS disciplined) and used to clock the high speed optical transceivers reaching the front-end electronics of every crystal. At the crystal receiving side the clock is reconstructed and filtered for jitter. The clock signals of each crystal may be equalized for delay and phase, thus accounting for different fibre lengths and different crystal locations in the array.

*2: Global clock counter*

A 48 bit digital pattern used to tag event fragments before Front-end buffer formatting. The pattern is the actual count of the global clock. It will be used by PSA and global event builders to merge the event fragments in one single event.

*3: Global event counter*

A 16 bit digital pattern used to tag event fragments before Front-end buffer formatting. The pattern is the actual count of the L1 validations.

*4: Trigger controls*

The Trigger Control must guarantee that sub-systems are ready to receive every L1 Accept delivered. This is essential to prevent buffers overflows and/or trigger signals missed when the crystals are not ready to receive them. In either case, the consequence would be a loss of synchronization between event fragments.

Warning signals sent from the crystal through the GTS network, indicating that some of its buffers are almost full, may be received centrally. However this feedback signal can take few microseconds to reach the Trigger Control, which meanwhile could have delivered a number of L1A signals that originate a buffer overflow. This problem is particularly acute in the front-end derandomizers which have a small storage capacity.

According to the front-end electronic logical model, the front-end derandomizers after the L1 latency pipelines are the first devices to overflow when the L1A rate is too high. Space and power constraints in the front-ends imply small derandomizer depth and hence these queues are very sensitive to bursty L1A. In general, the derandomizers behave like a first-in-first-out queue: the input/output frequency is directly the L1A rate. The overflow probability is strongly dependent on the ratio between the service time and the buffer depth. The consequence would be of resetting the whole front-end electronics which would cause a severe loss of efficiency in the DAQ. All front-end derandomizers behave identically. Therefore, their occupancy depend only on the L1A rate and on the service time. A state machine receiving the L1A signals can emulate the de-randomizer behavior and determine its occupancy at each new L1A. If a new L1A is estimated to cause a de-randomizer overflow, this L1A is throttled. In general, it would

be very difficult to guarantee that the state machine reproduces exactly the buffer status at every time. However in the present case the L1A accept signals are synchronous with the clock and the write and read latencies are measured in multiples of the clock period. It is this time quantization that makes the de-randomizer emulation really possible. A complementary solution to the same problem is to oblige the delivery of L1A signals to comply with a set of trigger rules. These rules take the general form 'no more than n L1A signals in a given time interval'. Suitable rules, inducing a negligible dead time, would minimize the buffer overflow probability.

*5: Trigger request*

The central core contact signal might be considered as the overlap of all the signals in the segments of a crystal; in fact a deposit of energy in any of the segment will induce a signal in the central core, thus acting as a sort of analog sum of single segment signals. Therefore, the central core can be processed for event localization in a crystal. Suitable algorithms for this task have been identified and tested. The outcome of the algorithm may issue a trigger request to the central trigger processor by asserting this signal which is transmitted via the high speed serial links of the GTS network upwards to the central trigger unit.

All the trigger requests collected from the crystals at each global clock cycle form a pattern that can be processed centrally for multiplicity or coincidence with ancillary detectors. The result of this processing stage constitutes the L1 validation.

*6: Error reports*

Abnormal conditions as buffer overflows, local faults, built-in self tests, etc. can be reported centrally for proper corrective actions.

**13.6.3. Implementation**

AGATA GTS has a tree topology as shown in Fig. 13.22, originating from the root node that will therefore act at the same time as the source of all global information (clock, timestamps, commands, L1 validations) and the sink of all trigger requests, fast monitoring signals and service requests coming from the crystals.

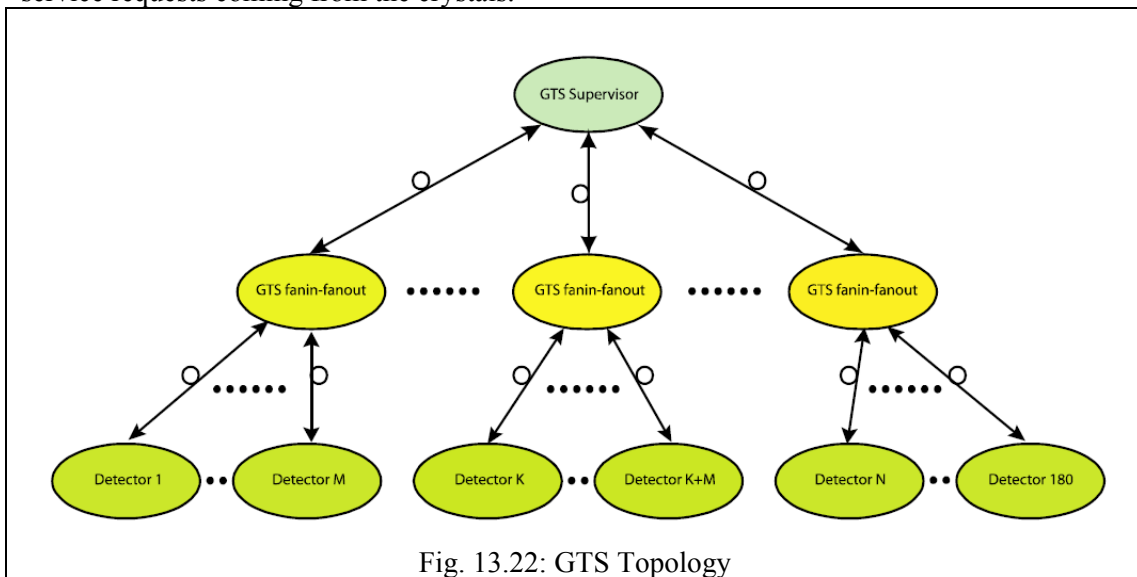


Fig. 13.22: GTS Topology

To solve the problems of building a bi-directional, high capacity and high speed tree network that drives hundreds of nodes displaced several tenths of meters apart, a certain number of technological issues have been addressed. Among them, the fan-out of a source synchronous

transmission, noise immunity, low error rate and throughput. Modern serial transceivers, as used in commercial high speed telecom networks, solve part of them. Simply stated, these devices basically transfer a digital pattern from one side of a transmission channel to the other (and vice versa) by serializing the pattern at a speed that equals the input clock frequency times the pattern width; the serialized pattern is then reconstructed identical at the receiving side of the transmission line by means of a serial to parallel conversion.

The hierarchy is composed of five different parts:

1. the root node
2. the backplane
3. the fanin-fanout nodes
4. the fibre connections
5. the mezzanine interface

A picture of a GTS mezzanine is shown in Fig. 13.23. Picture 13.24 shows an ATCA Carrier card on which the GTS mezzanine is plugged.

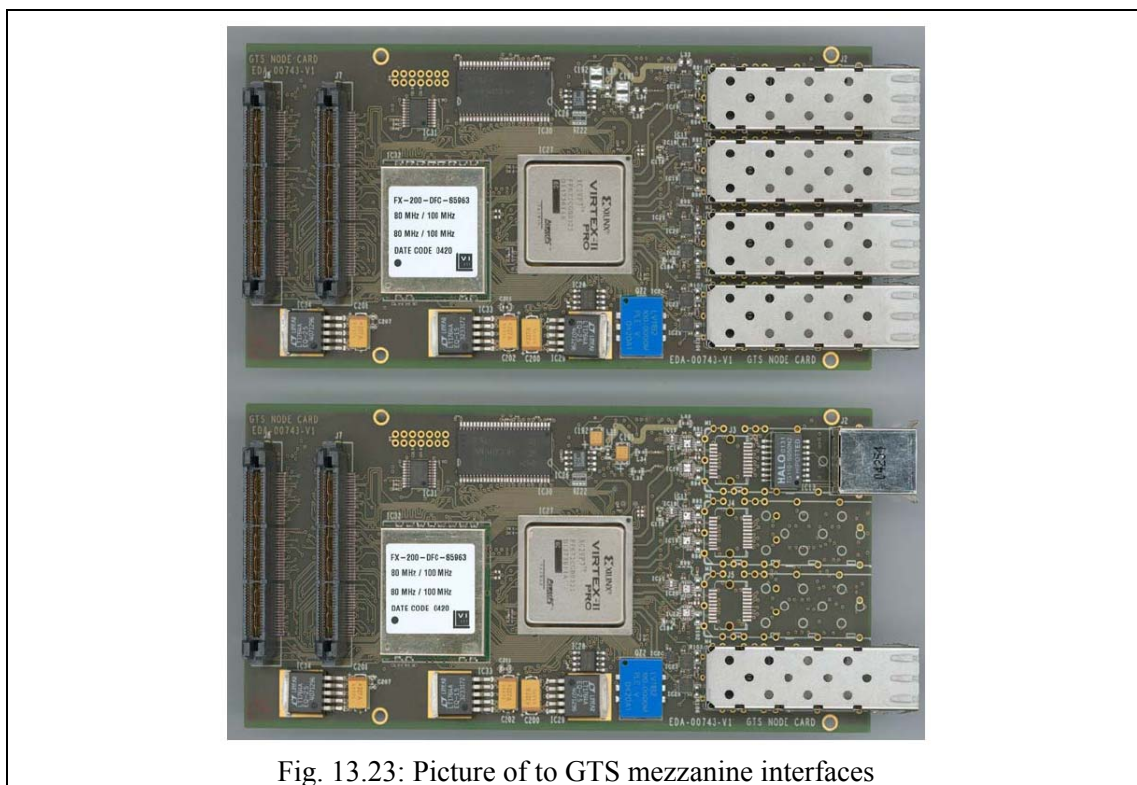


Fig. 13.23: Picture of to GTS mezzanine interfaces

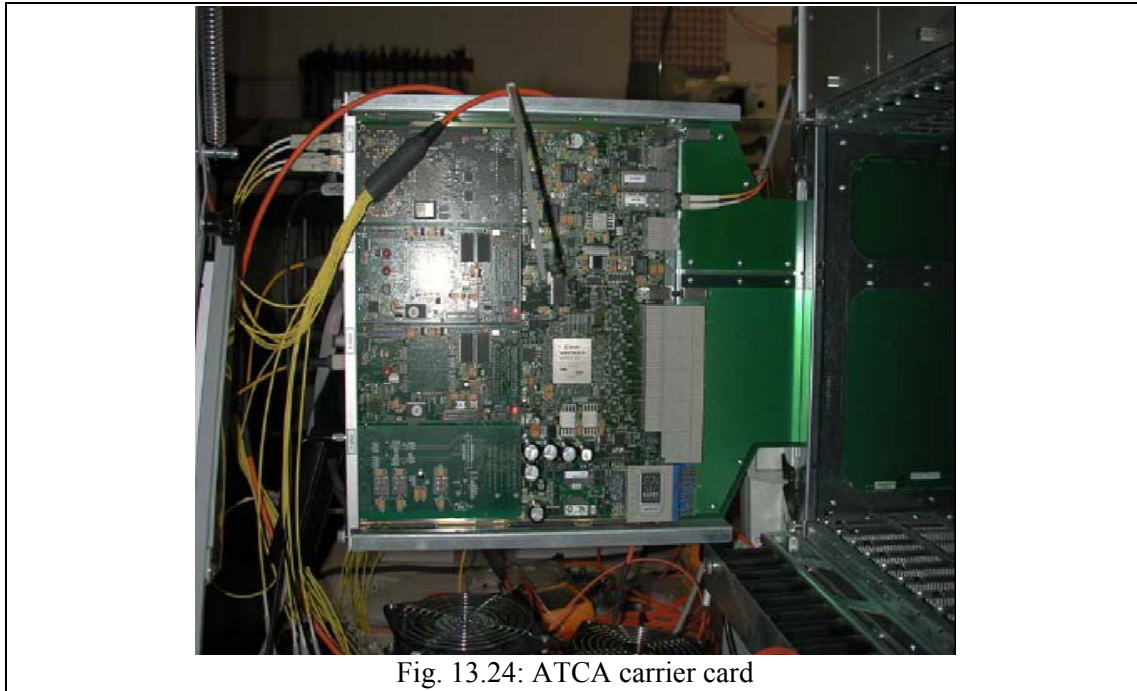


Fig. 13.24: ATCA carrier card

### 13.7. References

- [adf] “A library of services to decode/encode data through the AGATA Data Flow” available on the DAQ web site <http://csngwinfo.in2p3.fr/?q=node/18>
- [anc1] “Merge of ancillary detectors with AGATA”
- [cha] Chainsaw: <http://logging.apache.org/chainsaw/index.htm>
- [cre] J. Cresswell and X. Grave “AGATA PSA and Tracking Algorithm Integration” available on the DAQ web site <http://csngwinfo.in2p3.fr/?q=node/18>
- [elog] Elog web site: <https://midas.psi.ch/elog/>
- [enx] ENX web site: <http://enx.in2p3.fr>
- [flo] “Dataflow in the AGATA DAQ” available on the DAQ web site <http://csngwinfo.in2p3.fr/?q=node/18>
- [gridcc] Grid Enabled Remote Instrumentation with Distributed Control and Computation <http://www.gridcc.org>
- [leg] “GRU/ViGRU documentation” : <http://wiki.ganil.fr/gap/wiki/Documentation/Gru/Gru>
- [nar] X. Grave *et al.*, IEEE-NPSS 2005 proceedings
- [narw] NARVAL web site: <http://narval.in2p3.fr/>
- [puc1] V. Pucknell, “Data Base Access using XML/SOAP protocols” available on the web site <http://npg.dl.ac.uk/MIDAS/DataAcq/>
- [rcms]. RCMS wiki site: <https://twiki.cern.ch/twiki/bin/view/CMS/RunControl>
- [root] R. Brun, F. Rademakers, Nucl. Inst. Meth. A 389 (1997) 81.
- [rootw] ROOT web site : <http://cern.root.ch>
- [SyI] SystemImager wiki pages: <http://wiki.systemimager.org>
- [web] DAQ web site: <http://csngwinfo.in2p3.fr>
- [xdaq] XDAQ wiki pages: <http://xdaqwiki.cern.ch>
- [xen] Xen web site: <http://www.xen.org/>
- [zab] Zabbix web site: <http://www.zabbix.com/>



## 14. The AGAVA Interface

### 14.1. Introduction.

AGATA requires, in almost all circumstances, complementary devices to exploit all the capabilities of the tracking and get the best performance figures. The emission point of the gamma ray and the trajectory and velocity of the emitting nuclei are basic information for the reconstruction of the Doppler effects. In addition several complementary detectors will be needed to develop the experimental program with radioactive and stable beams. The present document describes the AGAVA (AGATA VME Adapter) module, a trigger interface (i.e. an interface for the AGATA GTS) for complementary detectors to be used with the AGATA demonstrator. Since most of the presently available detectors in our community have a front-end/read-out based in VME or VXI standard, the GTS-mezzanine interface has been developed in VME standard with full compatibility with the VXI read-out modes.

### 14.2. General Description.

AGAVA Interface is a 1-unit wide A32D32 type VME/VXI slave module. It is as well the carrier board for the GTS mezzanine card used in the AGATA for the global time stamp distribution. The main task of the Agava is to merge the triggerless time stamp based system with the acquisition system using trigger, based on the VME or VXI Exogam-like environment. It has also connections to the VME Metronome and Shark link systems. The logic and tasks are controlled by the FPGA Virtex II Pro. In Fig. 14.1 it is shown the block diagram of the Agava Interface. The AGAVA PCB includes all necessary connections for the trigger cycle and for the TDR (Total data readout) system (connectors on the Front Panel and connections to the Xilinx FPGA). AGAVA contains as well the Ethernet passive connection, providing directly Ethernet to the GTS mezzanine card.

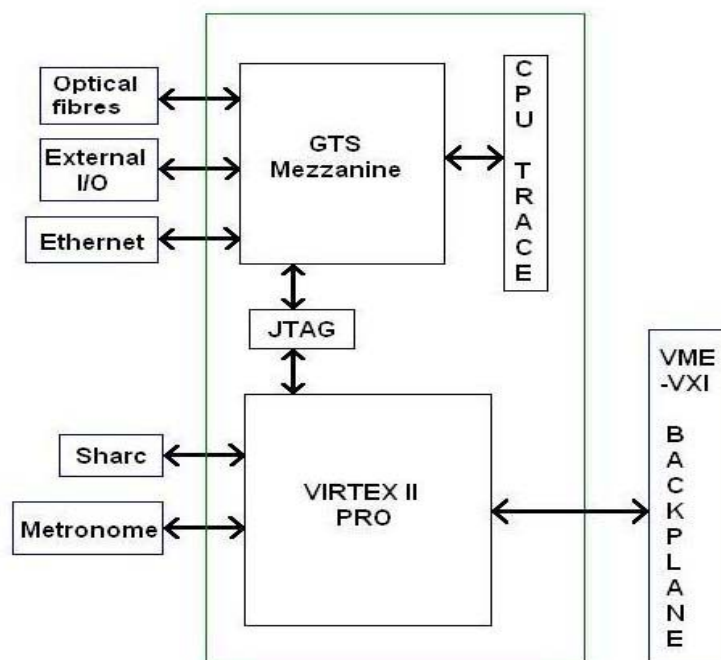


Fig.1 Block Diagram of AGAVA Module.

Fig. 14.1

### 14.3. The AGAVA operation.

#### 14.3.1. VME Interface.

In the AGAVA module few types of the VME/VXI access modes have been implemented. AGAVA can provide the VME single access read or write operations according to the standard VME handshake rules. It can also provide the block transfer readout in the CBLT (Chain Block Transfer) on the VME bus. On the startup special registers for CBLT mode have to be set in the AGAVA card. The CBLT readout uses one common address for all participating modules in the chain. They deliver their data in blocks of variable lengths starting from the module defined as the first in the chain, following by one or more intermediate and finished by the last one.

The CBLT mode is used for faster readout and is helpful for event building. CBLT readout has been successfully tested at Legnaro. In the AGAVA interface there is also VXI Exogam-like readout implemented. It has been successfully tested at Ganil in the VXI environment.

#### 14.3.2. GTS Interface.

The AGAVA module receives the trigger requests from the ancillary detector (named here “external” trigger) and the trigger request is pass to the GTS system. An “internal” trigger request can provide for testing purposes. After the trigger request is pass to the GTS system AGAVA waits for the Local Trigger and Tag and Validation/Rejection Signal and Tag coming from the GTS System. The AGAVA module stores the data in registers or RAM (depending on the Slow or Fast mode) and sets the Data Ready Flag to inform the VME/VXI system that the data can be transferred to the event builder part.

The Busy Flag is set after accepting a new Trigger Request. Release of the Busy (Dead time for new triggers) depends strongly on the VME/VXI readout mode and speed. The back pressure input is used by the GTS system for controlling trigger rates.

#### 14.3.3. Slow mode Trigger Cycle.

In the Slow Mode the Trigger Request from the ancillary detector arrives on the corresponding Front Panel Input. If there is no Busy status from the previous cycle, this signal is formed to a single 10 ns wide pulse and sent to the GTS mezzanine card. Then the Local Trigger and Local Trigger Tag are received from the GTS mezzanine card and AGAVA will wait for the GTS Supervisor response: either Validation Trigger with Validation Trigger Tag and Event Number or Rejection Trigger with Rejection Trigger Tag. After receiving them the Data Ready Flag is set in AGAVA module and the data can be read out by the VME system. Till this is done the Trigger Request input is disabled with the Busy Flag (can be observed on the Front Panel output and LED). This mode was used in all tests in Cracow, Legnaro and Ganil.

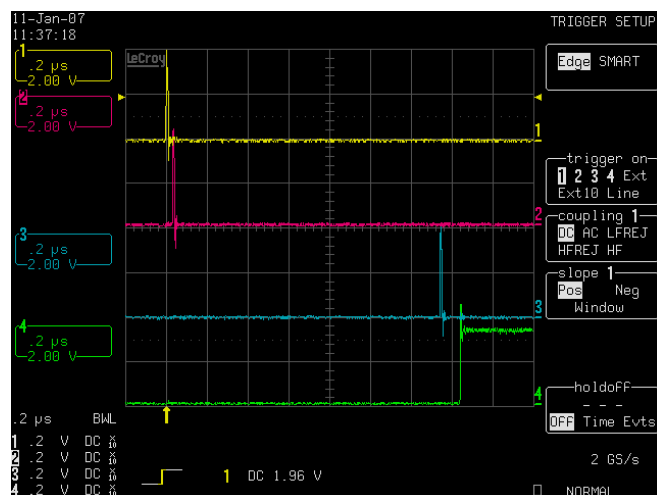


Fig.14.2. AGAVA and GTS response for the Trigger request. Measurement performed in Cracow: Ch1 (yellow): trigger request input, Ch2 (red): local trigger, Ch3 (blue): validation trigger, Ch4 (green): data ready

Parallel-like mode of Trigger Request.

**In this mode, the trigger request from the ancillary detector arrives on the Front Panel Input (as in the Slow Mode), the Busy status is set and held until the Local Trigger and Local Trigger Tag are received from the GTS mezzanine card and stored in AGAVA module in RAM. At the same time AGAVA can receive the Validation or Rejection Trigger and Tag. They are also stored in the RAM with another marker. The data can be read by the VME system. The Busy Flag is set after accepting the new Trigger Request. Release of the Busy (Dead time for the triggers) depends strongly on the VME/VXI readout mode and speed. This mode is prepared for the future purposes and has not been tested in the real conditions.**



Fig.14.3 Top View of the AGAVA board with GTS mezzanine card.



## 15. Event Data bases and Data analysis

### 15.1. Data bases for storage of event data

#### 15.1.1. Data rates

Simulations of data rates and data storage needs have been made for the different phases of AGATA, from the demonstrator to the complete  $4\pi$  array, with and without including ancillary detectors. An example of event and data rates expected for the AGATA Demonstrator is shown in table 15.1.

<i>Gamma-multiplicity</i>	<i>Core count rate [kHz]</i>	<i>Min. gamma-ray fold</i>	<i>Trigger rate [kHz]</i>	<i>Giga events per day</i>	<i>Zero-suppression in PP</i>	<i>Suppress storage of short traces</i>	<i>Online gamma tracking</i>	<i>Average event size [bytes]</i>	<i>Data rate [Mbyte/s]</i>	<i>Data rate [Tbyte/day]</i>
1	0.59	1	6.3	0.55	No	No	No	7.4k	47	4.0
					Yes	No	No	2.1k	13	1.2
					Yes	Yes	No	145	0.92	0.079
					Yes	Yes	Yes	40	0.25	0.022
15	8.8	1	63	5.4	No	No	No	11k	700	61
					Yes	No	No	3.2k	200	17
					Yes	Yes	No	220	14	1.2
					Yes	Yes	Yes	52	3.3	0.28
		2	25	2.1	No	No	No	17k	420	36
					Yes	No	No	4.9k	120	10
					Yes	Yes	No	340	8.2	0.71
					Yes	Yes	Yes	72	1.8	0.15
30	18	1	86	7.4	No	No	No	16k	1400	120
					Yes	No	No	4.6k	400	34
					Yes	Yes	No	320	28	2.4
					Yes	Yes	Yes	69	5.9	0.51
		2	58	5.0	No	No	No	21k	1200	100
					Yes	No	No	5.9k	340	29
					Yes	Yes	No	410	23	2.0
					Yes	Yes	Yes	83	4.8	0.41

Table 15.1 Estimated event and data rates at a reaction rate of 100 kHz for the AGATA Demonstrator setup consisting of 5 triple cluster detectors. The distance from the source to the front of the HPGe crystals was 23.5 cm. No ancillary detectors were included in the simulation.

#### 15.1.2. ROOT

One of the possible data base structures, which has been investigated, is based on the ROOT object oriented data analysis framework developed at CERN. ROOT has been used and evaluated for both real and simulated AGATA events.

The event data from the in-beam experiment with the triple symmetric AGATA cluster detector, performed at IKP Cologne in 2005, were sorted into so-called ROOT trees. The data was stored on a dual processor RAID server at Uppsala University and made accessible for the AGATA collaboration.

A large simulated AGATA data set was produced on a cluster of Linux PCs at IPN Lyon, using PROOF, the Parallel ROOT Facility. The time required to analyze this simulated data set on the PC cluster was evaluated.

### 15.1.3. Grid based archiving and distribution of AGATA event data

Another possibility, which has been investigated, is the use of the Grid for storage and distribution of the AGATA event data. Two possible uses of the Grid have been discussed:

1. Archiving of one copy of all AGATA event data sets
2. Offline data processing

The current decision is to implement the event data archive and to further investigate the suitability of the Grid for offline data processing.

Users of the computing and storage resources of the Grid are authenticated by personal certificates, which are issued by the Grid certification authorities. Once a user has obtained such a certificate he or she must register as a member of a GRID Virtual Organization (VO), through which access to specific Grid resource may become available. For this purpose, the AGATA VO, which is open to all members of the AGATA community, has been created. Information regarding the AGATA VO, how to request a Grid certificate, etc., will be posted at <http://www.agata.org/grid/>. At the start of the AGATA VO the following Grid resources were available specifically for AGATA (mainly for testing purposes):

- Orsay: Tier-2, 4 CPUs, 3 TB storage
- Lyon: 20 CPUs, 10+5 TB storage

The current plan regarding the archiving of the AGATA event data is to use the Tier-1 computing centre at CNAF-INFN in Bologna. For the transfer of the data from the AGATA Demonstrator DAQ system at LNL-INFN, the infrastructure of the Tier-2 at LNL will be utilized. The following hardware, located at the Tier-1 in Bologna, will be supplied by AGATA:

- 2-4 staging hard disks (1 TB/disk)
- 1 tape drive

The data will be archived on tapes (1 TB/tape) and can at any time be accessed by the members of the AGATA VO. It is estimated that the AGATA Demonstrator will produce

up to 50 to 100 TB of event data per year, when running in production mode. During the commissioning phase, when the zero suppression in the pre-processors is disabled and/or the digitized waveforms are stored, the data rates may be much higher (see table 4.1). The commissioning data will, however, not be transferred to CNAF for archiving.

A test of the transfer of data from the disk array of the AGATA DAQ system at LNL to the hard disk storage at the Tier-1 in Bologna has been performed. The measured transfer rate is shown in fig. 15.1. For the peak on the left side of the plot, one file of the size 11 GB was transferred. In this case the maximum transfer rate was about 30 MB/sec, limited by the readout speed of the hard disks of the disk array at LNL. The peak on the right hand side of the plot shows the rate during the transfer of 5 identical files in parallel. The maximum transfer rate was in this case about 120 MB/sec, which is the limit of the Gigabit Ethernet link between LNL and CNAF.

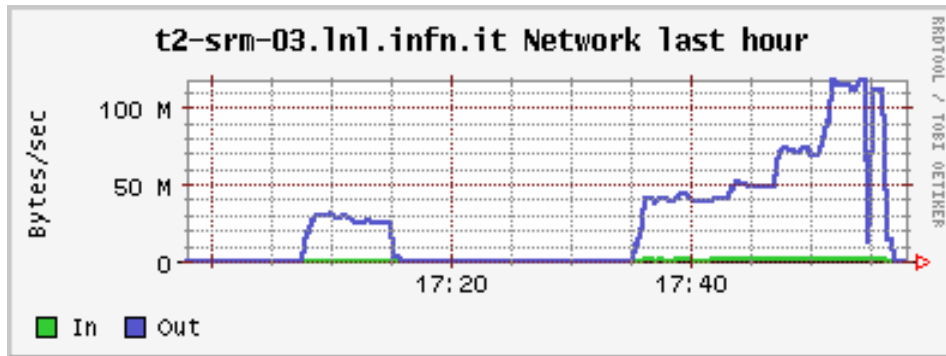
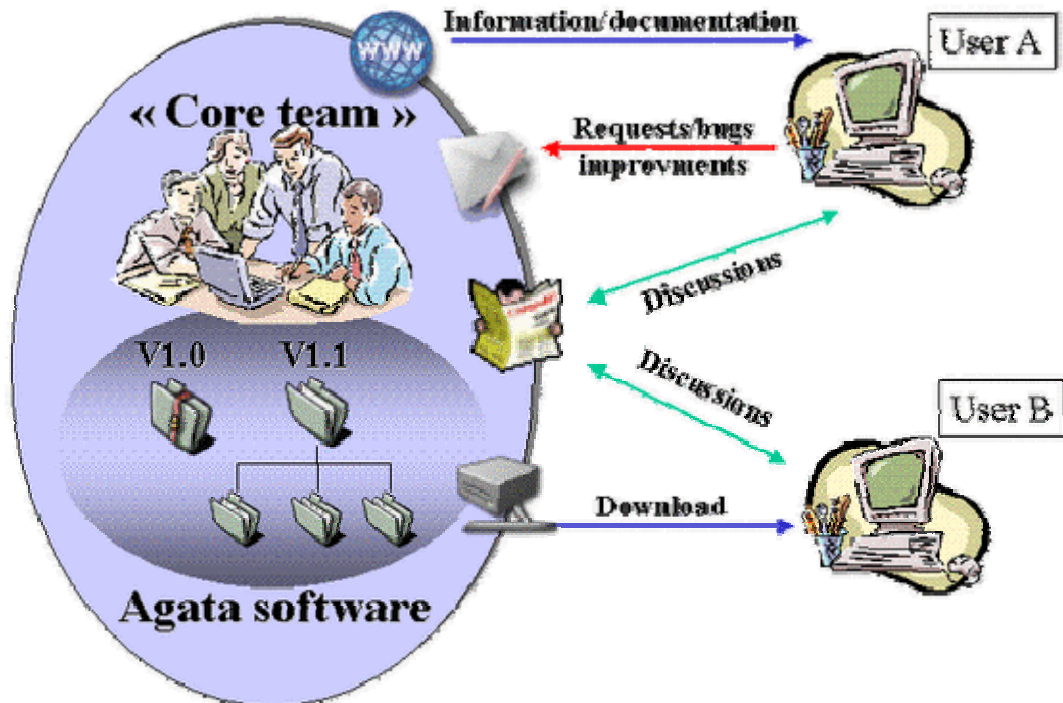


Fig. 15.1 Test of data transfer from LNL-INFN to CNAF-INFN. See text for further information.

A data transfer test was also performed both from the disk array of the AGATA DAQ at LNL and from the hard disk storage at CNAF to an AGATA user located in Uppsala, Sweden. The NORDUGRID client program *ngcp*, a command line based Grid storage access utility, which is freely available for many different Linux distributions, was used in the test. The measured transfer rate between CNAF and Uppsala was 10 MB/sec, a limit which was set by the 100 Mbit/sec local area network in Uppsala. Further tests by AGATA users at other sites will be performed in the future.

### 15.2. Data Analysis

The main goal of the AGATA Data Analysis Team is to define and propose a general framework to help the community to prepare an experiment, through simulations, and to analyze real data coming from the detector.



The development of such a platform involves the whole AGATA community in order to use/debug/improve the package and a small team to manage it.

To make it possible, the sources of the code are available and shared through a version control system (subversion). The repository is hosted at the in2p3 computer centre (<http://cc.in2p3.fr/>) and can be browsed using ViewVC (<http://svn.in2p3.fr/agata/>). In order to protect the repository, the ssh protocol is required to update it.

For such a project, an object oriented approach (C++ language) has been chosen. The package is itself composed of several sub-projects each one associated with a shared library.

Core: contains the base and the virtual classes, as well as all the abstract interfaces.

Physics: defines the main objects manipulated in nuclear structure physics (gamma-ray transitions, nuclear levels, level schemes, etc.).

Gem: facilities to emulate physics generators, in particular to produce randomly discrete gamma-ray cascades on basis of level schemes coming from the main databases (ENSDF and Radware).

Tools: defines several functionalities for the gamma-ray analysis (interactive gating on matrices, spectra conversions to other analysis framework, etc.).

In order to benefit from all the possibilities offered by the ROOT framework (<http://root.cern.ch/>), which is particularly designed for physics analysis, all the libraries are fully compliant and can then be used to extend the system.

The package also includes the ADF library, a standalone library developed, which will be loaded in the AGATA Data Acquisition system (see the DAQ section). It provides an abstract interface to Narval so that algorithms can be developed/debugged/tested/optimized outside Narval. As well it fully defines the data flow structure and give interfaces to algorithms to easily access the interesting data.

User guides, test and demonstration programs are provided within the package. A hyperlink (html) documentation of the code itself is automatically produced using Doxygen. The interaction between the users and the developers is done through a bugtracker (mantis) to report for bugs, ask for new issues, follow their status and be informed of major developments. Based on php and a mysql database, it is hosted at the in2p3 computer centre (<http://cc.in2p3.fr/>).

As well, an e-log for general discussions, to ask for tips, help and a weblog, to be informed of intermediate results (based on php with a mysql database), are available. Various RSS feeds are also provided. All the information concerning the data analysis software can be found at the following address <http://agata.in2p3.fr/>.

## 16. Mechanical Design

The mechanical requirements of the AGATA detector array were to design a support structure that meets the following requirements:

- The structure must rigidly hold 15 interchangeable detectors in a radial  $1\pi$  configuration, where the detectors are separated by 0.5mm.
- The structure must allow the detectors to be individually removed without touching adjacent detectors.
- The structure should allow the array of 15 detectors to rotate from  $-50^\circ$  to  $-110^\circ$  relative to the detector co-ordinate system.
- The structure should allow the detectors to be moved from 233.8mm to 143.8mm for experiments, and to retract the detectors to allow access to the reaction chamber.
- The structure must fit within the constraints of the Prisma Spectrometer, and allow for INFN Legnaro's infrastructure requirements.
- The detector support structure should be modular to allow for expansion to a  $4\pi$  ball.
- As much as reasonable of the support structure should be transferable to other labs when the detectors are moved.

The requirements were met by developing the design shown below.

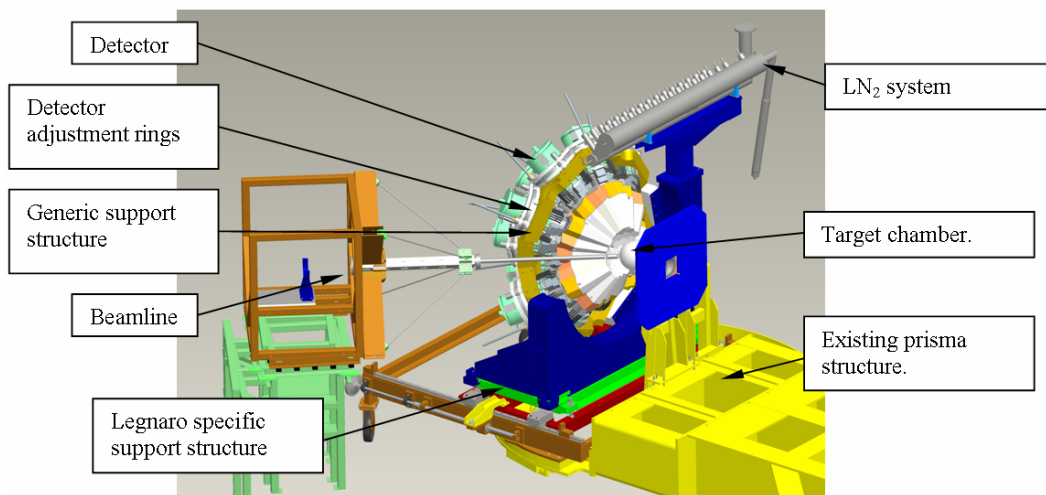


Figure 16.1  $1\pi$  detector array at Legnaro.

### 16.1. Detector Design

The first task on Agata was to determine the number and shape of detectors required. This work was carried out by INFN Legnaro using GEANT4. A Geodesic sphere was tiled using 60, 80, 110, 120, 150, 180, 200 and 240 hexagons and 12 pentagons as shown in Figure 16.2. In this figure each hexagon represents a germanium capsule, and the pentagons are ports through which a beampipe, target ladder, or other equipment may enter the array. Different shapes are shown in different colours. From Figure 16.2 the sphere can be tiled with 60 identical hexagonal shapes, as shown in the first sphere or if 240 hexagonal shapes are required, then there will be 4 slightly different hexagonal shapes as shown in the last image.

From this work, two configurations were shortlisted as highlighted, with 120 crystals or 180 crystals. Some further properties of these arrays are shown in Figure 16.3.

The collaboration chose the 180 configuration. This array is interesting in that it has a better Angular coverage of the rings, and only 1 detector cluster type is required, also the shape is highly symmetrical. The crystal configuration within the cluster uses three differently shaped asymmetrical hexagonal crystal designs as shown in Figure 16.4. One of each crystal shape is combined into an aluminium end cap to make a detector.

The shape of the crystals and the endcap that contains them was initially modelled in GEANT4. The co-ordinates of the endcap were then exported from GEANT4, and used to model the detector endcap in ProEngineer. Figure 16.5 shows the single cluster detector modelled in ProEngineer from the GEANT4 geometry. The endcap shape was extended to allow for space to accommodate the crystal support structure and preamplifiers.

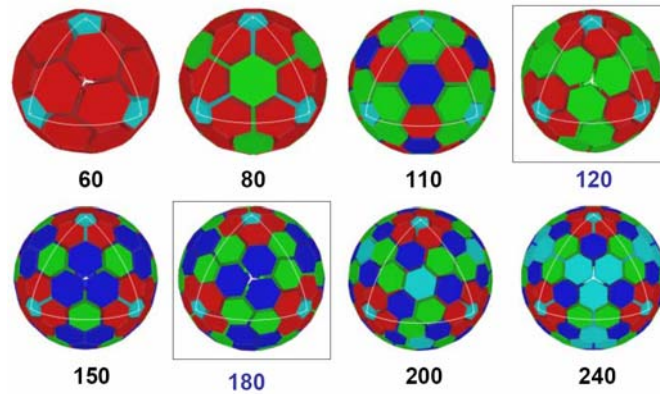


Figure 16.2 Tiling a Geodesic Sphere

Number of crystals	120	180
Solid Angle (%)	72	79
$\epsilon_{ph}$ / PT at M = 1 (%)	38 / 58	42 / 58
$\epsilon_{ph}$ / PT at M = 30 (%)	20 / 45	25 / 48
Inner free space (cm)	16	21*
Number of clusters / types	40 / 2	60 / 1
Rings of clusters	3-7-10-10-7-3	5-10-15-15-10-5
Angular coverage of rings	irregular	very regular
Electronics channels	4440	6660

Figure 16.3 Comparison of 120 and 180 hexagon crystal configurations

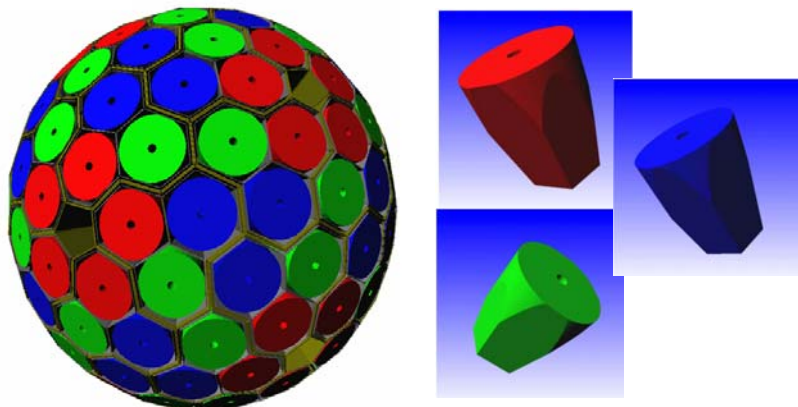


Figure 16.4 The 180 detector geometry and crystal shapes

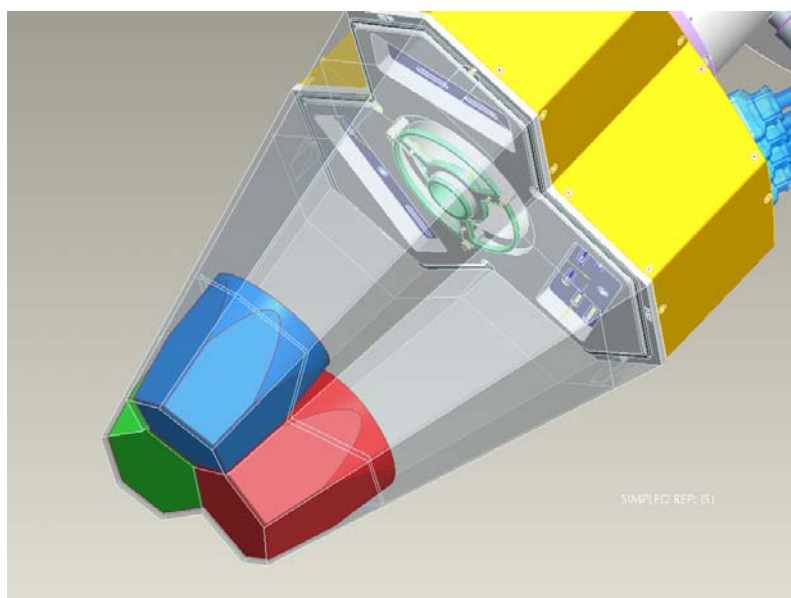


Figure 16.5 The crystals positioned within the endcap of the detector

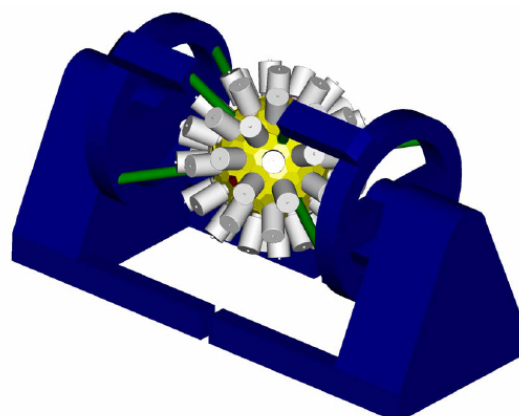


Figure 16.6 4 $\pi$  support structure

## 16.2. Generic Support Structure

When the design of the detector was established it was possible to look more closely at the detector support structure. A 4 $\pi$  structure based on the design at GammaSphere was examined as shown in figure 16.6. The concept here is that the ball of flanges is supported back to the blue structure with the green support rods. The ball is in two halves and the blue structure is motorised so that the experimental chamber can be accessed. The ball can also be rotated to allow for removal of the detectors.

The support structure for the Agata Demonstrator was then considered. This consists of 15 flanges assembled together to produce a 1 $\pi$  structure as shown in figure 16.7. This structure is used for the first phase of the Agata project and is now installed at Legnaro. It is modular in concept and so similar flanges can be manufactured to expand the coverage of the structure.

The precision of machining required for these flanges is very high especially on the angled faces. Any error on the angle is magnified 5 fold at the detector. Consequently an error

of between  $0.021^\circ$  and  $0.0086^\circ$  on angle, depending on which face is chosen gives a 0.1mm movement at the tip of the detector. This is the allowable error budget for the flange manufacture.

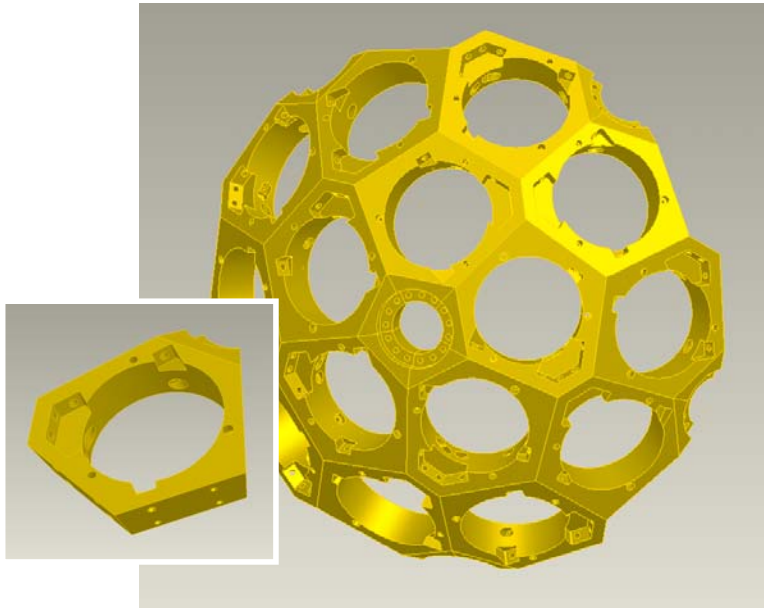


Figure 16.7  $1\pi$  Generic Support Structure



Figure 16.8 Images of the flanges being machined and inspected

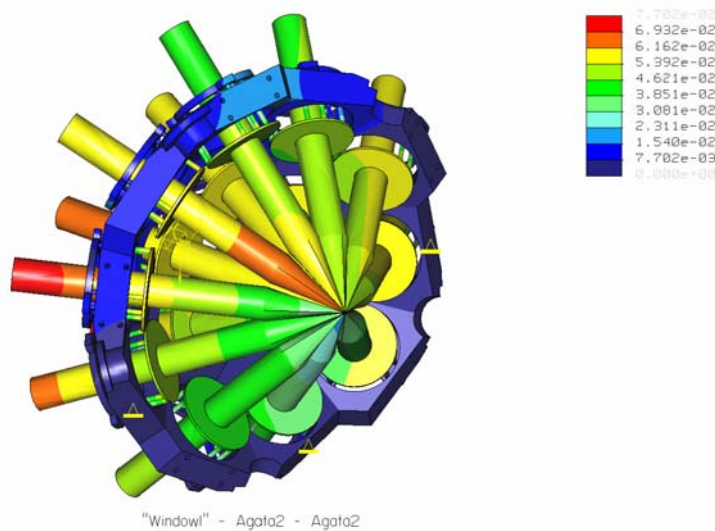


Figure 16.9 FEA of generic support structure under loading

To prove the machining procedure a prototype flange was made by INFN Legnaro and sent to Daresbury to inspect on a Coordinate Measuring Machine. The inspection

confirmed that the flange was within specification and so the production run of flanges commenced.

Finite Element Analysis was carried out on the flange array to identify the level of deflections and stresses that would be seen at the target point of the detectors under loading. A number of different cases were modelled; a 15 flange, 14 flange and 13 flange array to assess the implications of altering the array if required. Figure 16.9 shows the results from a 15 flange array.

The Assembly of the flanges was supervised and checked using a laser tracker to ensure that the flanges were accurately positioned as they were fastened together. A laser tracker was chosen to perform this task due to its measurement accuracy (approx  $10\mu\text{m}$ ). The other advantage is that this instrument can be used to check the position of each flange as it is assembled.



Figure 16.10 Flanges being positioned using the laser tracker

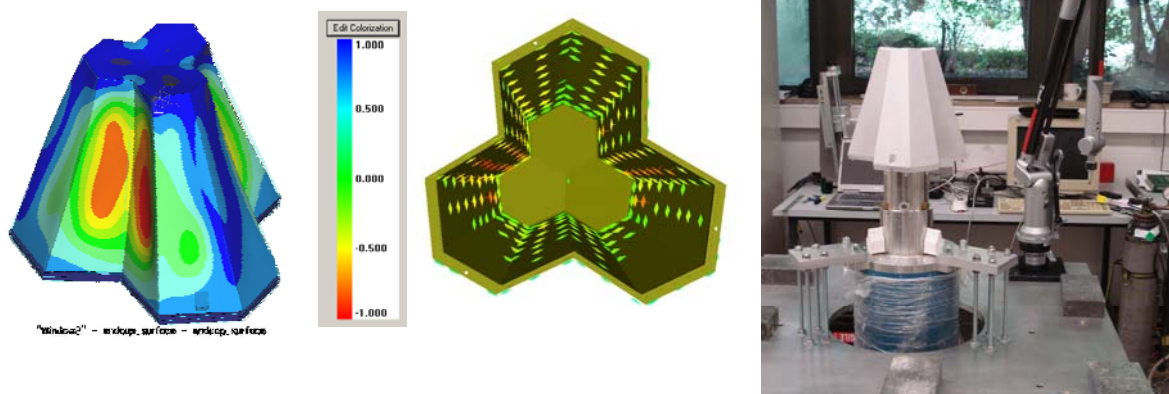


Figure 16.11 Image on right is Detector being measured at Cologne, middle image is measured results, left hand image is FEA deflection results

As well as the support structure being accurate, it is also important that the detectors are correctly positioned within the support structure. A Romer arm was taken to Cologne and used to measure 2 detectors under vacuum and atmospheric loading conditions. This instrument was used as it does not require a line of sight in order to take measurements, is very portable and its specification is 30micron over its measuring volume.

The results from this instrument showed that the endcap deflected more than expected under atmospheric loading. This was later confirmed by direct measurement and FEA modelling. It was from the measurements of this instrument that it was felt advisable to have individual adjustment for the detectors.

### Detector Adjustment Ring

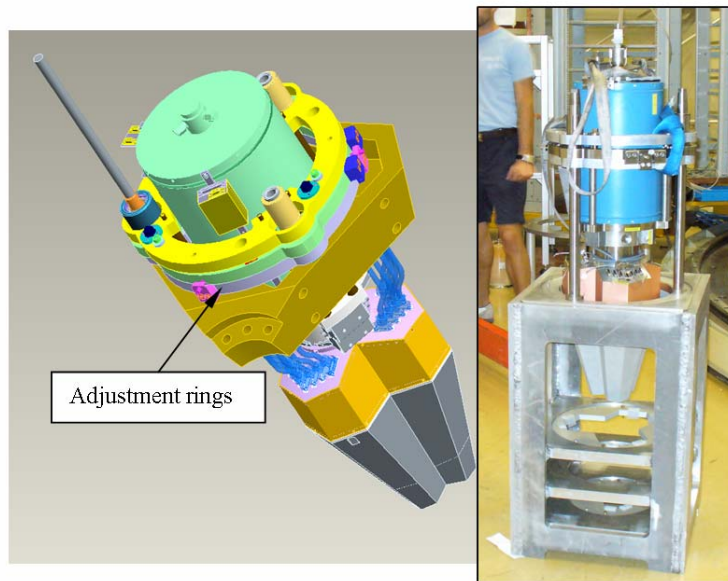


Figure 16.12 Detector adjustment rings and setting gauge

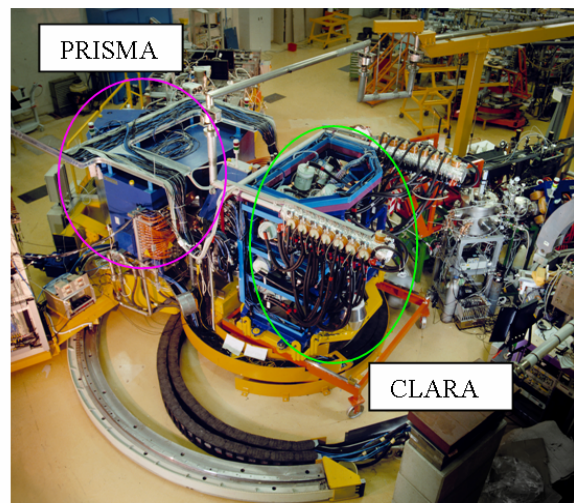


Figure 16.13 Location of AGATA demonstrator

Adjustment rings were provided for each detector so that every detector has full 6 degree of freedom adjustment capability. A detector gauge has been made such that the detector is in the correct location when it has been fully lowered into the gauge and is 1mm on all sides of

the shaped plates within the gauge. This allows the detector to be correctly positioned before it is loaded into the support structure. The detector is to be positioned within 0.1mm of its theoretical position, and so it was critical that this gauge be made to high tolerances. Hence the gauge plates were made using the spark erosion process, and the frame was welded and then turned on a large lathe in order to maximise the accuracy.

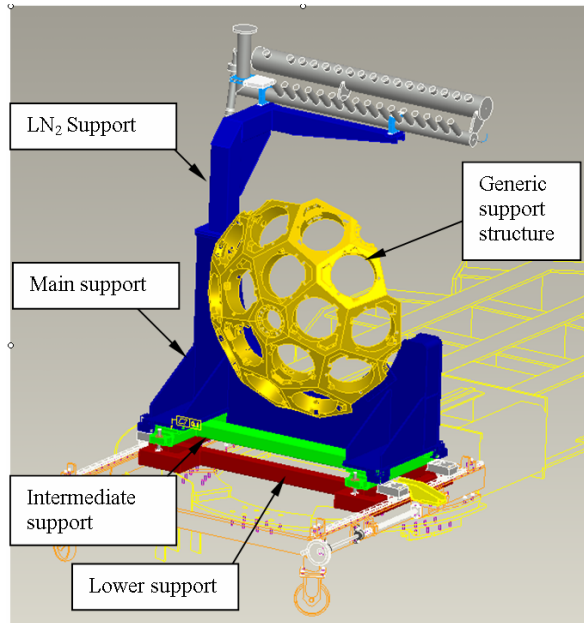


Figure 16.14 Legnaro Specific Framework



Figure 16.15 Using the laser tracker to position the generic support structure

### 16.3. Legnaro Specific Support Structure

The generic support structure already discussed can be moved between facilities along with the detectors without being altered. However, because the facilities are so diverse it is necessary to design a specific frame for each facility to allow the generic support structure to be installed. In the case of Legnaro the Agata Demonstrator was to replace the CLARA detector array and tie in with the existing PRISMA spectrometer.

The Legnaro specific support consists of a lower support frame, Intermediate support frame and Main support frame. This is designed to sit on the same support structure as that used by the Clara detector array.

The Intermediate support allows the position of the generic support to be altered in height, pitch and roll, while there are pushers on the main structure that give lateral motion and correction in yaw. This frame was engineered to be extremely rigid so that it will not deflect when additional detectors are added to the array.

This structure was positioned in the Legnaro facility using a Laser tracker. The machine datums were established using a telescope to position the laser trackers retroreflector, and then the structure was positioned to within 0.1mm using the datums on the flanges.

#### 16.4. Agata At Ganil

When the physics program is complete at Legnaro it is planned to move the Agata Demonstrator to Ganil. In view of this Ganil have already begun to look at how Agata could be best sighted on the existing Exogam platform.

Some of the challenges include removing two flanges from the structure, and yet keeping the integrity of the array, as shown in the bottom right image, and designing the structure to allow for easy access to the reaction chamber.

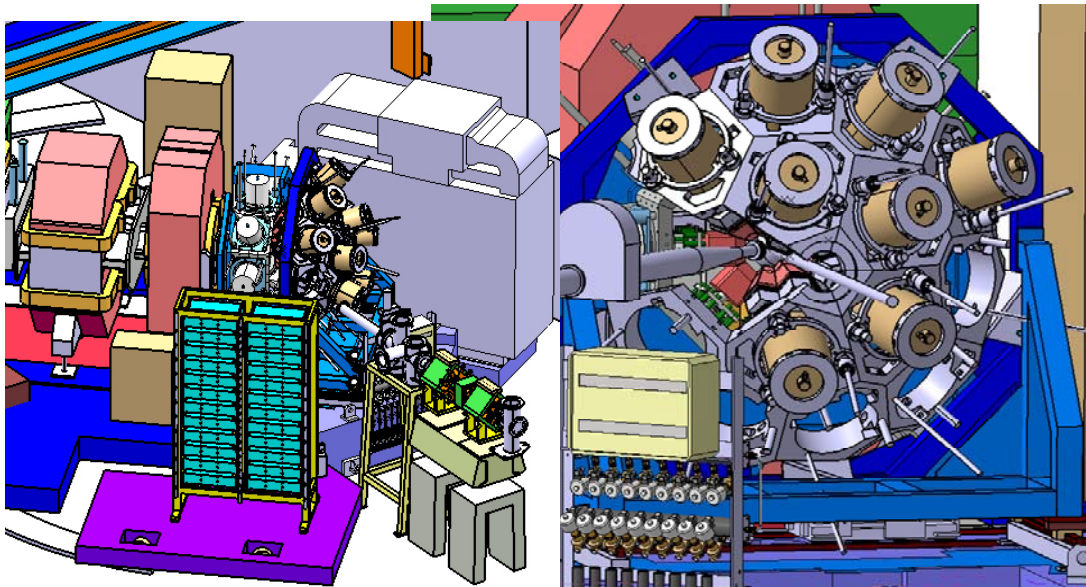


Figure 16.16 AGATA at GANIL

## 17. Mechanical Integration of the complementary detectors

Considering the present experimental programme of the AGATA demonstrator at LNL, it is foreseen to use mainly three complementary detectors, namely PRISMA, DANTE and HELENA. PRISMA is a large-acceptance magnetic spectrometer with tracking capabilities, and coupled to the AGATA Demonstrator, will be devoted to the study of neutron-rich nuclei. DANTE is a sensitive position heavy-ion detector to be placed at the grazing angle of the reactions to increase the gamma-gamma coincidences, but without isotope identification. HELENA is a multiplicity filter for gamma rays. These three detectors might be used even contemporarily during the experimental campaign of the AGATA demonstrator at LNL.

Multi-nucleon transfer reactions will be used to populate the neutron-rich nuclei of interest. These binary reactions present a maximum of the cross-section at the grazing angle, which varies from reaction to reaction. This feature places strong mechanical constraints to the experimental setup. Therefore the whole system has been designed to allow rotation and translation around the target position with a high accuracy. The beam line is retractile allowing in this way the rotation of the setup to the allowed angles.

In addition the reaction chamber has been designed to fulfil the intrinsic necessity of low-gamma absorption for the AGATA detectors, and therefore it presents thin-homogeneous aluminium walls. The whole system has a large rotation freedom; it can rotate from  $0^\circ$  to  $120^\circ$ . These features will be explained in more detail in the following sections.

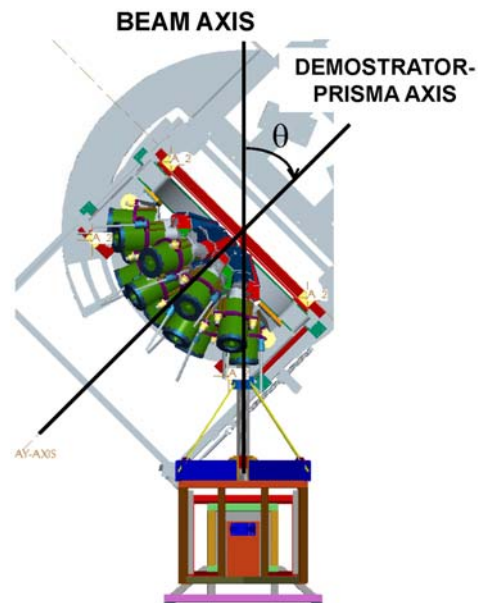
### 17.1. Reaction Chamber and Beam Dump

The reaction chamber has been designed to fulfil the requirements of the AGATA Demonstrator-PRISMA setup and considering the possible complementary detector i.e.:

- Allows the rotation of the setup in a continuous way and with a broad angular range
- Presents low gamma absorption in the angles corresponding to the AGATA Demonstrator.
- The beam-dump is an extension of the chamber and can be used in a large angular range without major mechanical changes
- The vacuum in the chamber is optimized for the use of MCP detectors inside the chamber as well as at the PRISMA entrance as start-detector.

Fig 17.1. Schematic view of the rotation axis between the beam direction and the AGATA demonstrator-PRISMA setup.

The chamber allows rotating the AGATA demonstrator together with the PRISMA spectrometer, respect to the beam line, with angles ranging from  $0^\circ$  to  $120^\circ$  in a continuous way, see Fig. 17.1. The rotation is accomplished via the use of a 2 mm-thick spherical shell Fig 13.2 B which is closed by a set of three different 2 mm-thick spherical caps Fig 13.2 C, which results in a low gamma absorption. Each of these caps can be positioned and moved **so that a total angular range that goes from 0 to 120 degrees is available**. Depending on the angular coverage of the DANTE array, there are two possible target positions (Fig 13.2 B<sub>1</sub> or B<sub>2</sub>) to be used. The chamber presents an internal radius of around 11 cm.



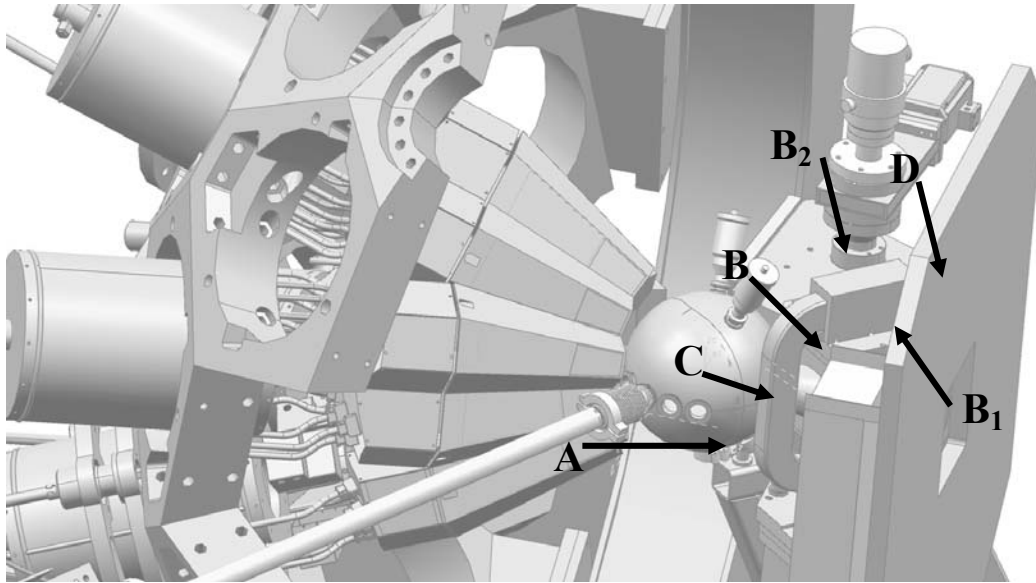


Fig.17.2. Schematic view of the reaction chamber for the AGATA demonstrator.

Coupled to the reaction chamber there is an external beam dump (about 50cm long Fig 17.2 **D**), which permits to completely shield the AGATA detectors from the gamma background produced by the beam. This external beam dump ranges from  $40^\circ$  to  $85^\circ$ . The beam dump has the possibility to place within it, small ancillary detectors, like Si monitors to measure Rutherford scattering, see Fig 17.3. The beam-dump extension incorporates a turbo-molecular pump to ensure a vacuum of the level of  $10^{-6}$  mbar in the chamber.

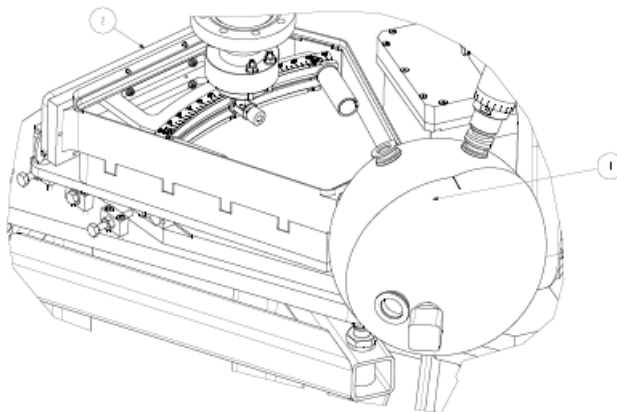


Figure 17.3: Schematic view of the external beam-dump coupled to the reaction chamber. It ranges from  $40^\circ$  to  $85^\circ$ .

## 17.2. Beam line

A telescopic beam line has been built to allow rotation to all the angles without interfering with the mechanical structure of the AGATA demonstrator. The beam line retracts up to 1 m allowing free space for the rotation around the target position, see Fig 17.4.

The inner tube (34,5mm outer-diameter) can slide inside the outer one when the global AGATA structure has to be moved at a different angular position.

Figure 17.5 shows the telescopic beam line connected to the reaction chamber and fully extended. The connection to the reaction chamber is made through a short bellow fitting (about 90mm long, Fig 17.2)

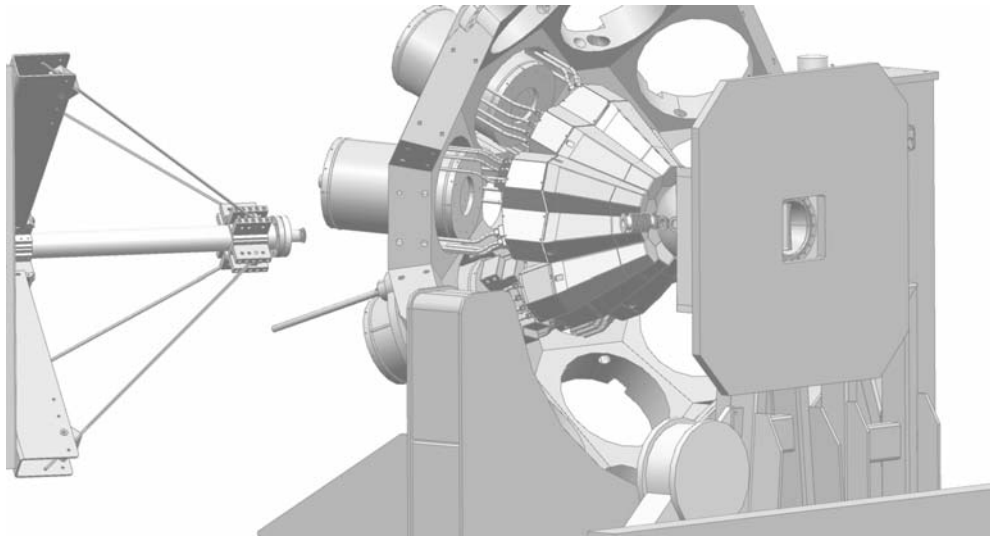


Fig. 17.4. Schematic view of the telescopic beam line when the inner part is retracted to allow rotation.

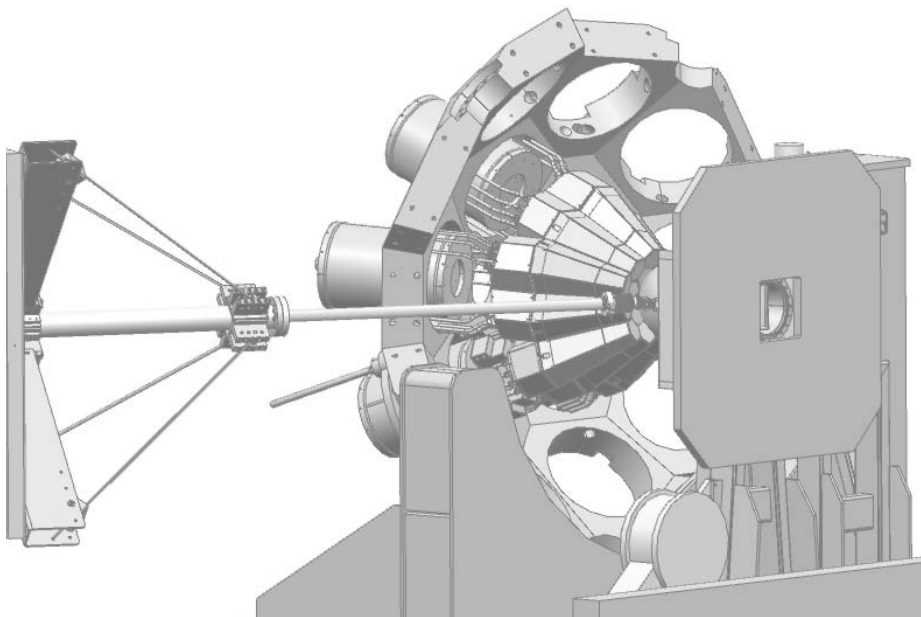


Fig. 17.5. Schematic view of the telescopic beam line when it is connected to the reaction chamber through a bellows fitting.

### 17.3. DANTE detector support

The chamber presents an internal radius of 11 cm which allows to place the different geometries of the DANTE detector, see Fig 17.6. A series of aluminium rings have been designed as a support of the DANTE array, and **will** be placed within the reaction chamber. The rings are done in such a way that **they** can cover all the angles of the ejectiles and **they** present a machining resolution better than 1 mm. Each of the rings can hold from 2 detectors in the case of the 26 degrees configuration up to 9 detectors in the 90 degrees configuration. The angular coverage **of each ring** is  $\pm 20^\circ$  in the azimuthal  $\theta$  direction.

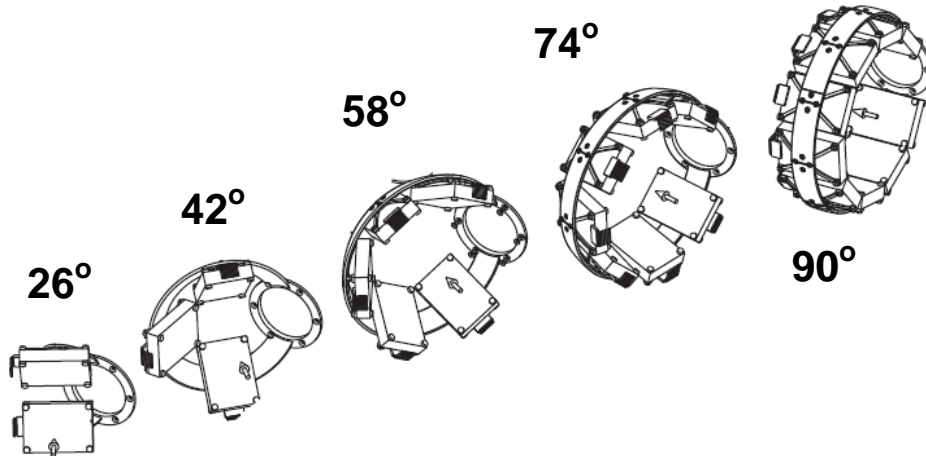


Fig 17.6: Schematic view of the support for the DANTE array, showing the different rings configuration. These arrays are to be placed within the reaction chamber.

#### 17.4. HELENA detector support

HELENA is a multiplicity filter that will allow both to disentangle lower and higher multiplicity regimes corresponding to deep-inelastic processes and Multi-Nucleon-Transfer as well as to select high-spin states in fusion reactions.

The project is based on the use of the 3''x3'' hexagonal BaF2 detectors from the HELENA array used by the Milano-group. To maximize the efficiency one has to maximize the number of detectors: 27 of them can be inserted between the AGATA flanges and PRISMA first quadrupole. They are grouped in 5 clusters: cluster 2 and 3 with 8 detectors each, clusters 1 and 4 with 4 detectors each and cluster 5 with 3 detectors, see Fig. 17.7.

A compromise has to be found to maximize both the  $\gamma$ -ray detection efficiency and the neutron rejection which is based on a time-of-flight technique. An optimum distance of 15cm has been chosen.

The total solid angle covered by the HELENA array will be about 45% of the  $4\pi$  and the total efficiency will be about 30%.

The mechanical support has been designed by the Mechanical Workshop of INFN-Milan, see Fig. 17.8. The basic support is an hexagonal frame which is anchored on the AGATA flange structure by adjustable jigs. To minimize deformations of the hexagonal frame a couple of additional brackets have been added. Each of the 5 HELENA's clusters will be held on the hexagonal frame with regulating support allowing all necessary adjustments.

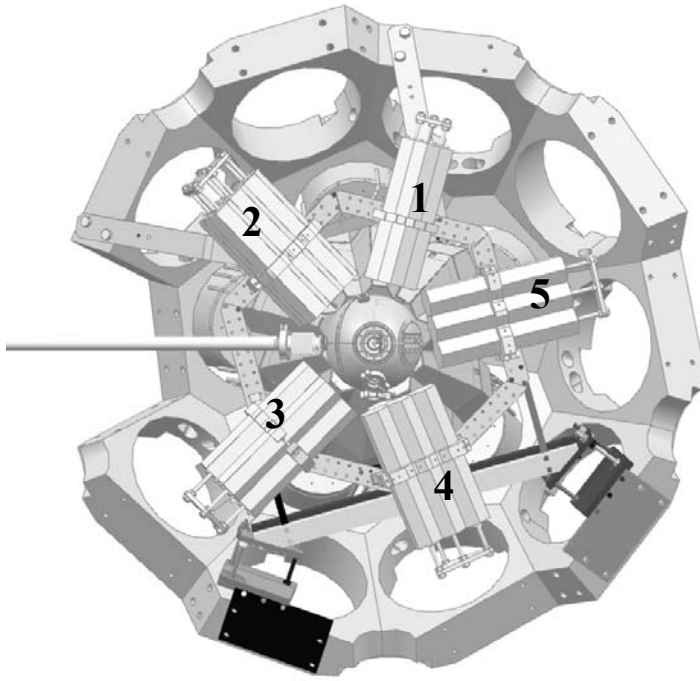


Figure 17.7: Schematic view of the HELENA array, grouped in 5 clusters: cluster 2 and 3 with 8 detectors each, clusters 1 and 4 with 4 detectors each and cluster 5 with 3 detectors.

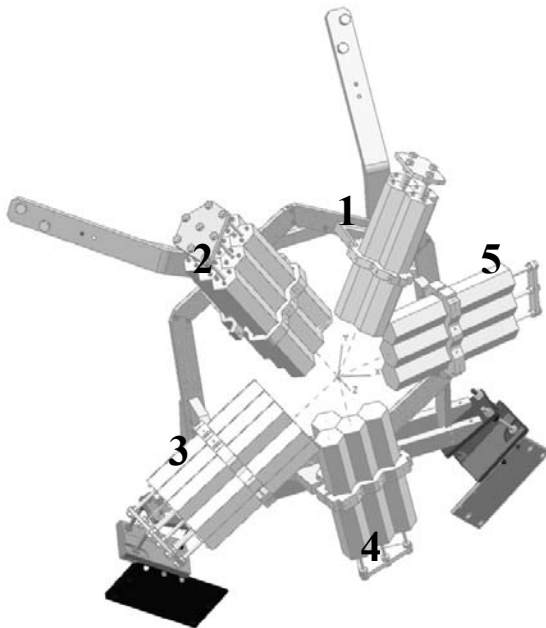


Fig. 17.8. Schematic view of the basic support, which consists in an hexagonal frame which is anchored on the AGATA flange structure by adjustable jigs.



## **18. Infrastructure**

### **18.1. Introduction**

The aim of the AGATA Infrastructure Team is to provide a front-level support for all aspects of the AGATA Demonstrator infrastructure at the Host Laboratories. This covers location and layout of the various systems of AGATA from the mechanics, detectors through the electronics to the final data collection. In addition the team provides and maintains the “life-support system” for the detectors, providing cryogenic cooling, both low- and high-voltage power supply, constant monitoring, a friendly user interface and actions on critical situations (detector warming, loss of power, etc.) This core system is the Detector Support System (DSS) and has been developed in collaboration with IRFU and GSI. Input on design, realization, and use has been undertaken from every other AGATA Team (preamplifiers, detectors, digitization, ancillary detectors, etc.) together with the Host Laboratories which will finally use the system.

### **18.2. Detector Support System**

#### Low Voltage

##### Preamplifiers

The DSS supplies low voltage to the detector preamplifiers. For each AGATA triple cluster, 111 preamplifiers have to be powered demanding a large current. For this reason sense wires are included to regulate the voltage within specified tolerance. The design of the low voltage uses a floating supply system, ensuring that the 0V reference is at the detector and all return currents pass through the supply to minimize detector noise.

##### Digitiser Supply

The detector signals are digitised at the front end by the AGATA Digitiser. As this coupled directly to the detector, power supply also has to be given to these devices. The power consumption is large in comparison to the detector, therefore attention has to be taken to avoid noise coupling. In times of laboratory power failure, it is the role of the Detector Support System to determine if the power to these devices is to be interrupted to extend the support of the detectors themselves.

##### High Voltage

The unique aspect of the AGATA triple cluster is the detector High Voltage (up to 5000V) is delivered directly on the cryostat. The voltage also needs to be controlled and monitored; therefore control over the voltage generation also needs to be performed at the cryostat. In addition the supply to the detector should be filtered. In cases of detector problems (increasing temperature, over current) then it is the role of the high voltage system to take action at the first level.

##### Cryogenic Autofill

Each AGATA triple cluster should be cryogenically cooled with liquid nitrogen at regular intervals. In addition the information on detector temperature and cryogenic volume are also available. The autofill system manages the process and control of the cryogenic feed and associated valves. The system should also be operated manually and manage emergency filling when required. The autofill should be flexible to provide adaptation to the various Host Laboratories.

## Process Control

The entire process of the Detector Support System should be extremely reliable; therefore the choice of controller and also control bus should be as robust as possible. On occurrence of major problems, an alarm procedure should be followed.

## Graphical User Interface

The entire human interface of the Detector Support System is via the Graphical User Interface. This should be user friendly and allow both overall view of the system, allow for trending of the many various parameters, and also allow for expert control of the system whenever needed.

### **18.3. Cabling**

Cable management is important that each detector can be dismounted and mounted without disturbance. The type and length of cables have been considered to be suitable for further installation of the Demonstrator at other Host Laboratories.

### **18.4. Grounding**

To provide the best signal to noise ratio for the detector signals, especially in the use of pulse-shape analysis, grounding is of utmost importance. In addition this is the first level that has to be considered before installation of mechanics or electronics. The front-end electronics and Detector Support System has been designed to be optically isolated from the rest of the other systems. Close collaboration with the Host Laboratories prior to installations has been important.

### **18.5. Integration and Testing**

Many aspects of the AGATA Demonstrator are completely new, and far more complicated than in previous generations of gamma-ray arrays. At each step of development and prototyping, both before and after installation, stringent testing has been undertaken to evaluate the performance and perturbation on the detectors and other systems. The initial results will be disseminated in the further sections.

### **18.6. Low voltage power supply**

The digitizers PS (48V and 5V) will be close to their loads (8m). On the other hand, the PS related to the preamplifiers, high-voltage and liquid-nitrogen level measurements will be at a distance of 15m. In this case, as the cross section of the wires should not exceed  $0.6\text{mm}^2$ , the voltage drop for the highest current (+6V) can reach 1.5V (taking into account 3 wires). Figure 18.1 lists all voltages and currents needed at the loads.

		+5V	+6V	-6V	+12V	-12V	+24V	+48
Preamp.	Nb		8	8	8	8		
	Vmin (V)		5.95	-6.05	11.8	-12.2		
	Vmax (V)		6.05	-5.95	12.2	-11.8		
	I (A)		4.2	3.2	1.5	0.7		
	P (W)		25	20	18	10		
HV Boards	Nb	8						
	Vmin (V)	6.5						
	Vmax (V)							
	I (A)	3.45						
	P (W)	22						
Digitizers	Nb	8						8
	Vmin (V)	4.5						36
	Vmax (V)	5.5						75
	I (A)	0.4						27
	P (W)	2						1500
LN2 capacitive preamp	Nb				8	8		
	Vmin (V)				11.5	-12.5		
	Vmax (V)				12.5	-11.5		
	I (A)				0.02	0.02		
	P (W)				0.24	0.24		
Profibus-DP Line term.	Nb						2	
	Vmin (V)						21.6	
	Vmax (V)						26.4	
	I (A)						1	
	P (W)						24	

Fig 18.1: Current and voltage needed at the loads

The solution kept to fulfil these specifications is the one from the AXIS company. AXIS proposed to provide a crate (4U high) in which all the needed PS are mounted. They are all controlled through Profibus-DP network and are all linear supplies.

As the 48V represents the most powerful module (hence, the warmest and the heaviest), we tried to use a switching mode PS instead of a linear one. Noise spectra done in Legnaro on ATC1 didn't give good results for the switching mode PS (see figure 18.2.)

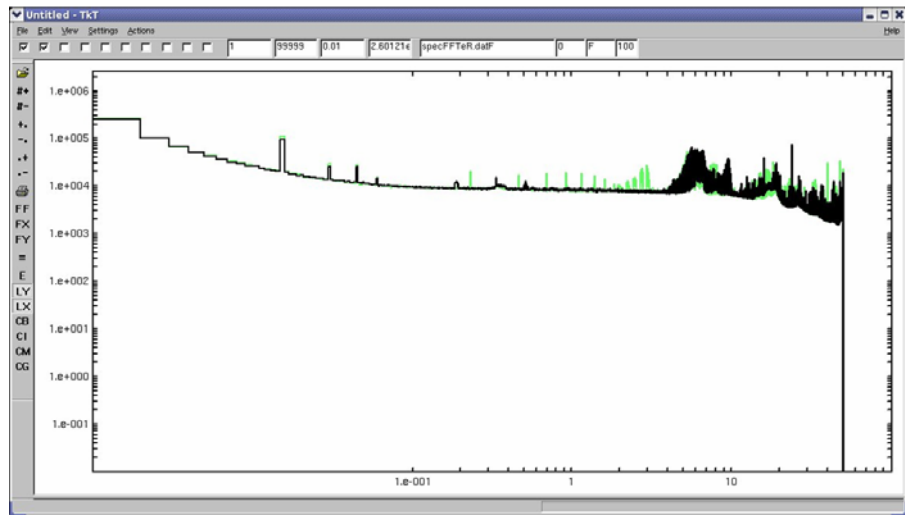
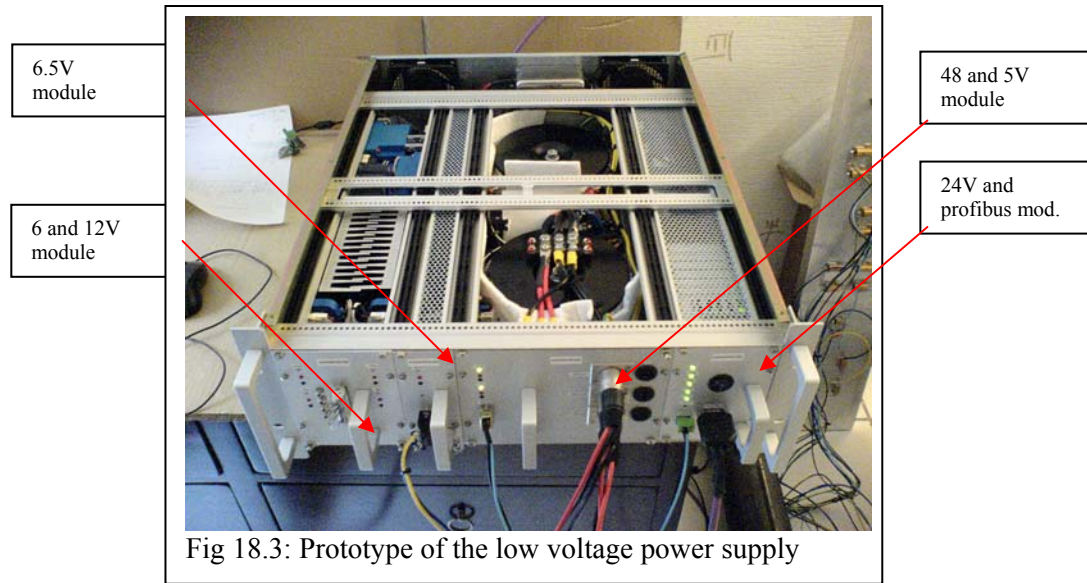


Fig 18.2: Digitizers 5 and 7 on linear PS (black) and on switching mode PS (green)

Nevertheless, it appeared that the consumption was close to 4A per digitizer. The maximum current could be 7A. A margin of 6A for 3 digitizers has been agreed as safe. So the maximum current that could be delivered per 48V module should be 27A instead of 38A.

A first prototype has been realized (figure 18.3) and tested this year. In spite of EMC problems difficult to solve in an experimental hall, we can say that results, as far as noise

produced at preamplifiers is concerned, are very similar to using NIM bins to supply an ATC [2] [3].



Several evolutions are foreseen for the production of the 3 first crates:

- the crate will be longer to improve the cooling,
- the nominal power of the 48V will be decreased from 1800W to 1300W,
- the 25 pin sub-D connector for 6 and 12V will be split into 2 sub-D 15 connectors (positive and negative voltages),
- the heat sinks will be modified so as to be more efficient,
- different cables will be used for 6 and 12V: individually shielded twisted pairs in a general shielding to try to reduce noise and therefore, oscillations.

### 18.7. High Voltage Infrastructure

An AGATA triple cluster is equipped with three HV Modules. Each one contains the ISEG HV unit, control electronics, HV filter and mechanical housing. The Module is fixed to the triple cryostat in a way that it makes also direct connection to the HV feedthrough. The connections from the electrical hardware (power supply and signals) are made by a total of 5 Fischer connectors, which is positioned in the side walls from the box. Because of the cryostat asymmetry and the limited space due to the ATC- cables, a specific difficulty by the installation has arisen as it is shown in figure 18.4.



Figure 18.4: The AGATA ATC complete with HV modules

The box has stepwise shape with the following dimensions:

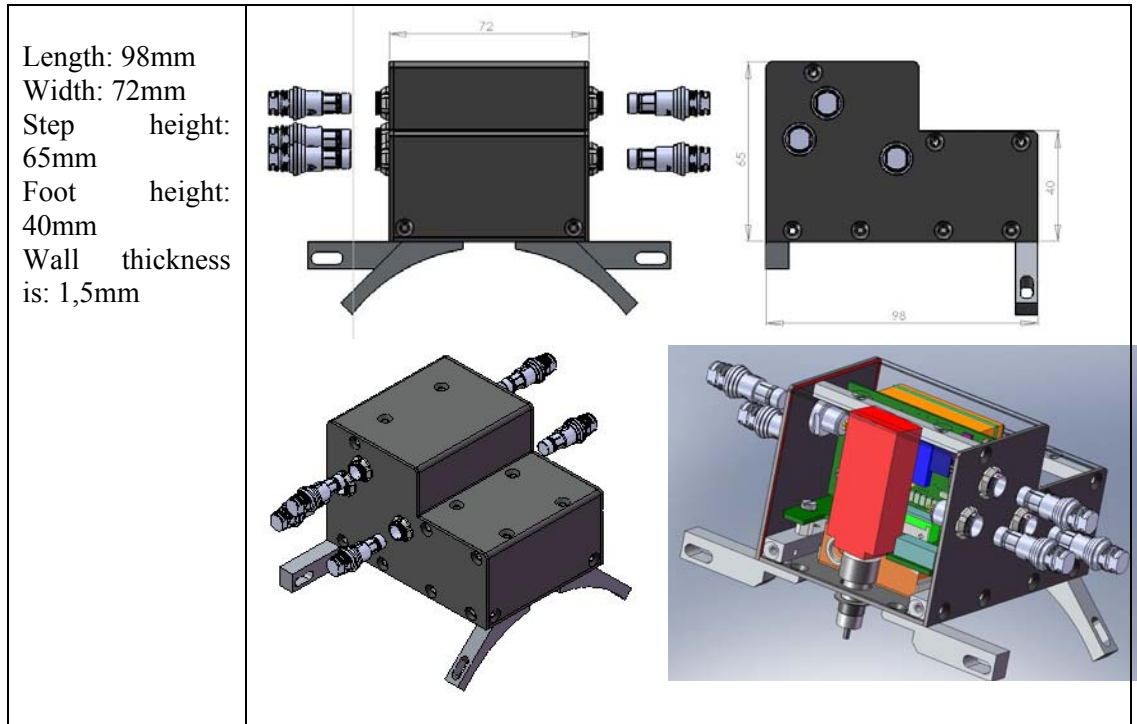


Figure 18.5: Main dimensions from the box and a fixed HV-Box on a cryostat

Positioning of the HV filter in the box is made in a special compartment at the upper part of the step as shown on Fig.18.5. It is a simple Low Pass filter second order (including the output impedance of the ISEG unit). The circuitry is shown on fig.18.6. The components are multiply coated by special resins in order to achieve low leak currents and breakdown stability. The contact feature is a special contact sleeve which protects the surfaces exposed to the environmental influence from humidity and contaminations. The HV Unit is connected by Teflon isolated wire and is contacting by Fischer pin.

Installation of the Box is relatively simple, straight forward until engaging the HV feedthrough pin

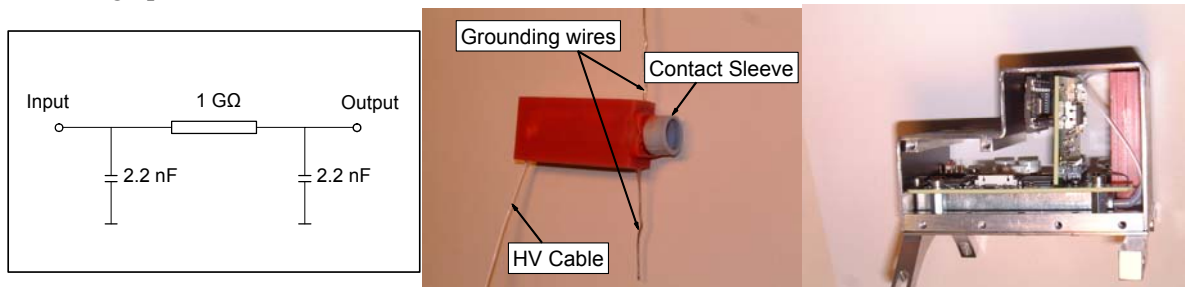


Figure 18.6: The HV filter circuitry and the implementation.

clicks in. Due to limited space tilting or other twisting manipulation is not possible. Do not force it if does not come in, perhaps something has gone in other direction. After engaging of the HV feedthrough the box is fixed by 4 screws which are providing also the ground and return path of the HV current.

### 18.8. High Voltage Module

High voltage modules will be mounted on the asymmetric triple cluster to avoid long HV cables and to reduce noise as much as possible. They will be driven by the control/command related to infrastructure but they need to be autonomous if the link with the GUI (more precisely, the PLC) is broken. This means each HV module is able to shut down if

for instance, the temperature of the detector is too high (Bias Shut Down). A schematic overview is given in figure 18.7.

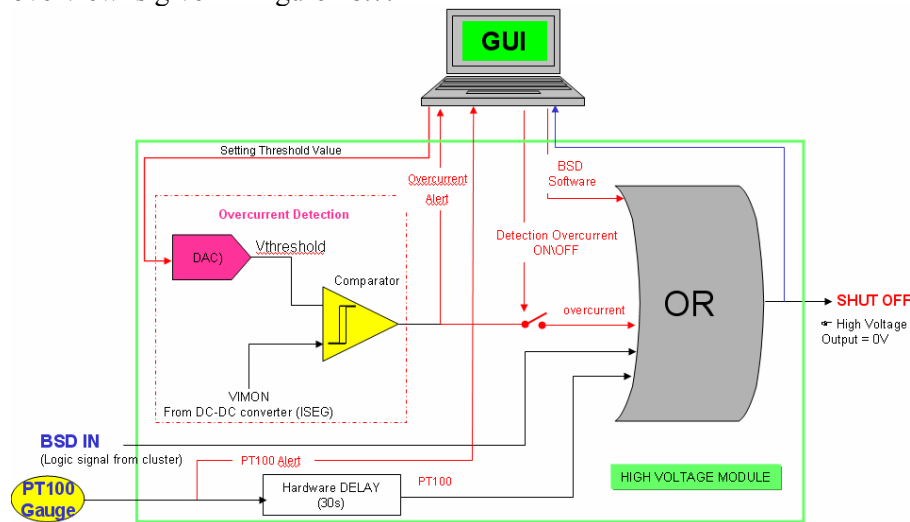


Fig 18.7: Bias shut down principle

This BSD is whether directly given by the Pt100 gauge placed on the cold finger or by a digital signal corresponding to a threshold generated by the HV box receiving the temperature gauge. Hence, when the first HV box of an ATC triggers, the three of them shut down.

To provide the 5kV needed to bias the crystals, a DC/DC ISEG unit (Mhp 50 103 5 2,5) will be embedded in each HV box (see figure 18.8.) As the other parts of the DSS, each HV box is able to communicate with the PLC thanks to the Profibus-DP fieldbus.

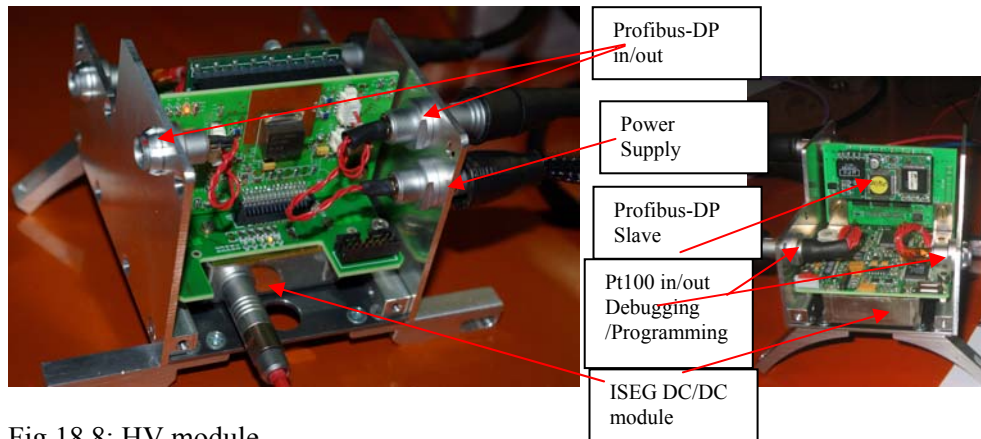


Fig 18.8: HV module

The lack of place around the cryostat led us to choose non standard elements for the Profibus-DP network. M12 or sub-D connectors have been changed for Fischer connectors. The cable is much thinner although its characteristic impedance is the same. The whole Profibus-DP architecture will be a mix of standard and non standard elements (Fig. 18.9). First tests showed good results.

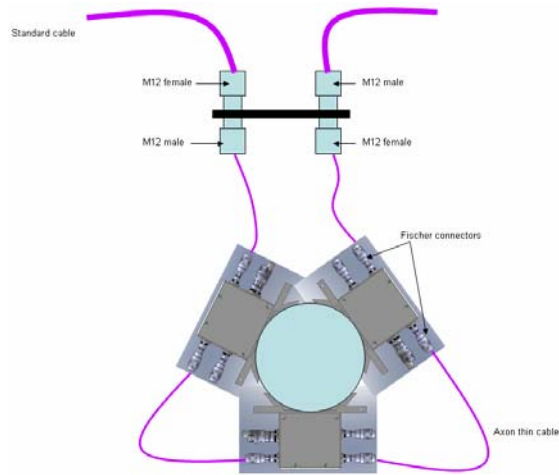


Fig. 18.9: Profibus-DP cabling on the cryostat

The setting of this DC/DC converter is done through one DAC and the readout of the output voltage and current through two ADCs controlled by a microcontroller and a [programmable logic device](#) (see figure 18.10.)

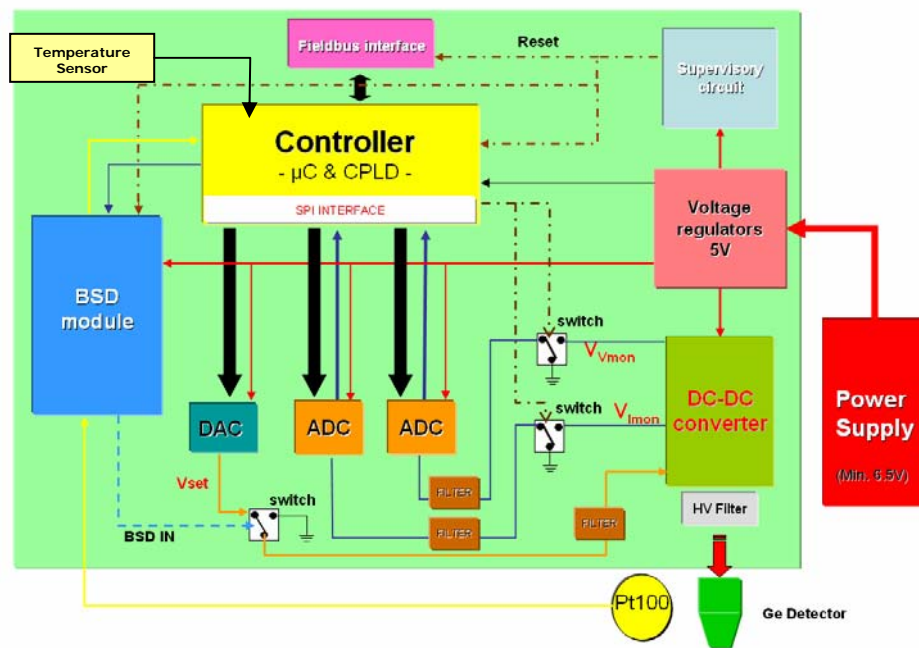


Fig 18.10: HV box architecture

The BSD module manages the safety as described in Fig 18.6. The communication with the PLC is done with an AGILIPLUG module.

The  $\mu$ controller has three main tasks to realize: communication, setup and monitoring. They are both realized (figures 18.11 and 18.12) within a period of 1s.

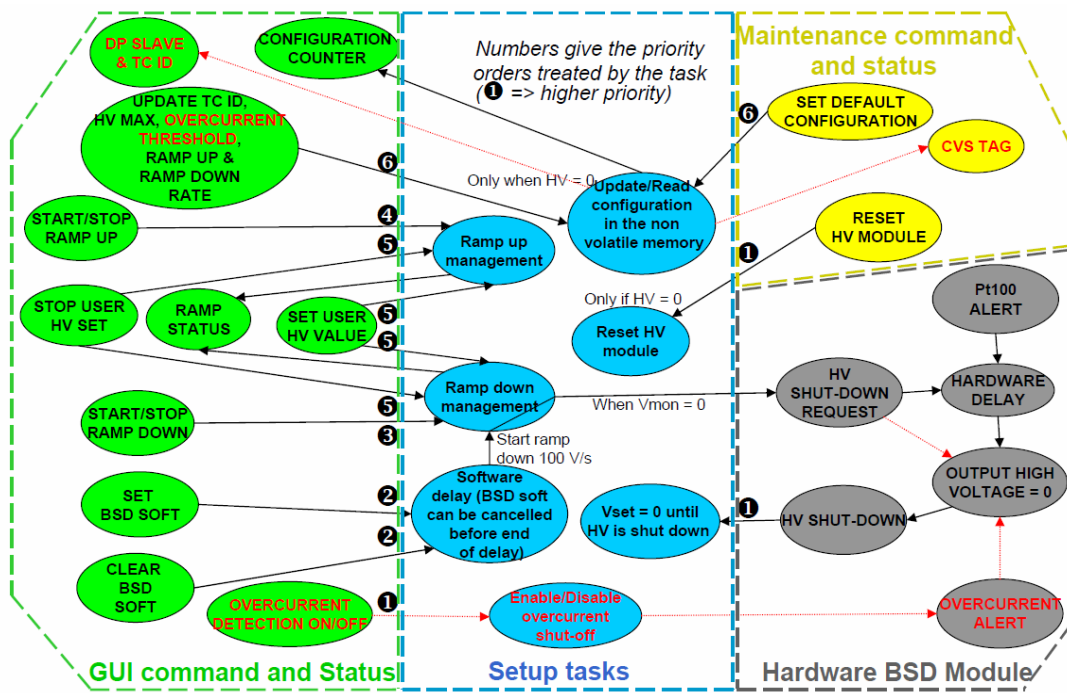


Fig. 18.11: setup task

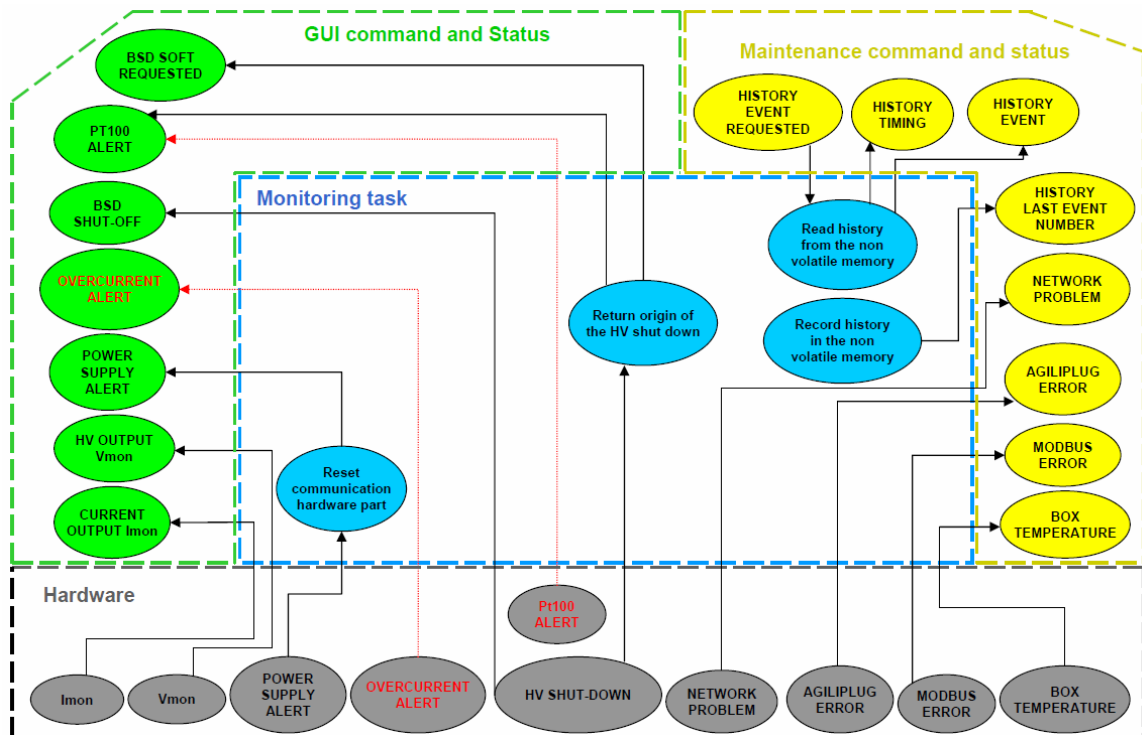


Fig 18.12: µcontroller monitoring task

Several parameters are embedded in the µcontroller for the safety and for the maintenance: the HV box ID, the serial number and the self-calibration values of the ISEG DC/DC converter, the maximum voltage, the maximum ramp up and ramp down rate and the setting threshold value for the overcurrent.

One prototype and three additional HV boxes have been produced yet to equip a full ATC. The production for the full demonstrator (5 ATC) will be done for beginning 2009.

## 18.9. Cryogenic Autofill

The AGATA Autofill System is based on PLC driven process under Profibus data acquisition and command standard. The algorithm of maintenance of the detector at LN2 temperature follows the following principles:

- Regular filling of the detectors within given schedule (Automatic Mode)
- forced fill of any detector if its temperature exceeds given threshold preserving the filling schedule even if one or several detectors have had forced filling (Legnaro exception – *Reschedule the filling if forced fill has occurred*)
- *Fill Now* feature based on software (Semiautomatic Mode) or hardware (Manual Mode)
- Manual actuating of any valves (Local Mode)
- Termination criterion based on the temperature measurements at the end of the exhaust line of LN2 recipient - *Terminate filling if LN2 temperature (-196 °C) is detected continuously for given time* (usually 5-9 sec)
- Utilization of Buffer Tanks (Legnaro exception – direct filling by Pipeline)
- Purge the Pipeline before filling of the Buffer Tanks or the detectors
- Monitor the pressure of the Buffer Tanks and if needed keep it within given pressure range
- Monitor the volume of LN2 in the Buffer Tanks and initialize filling if it drops below given threshold
- Issue warnings if any parameter declines from its regular values but is still within uncritical values range
- Issue alert if any of the parameters leaves the uncritical values range or any critical system or subsystem has malfunction

Fig.18.13a shows the generic structure of the Autofill and the Legnaro structure is given on Fig.18.13b.

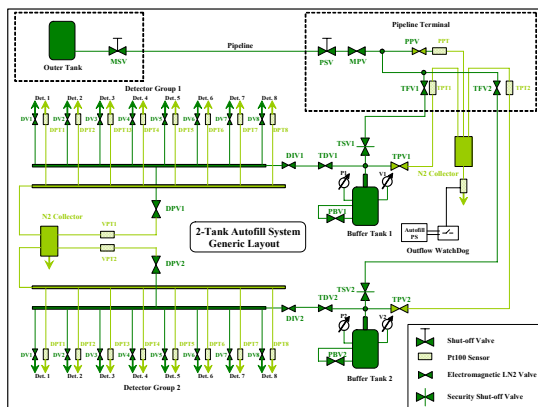


Fig.18.13a Generic Autofill Structure

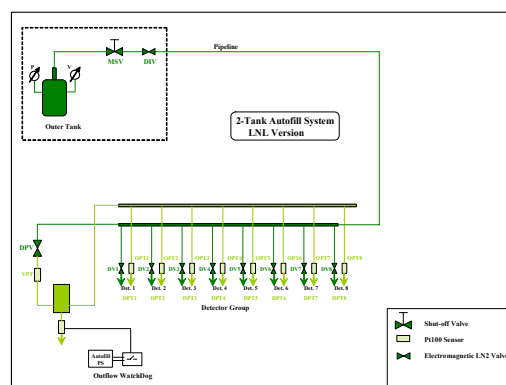


Fig.18.13b Legnaro Autofill Structure

Others tentative Labs – GANIL and GSI are supposed to follow generally the Generic structure. Technically the Autofill hardware is made out of the following components:

- PLC which steers the Autofill routine
- Profibus Crate (PbC) which contains Profibus terminals with various functions – Pt100 readout, Analogue (4-20 mA) readout, Digital input and output terminals, Profibus Watchdog and the relevant power supplies. The commands to the executors (valves, diallers) are sent via Valve Control Crate (VCC) and the signals from them are read out also via VCC.
- VCC, which contains 4 Valve Control Cards, Master Card and Dry Contacts Board

The crates and the connectors there are shown on Fig 18.14a and 18.14b. The power supply for the LN2 valves is fed into VCC fed from outside. The both crates are suitably interconnected.

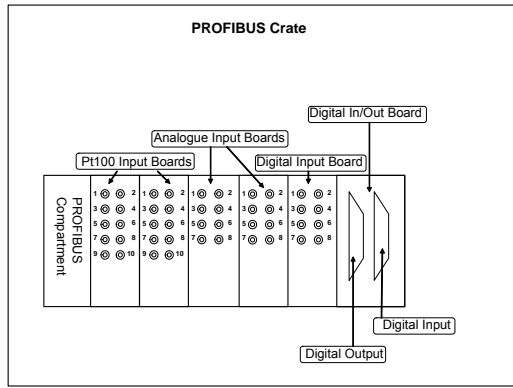


Fig.18.14a Profibus Crate structure

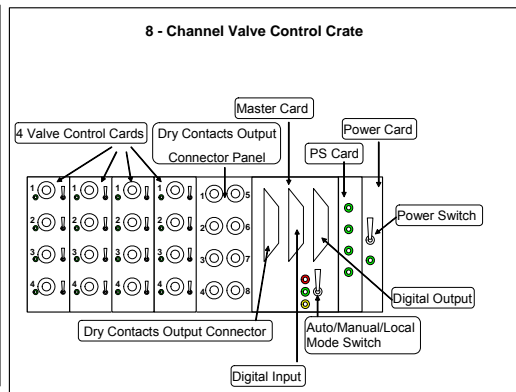


Fig.18.14b Valve Control Crate Structure

The cryogenic process has been evaluated in November 2008 on a preliminary setup but sufficient to simulate the filling of three Dewars. It is made up of three different modes:

- automatic mode: the PLC manages automatically the filling of the Dewars,

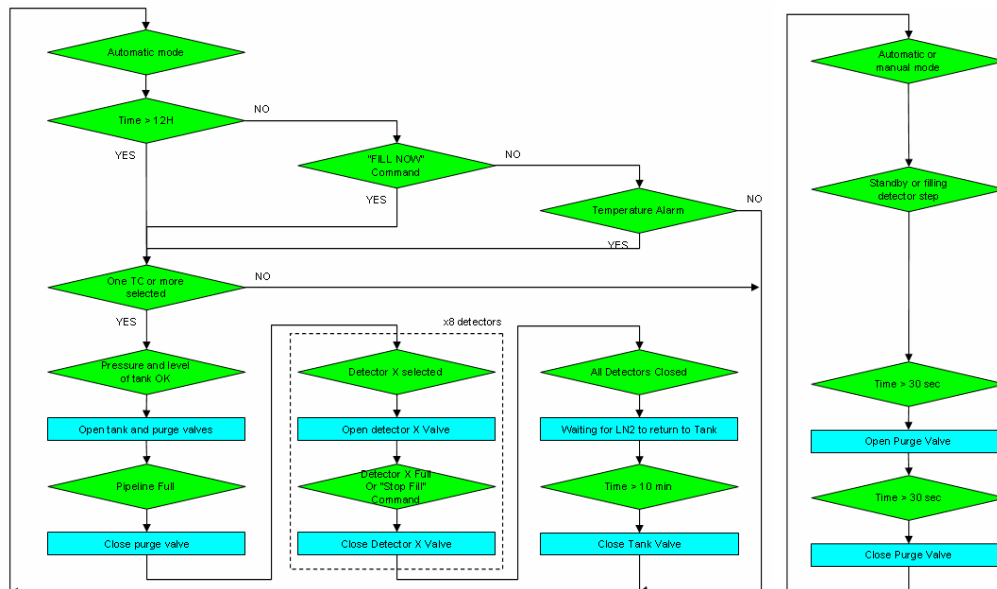


Fig 18.15: cryogenic process for automatic mode

- manual mode: the operator trigs the filling on the front panel of the Profibus crate but the PLC manages the filling of the line and actuates all the valves needed (tank, purge and detector valves),
- local mode: the operator actuates all the valves thanks to the switches on the front panel of the autofill crate. The PLC autofill process is disabled during this mode.

During the manual and automatic mode, the purge valve opens and closes periodically.

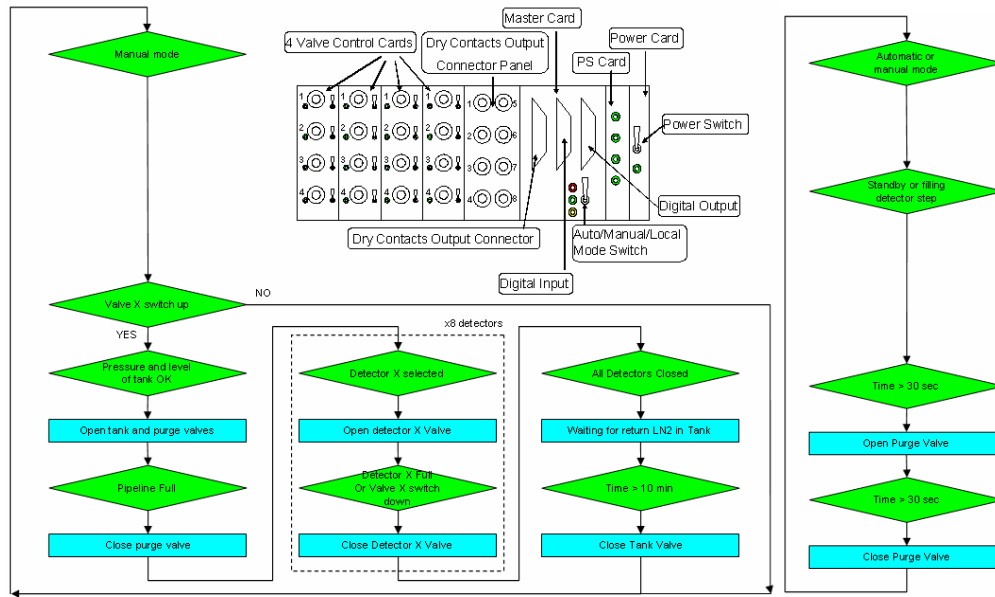


Fig 18.16: cryogenic process for manual mode

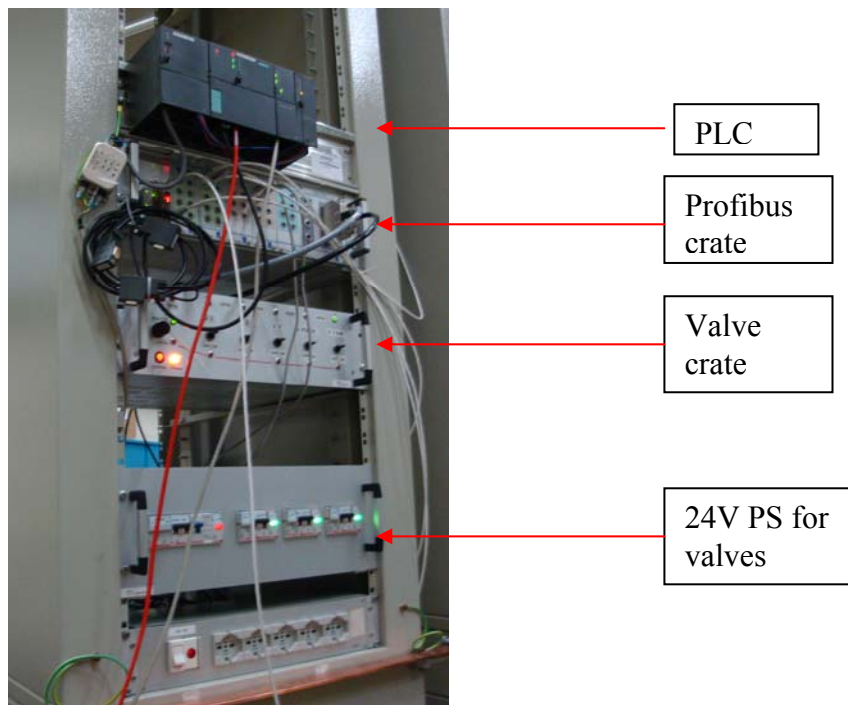


Fig 18.17: Autofill control/command setup for tests in Legnaro



The PLC will not only be a communication mean but it will also manage the cryogenic process needed to fill in the Dewars (see autofill section).

The maintenance server will be connected to Saclay for maintenance purpose. It will gather all data concerning the process so as to be able to diagnose a problem coming from the process itself, the PLC or the fieldbus. It is one of the most reliable parts of the system as it has no rotating parts as HDD or fan embedded. Its OS does not allow installing any software unless a particular procedure has been followed.

The yellow boxes of figure 18.19 correspond to optional functions that can be implemented if needed. Some of them will be directly connected to the digital output of the autofill crate.

### 18.11. Detector Support System Graphical User Interface

The DSS Graphical User Interface is designed to control and monitor the High Voltage, Low Voltage and the Autofill part of the Detector Support System, which is driven by the Process Control (PLC). To ensure a user-friendly and easy to use interface, different aspects had to be taken into account. First of all, there are different groups of users, which demand different kind of information to be displayed and functions to be offered. The operator is interested in detailed information on the state of the system. Both, the current status and the response of the system have to be displayed, to allow reliable controlling of the DSS. On the other hand, the regular user usually does not need to interact with the DSS, but demands a clear (more abstract) view of the overall system.

As the amount of data to be displayed will get quite large for the full array, it has to be distributed among different panels, such that only the relevant part is shown. The DSS GUI offers various ways to access the whole set of data. For example there are three tables, showing all parameters for one detector, user selected parameters for all detectors or the raw data block coming from the PLC. A graphical representation is provided in the trending section, where historical data is displayed (fig.18.20). Here the user can open multiple tabs and for each select the items to be displayed and updated periodically.



Figure 18.20 The trending section of the DSS GUI. The Graph shows the trend of the temperatures at the detectors and pipeline (yellow) purge valves, recorded during a test of the filling sequence. The time axis spans four hours and the y-axis is in Kelvin.

One of the main graphical elements of the DSS GUI is an icon that displays the status of a single detector by a simple traffic light colour scheme (Fig.18. 21). This icon is found on

different panels and is also used to navigate between the sections. There is a panel dedicated to get an overall view, before consulting more detailed panels. It shows the LN2 filling line together with the detector icons and some additional information.



Figure 18.21 The detector icon displays the LN2 filling level, the crystal temperature and the overall status of one triple detector.

Another important issue for the software design was to obtain certain flexibility with respect to future changes. The array will start with few detectors, before being installed in its full extend. Moving to different host labs, the DSS may face slightly different circumstances, which - despite the generic design - demand modifications. An object oriented approach (the DSS GUI is written in Java) allowed separating the two main threads: The GUI-PLC communication is independent of the user interaction with the GUI. Both threads communicate with the DSS-Hardware Interface which holds all the data and manages the reading and writing from both sides. If required, further changes on the graphical part can be implemented without touching the rest of the program. Also, the current PLC client, which is based on a simple TCP constant block exchange, can be exchanged by a more sophisticated OPC solution.

## 18.12. Cabling

Each Triple Cluster has a series of cables, for low voltage, detector signals, detector status (temperature, cryostat volume) and communication busses. These cables derive from various sources on the detector site. To facilitate the best grounding, all other output from these sources are extracted over fibre optical cables. A draft of the Demonstrator cabling is shown in figure 18.22.

Special care has been taken in cable management for the Triple Cluster to allow the detector cabling to be mounted and dismantled on the mounting structure itself. Ease of connections to the detector has been designed with collaboration with the Detector Working Group (see figure 18.23)

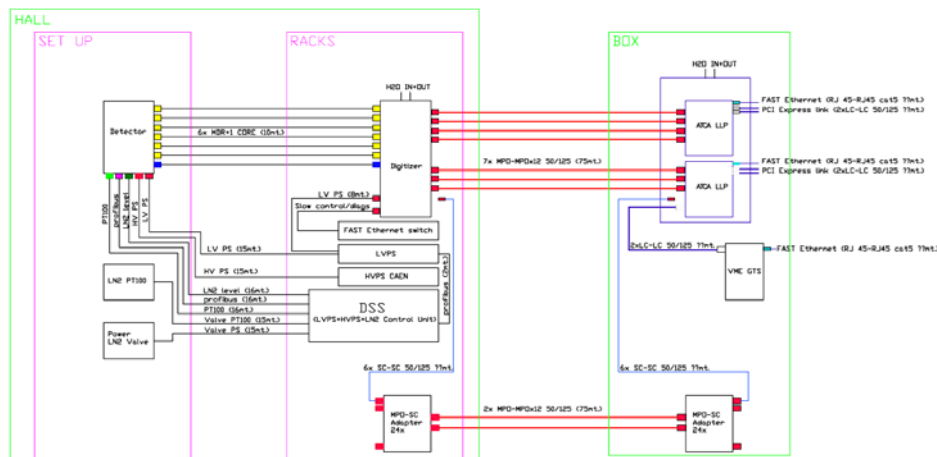


Figure 18.22: Draft of Demonstrator cabling at Legnaro

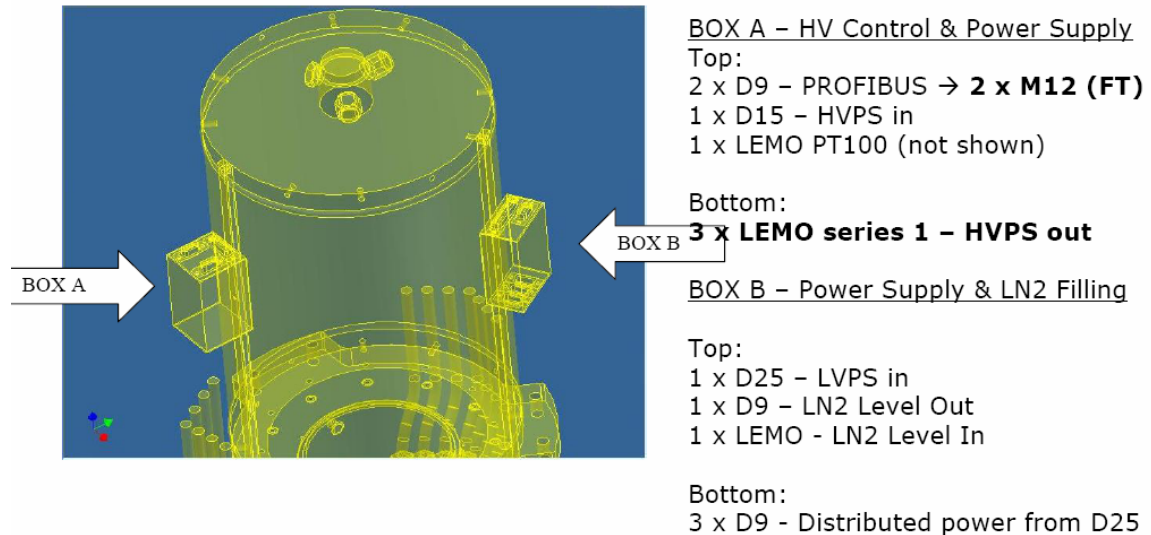


Figure18.23: Draft of ATC cabling

### 18.13. Grounding

In the past decades, the grounding of experimental setups had to deal with the noise generated by the 50 Hz. This low-frequency perturbation causes energy resolution degradation. In present time, the systems have to be protected also versus high-frequency emitters in the range of MHz up to 100 MHz. The high-frequency perturbation affects both energy and timing resolutions. The former effect can be strongly attenuated by use of appropriate filters but the latter is definitely polluted.

The new technologies are mostly based on high-frequency systems and are extensively used in the acquisition chain of the AGATA spectrometer. Therefore, it is mandatory that the AGATA grounding shields the various components towards both the low and the high frequencies.

A **mesh grounding** will be used for the AGATA Demonstrator. Mesh grounding requires:

- The whole array is grounded to a common voltage
- The common voltage is provided by a large common conductive plate
- The array itself is formed from interconnected conductive components using as short and thick grounding shunts as possible
- The ground of every component of the AGATA array, especially electronic devices, is grounded to the common voltage
- The power distribution to the front-end of the array is insured via a single uninterruptible power supply

#### 18.13.1. EMC performance

- AGATA front-end EMC performance is to be measured at both the low and the high frequencies.
- The 50Hz noise is to be less than 100 $\mu$ V rms.
- The high-frequency noise in a range 100 kHz - 100 MHz is to be less than 5mV maximum amplitude.

#### 18.14. References

- [1] G. Duchêne; A. Gadea; P. Jones; I. Kojouharov; Ch. Veyssière – Performance of AGATA demonstrator for HV, Autofill, DC Power Supply and General Monitoring and Management [https://project-agata.cea.fr/Groups/infrastructure/dss\\_performance\\_spec605](https://project-agata.cea.fr/Groups/infrastructure/dss_performance_spec605)
- [2] D. Bazzacco - Tests of the AGATA LV and HV prototype modules using the detector S001 at LNL [https://project-agata.cea.fr/Groups/infrastructure/basse\\_tension/tests\\_lv-hv-plc\\_in\\_14183](https://project-agata.cea.fr/Groups/infrastructure/basse_tension/tests_lv-hv-plc_in_14183)
- [3] R. Menegazzo - Report on LV-FFT test in Legnaro Oct 08 [https://project-agata.cea.fr/Groups/infrastructure/basse\\_tension/report\\_on\\_lv-fft\\_tes8001](https://project-agata.cea.fr/Groups/infrastructure/basse_tension/report_on_lv-fft_tes8001)

## 19. Installation at Legnaro

### 19.1. Introduction.

The first phase of the AGATA array, the AGATA Demonstrator, will operate initially at the INFN-Laboratori Nazionali di Legnaro (LNL). The campaign at LNL has two goals, the first is to validate the gamma-tracking concept in its first practical implementation and second to perform an experimental campaign at the LNL with the stable beams delivered by the Tandem-ALPI and the PIAVE-ALPI accelerator complex.

The validation of the gamma-tracking at LNL would be on the most demanding conditions achievable in a low-energy stable-beam facility, i.e. with reactions with velocities of the  $\gamma$ -emitting products up to  $\beta \sim 10\%$  and relatively high intensity beams. The experimental campaign, following commissioning period, will be with the sub-array coupled to the PRISMA magnetic spectrometer, replacing the previous array CLARA[1], therefore, the setup has been designed focusing on performing structure studies of moderately neutron rich nuclei populated by grazing reactions as multi-nucleon transfer or deep inelastic collisions. Nevertheless, the coupling of the AGATA Demonstrator with complementary detectors, other than PRISMA, opens experimental possibilities beyond the aforementioned reactions, with direct, Coulomb excitation as well as fusion-evaporation reactions.

### 19.2. The AGATA Demonstrator at LNL

The description of the AGATA demonstrator as an array of five triple cluster elements from AGATA, done previously in this TDR, is again the optimal geometry of the array for the experimental activity foreseen at LNL. The compact distribution of the five triple clusters adjacent to a pentagon opening, allowed to place the array in front of the PRISMA spectrometer input aperture, therefore, distributing the active volume in the best positions regarding Doppler broadening, considering that the nuclei of interest will be detected by PRISMA. The AGATA Demonstrator, due to the low solid angle coverage, can be also used at target-to-detector distances closer than the nominal 23.5 cm inner radius. The effect of this reduced distance from the  $\gamma$ -ray emitting source translates into a larger efficiency (a factor of  $\sim 2$  for 13.5 cm) without significant losses in the resolution and peak-to-total performance.

### 19.3. The high acceptance PRISMA spectrometer

PRISMA is a large acceptance magnetic spectrometer design to work with grazing reactions with the heavy ion beams provided by the LNL accelerator complex. The basic characteristics of PRISMA are described in ref. [2] and summarized in table 19.1. For the following discussion it is relevant to mention that PRISMA uses ion-tracking position-sensitive detectors to achieve the mass resolution. The tracking detectors provide the basic information to obtain the trajectory and velocity of the reaction products. According to the Monte Carlo simulations, up to velocities of approximately  $v/c=10\%$ , the intrinsic AGATA detector resolution is almost fully recovered if the recoil velocity module is measured with a relative precision better than 1%, and if the recoil velocity direction is measured with a precision better than  $1^\circ$ . These values are actually well within the possibilities of PRISMA.

Table 19.1: PRISMA performance figures

<b>Solid Angle</b>	<b>80msr</b>
<b>Momentum acceptance <math>\Delta p/p</math></b>	<b><math>\pm 10\%</math></b>
<b>Mass resolution <math>\Delta A/A</math></b>	<b>1/300</b>
<b>Z resolution <math>DZ/Z</math></b>	<b>1/60</b>
<b>Angular Range</b>	<b><math>-20^\circ +130^\circ</math></b>

### 19.4. Description of the installation

As mentioned before, the AGATA Demonstrator at LNL is strongly constrained by the experimental campaign coupled to PRISMA. The different elements of the mechanics and infrastructures are such that allow and facilitate the coupling and experimentation with both

setups. In the following paragraphs the different elements of the infrastructure will be described.

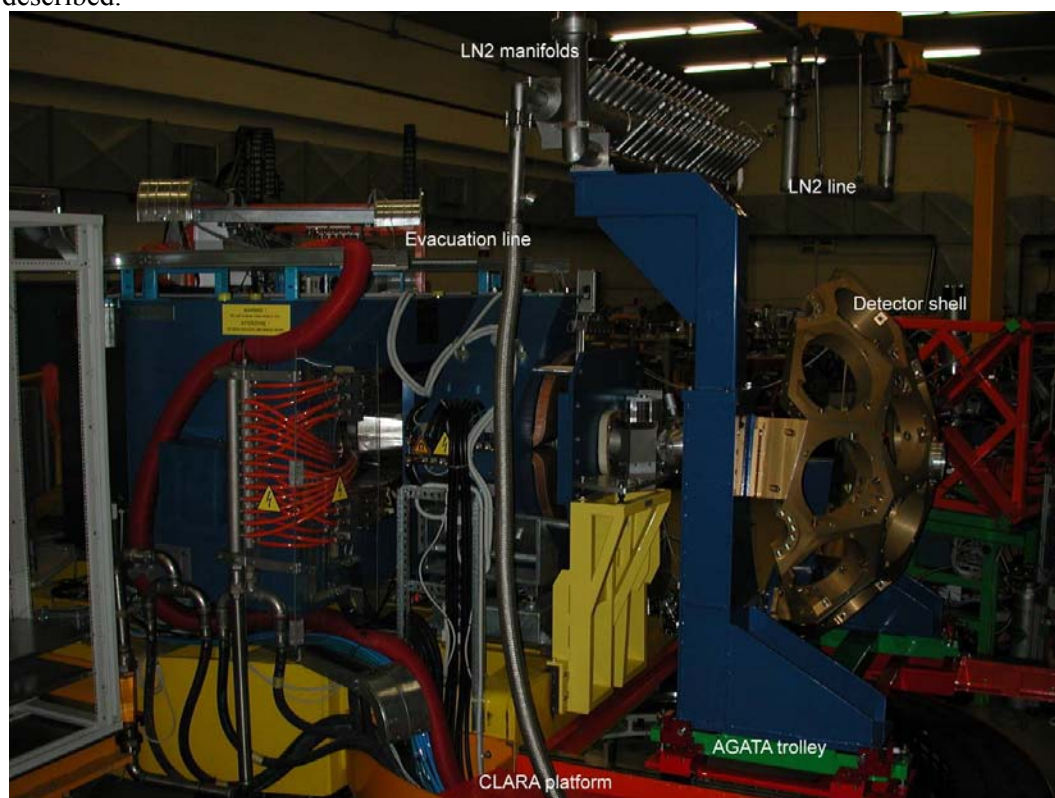


Figure 19.1: photo of the mechanical support of the AGATA Demonstrator array.

### 19.5. Mechanical structure

The setup is intended to measure coincidences between the  $\gamma$ -rays detected by the AGATA Demonstrator and the reaction products detected by PRISMA. The AGATA Demonstrator is installed on a mobile platform, that will rotate together with PRISMA in such a way that reaction products, detected in the spectrometer focal plane in coincidence with the  $\gamma$ -rays, will have a forward trajectory with respect to the array in order to benefit from the lowest Doppler broadening. The detectors are hosted into a shell made out of 15 elementary AGATA flanges, described in the Mechanical Design section. The shell is positioned on a trolley which can slide on the same platform, rigidly linked to PRISMA. It is thus possible to easily modify the target-detector distance and to access the scattering chamber and to the instrumentation placed closed to the target. The whole support structure has minimal impact on the rotation of PRISMA. Taking into account the rest of the mechanical structure (beam line, scattering chamber), the angular range  $58^\circ$  to  $130^\circ$  is possible (with the Demonstrator placed at the closest distance from the target), while for the largest distance from the target the possible range is  $38^\circ$  to  $130^\circ$ . If one of the detectors is removed, PRISMA can be positioned at smaller angles, respectively  $37^\circ$  and  $21^\circ$ . The mechanical structure for the Demonstrator Array is shown in Figure 19.1.

### 19.6. Cryogenic Infrastructures.

The liquid nitrogen (LN2) infrastructures of the AGATA Demonstrator setup at PRISMA are built by the incoming vacuum isolated LN2 line, the distribution manifold, the collector manifold and the nitrogen liquid and gas exhaustion line (see figure 19.1). The incoming line, already used during the CLARA project, copes with the roto-translation of the array through specially designed Johnston joints. The distribution manifold is vacuum isolated and allows the connection of up to 15 Ge-detectors. A new collector manifold, rigidly connected to the support structure of the array, was designed. In order to comply with the safety regulations, the excess fluids (gaseous and liquid nitrogen) produced during the filling cycle should be evacuated outside the Tandem building. Therefore, an evaporator was placed in the basement

to speed up the gasification of the excess liquid. The distribution manifold is connected to the evaporator via a flexible vacuum hose running through a dedicated flexible cable tray (cable chain) similar to the two previously used by PRISMA. The Infrastructure working group, in charge of the Detector Support System (DSS), has prepared the software to provide a filling cycle adapted to the LNL condition i.e. with an external tank and valve (see figure 19.2 and the cryogenic auto-fill section of this report).

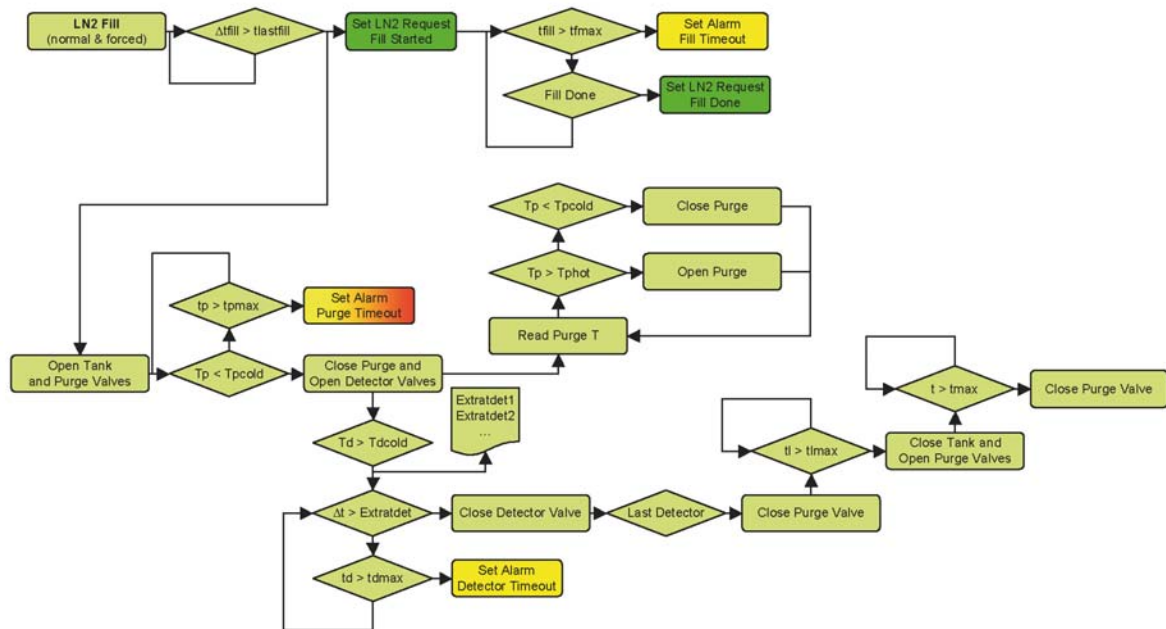


Figure 19.2: Standard LNL filling cycle for and array coupled with PRISMA

### 19.7. Beam line, reaction chamber and vacuum infrastructures.

The sliding seal scattering chamber previously used with CLARA was replaced with a lower absorption chamber, a detailed description of the reaction chamber as well as of the telescopic beam line can be found in the Mechanical Integration of complementary detectors section.

### 19.8. Electronics, Detector Support System and Data Acquisition Infrastructures

The digitizers and the Detector Support System (autofill and power supplies) will be hosted in racks, shown in Figure 3, mounted on the same platform used previously for the front-end electronics and power supplies of CLARA, which is rigidly linked to the structure of PRISMA. The optical fibres connecting the digitizers to the pre-processing electronics run into the same cable chain hosting the liquid nitrogen exhaust pipe, as shown in figure 19.3, and are then taken through the basement up to the Pre-Processing racks sitting in the AGATA-PRISMA control room. The racks for the pre-processing electronics, shown in figure 19.4, are water cooled and fully protected for thermal and noise insulation. The pre-processing racks are connected to the digitizers, placed in the experimental hall, via 75m long optical fibres, and to the PSA computer farm, placed instead in the main computer room of the Tandem building, via 15m long fibres. The PSA computing farm is shown in figure 19.5. The main computing farm for AGATA is instead placed in another building, at the location of the TIER-2 centre for the CMS and ALICE experiments. Again, the computing farms are connected via optical fibres.

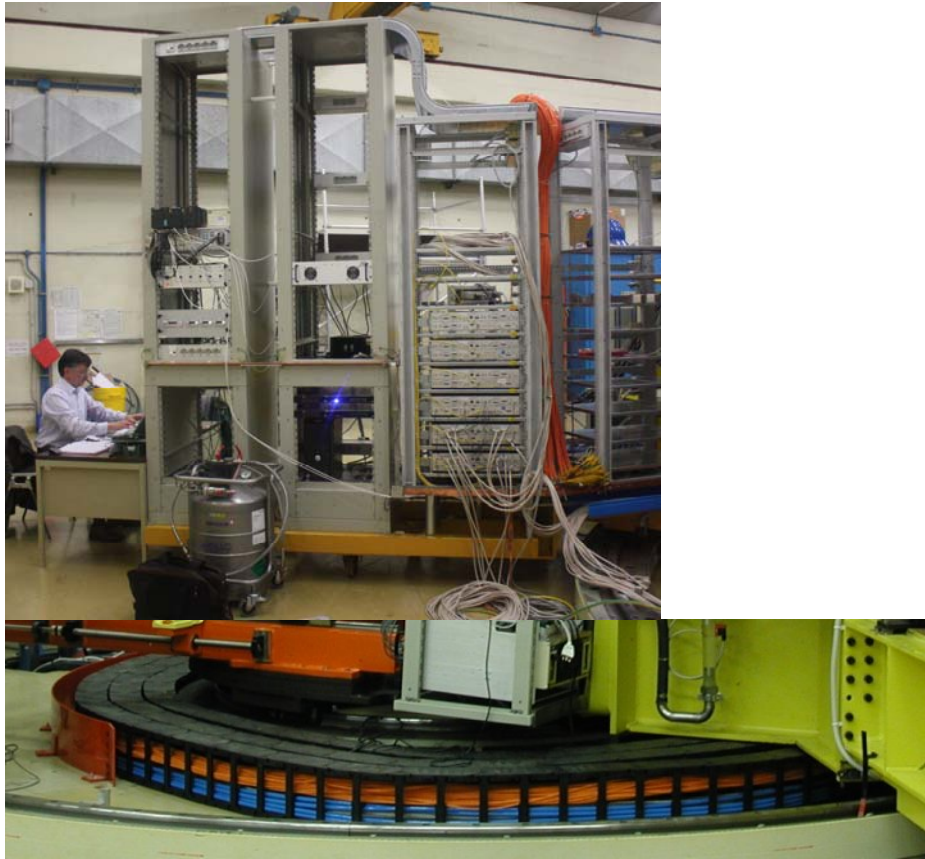


Figure 19.3 the racks hosting the AGATA Digitizers and the Detector Support System (upper panel) and the cable chain hosting the optical fibres (lower panel).



Figure 19.4: Racks for the pre-processing electronics, placed in the AGATA-PRISMA control room.

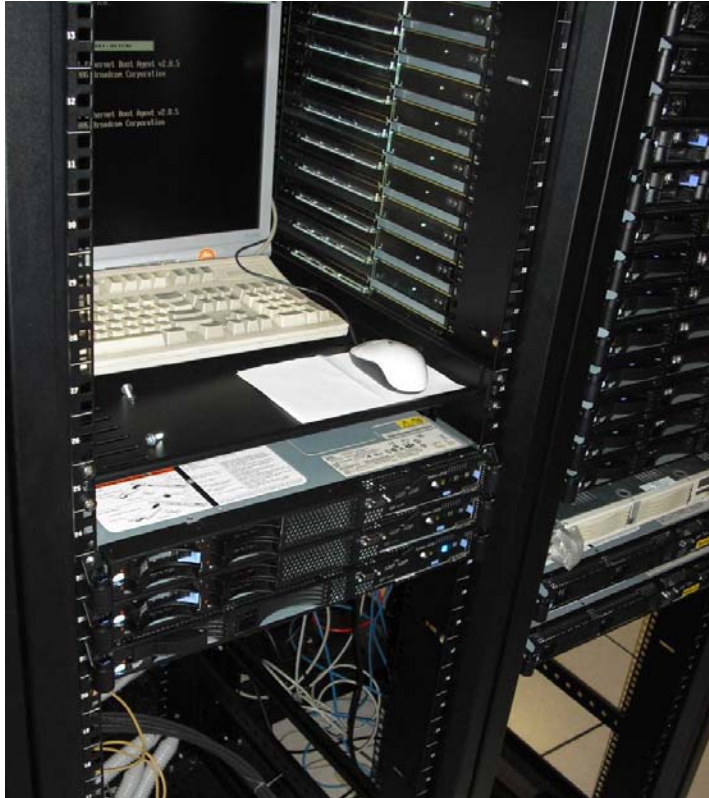


Figure 19.5: The PSA processing farm.

[1] A.Gadea et al., Eur.Phys.J. A 20, 193 (2004)

[2] A. Latina et al., Nucl. Phys. A734 (2004) E1



## 20. Complementary detectors

The coupling of large  $\gamma$ -ray detector arrays, such as EUROBALL and GAMMASPHERE, with complementary detectors has played a major role in spectroscopic investigations in the last decade. Complementary detectors will be essential for AGATA due to the need for high selectivity identifying the different reaction channels and providing information on the trajectory of the incoming and outgoing nuclei or particles. In most experimental conditions the uncertainty on the velocity of the emitting nuclei contributes significantly to the overall Doppler broadening, which means that in order to fully exploit the capabilities of AGATA, it will be essential to couple it to devices providing information on the velocity and trajectory of the reaction products. A  $\gamma$ -ray array, even with the high-performance capabilities of AGATA, cannot cover all the fundamental aspects of the nuclear structure without the use of the complementary detectors. In addition, the foreseen use of AGATA at different facilities makes some of the complementary devices (e.g. beam tracking devices in the case of fragmentation facilities) absolutely necessary for the normal working conditions of the array.

The current large arrays have been working for many years in stable heavy-ion beam facilities in which fusion evaporation reactions are the preferred production mechanism and only specific experiments used different mechanisms. The use of AGATA with radioactive or high-intensity stable beams will change the situation dramatically; fundamental information will be extracted from  $\gamma$  spectra produced using unstable ions by direct or grazing reactions or Coulomb excitation. On the other hand intense stable beams will allow the use of more exotic reaction mechanisms (multi-nucleon transfer, deep inelastic collisions, fission...) to populate nuclei not accessible by fusion evaporation reactions. Within the AGATA project dedicated new complementary detection systems will be developed in addition to adapting existing ones. The Demonstrator phase of the AGATA project is the starting point to prove the feasibility of the full array in experimental conditions. Therefore, extensive campaigns of in-beam measurements with ancillary devices are expected, that will be used to identify the reactions, corresponding to the key experiments, and to track the beam and products for Doppler correction purposes or to identify the trajectories of the ejectiles. During the coming years the coupling of AGATA with a number of existing complementary and ancillary instrumentation has been discussed for the "Key experiments", focused on the AGATA demonstration, as well as for the subsequent experimental campaigns at different facilities.

### 20.1. Complementary detectors or devices proposed for AGATA

#### 20.1.1. Life-time measurement devices

The IKP-Cologne University AGATA group has developed and is still developing several Plunger devices to measure lifetimes using the RDDS technique [1]. Recently a new device has been developed to be used with Grazing reactions (multi-nucleon transfer and deep-inelastic collisions) [2] and with setups including  $\gamma$ -detector arrays and magnetic spectrometers. This novel device, based on previous experience on differential Plungers [3], allows the use of RDDS technique for reaction products at the grazing angle. Several Letters of Intent for the AGATA experimental campaign at LNL propose a setup including this plunger device, and the LNL reaction chamber has been designed taking into account its use (see section on Complementary Detectors Mechanical Integration). The same group has designed a Plunger device to be used with fragmentation secondary beams of radioactive ions [4] that will be used in the campaigns of AGATA at the GSI Fragment Separator.

Life-times of 5 picoseconds or longer can be measured by the time-delayed multi-coincidence technique [5,6,7], using fast electronic timing with scintillators. A setup for time-delayed coincidences based on a BaF<sub>2</sub> array already exists and a new one based on the LaBr<sub>3</sub> scintillator material is being built.

### **20.1.2. Magnetic spectrometers**

The first demonstration and experimental campaign to be performed at LNL will be with the PRISMA spectrometer [8] (see the AGATA Installation at LNL section of this TDR). The subsequent experimental campaign will be with the AGATA coupled to the VAMOS spectrometer [9] at GANIL.

The possibility of coupling AGATA with RITU at the JYFL stable beam facility for the full identification of the out-coming products and with recoil decay tagging coincidences with multipurpose focal-plane detectors such as GREAT [10] is under discussion.

### **20.1.3. High energy gamma-ray detectors and multiplicity filter arrays**

Large-volume scintillator detectors are been used frequently to cover ranges of energies in the  $\gamma$ -ray spectra in which the Ge arrays, due to the limited dimensions of the Ge crystals, give low detection efficiency. The array HECTOR [11] is composed of 8 large volume BaF<sub>2</sub> detectors, and takes advantage of the pulse shape capability of BaF<sub>2</sub> material to discriminate between  $\gamma$  rays and neutrons. HECTOR has been coupled to the RISING array at GSI.

A new array  $4\pi$  array for high-energy  $\gamma$  rays, PARIS, is being design in the framework of the SPIRAL2 preparatory phase. It is foreseen that sub-arrays of PARIS will be operated with the AGATA.

Multiplicity Filters are also an important tool to select particular conditions in your reaction channel or to discriminate the reaction mechanism. Since early phases of the AGATA is foreseen to use the HELENA multiplicity filter, composed of 35 3" x 3" BaF<sub>2</sub> scintillator detectors, covering, coupled with the AGATA Demonstrator, a total solid angle of 57% of  $4\pi$  [12] (see section 17.4 of this document).

### **20.1.4. Light charged particles detector arrays**

Complementary arrays of light-charged particles detectors (sometimes extending the detection range to heavy ions), have been used extensively in recent years and have proved to have a very positive impact in the scientific production of the large  $\gamma$ -ray detector arrays. It has been proposed to couple several such arrays to AGATA: the DIAMANT [13] array of CsI(Tl) scintillator detectors, with high granularity and specially devoted to the detection of light charged particles emitted in fusion evaporation reactions; the EUCLIDES Si-telescope array [14] designed as well for fusion-evaporation reactions; the light particle filter CUP [15], based on a plastic scintillator detector.

Position sensitive detection systems for light particles and ions can be used to track and sometimes to identify the products in direct reactions or Coulomb excitation. The highly segmented LuSi Si-strip detector array [16] and the "CD" annular double sided Si strip detector are proposed to cover these experimental activities with AGATA.

### **20.1.5. Neutron detectors array**

Compact neutron detector arrays are key complementary systems for channel selection in structure studies of neutron-deficient nuclei. High efficiency and discrimination capability between  $\gamma$  rays and neutrons is required. One such system, based on high granularity array of liquid scintillators is the Neutron-Wall [17,18], which was designed to be used with the EUROBALL spectrometer, is fully functional and ready to be coupled with AGATA.

### **20.1.6. Binary reaction detectors**

Binary reaction product detectors coupled to large  $\gamma$ -ray detector arrays have been use to study phenomena as molecular states, and to tag in reaction mechanisms as the Coulomb excitation or grazing reactions with may be (QUITAR may be) less selectivity but more efficiency than the one provided by the magnetic spectrometers. Several of these setups have the capability to use kinematic coincidences to gain information on the reaction products. Several of these detectors were available during the EUROBALL campaigns, namely the BRS, and PPACs [19]. In addition to de already mentioned LuSi, there is also available the DANTE array of MCP detectors [20].

### 20.1.7. Recoil Filters

Recoil detectors are an efficient tool to select the fusion-evaporation reaction mechanism from the full reaction background. It is especially important when other mechanisms, for example fusion-fission, strongly compete with the channel of interest. The RFD is very useful in  $\gamma$ -spectroscopy measurements based on fusion-evaporation reactions with thin targets requiring a detailed knowledge of the velocity vector of recoiling nuclei. It is especially suited to experiments suffering from Doppler broadening resulting from a large recoil velocity caused straggling and particle evaporation. The RFD Doppler correction for every event is critical for measurements of fast light nuclei which have characteristic high energies of  $\gamma$  transitions [21,22].

### 20.1.8. Calorimeter Telescope Arrays for selection of products in relativistic reactions.

The selectivity of reaction products from secondary reactions of fragmentation beams has proven to be fundamental in the fast-beam RISING campaigns. The goal of this calorimeter is the identification on  $Z$  as well as in Mass for light or medium mass nuclei. This detection systems use  $\Delta E$ - $E$  and TOF identification techniques. The array CATE [23, 24] used in previous RISING campaigns is being replaced by the new detector array LYCCA [25].

### 20.1.9. Conversion electron spectrometers

Electron detection set-ups can help the determination of the character and multipolarity of the transitions and in addition will extend the detection capabilities to highly or fully converted (E0) electromagnetic transitions. They are of particular relevance for the structure-investigation program on heavy and super-heavy nuclear species. The use of detection systems as SAGE [26] or arrays of mini-orange spectrometers will be studied.

## References

- [1] A. Dewald et al., Nucl. Phys. A 545,822 (1992)
- [2] A.Gadea et al., Acta Phys.Pol. B 38, (2007)  
J.J. Valiente-Dobon et al., Phys Rev. In press.
- [3] A. Dewald et al., Phys.Rev.C 68, 034314 (2003)
- [4] K. Starosta, A. Dewald et al. Phys.Rev.Lett. 99, 042503 (2007)
- [5] H. Mach et al., Nucl. Instr. & Meth. A280 (1989) 49.
- [6] H. Mach et al., Nucl.Phys.A523, 197 (1991)
- [7] H. Mach et al., J.Phys.G:Nucl.Part.Phys.31, S1421 (2005)
- [8] A. Latina et al., Nucl. Phys. A734 (2004) E1
- [9] H.Savajols et al., Nucl Instrum Meth B 204, 146 (2003)
- [10] INTAG Proposal for the Joint Research Projects-I3NS to the EU 6<sup>th</sup> Framework Program
- [11] A. Maj et al., Nucl. Phys. A 571, 185 (1994), M. Mattiuzzi et al., NA612(1997)262
- [12] <http://agata.lnl.infn.it/AgataWeek2007/talks/Simulations> and Ancillary/BMillion.pdf
- [13] J.N. Scheurer, et al., Nucl. Instr. and Meth. A 385, 501 (1997)
- [14] E. Farnea et al., Nucl. Instr. and Meth. A in preparation
- [15] <http://www.slacj.uw.edu.pl/en/35.html>
- [16] <http://wwwnsg.nuclear.lu.se/lusia/>
- [17] O. Skeppstedt et al., Nucl. Instr. and Meth. A 421, 531 (1999)
- [18] <http://nsg.tsl.uu.se/nwall/>
- [19] Ancillary detectors and devices for EUROBALL, Ed. H.Grawe, GSI internal report
- [20] J.J. Valiente-Dobón et al., Acta Phys. Pol. B 37, 225 (2006)
- [21] W. Męczyński et al., Nucl. Instr. and Meth. A 580, 1310 (2007)
- [22] P.Bednarczyk et al., Eur. Phys. J. A 20, 45 (2004)
- [23] H.J. Wollersheim et al., Nucl. Instr. and Meth. A 537, 637 (2004)
- [24] R. Lozeva et al., Nucl. Instr. and Meth. B 204, 678 (2003)
- [25] <http://wwwnsg.nuclear.lu.se/lycca/>
- [26] <http://ns.ph.liv.ac.uk/~rdh/sage2.htm> & <http://www.superheavies.de/talk/SP9.pdf>



## 21. Impact of ancillary detectors on AGATA performance

### 21.1. Introduction

Ancillary detectors have since long played an essential role in nuclear structure studies when used in combination with large  $\gamma$ -ray arrays. Their influence on the performance of the array will be even more profound in case of AGATA. The ancillary detectors perform many different tasks:

- Track and identify beam particles prior to the reactions in the target.
- Register scattered beam and target-like particles in Coulomb excitation, transfer and deep-inelastic reactions.
- Register light-charged particles and neutrons emitted from the compound nucleus in fusion-evaporation reactions.
- Register recoiling nuclei produced in fusion-evaporation reactions, possible determining their mass and charge numbers, as well as providing information about their velocity vectors.
- Provide information about the multiplicity and sum energy of  $\gamma$  rays produced in the reactions.
- Register electrons.
- Enable lifetime measurements of short-lived states depopulated by  $\gamma$  rays, employing methods based on Doppler effects.
- Enable measurements of magnetic moments by providing suitable magnetic fields for the nucleus which emits the  $\gamma$  radiation.

In fact, the last two items in the list above refer to instruments which in a strict sense are not detectors, but they provide means for interpreting the  $\gamma$ -ray spectra, and thus certainly have an impact on the application of the  $\gamma$ -ray array and its performance. A more general term "impact of ancillary devices" is more appropriate for the discussion presented here.

At certain stages of its development, AGATA may be used together with other conventional HPGe based  $\gamma$ -ray detectors, which in such situations should also be treated as ancillary devices to AGATA. Finally, in some circumstances various elements of entire accelerator or separator devices will provide information which will be used in the evaluation of the data collected by AGATA, and thus their impact on AGATA should also be considered.

### 21.2. Coupling of ancillary detectors to tracking arrays

The following remarks are relevant for the coupling of ancillary detectors to tracking arrays:

- The AGATA array, with its novel concept of  $\gamma$ -ray tracking, is a non-collimated device, which means that it is sensitive to  $\gamma$ -ray radiation coming from any source in the experimental hall, not only from the target.
- The performance of tracking algorithms may decrease, if a significant number of interactions due to  $\gamma$ -rays originating from spurious sources, are registered. Scattering of  $\gamma$  rays on mechanical elements of the ancillary devices placed inside the array (between the target and the HPGe detectors) might thus have a larger impact on the performance than in the case of conventional  $\gamma$ -ray spectrometers.
- For the same reason, even a mere presence of other devices and mechanical structures in the vicinity of the array may affect the functioning of AGATA and should be evaluated.

A special feature of AGATA is that it will provide precise information regarding the position of the first interaction point of a  $\gamma$ -ray entering the detector. The expected position resolution is about  $\pm 5$  mm, corresponding to a precision of the  $\gamma$ -ray detection angle of about 1 degree, which is several times more precise than what conventional  $\gamma$ -ray arrays can provide. This makes it possible to apply a precise Doppler correction to the energies of the detected  $\gamma$ -rays,

providing that the velocity vector of the source of the radiation is known with a matching accuracy. One important assignment of the ancillary devices is thus to determine the velocity vector (absolute value and direction) of the investigated nuclei.

For the identification of the sequence of interaction points of each scattered  $\gamma$  ray, as well as for the reconstruction of its full energy and angle, the presently used tracking algorithms assume (in principle) that the  $\gamma$  radiation originates from a well defined point in space. It has been shown that the tracking algorithms are not very sensitive to this parameter. Therefore, any information that may be provided by the ancillary devices regarding the coordinates of the source of the  $\gamma$  rays, is valuable.

Note that there is an important technical difference between using the ancillary information for the Doppler correction and for determining the position of the source of a  $\gamma$  ray. The Doppler correction is applied to the reconstructed  $\gamma$ -ray energy after the tracking is completed, and thus can be done off-line, using data which contains information only about the reconstructed energy and position of the first interaction point. No information regarding the other registered interaction points is needed for the Doppler correction. The information of the source position, if significant, must on the other hand be provided to the tracking procedure itself. Thus, this parameter should either be available on-line, or alternatively the tracking can only be performed off-line, which implies storing a complete list of the registered interaction points.

### 21.3. Monte-Carlo simulations of ancillary detectors coupled to AGATA

The GEANT4 based AGATA simulation code [1] provides an excellent framework for simulation of the AGATA array connected to various ancillary devices. Geometries of several devices have already been included in the code and can easily be activated by command line switches. Other devices can be added in a relatively straightforward manner, using instructions given in the documentation and following available examples. Simultaneous use in the simulation of an arbitrary number of ancillary detectors is possible, providing of course, that this in reality is geometrically practicable.

Figure 21.1 presents a GEANT4 realization of the setup which includes the AGATA Demonstrator, the Neutron Wall [2], the light charged particle detector DIAMANT [3] and eight EXOGAM [4] conventional HPGe  $\gamma$ -ray detectors. Such a setup may be used for studies of exotic proton-rich nuclei, using fusion-evaporation reactions and the available GEANT4 code makes possible to perform simulations of such complete experiments.

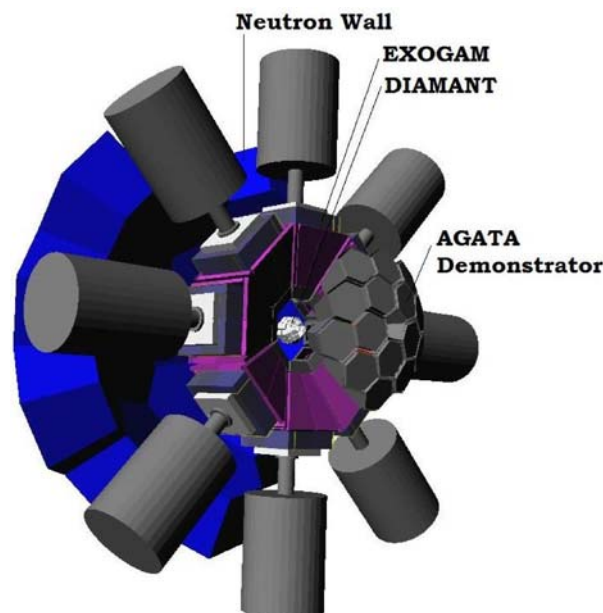


Figure 21.1 GEANT4 simulation of the AGATA Demonstrator connected to the Neutron Wall, EXOGAM and DIAMANT

Two approaches to the simulations of various ancillary devices are possible, depending on the type of impact effect on AGATA that is under consideration. Whenever an ancillary device is supposed to provide additional information to be used by AGATA, its active (presumably positive) impact should be simulated. This requires careful programming of active volumes of the detector, and proper evaluation of the data obtained. Passive mechanical structures, like the reaction chamber, the supporting frame, etc., are not important for this particular purpose, unless they affect the functioning of the ancillary device itself.

However, any device which is located close to AGATA may disturb the detection of the  $\gamma$  rays, due to absorption and scattering. Thus, for estimating the passive impact of the device (usually negative), a reasonable description of the amount, type and placement of all materials of the device should be provided. The definition of such passive parts in the GEANT4 code can in fact be a more troublesome and time consuming task than the description of the active volumes of the ancillary detector. For the completeness of the passive impact simulation, care must also be taken regarding various mechanical parts of the AGATA array itself, its supporting structure, detector capsules, the target chamber, the beam line, and even cables, etc., if they are located in sensitive areas.

Example results of the simulation of the passive impact are presented in Figure 21.2. The efficiency of the array and the P/T values of  $4\pi$  AGATA alone were compared with the numbers obtained with four different structures placed inside the array: an Al target chamber, a realistic model of the EUCLIDES charged particle detector, an ideal shell of 1 mm thick silicon, which emulates very schematically a Si-ball similar to EUCLIDES, and a 5 mm thick shell of CsI, which represents an array of CsI scintillators. It can be concluded that the impact of passive materials inside a tracking array is comparable with the impact that the same objects would have on a conventional array of Compton-suppressed HPGe detectors [5].

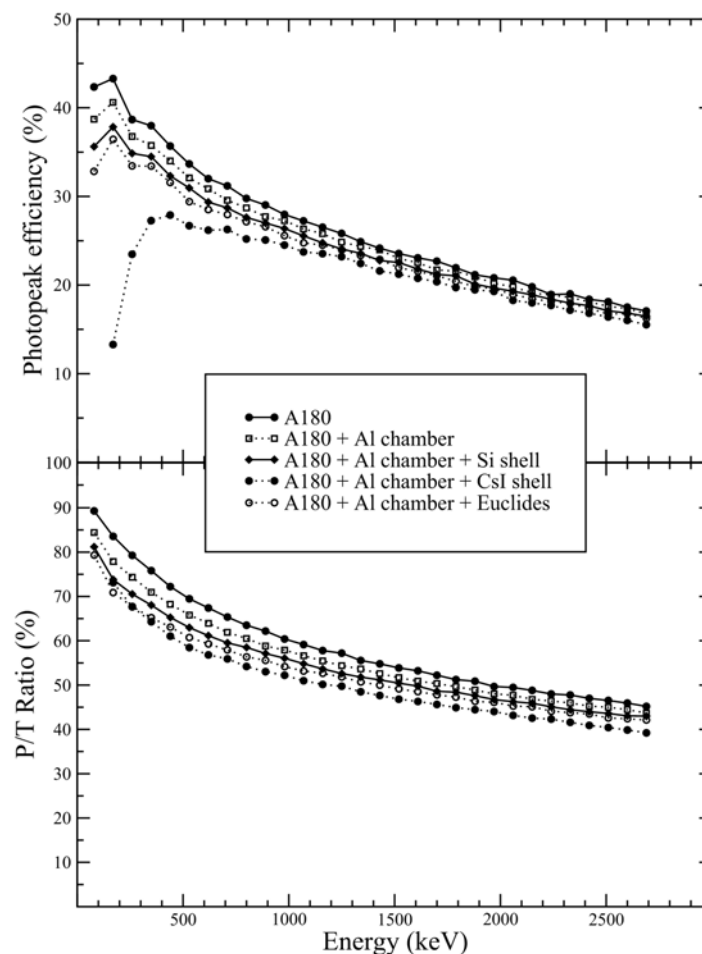


Figure 21.2: Passive impact on the AGATA performance of the chamber and detectors placed inside the array

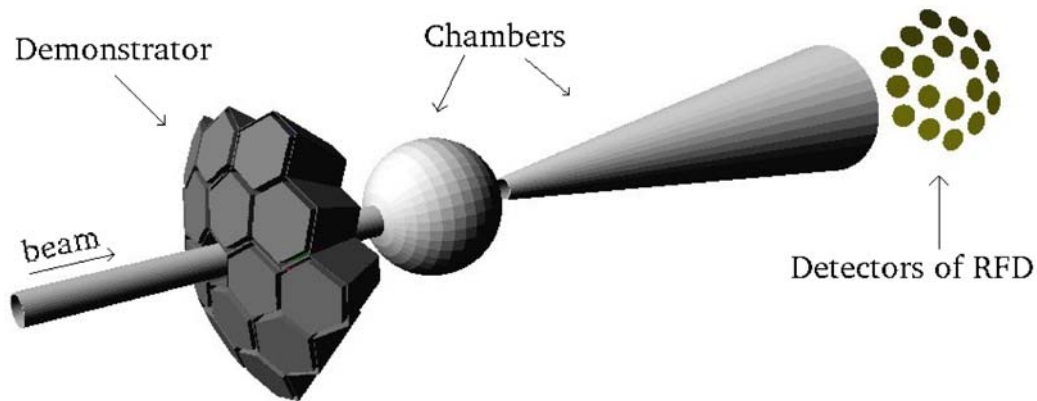


Figure 21.3: Geant4 simulation of the AGATA Demonstrator and RFD

As mentioned above, a precise event-by-event measurement of the velocity vector of nuclei which emit  $\gamma$  rays is essential for the full exploitation of the angular resolution of AGATA, and thus for the capability of applying precise Doppler correction. The Recoil Filter Detector (RFD) [6] is a device which is especially designed for this kind of measurement with recoiling nuclei produced in fusion-evaporation reactions. Fig. 21.3 illustrates the Geant4 simulation of the RFD. The results of the simulation for the reaction  $^{40}\text{Ca}(^{32}\text{S},2\alpha)^{64}\text{Ge}$ , with a beam energy of 110 MeV and a target thickness of  $0.7 \text{ mg/cm}^2$ , are shown in Fig. 21.4. A very significant reduction of the peak width is observed when RFD data is used to Doppler correct the  $\gamma$ -ray energies, compared to spectra obtained with a correction based on the average recoil velocity (compare also [6]). A similar effect can be obtained using another ancillary device, e.g. the PRISMA spectrometer [7, 8].

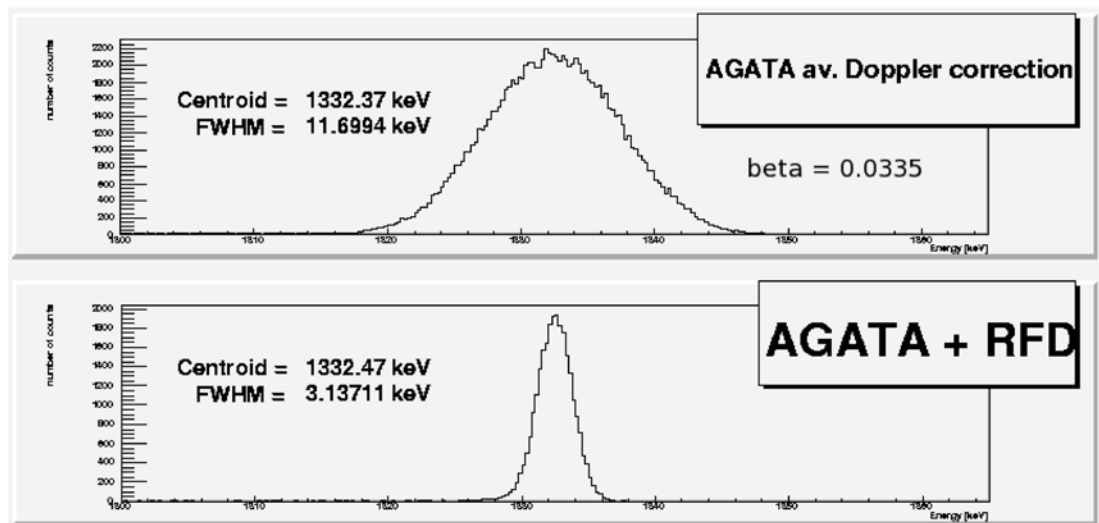


Figure 21.4: GEANT4 simulation of  $\gamma$  rays registered in the AGATA  $3\pi$  array. In the upper plot the Doppler correction was performed by using the average velocity and 0 degrees for the recoils while an event-by-event correction using RFD data was done in the lower plot. See text for further details.

#### 21.4. Conclusions

Ancillary detectors are essential for the full exploitation of the capabilities of AGATA. On the other hand their presence may significantly reduce the performance of the array due to scattering and absorption of the  $\gamma$  rays. Impact of various ancillary device on AGATA array has been evaluated, by means of GEANT4 based Monte Carlo simulations. Tools and

methods are available to perform similar analysis for any other devices which in the future may be used together with AGATA.

### 21.5. References

- [1] E. Farnea et al. [http://agata.pd.infn.it/agata\\_simul.htm](http://agata.pd.infn.it/agata_simul.htm)
- [2] Ö. Skeppstedt et al., Nucl. Instr. Meth. **A421** (1999) 531  
J. Ljungvall, M. Palacz, J. Nyberg, Nucl. Instr. Meth. **A528** 741 (2004)
- [3] J.N. Scheurer et al., Nucl. Instr. and Meth. **A385** 501 (1997)
- [4] <http://www.ganil.fr/exogam/>
- [5] E.Farnea et al. LNL Annual Report 2004
- [6] W. Meczynski et al., Nucl. Instr. and Meth. **A580** 1310 (2007)
- [7] P. Mason et al., Eur. J. Phys. Special Topics **150** 359-361 (2007)
- [8] E. Ince, 7<sup>th</sup> Agata Week, Legnaro, Legnaro, July 2008



## 22. R&D on other gamma detectors and associated technology

### 22.1. Introduction:

Historically speaking, the R&D on planar type Germanium detectors has started in the beginning of the nineties for the EUROGAM project. The idea was to develop a less expensive alternative to the high-efficiency, large-volume coaxial Germanium diodes and to allow better Doppler-correction capabilities. At that time the studied prototypes of stacks of planar detectors appeared to be less efficient than foreseen and the R&D was stopped.

With AGATA and the development of the gamma tracking, the idea of using planar diodes came back to life because they are cheaper to produce and easy to segment. Therefore, more R&D's were started in several laboratories of the collaboration taking advantage of the techniques developed in the frame of the AGATA project: they are about medical imaging, detection and identification of radioactive ions implanted at the focal plane of a spectrometer, complementary studies of the Pulse Shape Analysis (PSA).

Other more technologically driven developments were endorsed by this R&D AGATA team with the idea to develop techniques useful for all kind of Germanium detectors: new He-cooling methods (see report below), development of ASIC preamplifiers (contact person I. Lazarus STFC-Daresbury, UK), etc.

At the beginning of the AGATA project, up to four R&D were followed in parallel to develop efficient planar detectors with very good localisation capabilities in order to use the tracking techniques. They are namely:

- The University of Liverpool Department of Physics (UK) has worked closely with the detector manufacturer ORTEC (Oak Ridge, TN) to specify, develop and characterise position sensitive planar germanium detector sensors for use in medical imaging applications. The SmartPET project has demonstrated the feasibility of using such detector technology for Positron Emission Tomography (PET) and Single Photo Emission Computed Tomography (SPECT) and has allowed the development of novel PSA algorithms through a unique knowledge of the detector response function. The data has subsequently been used to reconstruct images from point and extended source distributions using custom written analytical and iterative image reconstruction algorithms (see report below).
- At the GSI laboratory in Darmstadt (Ge), an ambitious project of up to 24 stacks of 3 planar diodes is developed in the frame of the DESPEC project (Decay Spectroscopy: nuclear studies of stopped nuclei at FAIR) associated to the HISPEC (High-resolution in-flight Spectroscopy). This project might greatly benefit from the Liverpool R&D through high background rejection and high granularity allowing the detector system to recover from prompt atomic gamma flash. One should note also that the possibility to use less expensive and more reliable electromechanical cooling, is under study for this project together with industrial companies (contact person I. Kojouharov, GSI).
- At the Royal Institute of Technology (KTH) in Stockholm (*Se*), a segmented planar was used to develop the PSA methods to be used in a medical imaging SPECT project (Single Photon Emission Computed Tomography) (*contact person B. Cerderwall, KTH*).
- At the IPHC in Strasbourg (*Fr*) a prototype of restored electrical-field, segmented-planar detector was developed following simulations performed with the MGS code developed locally, with the idea to maximize the efficiency through a reduction of edge effects (*contact person G. Duchêne, IPHC*).

In the following, two of the main R&D projects that have come recently to achievements will be presented in more details.

## 22.2. Planar detector: the SmartPET detectors

The SmartPET system consists of two orthogonal strip High Purity Germanium (HPGe) planar detectors. Full characterisation of the SmartPET detectors has been completed in an attempt to better understand the response of the detector to incident radiation and to achieve improvements in spatial resolution from that of the raw pixellation. In order to realise this goal the detector crystals have been investigated utilising the Liverpool Detector Characterisation system.

The SmartPET detectors utilise a single 74x74x20mm orthogonal strip HPGe crystal with an active volume of 60x60x20mm. The raw spatial resolution is 5mm x 5mm in the x-y plane and 20mm through the depth profile; this is achieved by electrical segmentation of the contacts. The use of PSA techniques can be used to improve this position sensitivity. The performance of the SmartPET detectors to incident photons from a collimated source of gamma-ray photons has been investigated. Such a detector “scan” allows the charge pulse response of all the electrodes to be calibrated. The system consists of an automated 1mm diameter collimated source assembly that allows the detector crystal to be comprehensively investigated utilising a number of different energy radioactive sources  $^{241}\text{Am}$ ,  $^{57}\text{Co}$  and  $^{137}\text{Cs}$ . Such a detector “scan” has allowed both surfaces (AC and DC coupled sides) of the crystals to be studied.

Example results from the scanning process are shown in Figs. 22.1, 2 and 3. Figure 21.1 shows scan results for  $^{241}\text{Am}$  source measurements across SmartPET1. The count time per position for both data sets was 180 seconds. A – C are the photopeak gated intensity plots for the source on the AC coupled side. D – F are the intensity plots when the source is shining on the DC face of the crystal. A and D are position gated matrices produced from a 55-65keV energy gate. B and E are position gated matrices with the added constraint of only one strip per side containing an energy signal (fold 1). C and F are the matrices produced by subtracting the position gated fold=1 events from the position gated events, i.e. B from A and E from D. These subtracted plots illustrate the influence of charge sharing in this planar detector. The difference plots consist of ~8% of all 60 keV events. In the matrices A, B, D and E the detector shows a fairly uniform response across most of the crystal. The contacts for the AC strips are observed on DC01 in the AC scanned data and vice versa on the DC scanned data set.

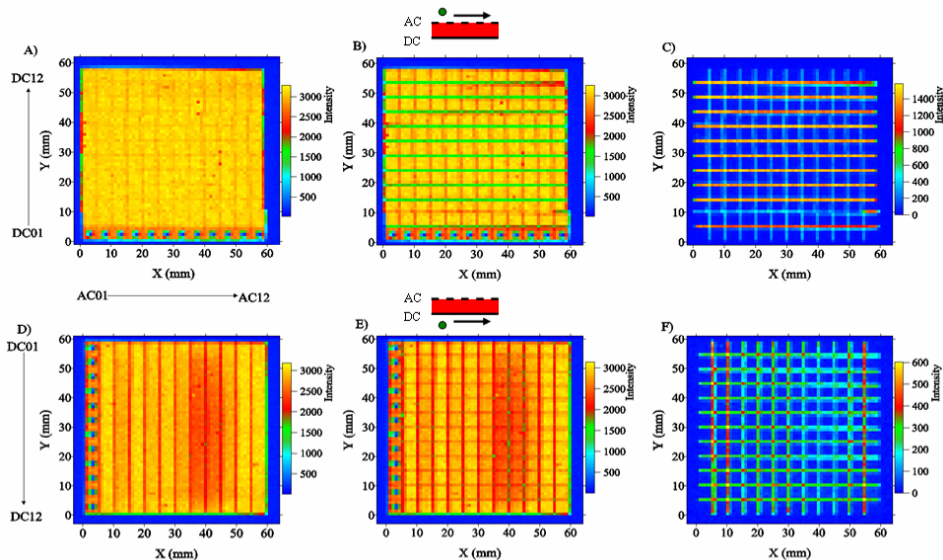


Figure 22.1 Scan results for  $^{241}\text{Am}$  source measurements across SmartPET1. The count time per position for both data sets was 180 seconds. A – C are the photopeak gated intensity plots for the source on the AC coupled side. D – F are the intensity plots when the source is shining on the DC face of the crystal. A and D are position gated matrices produced from a 55-65keV energy gate. B and E are position gated matrices with the added constraint of only

one strip per side containing an energy signal (fold 1). C and F are the matrices produced by subtracting the position gated fold=1 events from the position gated events

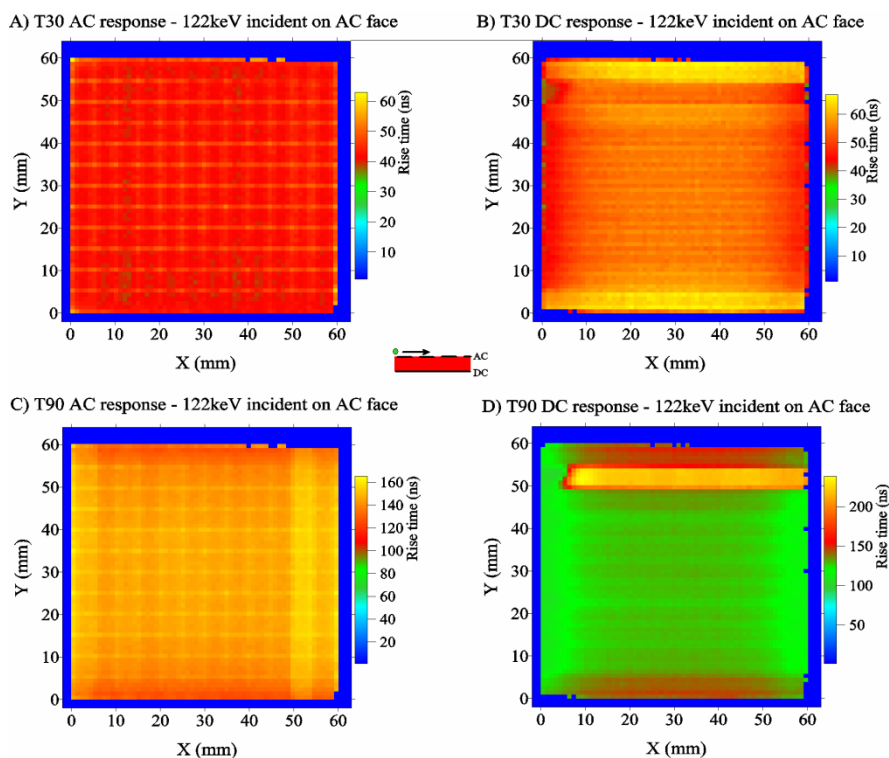


Figure 22.2: Pulse shape rise time plots illustrating the 10%-30% T30 and 10%-90% T90 response for the AC and DC faces.

Figure 22.2 shows the charge pulse rise time plots for 10%-30% (T30) and 10%-90% (T90) response from the AC and DC faces to  $^{57}\text{Co}$  122keV gamma-ray photons. The plots indicate the general uniformity of charge collection times inside the detector. One faulty strip (DC11) is clearly visible.

Differing approaches for deriving the position of a gamma-ray interaction have been investigated which include;

- No PSA [position information derived from the strips]
- Parametric PSA [pulse shape rise time/image charge asymmetry]
- Pulse shape Database [least squares minimization]

In order to assess the impact that application of PSA techniques has on a PET image, simple methods have been developed and implemented. In order to apply these Pulse Shape Analysis techniques to PET, the SmartPET system was used to image a number of  $^{22}\text{Na}$  sources using both analytical (FBP) and statistical (MLEM) image reconstruction techniques.

The two SmartPET HPGGe detectors were set up in a coincidence system, with analogue electronics providing a NIM logic trigger to the GRT4 digital electronics cards. Three  $^{22}\text{Na}$  sources were positioned between the two detectors on a rotation system and data was collected in  $5^\circ$  increments over a full  $180^\circ$ . The  $^{22}\text{Na}$  sources had activities of 2.5kBq, 4.9kBq and 43.9kBq respectively and data were collected to ensure high statistics for coincident single hit events from the camera.

The characterisation of each of the two SmartPET detectors by “scanning” allows for the implementation of PSA algorithms to improve the position resolutions of the detectors beyond that of the strip pitch. An average pulse shape response from a number of strips on one of the SmartPET detectors is shown in Figure 22.3. The pulse shapes shown result from a 662keV gamma ray interacting in a single strip of the detector. The figure shows a real charge pulse and corresponding transient signals in neighbouring segments. The real charge

signal contains information about the energy which the gamma-ray deposited in the detector and also the time taken to collect this charge.

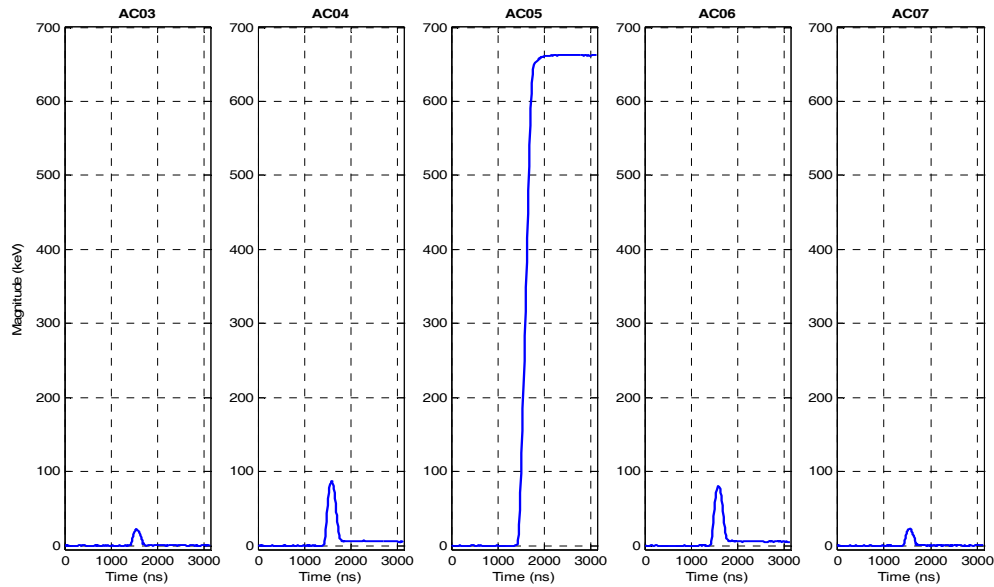


Figure 22.3: Average pulse shape response resulting from a 662keV gamma ray interacting in a single strip of a SmartPET detector.

Following a gamma-ray interaction in the detector, liberated charge carriers drift to the electrodes under the influence of the applied electric field. This induced current is integrated using fast charge sensitive preamplifiers and the resulting charge pulse provides information regarding the depth of the interaction. This information is extracted by analysis of the pulse shape rise time. This rise time describes the charge collection time within the detector and parameters such as T30 (the time taken for the pulse to rise from 10-30% of its maximum height) and T90 are typically used to calculate interaction depth.

In order to calculate the gamma ray interaction depth on an event by event basis, data resulting from a  $^{137}\text{Cs}$  surface scan of the detector was analysed and the T30-T10 value plotted against the T90-T10 parameter. For a typical strip on a SmartPET detector, this rise time correlation for single pixel interactions is shown in Figure 22.4.

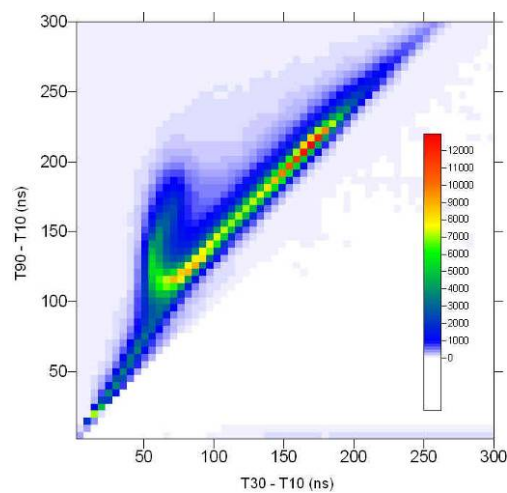


Figure 22.4: Typical pulse shape rise time correlation plot for single pixel interactions from a 662keV gamma ray. Application of polygonal gate allow regions through the depth profile of the detector to be selected.

While the charge carriers liberated by a gamma ray interaction are drifting to the collecting electrodes, transient signals known as image charges are induced in neighbouring strips. The relative area of these waveforms varies with the proximity of interaction and thus parameterisation of the asymmetry between the shapes is used to define the lateral interaction position. In this work, the asymmetry has been characterised according to,

$$A = \frac{Q_{left} - Q_{right}}{Q_{left} + Q_{right}},$$

where  $Q_{left}$  and  $Q_{right}$  refer to the areas underneath these transient charges. For all full energy, single pixel hits resulting from the same  $^{137}\text{Cs}$  scan discussed above, this asymmetry parameter was calculated and histogrammed event-by-event. The resulting distribution for strip AC05 is shown below in Figure 22.5 and is indicative of the typical performance of all non-edge strips.

By splitting the distribution in Figure 22.5 (left) into five regions with an equal number of counts, position sensitivity is achieved. The SmartPET detectors have a strip pitch of 5mm and thus this approach provides an effective spatial resolution of 1mm in the x-y plane. In order to validate this approach, the event-by-event asymmetry parameter was calculated and histogrammed as a function of collimator position. Figure 22.5 (right) shows how the distribution shifts as the collimator moves in 1mm steps across the strip.

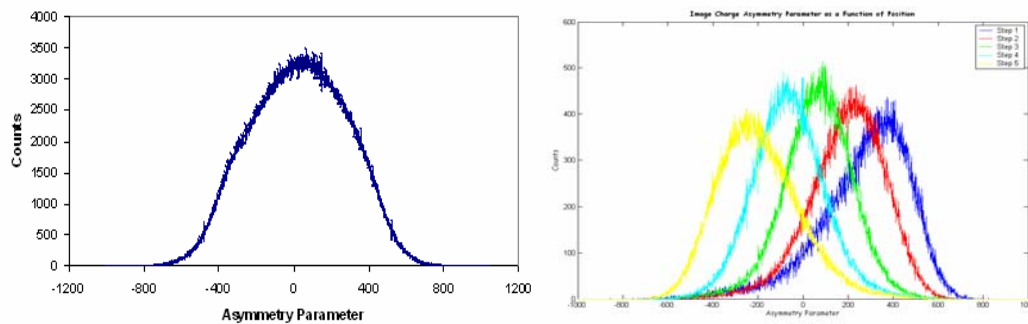


Figure 22.5: (left) Distribution of the event-by-event image charge asymmetry parameter resulting from a typical strip. Region of interest selection facilitates identification of the lateral interaction position. (right) The image charge asymmetry distribution is seen to shift as a function of interaction position (one on right difficult to see).

Coincident PET data were recorded with the SmartPET imager. Three  $^{22}\text{Na}$  sources were positioned between the two detectors on a rotation system and data was collected in  $5^\circ$  increments over a full  $180^\circ$ . Initially the data was analysed to select only those coincident interactions which deposited full energy in a single pixel of each detector. The excellent energy resolution of the SmartPET detectors (less than 1.5keV FWHM at 122keV) ensured that these were high quality events allowing accurate lines of response (LORs) to be defined between the two detectors. While the removal of events depositing energy in multiple pixels eliminates the majority of Compton scattered gamma ray interactions, no method for the identification of multiple interactions within a single pixel was employed. As the image reconstruction algorithms initially applied to the data only defined lines of response between directly opposite pixels, the effect of scattering through the depth profile of the detector is negligible. Similarly, depth of interaction identification was not required as no correction for parallax error is necessary. As a result, only image charge analysis was employed in processing the data.

For all non-edge strips, the total image charge asymmetry distribution was calculated and parameterised using the approach detailed previously. From this analysis a “look-up table” was produced allowing each strip to be effectively subdivided into five regions. The orthogonal double sided strip configuration of the detectors means that this technique results in each pixel being subdivided into twenty five position sensitive regions. The image charge asymmetry was then calculated and the interaction position of each gamma ray localised on an event-by-event basis. The output of this PSA routine forms the input to image

reconstruction algorithms. Images were reconstructed with and without the use of PSA in order to compare the spatial resolution achievable and investigate the impact on image quality.

The images were reconstructed using both statistical and analytic methods. Both approaches show good localisation of the point sources in space while the excellent energy resolution of the SmartPET system is reflected in a low background. In Fig. 22.6 images of one of the point sources are shown with (right) and without (left) processing of the data with image charge analysis algorithms.

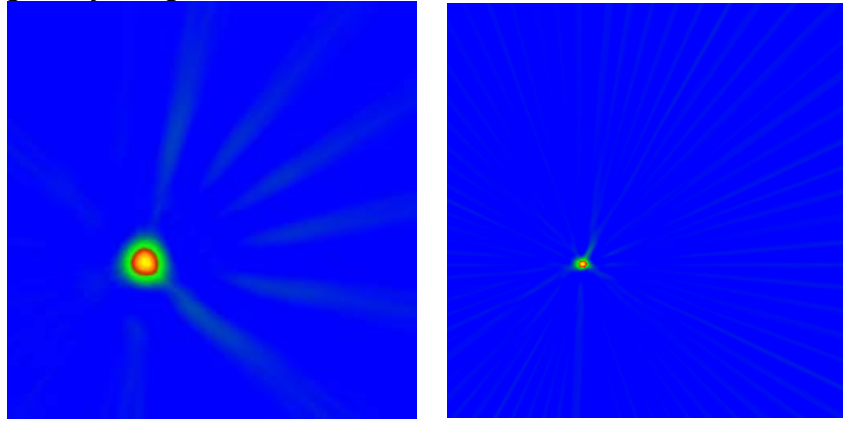


Figure 22.6: Point source images from the SmartPET system. Image (left) was reconstructed without the use of PSA while (right) used simple image charge asymmetry parameterisation to improve the lateral position sensitivity.

In order to quantify the improvement in image quality achieved through the use of PSA a simple calculation of the Full Width Half Maximum (FWHM) of the source peak was performed. As the peak may not be three dimensionally symmetric about the centroid, projections are taken through the x and y axes and a mean value calculated. The results are summarized in Table 22.1.

	<b>NO PSA</b>	<b>PSA</b>
<b>FWHM<sub>x</sub></b>	7.44mm	2.81mm
<b>FWHM<sub>y</sub></b>	8.01mm	3.75mm
<b>FWHM<sub>ave</sub></b>	<b>7.72mm</b>	<b>3.28mm</b>

Table 22.1: Summary of the FWHM values calculated for the reconstructed image

These results show how the spatial resolution of the PET images is improved by a factor of greater than two by the application of PSA techniques.

Further work is continuing to improve the performance of the simple parametric PSA algorithms.

### 22.3. New cooling method: He cooling

This R&D project consists of cooling down germanium detectors (Ge) and keep them cold with gaseous helium (GHe) cooled itself by liquid nitrogen (LN<sub>2</sub>). Usually these detectors are cooled down and kept cold with LN<sub>2</sub> when operating; requiring a large apparatus to fill up regularly the Ge Dewar's before and during the experiments. When this project began, the mean time between fillings was estimated to be around 4 hours for an array such as AGATA. The filling time is about 20 minutes long and might not allow data acquisition for physics during that time because of the increased background noise. Therefore to improve this duty cycle we have proposed a permanent cooling system based upon He gas which should be less noisy than LN<sub>2</sub>. This GHe would be cooled by LN<sub>2</sub> in a heat exchanger.

The R&D project was split into 2 parts, which means developing a He loop in 2 different phases:

- **Forced loop of GHe** (phase 1) using a pumping unit, to evaluate the noise induced on a Ge detector by He flow, and the thermal effects on the crystal and the cryostat.
- **Natural convection of GHe** (phase 2) without any forced circulation in order to reduce the maintenance (no motor), and to avoid the risk of vibrations due to motors.

Because this R&D project could be implemented on the AGATA array, several detectors will have to be cooled down with only one loop. So the specifications required by the AGATA experiments are focused on developing a thermal shunt in order to connect and disconnect the detectors when cold, without interrupting the cooling loop.

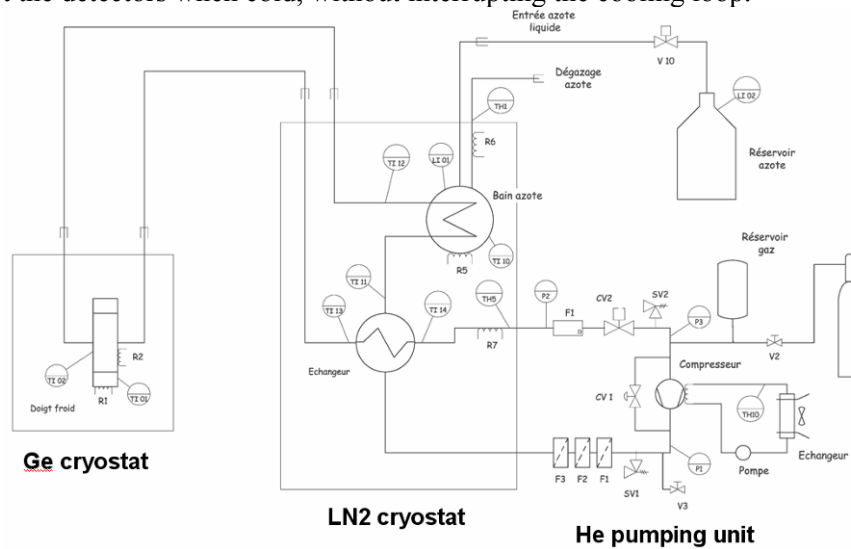


Figure 22.7: Forced He loop layout.

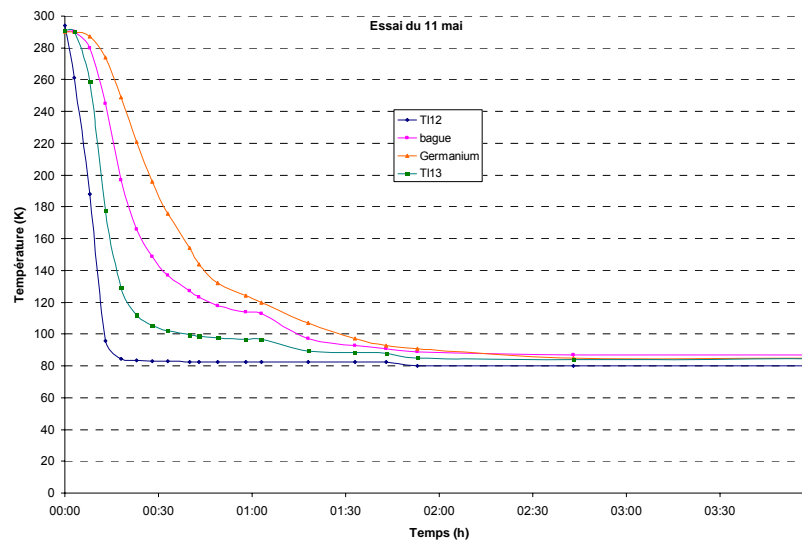


Figure 22.8: Temperature of a fake detector cooled with the forced He loop. The sensors were located at 4 places, at the output of the LN2 cryostat (blue line), at the entrance of the LN2 cryostat (after flowing in Ge cryostat) (green line), on the Ge crystal holding structure (pink line) and on the fake Ge crystal (orange line).

#### Phase 1: the forced He loop

The first step concerning the forced He loop was to build the pumping unit and to adapt a He exchanger inside a cryostat, previously developed to cool down Ge detectors with LN2 flow. Orsay laboratory took in charge the development of the He loop and the cryostat; the heat exchanger and the control/command was developed by the Saclay laboratory.

First a Ge crystal (fake detector) was integrated inside the Ge cryostat, in order to measure the temperature of the crystal with a Pt100 directly glued on it. All the thermal exchanges have been validated, both on cryostat and crystal.

The sensors were located at 4 places:

Blue: He leaving the LN2 cryostat

Green: He entering LN2 cryostat (after flowing in Ge cryostat)

Pink: Ge crystal holding

Orange: Ge crystal

A further step was to integrate a functional Ge detector and proceed to measure the energy resolution. After poor results due to the sensitive surface handled several times and a mechanical that was too microphonics, it was decided to modify the cryostat in order to integrate an existing Ge detector (relative efficiency of 20%, CANBERRA/EURISYS Strasbourg Fr) consisting in dismounting the detector assembly (capsule, gold finger and electronics) from its LN2 Dewar and to mount it on the He cryostat. That was done by the IPNO team in a clean room in order to protect the Ge crystal from contaminations, dust, humidity.

The results with  $^{60}\text{Co}$  were encouraging:

- 2.3 keV @1.332 MeV in its original cryostat (after thermal annealing);
- after assembly integration in the He loop : 2.7-2.8 keV @1.332 MeV.

Then it was decided to integrate another Ge detector, EUROBALL-type, encapsulated in a hermetically sealed can on the cryostat. This detector has been already tested in its original cryostat (made by CTT Company, Cologne Ge), in order to compare its performance after integration into the He loop.



Figure 22.9: Detector used for He Loop. Left : Eurisys cryostat. Right : IPNO cryostat.

Phase2: The thermal shunt

The main problem due to the specifications of AGATA is to be able to disconnect one detector from the general cooling system while it is cold. A specific mechanics has then been developed for that purpose (thermal shunt).

It is made up of three cones:

- the first one is the cold finger,
- the intermediate one will be in contact with air when the system is open,
- the outer one has the heat exchanger on it.

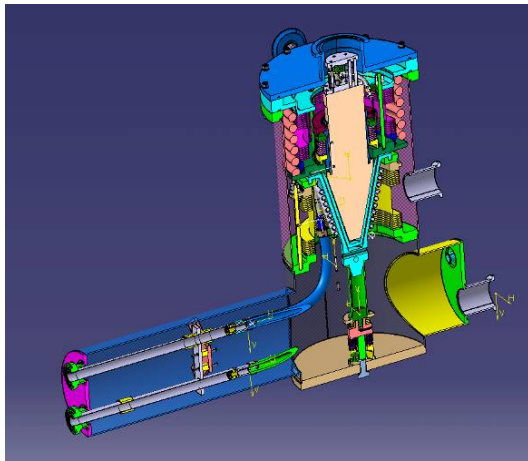


Figure 22.10: Drawing (left) and photograph (right) of the thermal shunt.

The whole system is in vacuum so as to avoid frost and thermal loss. A screw placed at the bottom of the shunt allows getting the outer cone in contact with the intermediate one. They can then be separated to disconnect the system or put together to start the cooling of the detector. He gas is added between the cold finger and the intermediate cone to improve the heat transfer.

A first test of the thermal shunt has been performed to characterize the thermal efficiency of the system.

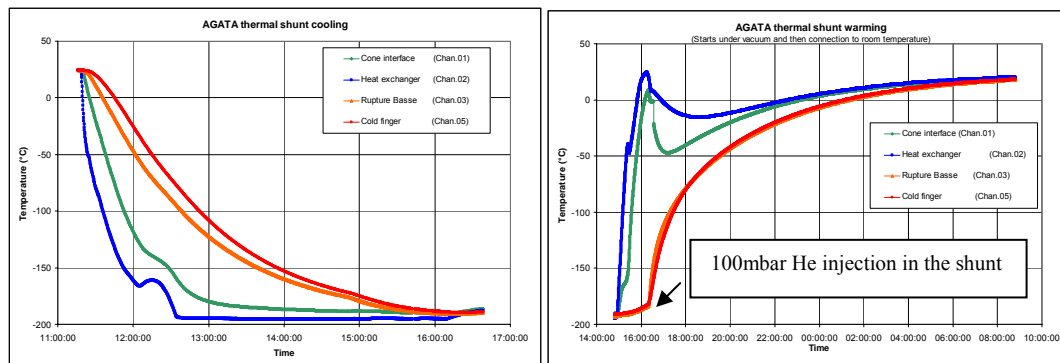


Figure 22.11: Cooling and warming of the thermal shunt

It appeared that the positioning of the cold finger was maybe not as expected and then a new mechanical part was realized to hold it precisely. The whole system will be mounted on the IPNO He loop for further thermal tests. Then, the thermal shunt will be sent to CTT to mount an encapsulated crystal in a dedicated cryostat.

#### 22.4. Conclusions

As we see from these reports, the R&D developments performed in the framework of the AGATA project will lead to applications that will go far beyond the nuclear basic research that is the aim of the core project. The main outputs will bring new opportunities for interdisciplinary or even industrial projects in various fields such as: satellite astrophysics, medical imaging, health and environmental physics or homeland security.



## 23. Organisational Structure and management

The operation and management of the AGATA project for the operation and construction phase is defined in the AGATA Memorandum of Understanding.

The organisation for the construction and the operation of the AGATA project comprises the following bodies:

The AGATA Steering Committee (ASC), acting on behalf of the Parties, is responsible for the Project coordination and the science policy of the collaboration.

The AGATA Collaboration Council (ACC), representing all the institutions collaborating under the AGATA project, advises the ASC on scientific matters.

The AGATA Project Manager (PM) and the AGATA Management Board (AMB) are responsible for the execution of the Project along the lines defined by the ASC.

The terms of reference of each of these bodies is given in more detail below.

### **AGATA Steering Committee (ASC)**

#### **Membership:**

Members are nominated by the Parties of the MoU. Contributing Parties of a country which represent more than 10% of the total capital investment will have two members, all other contributing Parties of a country will have one member.

The AGATA Project Manager and the AGATA Spokesperson attend meetings for consultation only and therefore without voting rights. The ASC can invite others to attend as needed for consultation only, for example the Campaign Spokespersons and Local Campaign Managers.

#### **Voting rights:**

Members have voting rights if they represent a Party having contributed at least one AGATA unit or the equivalent monetary value to the Project. Groups of Parties contributing together the equivalent of an AGATA unit can also have a vote by agreeing to join together. Additional voting rights will be attributed by ASC for each future commitment to the Project of one AGATA unit or the equivalent monetary value.

#### **Terms of reference:**

The ASC is the decision-making body of the AGATA Collaboration and responsible for the allocation of resources supplied by the Parties and the collaborating institutions. The ASC will ensure that the primary criterion for deployment of any equipment is based on scientific merit.

The tasks of the Steering Committee are as follows:

- define the scientific policy of the AGATA Collaboration taking advice from the AGATA Collaboration Council.
- elect a chair and vice-chair among its members who will each serve for a period of two years.
- appoint a project manager and members of the AGATA Management Board.
- monitor the Project based on reports received from the Project Manager.
- decide on any modification of the Project proposed by the Project Manager.
- decide on the experiment campaigns for AGATA and the timetable for the deployment of AGATA systems at various facilities.

- appoint the Campaign Spokesperson for each experiment campaign.
- review the scientific progress of each experimental campaign based on reports received from the Campaign Spokesperson.
- review the running cost statements and allocations

Decisions in the ASC shall be taken by consensus.

The ASC shall not make any decision unless a quorum of two thirds of the votes are represented.

Minutes of each meeting shall be drafted by the chairperson to the other members without delay. The minutes of each meeting shall be considered as accepted by the other members if, within thirty calendar days from receipt, the other members have not objected in writing to the chairperson.

The ASC chair signs on behalf of the ASC all written agreements.

### **AGATA Project Manager (PM)**

The AGATA Project Manager is appointed by the ASC to coordinate the execution and implementation of the project. For this purpose the PM can create and dissolve working groups as needed and after acceptance of the ASC. The PM will nominate the chairpersons of these working groups.

### **AGATA Management Board (AMB)**

#### **Membership of the AMB:**

The AGATA Project Manager; Chairpersons of the working groups; Chairperson of ASC (ex-officio). The AGATA Project Manager will chair the AMB.

The Local Campaign Manager(s) nominated by each Host are invited to attend.

#### **Voting rights:**

All members have equal voting rights.

#### **Terms of Reference:**

The AMB executes and implements the project. The AMB shall report to and be accountable to the ASC through the AGATA Project Manager.

The tasks of the AMB are as follows:

- supervise the effective and efficient implementation of the Project.
- collect information on the progress of the Project, examine that information to assess the compliance of the Project with the programme decided by the ASC and, if necessary, propose modifications of the programme to the ASC.
- provide reports of the progress of the Project to the ASC including an annual planning and resource report.
- advise the ASC on technical issues.
- work with the Local Campaign Manager of each Host to ensure the successful operation of AGATA.
- organise AGATA working group meetings as needed.

### **AGATA Collaborating Council (ACC) and AGATA Spokesperson**

#### **Membership:**

One representative from each collaborating institution and the AGATA Spokesperson. The AGATA Spokesperson chairs meetings of the ACC.

The Campaign Spokespersons are invited to attend.

**Voting:**

All members have equal voting rights. The AGATA Spokesperson is excluded from any vote concerning the Spokesperson role.

**Terms of Reference:**

The ACC is the advisory body of the ASC on scientific matters concerning the AGATA project.

The tasks of the ACC are as follows:

- elect the AGATA spokesperson who will serve for a period of two years.
- advise the ASC on scientific matters concerning the AGATA project and the research programme through the AGATA Spokesperson.
- nominate the Campaign Spokesperson for each experiment campaign to the ASC.
- hold meetings, at least annually, to receive reports from the ASC and AMB on the progress of the Project and from the Campaign Spokespersons on the progress of the research programme.
- hold an annual open meeting of the AGATA Collaboration to present the status of the Project and to discuss future experiment campaigns.